



UNIVERSITEIT VAN PRETORIA
UNIVERSITY OF PRETORIA
YUNIBESITHI YA PRETORIA
Denkies • Leading Minds • Dikgopolo tsa Dihalefi

Investigation into Simulation of Phase- Change Jet Impingement for Electronics Cooling

by

Daniell Wright

Submitted in partial fulfilment of the requirements for the degree

MASTER OF ENGINEERING (MECHANICAL ENGINEERING)

in the

Department of Mechanical and Aeronautical Engineering

**FACULTY OF ENGINEERING, Built Environment and Information
Technology**

UNIVERSITY OF PRETORIA

April 2022

Summary

Investigation into Simulation of Phase-Change Jet Impingement for Electronics Cooling

by

Daniell Wright

Supervisor: Prof KJ Craig
Co-Supervisors: Prof JP Meyer, Prof P Valluri (University of Edinburgh)
Department: Mechanical and Aeronautical Engineering
University: University of Pretoria
Degree: Master of Engineering (Mechanical Engineering)
Keywords: Jet Impingement, Boiling, Heat Transfer, Electronics Cooling, Computational Fluid Dynamics (CFD)

It is now widely accepted that conventional electronics cooling methods are no longer sufficient to keep modern-day electronic components below their maximum operating temperatures. As a result, thermal considerations have become the limiting factor in the improvement of semiconductors. To meet the cooling requirements of these devices, new cooling methods are needed. To keep up with the heat removal requirements of electronic components, researchers have investigated multiphase cooling methods extensively. They have identified jet impingement boiling as one of the most promising thermal management techniques for high heat flux applications.

Jet impingement boiling has been studied extensively in the literature, and researchers have identified the key jet parameters and their influence on heat transfer. Unfortunately, only a few numerical studies have been reported in the literature and they are limited to single jets. The numerical studies on jet impingement boiling available in the literature do not provide all the sub-models used in the numerical study, leaving much uncertainty. With the limited application of single jets and the limited information resulting from experimental studies, numerical studies on multijet arrays are essential for the advancement of jet impingement boiling and widespread use thereof in the electronics cooling industry.

In this study, both submerged single round jets and confined multijet arrays were investigated numerically, using the Eulerian multiphase framework with the Rensselaer Polytechnic Institute (RPI) boiling model to predict heat transfer, as implemented in ANSYS Fluent. The numerical results of the single-jet case correlated well with reported experimental data and with previously reported numerical results. The numerical results of the multijet array correlated well with experimental data reported in the literature, proving that the RPI boiling model could successfully predict the heat transfer of jet array boiling. The effect of conjugate heat transfer in jet impingement boiling heat transfer was also investigated for single- and multijet cases. The single-jet results agreed with previously reported numerical studies. To improve numerical convergence, especially for higher heat fluxes, a hydrostatic pressure gradient was used at the outlet. This allowed for significant improvement in the convergence of the continuity equation.

Finally, parametric analyses were conducted for both single- and multijet arrays in the fully developed nucleate-boiling regimes. Parameters included jet-to-surface spacing and jet Reynolds number for single submerged jets. Parameters for confined multijet arrays included jet-to-surface

spacing, jet-to-jet spacing and jet Reynolds number. The results of single submerged jets correlated well with experiments reported in the literature. The results of the multijet array cases showed less sensitivity to changes in jet velocity and jet-to-surface spacing than for the single-jet case. The multijet array cases showed much higher sensitivity to the jet-to-jet spacing than to the jet-to-surface spacing and jet Reynolds number, indicating that both jet-to-jet interaction and cross-flow played significant roles in the heat transfer of multijet arrays, confirming the observations of experiments reported in the literature.

The study concluded that the RPI boiling model could successfully predict the heat transfer of jet impingement boiling and could be used to conduct parametric investigations that align well with the experimental findings. The study further concluded that more experimental studies of multijet arrays in the nucleate-boiling regime with low degrees of subcooling were required to further validate the numerical models. It was found that a bubble departure frequency model applicable to flow boiling with high degrees of subcooling was essential to model boiling jets with high degrees of subcooling. Finally, the influence of the jet parameters on pressure drop and the influence of the heat transfer fluid on heat transfer as well as the operating pressure were identified as two major challenges that must be met before jet impingement boiling can be widely implemented.

Declaration of Originality

The **Department of Mechanical and Aeronautical Engineering** places great emphasis upon integrity and ethical conduct in the preparation of all written work submitted for academic evaluation.

The following declaration is required by the **Department of Mechanical and Aeronautical Engineering**:

Full names of student: Daniell Wright


Student number: 16003463

Topic of work: Investigation into Simulation of Phase-Change Jet Impingement for Electronics Cooling

Declaration

1. I understand what plagiarism is and am aware of the University's policy in this regard.
2. I declare that this dissertation is my own original work. Where other people's work has been used (either from a printed source, Internet, or any other source), this has been properly acknowledged and referenced in accordance with departmental requirements.
3. I have not used work previously produced by another student or any other person to hand in as my own.
4. I have not allowed and will not allow anyone to copy my work with the intention of passing it off as his or her own work.

SIGNATURE



Acknowledgements

I would hereby like to acknowledge the following people and organisations for their part in this dissertation and the accompanying journal article:

- my supervisor, Prof Ken Craig. I am grateful for his support and guidance throughout my honours and master's degrees and for all his input into the reviewing of my drafts for my dissertation and journal article. I am grateful for the relationship he has with all his students, allowing supervision at a personal level, allowing him to give much better guidance;
- my co-supervisor, Prof Prashant Valluri. I am grateful for his support and guidance throughout my master's degree and for his input into my journal article. I am grateful for his role in providing me with a bursary and my secondment to the United Kingdom;
- my co-supervisor, Prof Josua Meyer. I am grateful for his input into my journal article and dissertation. I am grateful for his role in providing me with a bursary and giving me the opportunity to visit the United Kingdom, my first time leaving South Africa;
- the University of Pretoria and ThermaSMART, for providing the funding for my postgraduate studies and my secondment to the United Kingdom;
- the University of Edinburgh and staff, for their warm welcome to Scotland and treating me as one of their own students during my stay there;
- the Centre of High Performance Computing (CHPC), South Africa, for providing the computational resources required for this project;
- my mother and my fiancée, for their endless love and support throughout my studies.

Publications

Wright, D., Craig, K.J., Valluri, P., Meyer, J.P., Computational investigation of single and multi-jet array impingement boiling, submitted to Applied Thermal Engineering, 17 May 2022.

Table of Contents

Summary	i
Declaration of Originality	iii
Acknowledgements.....	iv
Publications.....	v
List of Figures	viii
List of Tables	xii
Nomenclature	xiii
Greek Symbols	xiii
Subscripts	xiii
Acronyms and abbreviations	xiv
1 Introduction	1
1.1 Background and Motivation	1
1.2 Problem Statement	4
1.3 Objectives and Scopes	4
1.4 Layout of Dissertation	5
2 Literature Study	6
2.1 Introduction	6
2.2 Liquid Jet Impingement.....	6
2.2.1 Hydrodynamics of Jet Impingement	6
2.2.2 Characterising Heat Transfer in Liquid Jet Impingement.....	8
2.2.3 Jet Arrays.....	9
2.2.4 Enhancement Techniques.....	10
2.3 Boiling	11
2.3.1 Pool Boiling Background	11
2.3.2 Flow Boiling.....	13
2.3.3 Nucleate Boiling	16
2.3.4 Heat Transfer Enhancement	19
2.4 Jet Impingement with Boiling	19
2.4.1 Boiling Curve for Jet Impingement Boiling.....	19
2.4.2 Nucleate Boiling	20
2.4.3 Effect of jet parameters in jet impingement boiling.....	22
2.5 Numerical Framework	24
2.5.1 Eulerian Multiphase Framework.....	24
2.5.2 Governing Equations.....	25
2.5.3 Turbulence Modelling	25



2.5.4	Interphase Transfer Models.....	26
2.5.5	RPI Wall-Boiling Model.....	29
2.5.6	Solution Method	31
3	Computational Fluid Dynamics Model and Validation	32
3.1	2D Axisymmetric Single Jet	32
3.1.1	Problem Description	32
3.1.2	Numerical Modelling.....	33
3.1.3	Results and Discussion	36
3.2	3D Multijet Array with Cross-flow	43
3.2.1	Problem Description	43
3.2.2	Numerical Modelling.....	47
3.2.3	Results and Discussion	50
4	Parametric Analyses.....	64
4.1	2D Axisymmetric Single Jet	64
4.2	3D Jet Array.....	71
4.2.1	Jet-to-Surface Spacing and Reynolds Number.....	71
4.2.2	Jet-to-Jet Spacing	84
5	Conclusions and Future Work.....	92
5.1	Conclusions	92
5.2	Future work.....	93
	References	95
	Appendix A: Influence of Virtual Mass Coefficient	A
	Appendix B: Surface Temperature and Heat Flux Contours for 3D Multijet Array Without Considering Conjugation.....	C
	Appendix C: Numerical Procedure.....	F
	Appendix D: Data Processing	H
	Data Processing Code for 2D Axisymmetric Jet	H
	Matlab Data Processing Code for 3D Jet Array.....	N

List of Figures

Figure 1: Layout of remote cooling of a CPU, adapted from Ref. [3]	1
Figure 2: Embedded jet impingement cooling solution, adapted from Ref. [13]	3
Figure 3: Liquid jet impingement categories, adapted from Ref. [14].....	6
Figure 4: Jet flow regions for a single confined jet [15].....	7
Figure 5: Typical circulation pattern in the confined jet array [16]	9
Figure 6: Typical pool-boiling curve for water at atmospheric pressure [17]. Critical heat flux (CHF), minimum heat flux (MHF) and onset of nucleate boiling (ONB)	12
Figure 7: Flow and heat transfer progress of subcooled flow boiling in a heated pipe [20]	14
Figure 8: Variation in heat transfer coefficient with heat flux in flow boiling, where the heat flux increases from (a) to (d), adapted from Ref. [20].....	16
Figure 9: Boiling heat transfer mechanism under an isolated bubble, adapted from Ref. [22]	17
Figure 10: Isolated bubble growth and departure cycle in nucleate pool boiling, adapted from Ref. [22]	17
Figure 11: Bubble behaviour and local wall temperature under the isolated bubble ($\Delta T_{\text{sat}}=10.8$ K, $D_{\text{max}}=4.4$ mm) [22].....	18
Figure 12: Spatiotemporal distributions of local wall temperature (left) and local wall heat flux (right), ($\Delta T_{\text{sat}}=10.8$ K, $D_{\text{max}}=4.4$ mm), adapted from Ref. [22]	19
Figure 13: Liquid jet impingement boiling curve [23].....	20
Figure 14: Free-surface jet impingement with nucleate boiling bubble behaviour. Nucleate boiling (left) and CHF (right) [24].....	21
Figure 15: Schematic of the RPI boiling model, illustrating the heat flux components of the RPI wall-boiling model [43].....	29
Figure 16: Experimental set-up used in the Katto and Kunihiro experimental study to investigate the burnout characteristics of jet impingement boiling [28].....	32
Figure 17: 2D Axisymmetric domain based on the Katto and Kunihiro experiment [28] without considering conjugation heat transfer effects [42]. Hydrostatic pressure gradient included at the radial outlet.....	33
Figure 18: 2D Axisymmetric domain based on the Katto and Kunihiro experiment [28] considering conjugation heat transfer effects [42]. Hydrostatic pressure gradient included at the radial outlet ..	34
Figure 19: Coarse mesh for 2D axisymmetric domain used for the approximation of the Katto and Kunihiro experiment [28] without considering conjugation heat transfer effects [42]	35
Figure 20: Boiling curve validation for the Katto and Kunihiro experiment [28] using the stagnation region wall temperature	36
Figure 21: Stagnation region wall superheat, heated surface average wall superheat and wall heat flux vs flow time for 2D single-jet case without conjugation heat transfer effects	37
Figure 22: Stagnation region wall superheat, heated surface average wall superheat and wall heat flux vs flow time for 2D single-jet case with conjugation heat transfer effects	38
Figure 23: Single-jet velocity contours [m/s] with overlaid vectors, at various wall heat fluxes: (a) 50 W/cm ² , (b) 100 W/cm ² , (c) 150 W/cm ² , (d) 200 W/cm ² , and (e) 250 W/cm ²	39
Figure 24: Single-jet liquid temperature contours [°C] at various wall heat fluxes: (a) 50 W/cm ² , (b) 100 W/cm ² , (c) 150 W/cm ² , (d) 200 W/cm ² , and (e) 250 W/cm ²	40
Figure 25: Single-jet vapour volume fraction contours at various wall heat fluxes: (a) 50 W/cm ² , (b) 100 W/cm ² , (c) 150 W/cm ² , (d) 200 W/cm ² , and (e) 250 W/cm ²	41
Figure 26: Vapour distribution plots for 2D axisymmetric case with conjugation at various heat fluxes	42

Figure 27: Single-jet boiling curve based on minimum, average and maximum surface temperatures for both the case without conjugation heat transfer as well as the case with conjugation heat transfer 42

Figure 28: Contribution of the RPI boiling model heat flux components to the wall heat flux for the single jet without and with conjugation heat transfer, as well as the results of the study by Ref. [42] 43

Figure 29: Devahdhanush and Mudawar experimental loop schematic [63]..... 44

Figure 30: Exploded view of jet impingement test module [63] 44

Figure 31: Sectional view of jet plate (left) and top view of jet plate and heated block (right)..... 45

Figure 32: Heated block thermocouple locations..... 46

Figure 33: 3D Quarter symmetry multijet array domain, adapted from the experiments of Devahdhanush and Mudawar [63] without considering conjugation heat transfer effects (no solid modelled)..... 48

Figure 34: 3D Quarter symmetry multijet array domain, adapted from the experiments of Devahdhanush and Mudawar [63] considering conjugation heat transfer effects (with solid copper and fibreglass insulation) 48

Figure 35: Coarse mesh for the 3D multijet array quarter symmetry domain without considering conjugation heat transfer effects (no solid modelled). The left and right views are referred to in figures presented in later chapters..... 50

Figure 36: Boiling curve validation of the multijet array numerical model against the experiment of the Devahdhanush and Mudawar [63] study using the average heated wall temperature..... 51

Figure 37: Heated surface average wall superheat and wall heat flux vs flow time for 3D multijet array case without conjugation heat transfer effects..... 52

Figure 38: Heated surface average wall superheat and wall heat flux vs flow time for 3D multijet array case with conjugation heat transfer effects 53

Figure 39: Liquid velocity contours [m/s] of the multijet array considering conjugation, using R134a as heat transfer fluid, at various wall heat fluxes: (a) 62 W/cm², (b) 109 W/cm², and (c) 156 W/cm² 55

Figure 40: Liquid temperature contours [°C] of the multijet array considering conjugation, using R134a as heat transfer fluid, at various wall heat fluxes: (a) 62 W/cm² and (b) 109 W/cm² 56

Figure 41: Liquid temperature contours [°C] of the multijet array considering conjugation, using R134a as heat transfer fluid, at 156 W/cm²..... 57

Figure 42: Vapour volume fraction contours of the multijet array considering conjugation, using R134a as heat transfer fluid, at 62 W/cm²..... 57

Figure 43: Vapour volume fraction contours of the multijet array considering conjugation, using R134a as heat transfer fluid, at various wall heat fluxes: (a) 109 W/cm² and (b) 156 W/cm² 58

Figure 44: Solid temperature contours [°C] for the multijet array considering conjugation, using R134a as heat transfer fluid, at various wall heat fluxes: (a) 62 W/cm², (b) 109 W/cm², and (c) 156 W/cm². Figures on the left are the left-side view, figures on the right are the right-side view..... 59

Figure 45: Heated surface temperature contours [°C] (left) and surface heat flux contours [W/m²] (right) of the multijet array considering conjugation, using R134a as heat transfer fluid, at various wall heat fluxes: (a) 62 W/cm², (b) 109 W/cm², and (c) 156 W/cm²..... 60

Figure 46: Wall heat transfer coefficient contours [W/m²·K] of the multijet array considering conjugation, using R134a as heat transfer fluid, at various wall heat fluxes: (a) 62 W/cm², (b) 109 W/cm², and (c) 156 W/cm² 61

Figure 47: Iso-surfaces of vapour volume fraction of 0.5 coloured by velocity magnitude for the multijet array considering conjugation, using R134a as heat transfer fluid, at various wall heat fluxes: (a) 109 W/cm² and (b) 156 W/cm² 62

Figure 48: R134a multijet array boiling curve based on minimum, average and maximum surface temperatures for both the case without conjugation heat transfer as well as the case with conjugation heat transfer 63

Figure 49: Contribution of the RPI boiling model heat flux components to the wall heat flux for the R134a jet array without and with conjugation heat transfer 63

Figure 50: Velocity contours [m/s] for the single-jet case with $Re = 20000$ for various jet-to-surface spacings, at 50 W/cm^2 with conjugation: (a) $H/D = 1$, (b) $H/D = 2$, (c) $H/D = 4$, and (d) $H/D = 8$ 65

Figure 51: Velocity contours [m/s] for the single-jet case with $H/D = 8$ for various jet Reynolds numbers, at 50 W/cm^2 with conjugation: (a) $Re = 10\ 000$, (b) $Re = 15\ 000$, (c) $Re = 20\ 000$ 66

Figure 52: Vapour volume fraction distribution plots for the single-jet case with $Re = 20\ 000$ for various jet-to-surface spacings, at 50 W/cm^2 with conjugation 67

Figure 53: Vapour volume fraction distribution plots for the single-jet case with $H/D = 8$ for various jet Reynolds numbers, at 50 W/cm^2 with conjugation 68

Figure 54: Heated wall temperature plots [$^{\circ}\text{C}$] for the single-jet case with $Re = 20\ 000$ for various jet-to-surface spacings, at 50 W/cm^2 with conjugation 68

Figure 55: Heated wall temperature plots [$^{\circ}\text{C}$] for the single-jet case with $H/D = 8$ for various jet Reynolds numbers, at 50 W/cm^2 with conjugation 69

Figure 56: Heat transfer coefficient (HTC) as calculated for a single water jet as a function of jet Reynolds number (Re) and jet-to-surface spacing (H/D), at 50 W/cm^2 with conjugation: (a) based on the total heat flux, (b) based on the quenching heat flux component, and (c) based on the evaporative heat flux component. (d) is the pressure drop over the impinging device 70

Figure 57: Liquid velocity contours [m/s] for the multijet array case with $Re = 50\ 000$ for various jet-to-surface spacings, at 100 W/cm^2 with conjugation: (a) $H/D = 1$ and (b) $H/D = 2$. Figures on the left are the left-side view, figures on the right are the right-side view. The views are shown in Fig. 35. .. 71

Figure 58: Liquid velocity contours [m/s] for the multijet array case with $Re = 50\ 000$ for various jet-to-surface spacings, at 100 W/cm^2 with conjugation: (a) $H/D = 4$ and (b) $H/D = 8$. Figures on the left are the left-side view, figures on the right are the right-side view. The views are shown in Fig. 35. .. 72

Figure 59: Liquid velocity contours [m/s] for the multijet array case with $H/D = 8$ for various jet Reynolds numbers, at 100 W/cm^2 with conjugation: (a) $Re = 30\ 000$, (b) $Re = 40\ 000$ and (c) $Re = 50\ 000$. Figures on the left are the left-side view, figures on the right are the right-side view. The views are shown in Fig. 35. 73

Figure 60: Vapour volume fraction contours (left) and surface heat flux contours [W/m^2] (right) for the multijet array case with $Re = 50\ 000$ for various jet-to-surface spacings, at 100 W/cm^2 with conjugation: (a) $H/D = 1$, (b) $H/D = 2$, (c) $H/D = 4$, and (d) $H/D = 8$. The red line in the figures encloses the heated region. 76

Figure 61: Vapour volume fraction contours (left) and surface heat flux contours [W/m^2] (right) for the multijet array case with $H/D = 8$ for various jet Reynolds numbers, at 100 W/cm^2 with conjugation: (a) $Re = 30\ 000$, (b) $Re = 40\ 000$, and (c) $Re = 50\ 000$. The red line in the figures encloses the heated region. 78

Figure 62: Heated surface temperature contours [$^{\circ}\text{C}$] (left) and surface heat flux contours [W/m^2] (right) for the multijet array case with $Re = 50\ 000$ for various jet-to-surface spacings, at 100 W/cm^2 with conjugation: (a) $H/D = 1$, (b) $H/D = 2$, (c) $H/D = 4$, and (d) $H/D = 8$. The red line in the figures encloses the heated region..... 80

Figure 63: Heated surface temperature contours [$^{\circ}\text{C}$] (left) and surface heat flux contours [W/m^2] (right) for the multijet array case with $H/D = 8$ for various jet Reynolds numbers, at 100 W/cm^2 with conjugation: (a) $Re = 30\ 000$, (b) $Re = 40\ 000$, and (c) $Re = 50\ 000$. The red line in the figures encloses the heated region. 82

Figure 64: Heat transfer coefficient (HTC) as calculated for a multijet array as a function of jet Reynolds number (Re) and jet-to-surface spacing (H/D), at 100 W/cm^2 with conjugation: (a) based on the total heat flux, (b) based on the quenching heat flux component, and (c) based on the evaporative heat flux component. (d) is the pressure drop over the jet array. 83

Figure 65: Domain modifications for the jet-to-jet spacing parametric study keeping all other jet parameters constant..... 84

Figure 66: Liquid velocity contours [m/s] for the multijet array case with $V_{jet} = 4.01 \text{ m/s}$ and $H/D = 2$ for various jet-to-jet spacings, at 50 W/cm^2 with conjugation: (a) $p_{jet}/D = 2$, (b) $p_{jet}/D = 4$, (c) $p_{jet}/D = 6$, and (d) $p_{jet}/D = 8$. Figures on the left are the left-side view. The views are shown in Fig. 35. 85

Figure 67: Vapour volume fraction contours (left) and surface heat flux contours [W/m^2] (right) for the multijet array case with $V_{jet} = 4.01 \text{ m/s}$ and $H/D = 2$ for various jet-to-jet spacings, at 50 W/cm^2 with conjugation: (a) $p_{jet}/D = 2$, (b) $p_{jet}/D = 4$, (c) $p_{jet}/D = 6$, and (d) $p_{jet}/D = 8$. The red line in the figures encloses the heated region..... 87

Figure 68: Heated surface temperature contours [$^{\circ}\text{C}$] (left) and surface heat flux contours [W/m^2] (right) for the multijet array case with $V_{jet} = 4.01 \text{ m/s}$ and $H/D = 2$ for various jet-to-jet spacings, at 50 W/cm^2 with conjugation: (a) $p_{jet}/D = 2$, (b) $p_{jet}/D = 4$, (c) $p_{jet}/D = 6$, and (d) $p_{jet}/D = 8$. The red line in the figures encloses the heated region..... 89

Figure 69: Heat transfer coefficient (HTC) as calculated for a multijet array as a function of jet-to-jet spacing (p_{jet}/D), at 50 W/cm^2 with conjugation: (a) based on the total heat flux, (b) based on the quenching heat flux component, and (c) based on the evaporative heat flux component. 91

Figure A - 1: Vapour volume fraction contours for the single axisymmetric jet not considering conjugation for various virtual mass coefficients: (a) $C_{VM} = 0$, (b) $C_{VM} = 0.25$, (c) $C_{VM} = 0.5$, (d) $C_{VM} = 0.75$, (e) $C_{VM} = 1$, (f) $C_{VM} = 1.25$, and (g) $C_{VM} = 1.5$ B

Figure A - 2: Heated surface temperature contours [$^{\circ}\text{C}$] (Left) and surface heat flux contours [W/m^2] (Right) of the multi-jet array without considering conjugation, using R134a as heat transfer fluid, at various wall heat fluxes: (a) 62 W/cm^2 , (b) 109 W/cm^2 , and (c) 156 W/cm^2 D

Figure A - 3: Heated surface temperature contours [$^{\circ}\text{C}$] (Left) and surface heat flux contours [W/m^2] (Right) of the multi-jet array considering conjugation, using R134a as heat transfer fluid, at various wall heat fluxes: (a) 62 W/cm^2 , (b) 109 W/cm^2 , and (c) 156 W/cm^2 E

Figure A - 4: Data processing Matlab code for single axisymmetric jet without conjugation. I

Figure A - 5: Data processing Matlab code for single axisymmetric jet with conjugation. J

Figure A - 6: Matlab code for plots of the single axisymmetric jet..... L

Figure A - 7: Python code for contours of the single axisymmetric jet parametric study. N

Figure A - 8: Data processing Matlab code for multi-jet array without conjugation..... O

Figure A - 9: Data processing Matlab code for multi-jet array with conjugation. P

Figure A - 10: Matlab code for plots of the multi-jet array..... S

Figure A - 11: Python code for contours of the multi-jet array parametric study..... T

List of Tables

Table 1: Influence of jet-to-surface spacing on jet interaction in jet arrays [16]	10
Table 2: Inlet and outlet conditions of the 2D axisymmetric domain based on the Katto and Kunihiro experiment [28] for both the case with conjugation and the one without it.....	34
Table 3: Properties of water at 1 atm pressure [42].....	34
Table 4: Properties of copper [61]	35
Table 5: 2D Axisymmetric single-jet mesh refinement study results at 50 W/cm ² applied heat flux. .	35
Table 6: 3D Jet array in nucleate-boiling regime parameters, adapted from Ref. [63].....	46
Table 7: Properties of R134a at saturation pressure [35].....	49
Table 8: Properties of fibreglass [61]	49
Table 9: Inlet and outlet conditions of the 3D quarter symmetry multijet domain based on the experiments of Devahdhanush and Mudawar [63] for both the case with conjugation and the one without it.....	49
Table 10: 3D multijet array mesh refinement study results at a wall heat flux of 80 W/cm ²	50
Table 11: Sensitivity analysis of numerical model for the 3D multijet array case without conjugation at 109 W/cm ²	53
Table A - 1: Influence of virtual mass coefficient on wall temperature for the single axisymmetric jet without conjugation, at 50 W/cm ²	A
Table A - 2: Under-relaxation factors used in the present study.....	G

Nomenclature

A	area [m ²]
A_b	area of influence
A_i	interfacial area concentration
A_w	interfacial area density of the wall
C	correlation constant
C_p	constant pressure specific heat capacity [J/kg·K]
C_{vm}	virtual mass coefficient
D	diameter [m]
f	bubble departure frequency [Hz]
F	force [N]
g	gravitational acceleration [m/s ²]
G	turbulence production rate [kg/m·s ³]
h	convection heat transfer coefficient [W/m ² ·K]
h_{fg}	latent heat of vaporisation [J/kg]
H	jet height [m]
H/D	jet-to-surface spacing
Ja	Jacob number
k	turbulent kinetic energy [m ² /s ²]
\dot{m}	mass transfer rate [kg/s]
N	number of jets
Nu	Nusselt number
p	pressure [Pa]
p_{jet}	jet-to-jet spacing
p_{jet}/D	jet spacing to nozzle diameter ratio
Pr	Prandtl number
\dot{q}	heat flux [W/m ²]
Q	interfacial heat transfer [W/m ³]
Re	Reynolds number
S	source term in energy equation [W/m ³]
$S_{k,m}$	source term in kinetic energy equation [kg/m·s ³]
$S_{\epsilon,m}$	source term in dissipation rate equation [kg/m·s ⁴]
t	time [s]
T	temperature [K]
ΔT_{sat}	surface superheat [K]
ΔT_{sub}	liquid subcooling [K]
u, U	velocity [m/s]

Greek Symbols

α	phase volume fraction
ϵ	dissipation rate [m ² /s ³]
λ	liquid phase diffusivity [m ² /s]
μ	dynamic viscosity [N·s/m ²]
ρ	density [kg/m ³]
σ	surface tension [N/m]

Subscripts

b	bottom of base plate
-----	----------------------



<i>C</i>	liquid phase convection
<i>E</i>	evaporation
<i>G</i>	gas
<i>i</i>	inlet
<i>j</i>	junction
<i>L</i>	liquid
<i>lid</i>	lid
<i>L_s</i>	liquid side of the interfacial area
<i>L_v</i>	interaction between liquid and vapour phases
<i>m</i>	mixture
<i>N</i>	jet nozzle exit
<i>p</i>	phase <i>p</i>
<i>pq</i>	interaction between phases <i>p</i> and <i>q</i>
<i>q</i>	phase <i>q</i>
<i>Q</i>	quenching
<i>S</i>	surface
<i>sat</i>	saturation
<i>sub</i>	subcooling
<i>V</i>	vapour
<i>vs</i>	vapour side of the interfacial area
<i>w, W</i>	wall

Acronyms and abbreviations

<i>CFD</i>	computational fluid dynamics
<i>CHF</i>	critical heat flux
<i>HTC</i>	heat transfer coefficient
<i>MHF</i>	minimum heat flux
<i>ONB</i>	onset of nucleate boiling
<i>ONBD</i>	onset of nucleate boiling departure
<i>RNG</i>	renormalisation group methods
<i>TIM</i>	thermal interface material

1 Introduction

1.1 Background and Motivation

With the rapidly growing multibillion-dollar tech industry, the demand for high-performance semiconductors has increased exponentially. In recent decades, materials and manufacturing methods have experienced drastic improvement, resulting in smaller semiconductors, especially transistors. Transistors are commonly used in integrated circuits, such as microprocessors, and power applications such as amplifiers. Smaller transistors mean that more transistors can fit onto an integrated circuit, resulting in higher performance at the expense of more heat. To ensure optimal performance and lifetime of integrated circuits, heat must be extracted at the same rate at which it is generated without exceeding the operating temperature of the components. With high density transistors, heat is generated over a very small surface area, resulting in very high heat fluxes. Current microprocessors can generate heat fluxes of more than 100 W/cm^2 . With the significant rate of improvement, microprocessors are expected to generate heat fluxes of over 1 kW/cm^2 in coming years [1]. Wide bandgap devices such as silicon carbide metal-oxide-semiconductor field-effect transistors are commonly used in automotive power applications and these devices experience heat fluxes between 100 W/cm^2 and 1 kW/cm^2 [2]. In addition to these high heat fluxes, local hotspots can develop on the surface, which can result in even higher local heat fluxes. Conventional cooling methods are no longer sufficient to cool microprocessors. As a result, thermal considerations have become the limiting factor in the improvement of semiconductors. To meet the cooling requirements of these devices, new cooling methods must be investigated.

Conventional electronics cooling methods adopt the remote cooling approach where heat is conducted through layers of thermal interface materials (TIM) from the device to a heat spreader to the base plate of the cooling device (heat sink or cold plate). Heat is then rejected from the base plate by means of natural convection, forced convection or phase-change methods. Although remote cooling devices tend to be bulky and heat transfer is limited by the thermal resistance of the thermal interface materials, these devices are easy to implement and provide adequate cooling for many applications. Figure 1 [3] provides the layout of conventional remote (or indirect) cooling solutions for electronics, more specifically microprocessors. In the figure, T_j is the junction temperature (the part that must be cooled), T_{lid} the lid temperature, T_b the bottom of the base plate temperature, T_i the inlet air/water temperature, and the resistances are the thermal resistances of the interfaces between the die and cooling device. The cooling device can employ any of the cooling methods discussed next.

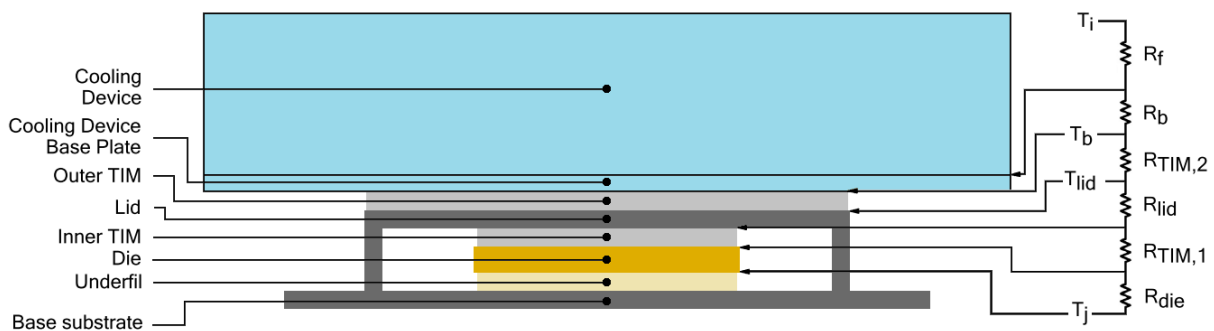


Figure 1: Layout of remote cooling of a CPU, adapted from Ref. [3]

Cooling methods can be classified into the following categories in ascending order of heat transfer effectiveness: natural convection, forced air cooling, forced liquid cooling, and boiling. Natural convection cooling methods are not suitable for cooling high-power density electronic devices; however, they are very popular in low-power density electronic devices due to very low cost, simplicity, and reliability [4]. Forced air cooling can achieve much higher heat transfer rates than with natural convection and is widely implemented in electronic devices such as personal computers and

amplifiers. State-of-the-art electronics cooling solutions use liquid cooling due to the increased rates of heat transfer compared with those of air cooling. Liquid cooling is commonly configured in microchannel heat sinks or jet impingement arrays.

Channel flow can be subdivided into three categories, namely conventional channels, minichannels and microchannels. The concept of microchannel heat sinks was first introduced in 1981 by Tuckerman and Pease [5]. They designed and tested microchannel heat sinks for very large-scale integrated circuits with power densities of up to 790 W/cm^2 . Although there is no formal definition or criterium to differentiate between mini- and microchannels, the hydraulic diameter is often used to define a microchannel. Kandlikar and Grande [6] note that microchannels have hydraulic diameters between $10 \mu\text{m}$ and $200 \mu\text{m}$. They found that smaller channel dimensions resulted in larger surface area to volume ratios and thus higher heat transfer coefficients at low liquid flow rates. However, the increase in heat transfer does come at the expense of increased pressure drop. A major drawback of microchannels is that the flow heats up along the length of the channel, which can result in large surface temperature gradients in the flow direction.

Jet impingement has been studied extensively and has become a very attractive method for heat extraction from hot surfaces. Jet impingement has been successfully implemented in a variety of industries such as heat treatment of materials, electronics cooling and turbine blade cooling. Jet impingement can achieve much higher heat transfer coefficients than with conventional convection cooling methods. One significant advantage of jet impingement over conventional cooling methods is the concentrated heat extraction capabilities, enabling it to alleviate hotspots on a surface. Like the case with microchannels where the fluid heats up along the length of the microchannels, the fluid heats up moving radially from the jet centre, causing large temperature gradients over the heated surface. This can be alleviated by configuring multiple jets in an array, which can achieve very high rates of heat transfer over a large surface area. Compared with microchannel liquid cooling, jet impingement can achieve much higher average heat transfer coefficients at lower pressure drops and thus pumping requirements. Due to the excellent heat transfer characteristics of jet impingement, it has become the focus of many researchers and engineers and is currently one of the most promising liquid cooling solutions. Researchers have identified the influence of various design parameters on heat transfer, pressure drop and various other design considerations such as required pumping power. Chapter 2 provides a literature review of the fundamentals of jet impingement and the influence of design parameters on heat transfer performance.

Even though single-phase cooling methods such as jet impingement can achieve very high rates of heat transfer, it is still inadequate for many applications. This led researchers to investigate phase-change cooling methods, and more specifically, boiling. Boiling can achieve very high rates of heat transfer due to the bubble-induced flow and accompanying latent heat transfer during liquid to vapour phase change. Pool boiling experiences a drastic drop in heat transfer once the critical heat flux (CHF) has been reached, which can severely damage the device being cooled. To prevent this from occurring, El-Genk and Ali [7] advised that the maximum design heat flux should not exceed 70% of the CHF. Flow boiling can achieve very high heat transfer rates and is one of the most successful heat removal methods for high heat density electronics. Microchannel flow boiling is an attractive cooling method due to the high heat transfer rates and compactness compared with conventional channel flow boiling. However, there are some challenges with implementation. Like single-phase microchannel heat sinks, microchannel flow boiling suffers from a high pressure drop over the device resulting in higher pumping power requirements [8]. Another major concern is flow boiling-instability, which can lead to flow oscillations resulting in premature CHF. Flow-boiling instability can be triggered by a variety of factors such as bubble clogging, rapid bubble growth, parallel channel interaction, upstream compressibility, and flow reversal [9].

Jet impingement boiling offers superior heat transfer performance compared with microchannel flow boiling as well as lower pressure drops [8]. The lower pressure drop reduces the pumping power requirements and makes it easier to regulate the system pressure as well as flow rate. Mudawar [10] suggests in a comprehensive literature review of two-phase cooling solutions that jet impingement boiling is one of the most promising two-phase thermal management solutions for very high heat flux applications, confirming that it has received considerable attention in the literature. There are a large number of adjustable geometric and hydrostatic parameters in jet impingement thermal management devices, thereby giving ample opportunities to tailor designs for high levels of heat dissipation or for large surface areas in low-pressure drop applications [11]. Jet impingement in the nucleate-boiling regime can achieve high rates of heat transfer for only a modest increase in wall superheat, making it an attractive option for thermal management devices [12]. Numerous experimental studies have been conducted of different jet impingement configurations to investigate the influence of various design parameters on heat transfer and pressure drop for both single jets as well as for multijet arrays. However, very few numerical studies are available in the literature, and none have been found in the literature for multijet arrays with boiling. Chapter 2 provides a detailed literature review of jet impingement boiling.

Remote cooling solutions are not sufficient for some extreme heat density electronic devices due to the high thermal resistance between the die and cooling device. To cool these devices, researchers recommend that the cooling solution must be embedded into the chip or package, which is known as embedded (or direct) cooling. An embedded jet impingement cooling solution is illustrated in Figure 2 [13]. By embedding the cooling solution into the package of the electronic device, the thermal resistance of the cooling system is greatly reduced, resulting in lower die level temperatures and higher concentrated heat removal. Embedded cooling solutions implement state-of-the-art cooling methods such as microchannels and jet impingement with or without boiling. A few important considerations for embedded cooling solutions are that the heat transfer fluid must be dielectric and, in the case of jet impingement, that the jet velocity must not be too high because it can damage the electronic component. To date, no embedded jet impingement boiling studies are available in the literature.

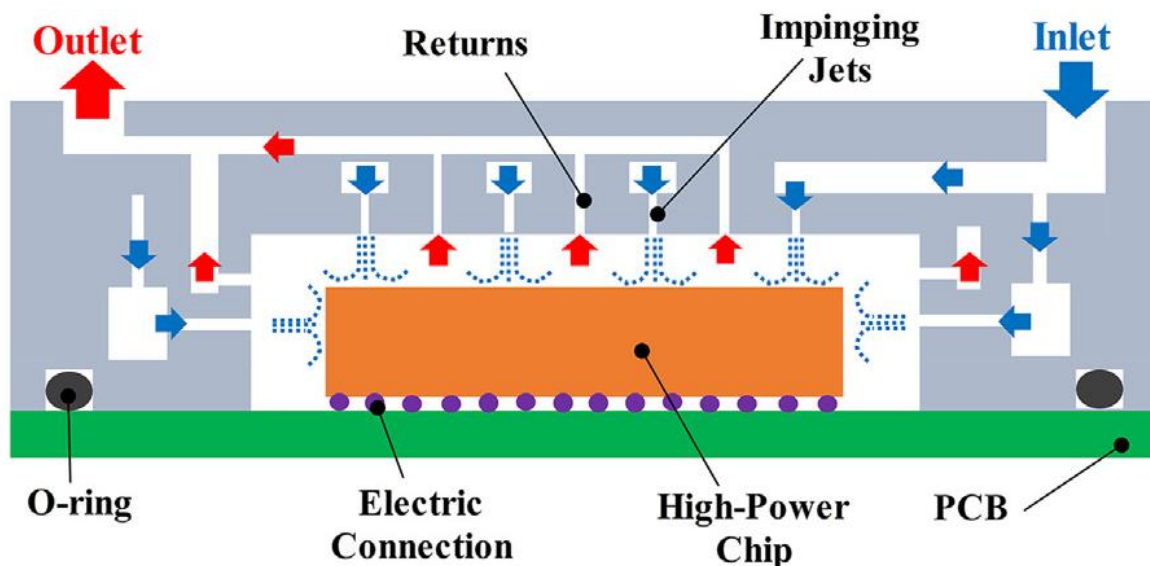


Figure 2: Embedded jet impingement cooling solution, adapted from Ref. [13]

Jet impingement boiling has been the topic of many experimental studies and researchers have identified key design parameters as well as their influence on the heat transfer and pressure drop of both single jets and multijet arrays. However, with the small scale at which impinging jets are implemented, experimental methods may fail to visually capture the complex flow behaviour and

boiling phenomenon of jet impingement boiling. Simplifying assumptions such as one-dimensional heat conduction and time averaging are required to analyse the experimental data resulting in area-weighted averaged heat transfer results. As a result, experimental studies may fail to capture local hotspots on the heated surface, making it difficult to quantify the influence of design parameters on local heat transfer, which is essential for design purposes. Experimental investigations are limited in the complexity of the set-up due to manufacturability and cost, complicating the study of the influence of certain parameters and scenarios.

Computational fluid dynamics (CFD) software enables researchers to conduct numerical investigations into complex geometries with complex flow conditions such as impinging jet arrays with boiling. CFD gives researchers the ability to visualise complex flow behaviour (such as turbulence and mixing), the heat transfer process as well as the boiling process, even at microscale. CFD enables researchers to extract information such as velocity and turbulence quantities as well as temperature and heat transfer data at discrete points in space and time, making it possible to identify local hotspots, oscillating behaviour, etc. Once a numerical model has been validated against experimental results, many alterations can be made to the geometry and flow conditions to investigate the influence of these parameters on heat transfer, pressure drop and other design considerations at a fraction of the time and cost of experimental investigations. This allows researchers to consider a wide range of parameters in a short time, which can aid the development of heat transfer correlations for design purposes. Unfortunately, very few numerical studies of impinging jets with boiling are available in the literature, with all of them limited to single jets. The behaviour of impinging jet arrays with boiling is of particular interest since most practical applications require heat transfer over a large surface area.

1.2 Problem Statement

Current state-of-the-art single-phase cooling solutions are not capable of removing the required heat fluxes of modern-day electronic devices without exceeding the operational temperature limit. Therefore, there is a need for cooling methods that can be implemented on a small scale and which can remove the required heat fluxes. Jet impingement boiling is one of the most promising phase-change cooling methods for electronics cooling. However, there are still a few challenges that must be met before jet impingement boiling can be widely implemented in electronics cooling. These challenges include management of spent flow, pumping requirements and an understanding of the influence of design parameters on local heat transfer.

Knowledge of the influence of design parameters on the local heat transfer in jet arrays are essential to alleviate hotspots and prevent local dry-out. Since experimental investigations fail to capture the local heat transfer effects, numerical investigations are essential to fully understand the influence of design parameters in jet arrays. Knowledge of vapour bubble behaviour in jet arrays is essential for proper management of spent flow. Since only a few experimental investigations visually recorded the vapour bubble behaviour in jet arrays, numerical investigations are essential to study the influence of spent flow management on heat transfer, fluid supply rates and pumping requirements.

1.3 Objectives and Scopes

To resolve the problem statement, the objectives of the current study were:

- to conduct a literature study of the hydrodynamics of liquid jet impingement, the boiling process, jet impingement boiling, and numerical modelling of turbulent, multiphase flow with boiling;
- to validate a two-dimensional (2D) axisymmetric single-jet model against experimental results;
- to validate a three-dimensional (3D) jet array model against experimental results;
- to conduct a parametric study of the influence of jet-to-surface spacing, jet Reynolds number, and jet-to-jet spacing on heat transfer;

- to present computational enhancements for predicting the boiling curves of jet impingement boiling close to the CHF point.

1.4 Layout of Dissertation

Chapter 1 presented the development trends and heat removal requirements of modern-day electronic components. Additionally, conventional cooling methods, state-of-the-art cooling methods, and recent advancements in electronic cooling methods were discussed to provide context for the current work. The shortcomings of experimental investigations into jet impingement boiling as well as the advantages of numerical investigations into jet impingement boiling were also presented.

Chapter 2 consists of a literature study of the fundamentals of jet impingement, boiling and numerical modelling. The possible configurations, hydrodynamics and heat transfer of liquid jet impingement are discussed in Section 2.2, with the focus on the submerged and confined configurations. The fundamentals of boiling are presented in Section 2.3, with the focus on the fully developed nucleate-boiling regime and flow boiling. A literature review of jet impingement boiling is presented in Section 2.4, with the focus on submerged and confined jets in the fully developed nucleate-boiling regime. The numerical multiphase framework and Rensselaer Polytechnic Institute (RPI) wall-boiling model are discussed in Section 2.5, with the focus on how the models are implemented in the commercial CFD solver, ANSYS FLUENT.

In Chapter 3, two numerical cases are validated against experimental results. In particular, a circular 2D axisymmetric single water jet in the subcooled nucleate-boiling regime is presented in Section 3.1 and a 3D multijet array in the subcooled nucleate-boiling regime is presented in Section 3.2. The focus of the validation cases is the ability to accurately predict the boiling curve in the fully developed nucleate-boiling regime. Information such as contours of the fluid flow and boiling phenomenon is extracted from the numerical results and illustrated in Chapter 3 as well. The importance of conjugation heat transfer in the solid is highlighted in this chapter, confirming the previous findings in the literature.

Chapter 4 presents a numerical parametric study of the influence of jet Reynolds number, jet-to-surface spacing, and jet-to-jet spacing on heat transfer. The results are discussed in detail and suggestions are made for design purposes based on the trends of the parametric study. The influence of the jet parameters on the local surface heat transfer as well as the local surface temperature is illustrated in this chapter.

The study is summarised in Chapter 5 and future directions are provided. Gaps in the literature, important design considerations and challenges are highlighted in this chapter.

2 Literature Study

2.1 Introduction

Jet impingement boiling has been the topic of many studies and has become a very attractive method for heat extraction from hot surfaces. It has been successfully implemented in a wide variety of industries such as heat treatment of materials, electronics cooling, turbine blade cooling and many more. The literature study briefly considers liquid jet impingement and boiling in Sections 2.2 and 2.3 respectively to establish the foundation of these two topics. Once a basic understanding of these concepts has been established, a literature review of jet impingement boiling is provided in Section 2.4. The numerical framework is then established in Section 2.5 to lay the foundation of the numerical validation to follow in Chapter 3.

2.2 Liquid Jet Impingement

Jet impingement consists of a fluid exiting an orifice or nozzle that impinges on a heated target surface. The working fluid can either be in the liquid or gas phase; however, the present section only considered liquid jets. Liquid jets can be classified into five categories: free surface, submerged, confined, plunging, and wall jets. The first three categories, especially the first one, have received much attention in the literature. The five jet impingement categories are illustrated in Figure 3 [14]. The present study focused on submerged and confined jet impingement; therefore, the submerged and confined categories are emphasised in this section.

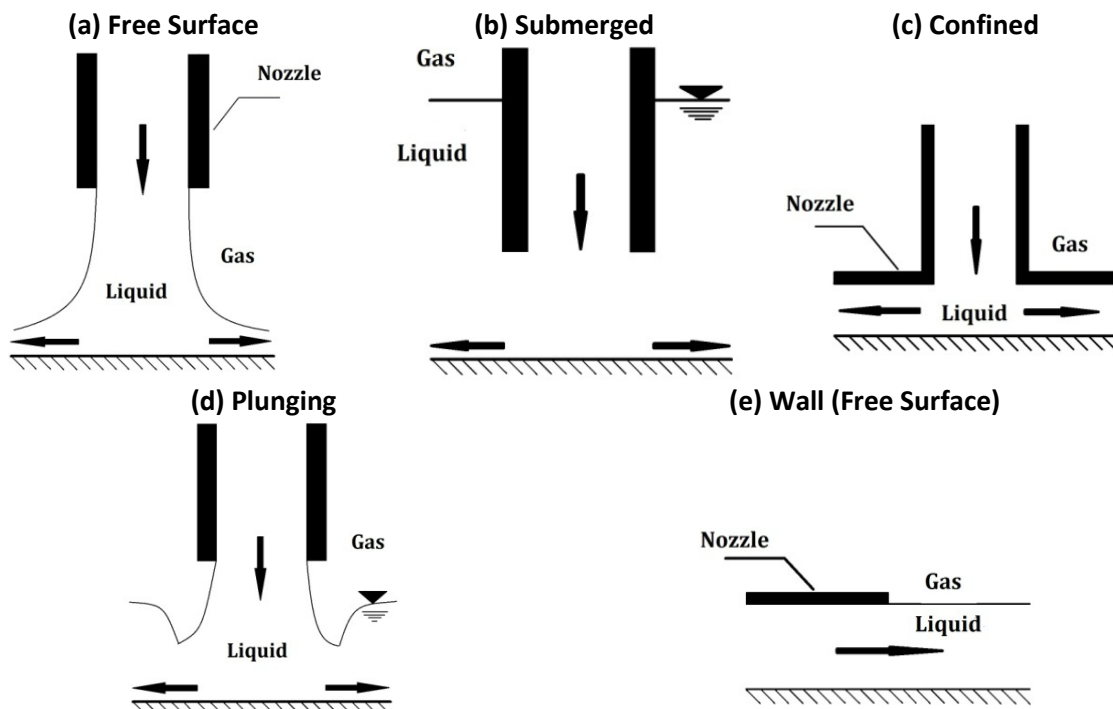


Figure 3: Liquid jet impingement categories, adapted from Ref. [14]

2.2.1 Hydrodynamics of Jet Impingement

The fluid flow of impinging jets can be classified into distinct flow regions, known as the jet flow regions, which are illustrated in Figure 4 for single confined jets [15]. The jet flow regions are the free-jet region, the stagnation region, and the wall-jet region. Before these jet regions can be discussed, it is necessary to define two key jet parameters. The first important jet parameter is the jet-to-surface spacing (H), which is the distance between the nozzle exit and the target surface. The second parameter is the jet diameter (D), or jet width (B) in the case of slotted jets. These parameters are important as they dominate the jet flow regions discussed in Section 2.2.1.1.

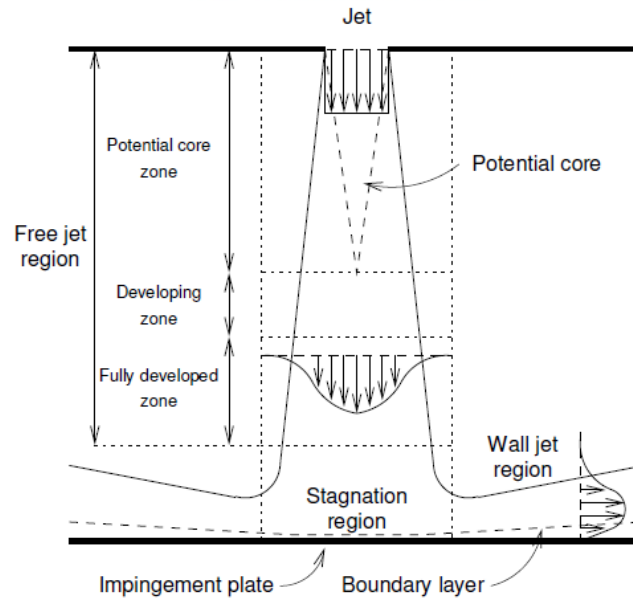


Figure 4: Jet flow regions for a single confined jet [15]

2.2.1.1 Jet flow regions

The free-jet region typically extends from the nozzle exit to the stagnation region; however, it depends on the target-to-surface spacing. Given that the target-to-surface spacing is at least two nozzle diameters, the free-jet region is present, and the flow behaves as a free submerged jet in this region. A shearing layer is found at the edges of the jet due to high-velocity gradients between the jet and the stationary liquid around it. The shearing layer transfers the jet momentum out laterally, entraining additional fluid from the surroundings, resulting in increased jet mass flow at the expense of jet energy and reduced velocity at the edges of the jet. The flow at the centre of the jet, interior to the shearing layer, is not affected by the lateral momentum transfer and thus forms a core region, known as the potential core, with higher total pressure and velocity. Due to high-velocity gradients at the nozzle exit, the pressure and velocity in the core may experience a slight decrease in magnitude [16].

Should the jet-to-surface spacing be sufficiently large, the shearing layer expands all the way to the centre of the jet before the jet reaches the target surface. In this case, the free-jet region can be subdivided into two distinct regions: the **potential core zone** and the **decaying jet zone**. The axial position where the centre line velocity is 95% of its original value defines the exact location where the potential core zone ends. The length of the potential core zone strongly depends on the nozzle geometry and exit conditions. In the decaying jet zone, large shear stresses at the edges of the jet result in a decrease in the axial velocity at the central part of the jet. This causes the velocity profile of the jet to become flatter and wider up to the point where the profile is fully developed and resembles a Gaussian curve. This further subdivides the decaying jet zone into a **developing zone** and a **fully developed zone**. The fully developed profile is maintained up to the stagnation region [16].

In the stagnation region, the jet strikes the target surface and forms a high-pressure zone, where the jet velocity reduces significantly. The flow velocity reduces to zero and the pressure reaches a maximum at the intersection of the jet centre line and the target surface. This point is known as the stagnation point. Due to the decrease in the axial velocity, the flow turns away from the jet centre and moves out parallel to the wall and enters the wall-jet region. The stagnation region typically extends 1.2 nozzle diameters from the wall for round jets and 13% of the jet-to-surface spacing for slot jets [16]. The flow in the stagnation region experiences strong normal and shear stresses that increase turbulence and stretch vortices if any are present [16].

In the wall-jet region, the fluid flows laterally outwards parallel to the wall. Shearing layers are present in the flow due to high-velocity gradients resulting from the no-slip condition at the wall-jet interface, and the interface between the wall jet and stationary fluid above. As the wall jet moves further along the wall, it entrains the fluid above it, increasing the wall-jet thickness, reducing its average velocity, and shifting the location of the maximum velocity further away from the wall. The wall-jet thickness is a minimum within 0.75 to 3 nozzle diameters from the impinging jet axis, and its thickness is typically less than 1% of the nozzle diameter. In the case of round jets, additional wall-jet deceleration is present due to the conservation of mass [16].

2.2.2 Characterising Heat Transfer in Liquid Jet Impingement

The geometry and set-up of impinging jets are described by jet parameters, which play an essential role in the heat and mass transfer of impinging jets. The jet parameters commonly used in heat transfer studies are [16] as follows:

- D – nozzle diameter;
- B – slot width;
- h – submergence depth (distance between free surface/confinement plate and the impingement surface);
- H – jet height (distance between nozzle exit and impingement surface);
- H/D – jet-to-surface spacing;
- V_{jet} – jet velocity at nozzle exit;
- Re – Reynolds number at nozzle exit;
- p_{jet} – jet-to-jet spacing (or pitch) in the case of multiple jets/jet arrays;
- p_{jet}/D – jet spacing to nozzle diameter ratio.

Liquid jet impingement is a form of forced convection. The heat transfer can thus be described by adjusting the convective heat transfer equations. The Nusselt number relationship for liquid jet impingement can be obtained by adjusting the Nusselt number correlation for forced convection to give

$$Nu = \frac{hD_h}{k} = \frac{\dot{q}D_h}{k(T_W - T_{jet})} \quad (1)$$

where \dot{q} is the surface heat flux, D_h is the hydraulic diameter of the nozzle, T_W the wall temperature, T_{jet} is the jet temperature at the nozzle exit and k is the thermal conductivity of the fluid evaluated at the nozzle exit temperature. The hydraulic diameter depends on the nozzle type. For a circular or round nozzle, the hydraulic diameter is simply the diameter of the nozzle (D). For a slotted jet, the hydraulic diameter is twice the slot width, $2B$. The convection heat transfer coefficient is then given by

$$HTC = \frac{\dot{q}}{(T_W - T_{jet})} \quad (2)$$

Fluid properties also affect heat transfer. One of the most significant properties that influence heat transfer is the fluid Prandtl number (Pr), given by

$$Pr = \frac{\mu C_p}{k} \quad (3)$$

where μ is the dynamic viscosity, k the thermal conductivity and C_p the specific heat capacity of the fluid. Although the Reynolds number is not a fluid property, it is highly dependent on the fluid

properties and jet velocity and has a significant influence on the heat transfer of liquid jet impingement. The jet Reynolds number for liquid jet impingement is given by

$$Re = \frac{\rho V_{jet} D_h}{\mu} \quad (4)$$

where ρ is the fluid density, V_{jet} the jet velocity.

2.2.3 Jet Arrays

Jet impingement can achieve much higher heat transfer coefficients than for traditional convection cooling flows. However, it can only achieve these high heat transfer coefficients in small, concentrated areas, since the heat transfer decreases exponentially moving further away from the jet centre line. For many cooling applications, uniform or close to uniform heat transfer over a larger surface area is required. Jet impingement can achieve close to uniform heat transfer over large surface areas by implementing multiple jets in an array. The Nusselt number profile can vary by a factor of up to five moving from the jet centre to nine nozzle diameters away. By implementing an impingement array, this factor can be reduced to two [16].

For the case of multiple jets, the jet-to-jet spacing or pitch (the distance between the centre of two adjacent jets) is an important parameter with a significant influence on the heat transfer. The pitch-to-nozzle diameter ratio determines to what extent the jets interact with each other. For pitch-to-nozzle diameter ratios below four, significant interaction occurs between the adjacent jets. Studies found that at a jet-to-surface spacing of $H/D = 2$, the interaction between jets persisted for jet spacings of up to ten nozzle diameters with a maximum Nusselt number for a spacing of eight nozzle diameters [16].

Jet interaction is an important design consideration and the influence of design parameters on the jet interaction is therefore essential to consider. The nature of interaction between jets and its effects as well as the influence of jet-to-surface spacing are discussed in detail in the sections to follow.

2.2.3.1 Shear layer interaction

For low jet spacings and large jet-to-surface spacings, the shear layers in the free-jet region of adjacent jets may combine. This combination results in lower velocity gradients in the free-jet regions, reducing turbulence generation. Reduced turbulence results in lower heat transfer coefficients, especially in the stagnation region as discussed previously. Low jet spacings may further cause wall jets of adjacent jets to collide on the target wall. The collision of two wall jets results in a secondary stagnation point where the flow turns up away from the wall to form a fountain, as illustrated in Figure 5 [16]. These fountains can have a significant effect on the heat transfer rates in the region of the collision. For cases with larger jet spacings, the fountains can improve heat transfer in the vicinity of the colliding wall jets due to high turbulence in the secondary stagnation regions. For low jet-to-surface spacings, the fountains may exchange momentum with the free-jet-shearing layers, resulting in reduced heat transfer coefficients [16].

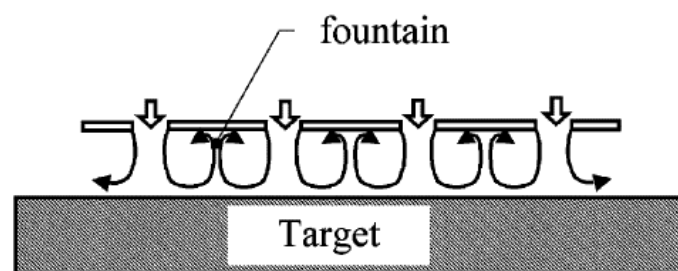


Figure 5: Typical circulation pattern in the confined jet array [16]

2.2.3.2 Small jet-to-jet spacings and highly confined jets

Confinement and jet-to-jet spacing are two major contributors to jet interaction in a jet array. For jet arrays with low jet-to-surface spacings and small jet-to-jet spacings, space for the fluid to exit the impingement region is very limited. This causes the wall jets to form cross-flow, which interferes with other wall jets. Cross-flow is undesired in jet arrays as it results in asymmetric jet flow fields, moves stagnation points, and increases the boundary layer thickness of other wall jets resulting in lower heat transfer. Interaction between jets does not have a significant influence on the peak Nusselt number; however, the average Nusselt number is reduced. Experimental studies found that the decrease in heat transfer due to jet interaction was mainly due to the interaction between jets before reaching the stagnation region. For highly confined jet arrays with low jet-to-jet spacings, flow patterns develop, which shift the peak Nusselt number further away from the jet centre axis. Table 1 [15] summarises the effect of confinement and jet-to-surface spacing on jet interaction. For large jet-to-jet spacings, $p_{jet}/D > 8$ at $H/D > 2$, jet interaction has no significant effect. However, at lower jet-to-jet spacings, the interaction between jets can have a detrimental effect on heat transfer. Experimental studies found that jet interaction was more sensitive to jet-to-jet spacing and jet-to-surface spacing than to the jet Reynolds number [16].

Table 1: Influence of jet-to-surface spacing on jet interaction in jet arrays [16]

H/D	Effect upon jet array
0 to 0.25	Highly constrained flow may have strong cross-flow and high additional backpressure (on the order of magnitude of the nozzle exit dynamic pressure). Additional flow acceleration expected to shift peak Nu laterally by 0.5–1.5D.
0.25 to 1.0	Fountain flow may greatly affect heat transfer in confined arrays.
1.0 to 2.0	Mild fountain effects may occur. Minor turbulence generation. Flow will be affected by confinement wall, need to ensure a clear exit pathway.
2.0 to 8.0	Shear layers may interact, need to maintain sufficient p_{jet} . Best performance tends to lie in this range.
8.0 to 12.0	Minimal, confinement effect is overshadowed by nozzle type. Need to ensure that neighbouring jets remain separate.
12+	Confining wall does not influence flow, instead nozzle type and jet-to-jet spacing dominate the flow field. Nu affected by jet energy loss approaching the wall. Need to ensure that neighbouring jets remain separate.

2.2.3.3 Cross-flow

Cross-flow can significantly degrade heat transfer rates. It is important to design jet arrays such that flow can exit the impingement region without interfering with other wall jets. The ratio of spent flow speed to jet speed is known as the cross-flow ratio and is used to describe the significance of cross-flow present in a jet array. As the cross-flow ratio increases, heat transfer decreases up to the point where there is no benefit from impingement and heat transfer coefficients are similar to that of regular channel flow. Experimental studies found that decreasing jet diameters with larger jet-to-jet spacings increased heat transfer significantly [16], due to there being sufficient space between jets to channel spent flow from the domain without interfering with the wall jets. In addition to the reduced interference with wall jets, the cross-flow can increase heat transfer downstream.

2.2.4 Enhancement Techniques

Various techniques have been implemented to improve heat transfer, reduce pressure loss, improve manufacturability and control spent flow. These techniques include alterations of the nozzle geometry, adding effusion holes to alleviate the effects of cross-flow in jet arrays, use of swirling jets to increase jet spreading, use of pulsating jets to increase turbulence, and surface enhancements to increase the heat transfer surface area [16].

2.3 Boiling

This section aims to capture the fundamental concepts of the boiling process and is focused on the nucleate-boiling regime. It also considers methods of increasing the heat transfer in the nucleate-boiling regime. The aim of this section is to lay the foundation of the boiling phenomenon for the jet impingement boiling work to follow.

2.3.1 Pool Boiling Background

The boiling process utilises the latent heat of a fluid by means of phase change, from the liquid to the vapour phase, to absorb large quantities of heat for a relatively small increase in the surface temperature. Convective heat transfer can thus be greatly improved if boiling occurs. Boiling is classified either as saturated boiling or subcooled boiling. Saturated boiling occurs when the bulk of the fluid is at the saturation temperature of the fluid. When heat is applied to the fluid, vapour formation occurs throughout the fluid as it absorbs heat due to phase change. The vapour bubbles do not collapse in the surrounding saturated liquid, and proceed to the free surface due to buoyancy, where the vapour bubbles burst and release their contents into the atmosphere. Subcooled boiling occurs when the bulk of the fluid is below the saturation temperature of the liquid, but the heated surface is above the saturation temperature of the liquid. The fluid close to the heated surface forms vapour bubbles on the heated surface due to phase change, the bubbles then break away from the surface and collapse in the cooler bulk fluid as heat transfer from the bubble to the liquid occurs. Therefore, boiling only occurs close to the heated surface and is commonly referred to as local boiling. The vapour bubbles greatly increase heat transfer to the liquid since they absorb energy from the heated surface and transfer the heat to the bulk of the liquid due to buoyancy effects in addition to natural convection currents [17].

Boiling can further be classified into pool boiling or flow boiling. Pool boiling is the simplest form of boiling and occurs when a hot surface or heat source such as an electrical heating element is submerged into a stationary liquid, thus with no bulk fluid motion. Vapour is formed on the heated surface when the surface temperature is above the saturation temperature of the fluid, the temperature difference between the heated surface and the saturation temperature is known as the wall superheat. This vaporisation process is known as pool boiling and is commonly encountered in our daily lives and in industrial applications. Although there is no bulk fluid motion present in pool boiling, natural convection currents and strong mixing due to the buoyancy of the vapour bubbles combine in pool boiling and are partly responsible for the high heat transfer in pool boiling. The relationship between wall heat flux and the wall superheat for saturated pool boiling was first identified by Nukiyama [18] and is illustrated in Figure 6. The graph in Figure 6 is now commonly known as the boiling curve.

Four distinct regions are visible in the boiling curve, shown in Figure 6, and are defined as the boiling regimes. The boiling regimes are the natural convection regime, nucleate-boiling regime, transition-boiling regime, and film-boiling regime. These regimes are separated by three points on the boiling curve, the onset of nucleate boiling (ONB), critical heat flux (CHF) otherwise known as the burnout heat flux, and minimum heat flux (MHF) otherwise known as the Leidenfrost point. At heat fluxes below the ONB heat flux, heat transfer is dominated by natural convection and no vapour formation occurs. The ONB point is highly dependent on the surface roughness and wettability [17].

At heat fluxes between the ONB and CHF, nucleate boiling occurs. The nucleate-boiling regime is characterised by two stages, isolated bubble boiling and fully developed nucleate boiling. The former is a low heat flux region where isolated bubble formation occurs and discrete bubbles are randomly released from activated cavities. The discrete bubbles tend to remain isolated and collapse in subcooled pool boiling. Fully developed nucleate boiling is a high heat flux region where bubbles are released at a much higher rate and coalesce to form vapour columns. Heat transfer in the fully

developed nucleate-boiling regime is much higher than in the isolated bubble regime and is controlled by a very thin fluid layer adhering to the surface. The bulk fluid motion and surface conditions hardly influence this thin layer, resulting in the heat transfer to become almost independent of the surroundings. Various correlations exist in the literature to predict the heat transfer coefficient for pool boiling in the nucleate-boiling regime. These correlations are discussed in Section 2.3.3.

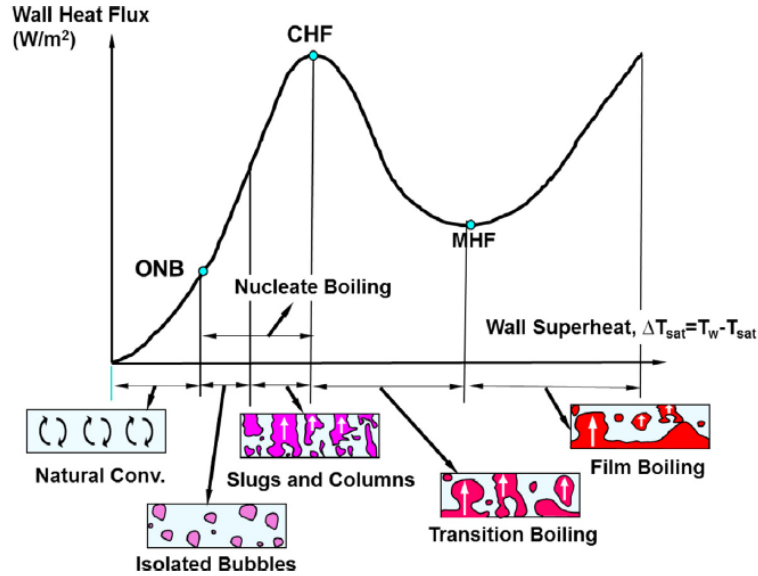


Figure 6: Typical pool-boiling curve for water at atmospheric pressure [17]. Critical heat flux (CHF), minimum heat flux (MHF) and onset of nucleate boiling (ONB)

The relationship between the heat flux, \dot{q} , and the wall superheat, $(T_W - T_{sat})$, in the nucleate-boiling regime is given by the following correlation:

$$\dot{q} = C(T_W - T_{sat})^m \quad (5)$$

where C and m are constants dependent on the liquid properties and heated surface conditions, T_W the surface temperature, and T_{sat} the saturation temperature of the fluid. The most widely used correlation for the heat transfer rate in the nucleate-boiling regime for pool boiling is the one proposed by Rohsenow in 1952 and is expressed as

$$\dot{q} = \mu_l h_{fg} \sqrt{\frac{g(\rho_l - \rho_v)}{\sigma}} \left[\frac{C_{pl}(T_W - T_{sat})}{C_{sf} h_{fg} Pr_l^n} \right]^3 \quad (6)$$

where μ_l is the dynamic viscosity of the liquid, h_{fg} the latent heat, g the gravitational acceleration, ρ_l the liquid density, ρ_v the vapour density, σ the surface tension, C_{pl} the liquid specific heat, C_{sf} an experimental constant dependent on the surface-fluid combination, Pr_l the liquid Prandtl number and n an experimental constant dependent on the fluid [19]. Due to the high rates of heat transfer achievable with relatively low wall superheats and thus heated surface temperatures, the nucleate-boiling regime is preferred for design applications and was the focus of the present study [17].

The CHF defines the upper limit of the nucleate-boiling regime and defines the start of the transition-boiling regime. The CHF is of great importance for industrial design applications because it should be avoided to prevent damage of equipment or components due to dry-out at the surface and a rapid decrease in heat transfer. Various empirical correlations and theoretical equations exist in the literature and converge into

$$\frac{\frac{\ddot{q}_{CHF}}{\rho_v h_{fg}}}{\sqrt[4]{\sigma g (\rho_l - \rho_v)}} = K = (0.13 - 0.19) \quad (7)$$

for a saturated liquid boiling on a large horizontal surface. Equation (7) is known as the Kutateladze correlation and was derived for various liquids at a wide range of pressures using dimensional analysis. Modified correlations based on the Kutateladze correlation have been proposed for a fine heated wire, a vertical heater as well as for subcooled liquids [17].

Exceeding the CHF, nucleate boiling can no longer transport heat from the surface to the liquid in a stable manner. Boiling transitions to the next stage are known as unstable film boiling or the transition-boiling regime. A sudden drop in heat transfer occurs when the heat flux is increased beyond the CHF due to surface dry-out where large portions of the surface are covered by a vapour film. Since the thermal conductivity of vapour is much lower than that of liquid, the vapour film acts as an insulating barrier, resulting in lower rates of heat transfer from the heated surface. In the case of constant heat flux heaters such as an electrical heating element, the excess heat is stored in the heater, causing the surface temperature to increase rapidly until a stable point has been reached in the film-boiling regime. In most cases, this point is above the melting point of the heater, causing equipment failure before a stable point in the film-boiling regime has been reached. Experiments that utilised a controlled heat flux heater managed to artificially realise the transition-boiling regime by controlling the heat flux to prevent equipment meltdown once the CHF was exceeded. In most cases, the stable transition-boiling regime is hardly ever realised as the heat transfer oscillates between film and nucleate boiling at any point on the heater surface [17].

Stable film boiling is reached at very high surface temperatures where the surface is completely covered by a vapour film. The lowest heat flux where stable film boiling can be reached is at the Leidenfrost point, denoted by MHF on the boiling curve in Figure 6. Heat transfer in the film-boiling regime is dominated by radiation heat transfer from the heated surface through the vapour film to the liquid. Radiation heat transfer only becomes significant at very high surface temperatures, which are normally temperatures well above the melting point of most metals. Due to the high surface temperatures required for film boiling, film boiling was not of interest in the present study [17].

2.3.2 Flow Boiling

Flow boiling occurs when the bulk of the fluid is in motion such as water being forced over a heated surface, external flow boiling, or through a heated pipe, known as internal flow boiling. In saturated internal flow boiling, liquid flows through a heated channel, once the liquid has reached the saturation temperature, boiling is initiated, and vapour formation occurs. As the fluid moves downstream in the channel, the amount of vapour increases until the entire channel is filled with vapour. Subcooled flow boiling is a more complex process than saturated flow boiling. The progress of subcooled internal flow boiling in a uniformly heated pipe is illustrated in Figure 7 [20]. To identify the initiation of boiling and to describe the boiling progress, the thermodynamic equilibrium quality, x_e , is sometimes used rather than the axial position, z . The thermodynamic equilibrium quality, x_e at z from the inlet of the pipe is given by

$$x_e = \frac{h_{in} + \left(\frac{\pi D \dot{q} z}{\dot{m}}\right) - h_{ls}}{h_{fg}} \quad (8)$$

where h_{in} is the liquid inlet enthalpy, D the pipe diameter, \dot{q} the heat flux, z the axial position, \dot{m} the mass flow rate, and h_{ls} the saturated liquid enthalpy. The bulk fluid is subcooled when $x_e < 0$, saturated when $0 \leq x_e \leq 1$ and superheated when $x_e > 1$. When the bulk flow is subcooled, boiling

occurs on the pipe wall when the temperature of the wall is above the saturation temperature of the fluid. The initiation of boiling is called incipient boiling and the boiling state is called subcooled boiling. As the fluid moves further downstream, the bubbles start to detach from the wall. This process is called net vapour generation initiation. When the bulk flow becomes saturated, $x_e \geq 0$, and further downstream, the boiling state is called saturated boiling. As the flow moves further downstream and the thermodynamic equilibrium quality increases, the net vapour volume increases, and the flow turns from bubbly flow to slug/churn flow. The heat transfer in this region is dominated by nucleate boiling [20].

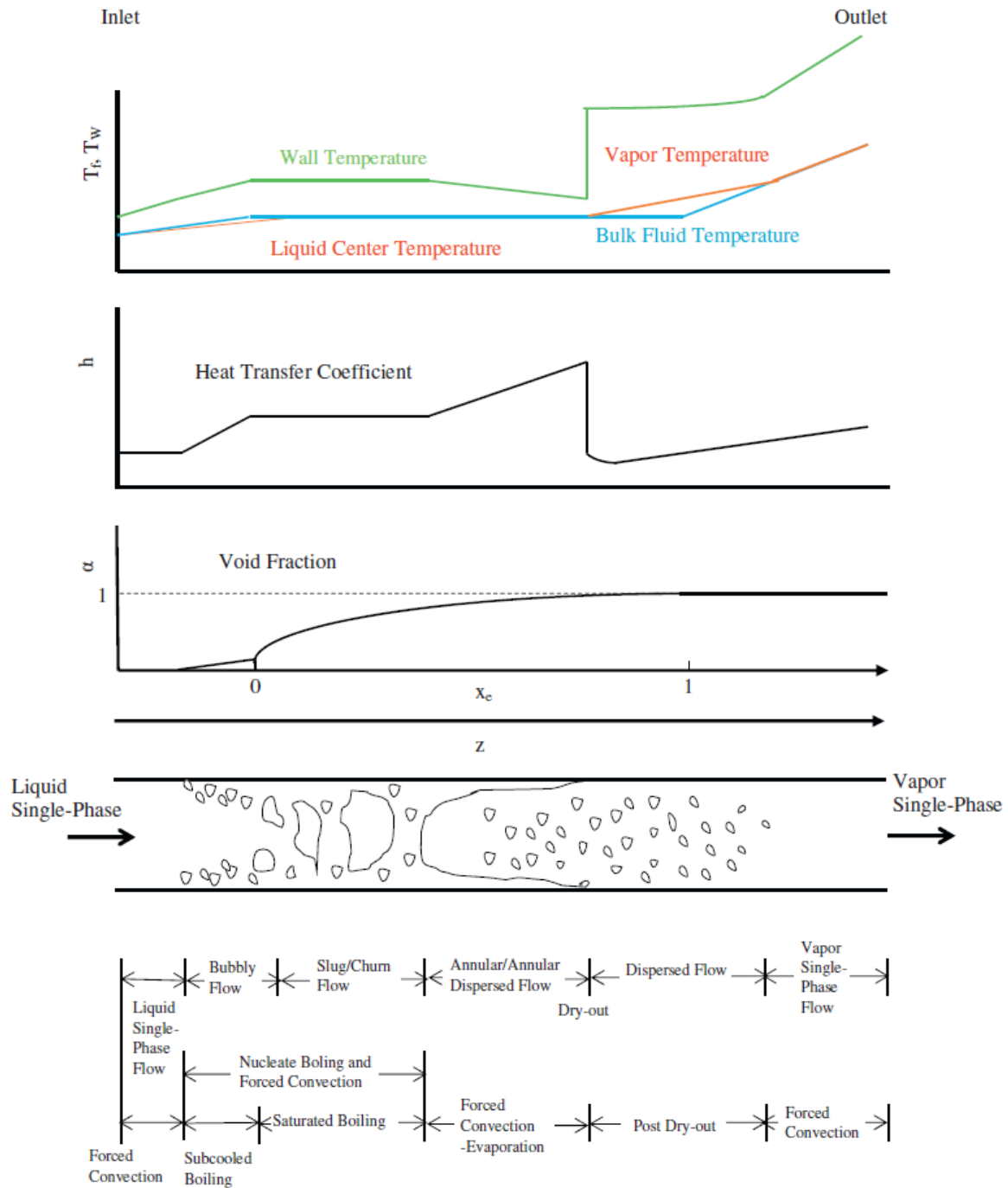


Figure 7: Flow and heat transfer progress of subcooled flow boiling in a heated pipe [20]

For most fluids, the density of the liquid phase is considerably larger than that of the vapour phase and as a result, phase change from a small volume of liquid produces a large volume of vapour. This is

illustrated by the void fraction, α , in Figure 7, which is the ratio of vapour volume to the combined volume of liquid and vapour at a cross-section of the pipe. The void fraction is seen to increase drastically after the initiation of boiling. Moving further downstream, the centre core of the pipe flow consists mainly of vapour and is surrounded by a thin film of liquid flowing on the pipe wall. Some entrained liquid droplets are also present in the vapour core. This state is known as annular flow or dispersed annular flow. The liquid film at the wall is usually so thin that heat transfer in this region is governed by conduction from the wall to the liquid film, by convection through the liquid film and then by evaporation at the liquid-vapour interface. This state is known as forced convection evaporation. In cases where the heat flux or flow rate is high enough, bubble nucleates occur on the wall in the liquid film. This state is known as forced convection boiling and evaporation [20].

Moving further downstream, the liquid film starts to disappear and a rapid increase in the wall temperature is observed. This phenomenon is known as dry-out. The flow region after dry-out is called dispersed flow, since only a few entrained liquid droplets are present in the bulk flow in this region. Heat transfer in this region is dominated by convective heat transfer of the vapour phase. Given that wall boiling no longer occurs, the vapour becomes superheated. In this region, a thermal non-equilibrium condition emerges where liquid droplets and superheated vapour coexist. The entrained liquid droplets evaporate in the superheated vapour as the flow moves further downstream and the flow turns to single-phase vapour flow. The state after dry-out first occurs until the transition to single-phase vapour flow is known as the post dry-out region [20].

Typical heat transfer coefficient and wall temperature variations for internal flow boiling are also illustrated in Figure 7. The heat transfer coefficient is almost constant for the liquid forced convection up to incipient boiling, while the wall temperature increases slightly with the flow direction, due to the heating of the liquid. Once the incipient boiling point has been reached, the heat transfer coefficient increases linearly with the flow direction and the wall temperature increase slows down until it becomes constant when the saturated boiling has been reached. The heat transfer coefficient and wall temperature remain close to constant for the entire saturated boiling region. In the forced convection evaporation region, the heat transfer coefficient starts increasing again due to the thinning of the film thickness with increasing x_e , resulting in a slight decrease in the wall temperature. At dry-out, the heat transfer coefficient experiences a drastic drop, resulting in a sudden increase in the wall temperature. After dry-out, the wall temperature continues to increase gradually until all entrained liquid droplets have evaporated and single-phase vapour flow has been reached. The heat transfer coefficient and wall temperature both increase with the vapour temperature in the single-phase vapour flow region, where the wall temperature can be determined by the single-phase vapour forced convection heat transfer. A rapid increase in the wall temperature due to dry-out is an important observation because high wall temperatures can cause the pipe wall to melt. It is thus an important design consideration [20].

The progression of the heat transfer coefficient in flow boiling with x_e depends on the wall heat flux. The influence of the wall heat flux on the progression of the heat transfer coefficient is illustrated in Figure 8 [20]. The heat transfer coefficient progression changes from (a) to (d) with increasing heat flux. Boiling incipience tends to occur further upstream for higher heat fluxes. The heat transfer coefficient tends to be higher for higher wall heat fluxes, while the nucleate-boiling regime tends to occur over a longer section of the pipe flow. The forced convection evaporation region tends to decrease in length for increasing heat flux. The heat transfer coefficient in the nucleate-boiling regime is very high for cases (c) and (d). However, due to the low thermodynamic equilibrium quality, the wall tends to be covered with a vapour film, while the core of the pipe flow is a liquid. This is similar to the film boiling regime in pool boiling and marks the burnout point, where the heat transfer coefficient drops drastically. This point is called the departure from nucleate boiling (DNB) or burnout and is referred to as the critical heat flux (CHF) for flow boiling. [20]

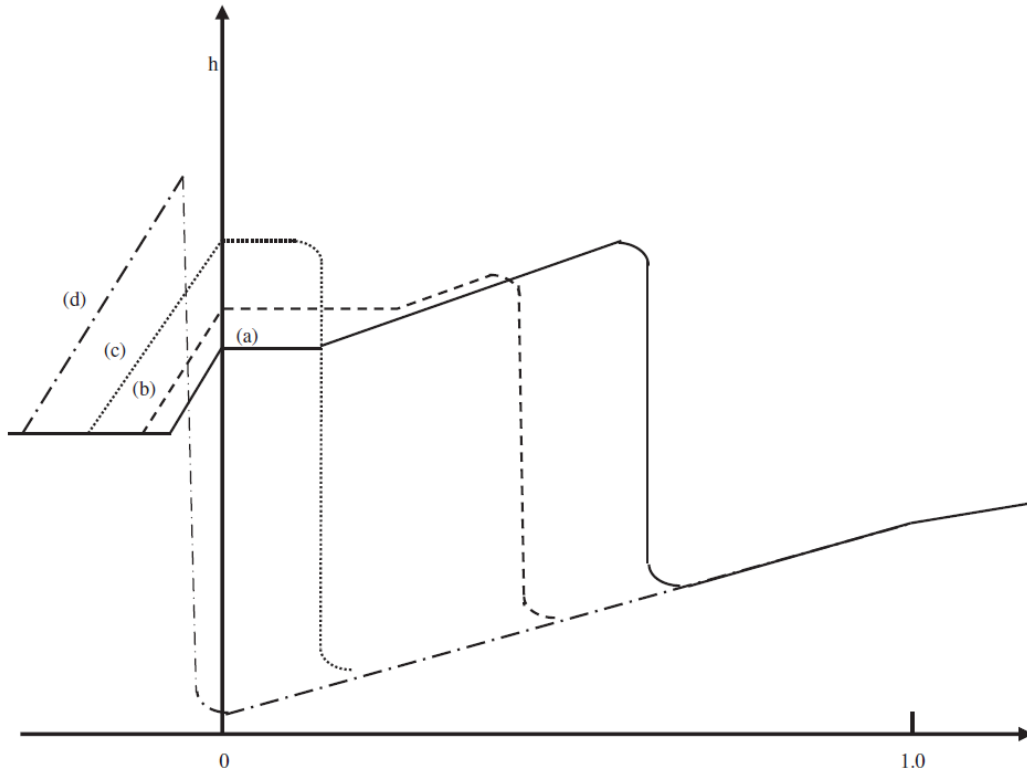


Figure 8: Variation in heat transfer coefficient with heat flux in flow boiling, where the heat flux increases from (a) to (d), adapted from Ref. [20]

2.3.3 Nucleate Boiling

This section aims to explain the microscopic aspects of the nucleate boiling process with an in-depth discussion of the isolated bubble region and a brief discussion of the continuous bubble boiling region. The microlayer thickness in pool boiling and microchannel flow boiling and its influence on nucleate boiling heat transfer are also discussed in this section. Vapour bubble dynamics after departure from the nucleation site in subcooled flow boiling is also discussed.

2.3.3.1 Mechanism of isolated bubble nucleate boiling

Cooper and Lloyd [21] conducted an experimental investigation into the formation of the liquid layer beneath the vapour bubble in nucleate pool boiling. They identified the bubble growth mechanism in pool boiling, where the departing vapour bubble is grown by the evaporation of the surrounding superheated liquid and microlayer beneath the vapour bubble. Figure 9(a) to (d) illustrates the heat transfer phenomena during the bubble growth and departure cycle [22].

Figure 9(a) depicts the growing vapour bubble just after nucleation. During this growth period, the vapour bubble displaces the surrounding fluid, leaving behind a thin liquid film beneath it, known as the microlayer. Figure 9(b) shows dry-out occurring forming a dry patch at the centre of the interface between the vapour bubble and the heated surface. Due to the low thermal resistance of the microlayer, it evaporates vigorously during this period, causing the dry patch to spread rapidly from the centre. Once the microlayer has completely evaporated, the contact area between the vapour bubble and heated surface area shrinks due to the bubble stretching upwards away from the surface, as shown in Figure 9(c). Figure 9(d) illustrates bubble departure where the bubble separates from the heated surface and moves upwards. The rising bubble causes strong liquid convection currents as the surrounding liquid rewets the nucleation site [22].

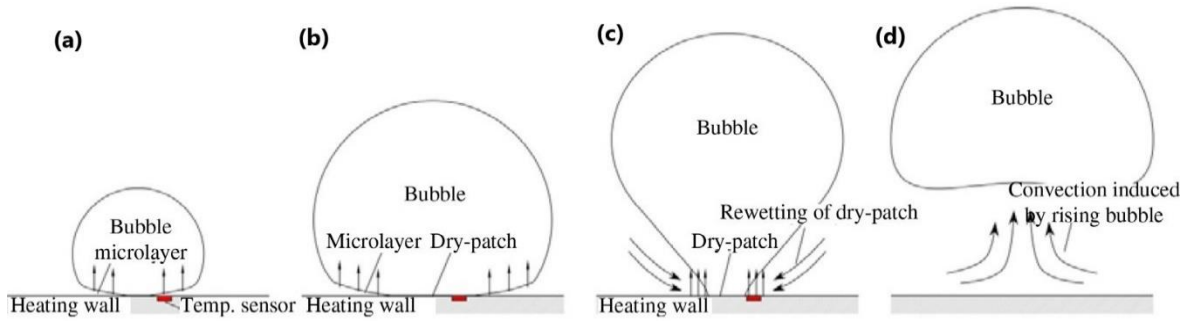


Figure 9: Boiling heat transfer mechanism under an isolated bubble, adapted from Ref. [22]

The same cycle was later captured experimentally and is illustrated in Figure 10 [22]. Initially, the bubble grows rapidly in an oval-spherical shape. As the bubble growth rate slows down, the contact area between the bubble and heated surface decreases due to the upward shift of the bubble's centre of gravity. The bubble then departs from the surface and rises in the liquid.

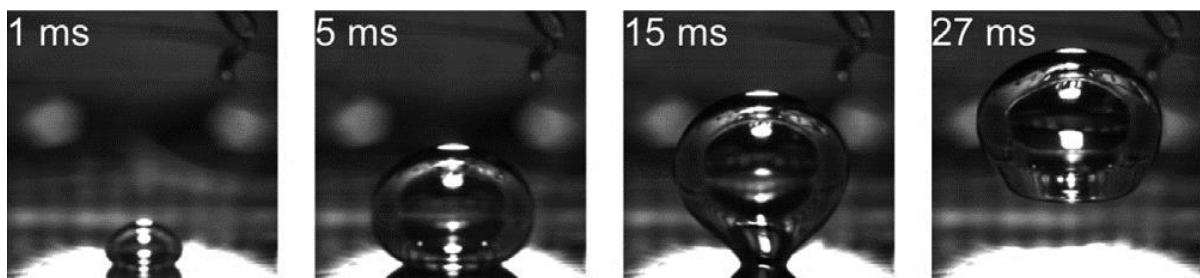


Figure 10: Isolated bubble growth and departure cycle in nucleate pool boiling, adapted from Ref. [22]

The fundamental heat transfer phenomena during the bubble growth and departure cycle illustrated in Figure 9 can be observed by looking at the local wall temperature beneath an isolated bubble. The local wall temperature vs time plot and bubble images at various time frames are shown in Figure 11 for a wall superheat of 10.8 K [22]. The local wall temperature is plotted for various distances from the bubble-surface interface centre. The evaporation and dry-out of the microlayer as well as the rewetting of the surface are clearly visible in the wall temperature vs time plot. The wall temperature at the centre of the bubble-surface interface experiences a drastic drop directly after bubble nucleation. This wall temperature drop is due to the formation and vigorous evaporation of the microlayer, resulting in very high local heat transfer coefficients. The wall temperature at the centre reaches a minimum shortly after the sudden drop, before starting to increase again. The minimum is reached due to the onset of dry-out. The surface temperature shows similar temperature variation with time further away from the centre, indicating radial spreading of the microlayer and the dry patch. The wall temperature forms second minima at radial distances 50 and 200 μm from the centre due to the spanwise heat conduction in the wall from the dry-out region in the centre to the evaporating area at the outside [22].

The minimum indicates the onset of the bubble departure process, where the contact area shrinks and the centre of gravity of the bubble moves upwards due to the elongation of the bubble. The dry-out region is rewetted by the surrounding liquid, resulting in small negative peaks in the wall temperature. The microlayer is formed at a radial distance of 1 000 μm from the centre; however, it does not dry out. Here the temperature reaches a minimum before starting to gradually increase after the passage of the advancing apparent contact line in the bubble departure process. However, no negative peaks are formed, indicating that there is no rewetting of the dry-out regions. The wall temperature recovers to the levels of pre-bubble nucleation, after bubble departure, indicating that the convective currents formed by the rising bubble do not have a significant influence on the wall heat transfer [22].

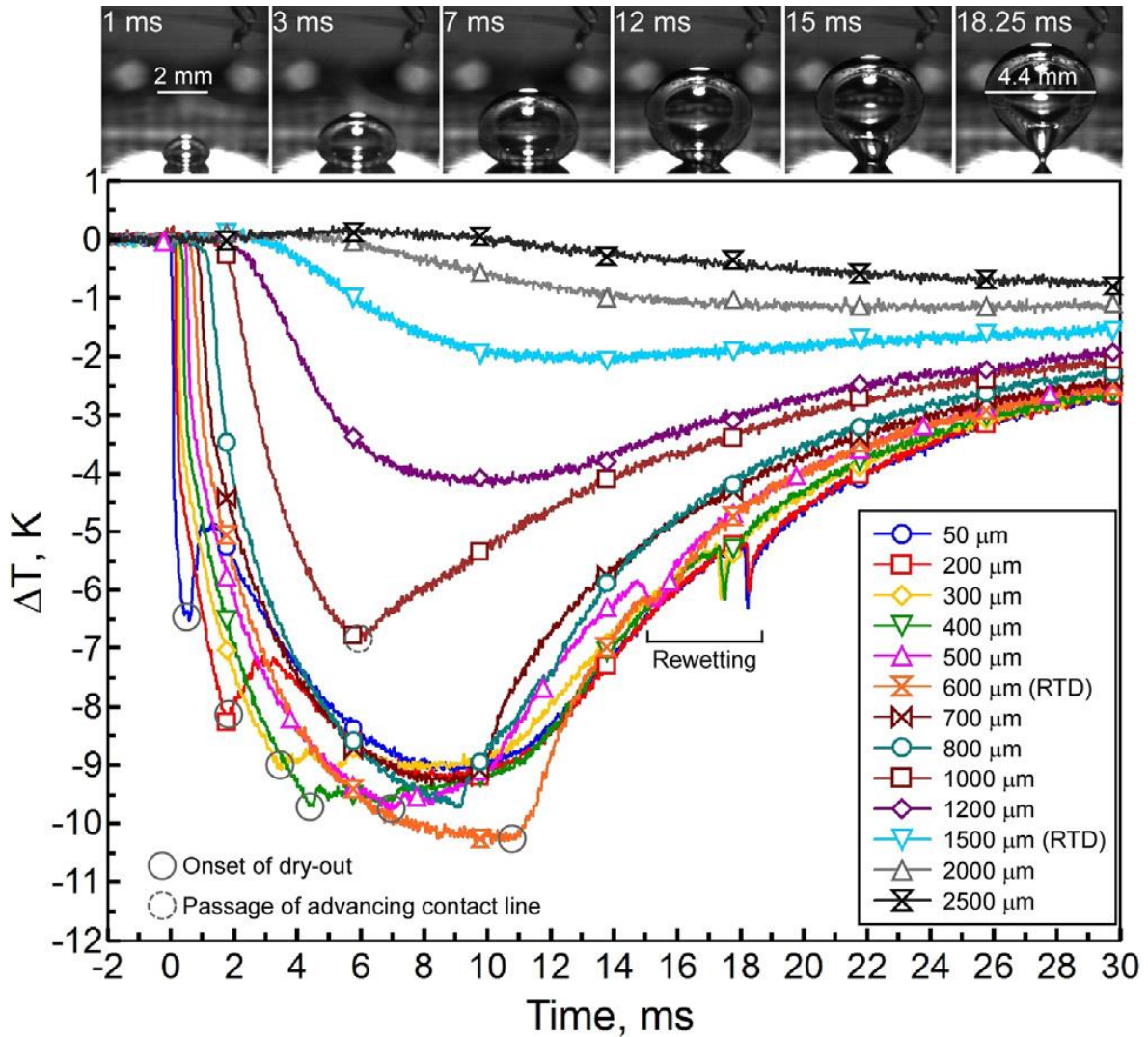


Figure 11: Bubble behaviour and local wall temperature under the isolated bubble ($\Delta T_{sat}=10.8$ K, $D_{max}=4.4$ mm) [22]

The spatiotemporal distribution of the local wall temperature and calculated local wall heat flux, bubble radius and apparent contact radius are illustrated in Figure 12 [22]. The local wall heat flux was calculated from a transient heat conduction analysis. The drop in wall temperature expanded radially outwards with the expanding microlayer. Local surface heat fluxes above 1 MW/m^2 are observed in the apparent contact area, which is comparable with the normal CHF of water in pool boiling. The local surface heat flux increases moving closer to the nucleation site due to the thinning of the microlayer towards the bubble-surface interface centre, with a maximum of 2.8 MW/m^2 for the case illustrated in Figure 12. Vapour velocities were calculated to be 2 m/s for the vapour generated from the microlayer surface at the maximum heat flux, which equates to very high velocities inside the vapour bubble with a diameter on the millimetre scale. The maximum heat flux increased linearly with wall superheat, reaching a maximum of 3.9 MW/m^2 for a wall superheat of 15.3 K . Dry-out first appeared at 1 ms , with a dry patch forming at the centre of the bubble-solid interface, which eventually expanded to $600 \mu\text{m}$. The temperature outside the apparent contact area decreased; however, no apparent increase in the wall heat flux in this region was detected, indicating that the temperature drop outside the apparent contact area was not due to the heat transfer between the liquid and the wall, but rather due to the spanwise conduction inside the wall solid material, between the microlayer formation area and the outside of the microlayer [22].

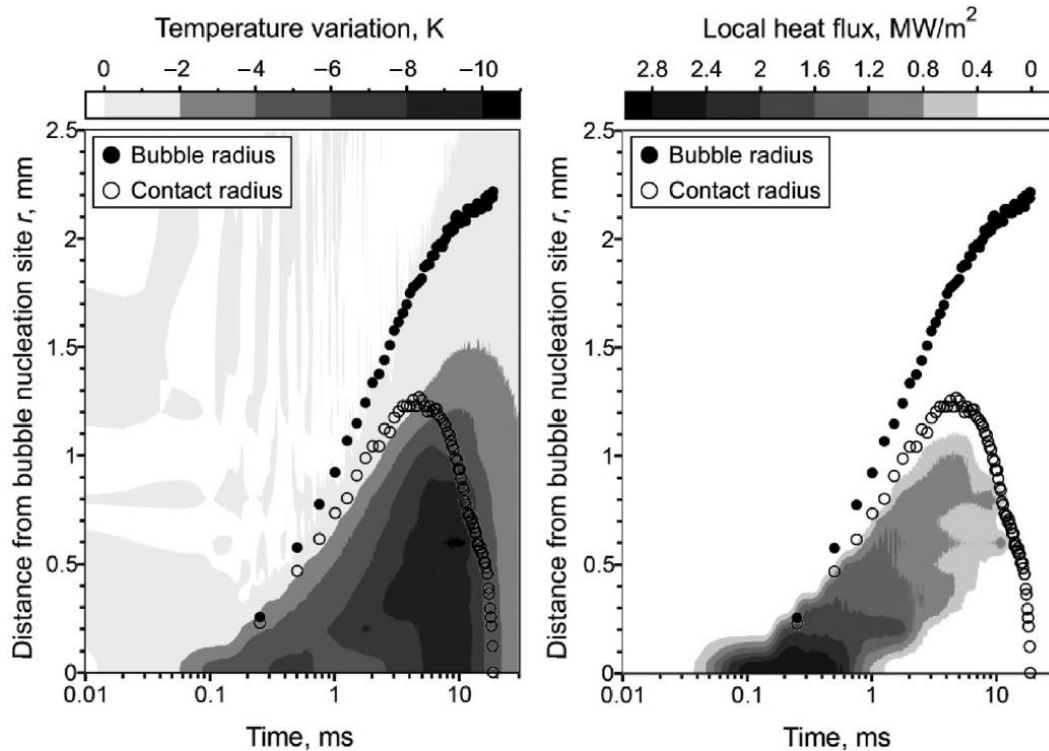


Figure 12: Spatiotemporal distributions of local wall temperature (left) and local wall heat flux (right), ($\Delta T_{sat}=10.8\text{ K}$, $D_{max}=4.4\text{ mm}$), adapted from Ref. [22]

2.3.4 Heat Transfer Enhancement

Heat transfer in the nucleate-boiling regime is dominated by nucleation. Therefore, it is desirable to increase the number of nucleation sites on the heating surface as well as the rate of bubble formation at the sites. The number of active nucleation sites can be increased by increasing the surface roughness. Studies found that increasing the surface roughness increased the heat flux up to ten times that of a smooth surface. Unfortunately, prolonged use of a heating surface reduces the surface roughness and is thus not a long-term solution. Various surface treatments are available to increase the number of nucleation sites on a heating surface in the long term. Common methods are porous coatings and mechanical cavity formation. These surface treatments not only increase the heat transfer in the nucleate-boiling regime, but also the critical heat flux by a factor of up to three times that of a smooth surface. Various other methods are available to increase heat transfer such as packing the heating surface with a microporous layer in cases where the fluid is not stationary [22].

2.4 Jet Impingement with Boiling

This section discusses the fundamentals of jet impingement boiling heat transfer in the nucleate-boiling regime. A literature review of jet impingement boiling was conducted to identify the influence of jet parameters, subcooling and heat transfer fluid on heat transfer in the nucleate-boiling regime. The literature review of jet impingement boiling should help to identify gaps in the literature and lead the direction of the present research.

2.4.1 Boiling Curve for Jet Impingement Boiling

The boiling curve has the same shape for all heating surface geometries and is mainly a function of the fluid, pressure, and a combination of the fluid-heating surface material. This holds true for jet impingement. However, due to the nature of jet impingement and the pressure variation in the different jet regions, the boiling curve shape has been altered to some extent. The boiling curve illustrated in Figure 6 is for pool boiling where the only fluid movement is due to the formation of bubbles, buoyancy, and convection currents. In the case of jet impingement, the motion of the fluid has a significant influence on the heat extracted from the surface since the hot liquid close to the

surface is continuously replaced by colder liquid. As a result of jet impingement, much higher heat fluxes can be achieved with jet impingement boiling. The addition of an impinging jet has a significant influence on the shape of the boiling curve. The boiling curve for the quenching of a hot surface by liquid jet impingement is illustrated in Figure 13 [23].

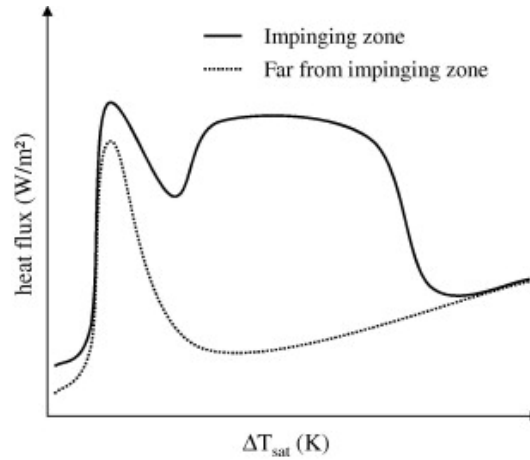


Figure 13: Liquid jet impingement boiling curve [23]

Figure 13 indicates that the critical heat flux decreases moving away from the stagnation region. The boiling curve sufficiently far away from the stagnation region has a shape similar to that of pool boiling, shown in Figure 6. The transition boiling region was much wider in the stagnation region with a significantly higher Leidenfrost temperature due to the impinging jet breaking up the vapour layer in the stagnation region causing the wall to be rewetted. The rewetting of the stagnation region results in an increase in heat flux. The wall superheat rose until the vapour layer stabilised, that is, at the Leidenfrost temperature. This effect is known as shoulder heat flux [23].

As mentioned in Section 2.3.1, nucleate boiling is the most attractive boiling regime for design applications due to the high heat fluxes achievable with relatively low wall superheat. This holds for jet impingement boiling. However, unlike pool boiling where the transition-boiling regime is avoided in design, the transition-boiling regime is desired for some applications with jet impingement boiling. In applications such as nuclear power plants and quenching of hot steel plates during production, very high wall temperatures are unavoidable, and the transition-boiling regime is required for jet impingement cooling. The nucleate-boiling regime for jet impingement boiling is discussed in detail in the following section. The film-boiling regime is still not a preferred choice due to the very high wall superheat and is therefore not considered.

2.4.2 Nucleate Boiling

Jet impingement in the nucleate-boiling regime has been studied extensively in the literature for free-surface jets, submerged jets, and confined jets in the single-jet and multijet array configurations. Most correlations for surface heat flux reported in the literature regarding jet impingement boiling in the nucleate-boiling regime are of the form:

$$\dot{q} = C \Delta T_{sat}^m \quad (9)$$

where C and m are empirical constants determined from experimental data and ΔT_{sat} is the wall superheat ($T_W - T_{sat}$). Equation (9) can be modified to give the heat transfer coefficient as follows:

$$HTC = \frac{\dot{q}}{\Delta T_{sub} + \left(\frac{\dot{q}_{sat}}{C}\right)^{\frac{1}{m}}} \quad (10)$$

where h is the adjusted convective heat transfer coefficient and ΔT_{sub} is the jet subcooling.

As stated in Section 2.3.1, the nucleate-boiling regime and the upper boundary of the nucleate-boiling regime, namely the CHF, are of particular interest in design. The vapour bubble behaviour for a free-surface jet in the nucleate-boiling regime as well as at CHF is illustrated in Figure 14 [24].

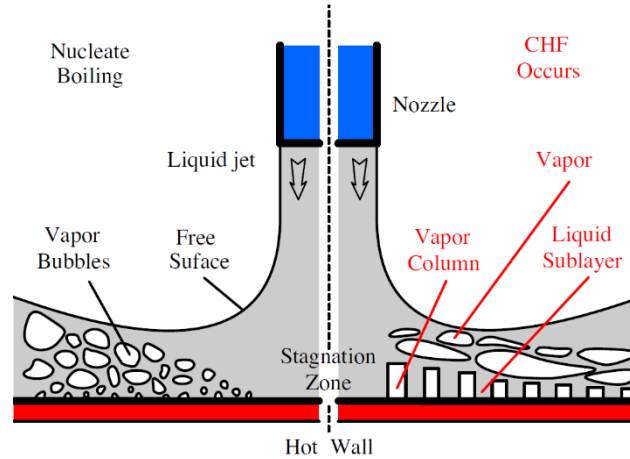


Figure 14: Free-surface jet impingement with nucleate boiling bubble behaviour. Nucleate boiling (left) and CHF (right) [24]

As the wall superheat increases in the nucleate-boiling regime, the number of nucleation sites as well as the number of bubbles forming at the nucleation sites increases. As illustrated in Figure 14, the bubbles formed at such a great rate at the CHF that columns of vapour were present at the surface. When increasing the wall superheat beyond the CHF wall superheat, bubbles form at such a significant rate that most of the surface is covered by a vapour film and represents the start of the transition-boiling regime/unstable film-boiling regime.

For pool boiling in the fully developed nucleate-boiling regime, heat transfer is governed by the formation of bubbles and mixing due to the bubble motion as they rise to the free surface. For jet impingement in the nucleate-boiling regime, the same is true. Therefore, the heat transfer is not nearly as dependent on the jet parameters as in single-phase jet impingement. The influence of jet parameters, subcooling and heat transfer fluid on the heat transfer of jet impingement in the nucleate boiling are investigated in Section 2.4.3.

Rau and Garimella [25] conducted experiments for free-surface jets impinging on a thin-foil heater at moderate wall heat fluxes. They found that heat transfer in the stagnation region was dominated by single-phase convection. Downstream in the wall-jet region, boiling occurred, which was the main contributor of heat transfer in that region. The heat transfer coefficient of single-phase convection was not influenced by the wall heat flux, this resulted in a constant heat transfer coefficient in the stagnation region with increasing wall heat flux, and thus increased wall temperature. In the wall-jet region where boiling was present, the heat transfer coefficient was a strong function of wall heat flux; when the wall heat flux increased, the heat transfer coefficient also increased. As the wall heat flux increased, the boiling front moved closer to the stagnation region until the entire surface was dominated by boiling heat transfer. Once boiling occurred over the entire surface, the surface temperature as well as the heat transfer coefficient profile became close to uniform. The same observations would not hold for thicker target walls as the spanwise conduction within the wall material would have a significant influence on the wall temperature distribution and thus on the wall heat flux into the fluid adjacent to the wall, suggesting that conjugation heat transfer should be considered in numerical analysis especially when comparing the results with experimental data where a significant thickness of the heated surface is present [24].

Similar behaviour was observed in the studies of Dukle and Hollingsworth [26] for submerged and confined jets. They proposed the following correlation for the radius of the boiling front:

$$r_f = \frac{D}{2} \sqrt{-C_8 \ln \left(\frac{\dot{q}_f}{C_9 \Delta T_{ref,ONB}} - C_{10} \right)} \quad (11)$$

where C_8 , C_9 and C_{10} are empirical constants from experimental data and are dependent on operating conditions, while the subscript f implies a boiling front. $\Delta T_{ref,ONB}$ is defined as:

$$\Delta T_{ref,ONB} = (T_{wall} - T_{ref})_{ONB} = \frac{\dot{q}_f}{HTC_f} \quad (12)$$

with HTC_f the heat transfer coefficient and T_{ref} the local bulk fluid temperature. The two equations above result in good approximations to the boiling front based on the single-phase heat transfer coefficient profile. The influence of design parameters is not present in the above correlations. However, an increase in the single-phase heat transfer coefficient profile (by means of increased jet velocity, reduced jet-to-surface spacing, etc.) results in a larger boiling front radius [24].

2.4.3 Effect of jet parameters in jet impingement boiling

Fundamental investigations into jet impingement boiling were first reported in the literature in 1970, when Copeland [27] experimentally investigated a water jet impinging on a heated nickel-plated copper block. Since then, researchers have identified various key parameters and their influence on heat transfer as well as on pressure drop. The influence of the key parameters on the heat transfer in the nucleate-boiling regime as well as the CHF is discussed in the sections to follow.

2.4.3.1 Jet velocity

In 1973, Katto and Kunihiro [28] experimentally investigated the burnout characteristics of a pool-boiling system by using mechanical means and a submerged liquid jet impinging on the heated surface to reduce the vapour mass. It was shown that the addition of an impinging jet resulted in a completely different burnout mechanism from pool boiling as well as a higher burnout heat flux, which increased with jet velocity. However, jet velocity also had little influence on the average heat transfer of submerged jet impingement in the fully developed nucleate-boiling regime.

Similarly, Struble and Witte [29], while studying heat flux measurement techniques for R113 boiling jets, observed that heat transfer in the fully developed nucleate-boiling regime increased only marginally with jet velocity and subcooling. Zhou and Ma [30] investigated the heat transfer of submerged round jet impinging on simulated microelectronic chips using R113 as the heat transfer fluid. They found that varying jet velocity from 0 to 11.355 m/s had a negligible influence on heat transfer in the fully developed nucleate-boiling regime.

Cardenas and Narayanan [31] experimentally investigated the heat transfer characteristics of submerged round impinging jets in the saturated nucleate-boiling regime using FC-72 as the heat transfer fluid. They found that the incipient boiling wall superheat was not a function of the jet Reynolds number and jet diameter. They concluded that jet kinetic energy was the key to CHF enhancement, noting that the critical heat flux (CHF) increased with jet velocity. Zhao *et al.* [32] investigated confined water jet heat transfer from porous surfaces finding that CHF increased with jet Reynolds number but that heat transfer in the fully developed nucleate-boiling regime was not a function of jet Reynolds number. CHF increased with jet velocity in free-surface jets, submerged jets, as well as confined jets [33].

Various studies were conducted to investigate the influence of jet velocity on the CHF and these found that for free-surface jets as well as confined jets with jet velocities below 10 m/s, the CHF scaled proportional to $(V_{jet}/D)^{1/3}$, with V_{jet} the jet velocity and D the jet diameter. This implies that for a constant jet velocity, increasing the jet diameter reduces the CHF given that the area ratio is 1. For highly confined jets, a much stronger relationship exists between jet velocity and CHF. Recent studies found that for confined jets with $H/D \leq 3$, a near-linear relationship existed between the CHF and jet velocity [33]. For jet velocities in the range of 10-40 m/s, the static pressure rise in the stagnation region resulted in an increase in the wall superheat of the ONB point [24].

2.4.3.2 Jet-to-surface spacing

Studies found that larger jet-to-surface spacings yielded lower heat transfer coefficients, thus higher wall superheat and lower CHF. The effect of jet-to-surface spacing is strongly influenced by the jet velocity, with influence of jet-to-surface spacing on heat transfer becoming less significant for higher jet velocities [24]. Clark *et al.* [33] found that for confined jets, the jet-to-surface spacing had a more significant influence on the heat transfer and CHF than for free-surface and submerged jets. They observed that for jet velocities between 1 m/s and 9 m/s, there was little difference between $H/D = 1, 3$ and 10 and the boiling curves matched that of pool boiling. However, for a jet-to-surface spacing of $H/D = 0.5$ at 9 m/s, there was a significant influence on the boiling curve in the fully developed nucleate-boiling regime and the CHF. For this low jet-to-surface spacing, a significant decrease in heat transfer was observed, which resulted in higher wall superheat and lower CHF. At a jet velocity of 1 m/s, they found that all the orifice spacings matched those of pool boiling with a slight to no increase in CHF. The maximum CHF was observed for a jet-to-surface spacing of $H/D = 3$ (roughly 27% increase over pool boiling).

2.4.3.3 Jet subcooling

Studies found that the amount of jet subcooling had very little influence on the boiling curve in the fully developed nucleate-boiling regime for free-surface, submerged and confined jets [29, 30]. However, it did have a significant influence on the wall superheat of the ONB point. It was observed that an increase in subcooling delayed the ONB and resulted in a higher wall superheat at the ONB [34]. It was observed that the amount of subcooling could have a significant influence on the CHF. Researchers found that the CHF increased with increasing jet subcooling [31, 32]. Various correlations exist in the literature relating the subcooled CHF to the saturated CHF. Monde *et al.* [35] proposed the following correlation:

$$\frac{\ddot{q}_{CHF}}{\ddot{q}_{CHF,sat}} = \frac{1 + \sqrt{1 + 4C_2Ja}}{2} \quad (13)$$

with

$$C_2 = \frac{0.95 \left(\frac{D}{d}\right)^2 \left(1 + \frac{D}{d}\right)^{0.364}}{\left(\frac{\rho_v}{\rho_l}\right)^{0.43} \left(\frac{2\sigma}{\rho_l U^2 (d - D)}\right)^{0.343}} \quad (14)$$

$$Ja = \left(\frac{\rho_v}{\rho_l}\right) \left(\frac{C_{p,l} \Delta T_{sub}}{h_{fg}}\right) \quad (15)$$

where D is the jet diameter and d the heater diameter. Qiu and Liu [36] proved that this correlation worked extremely well for superhydrophobic surfaces for subcooling in the range of 0 - 74 K. Liu *et al.* [37] proposed the following linear correlation for water jets with $15 \text{ K} \leq \Delta T_{sub} \leq 80 \text{ K}$:

$$\frac{\dot{q}_{CHF}}{\dot{q}_{CHF,sat}} = 1 + 11.82 \left(\frac{C_{p,l} \Delta T_{sub}}{h_{fg}} \right) \quad (16)$$

More correlations exist in the literature; however, they require additional empirical constants based on experimental data, limiting their general usefulness.

2.4.3.4 Multiple jets

Hong *et al.* [38], while investigating confined subcooled jet array boiling using an aqueous ethylene glycol solution, found that the liquid subcooling and jet-to-jet spacing played a significant role. They found that for a constant total mass flow rate, increasing the number of jets improved overall heat transfer and increased the CHF. They concluded that there existed an optimal jet-to-jet spacing for a fixed flow rate as too many jets and thus too small a jet-to-jet spacing could degrade heat transfer. There also existed an optimal jet-to-surface spacing to achieve the highest CHF. Cui *et al.* [39] observed that cross-flow in multijet arrays had a significant influence on the boiling curve for both smooth and pin-fin surfaces.

2.4.3.5 Numerical studies

Only a few numerical investigations are described in the literature. Narumanchi *et al.* [40] reported the first numerical investigation into jet impingement boiling, when they successfully predicted the heat transfer of the single water jet experiment by Katto and Kunihiro [28], using the Rensselaer Polytechnic Institute (RPI) boiling model implemented in the CFD code Fluent. Studying a single jet, Abishek *et al.* [41] investigated the effect of heater size and Reynolds number on the heat flux partitioning of the RPI boiling model in subcooled jet impingement boiling. They found that the liquid phase convective heat flux component increased with jet velocity, while the quenching and evaporative heat flux components were nearly unaffected. They also found that for any specified heat flux, the surface temperature reduced with an increase in the heater surface size, implying higher effectiveness of jet impingement boiling for localised heat sources. For the same geometry used by Narumanchi [40], Qiu *et al.* [42] found that the effects of conjugate heat transfer had to be considered should the experimental set-up have a copper block of significant mass. Esmailpour *et al.* [43] conducted a numerical parametric study for a subcooled single water jet showing that heat transfer decreased with increasing jet-to-surface spacing for $2 \leq H/D \leq 6$, but increased with jet velocity for $2500 \leq Re \leq 10000$. These numerical studies provided valuable insights into jet impingement boiling heat transfer, the influence of various parameters on heat transfer, and the local heat transfer effects of jet impingement boiling. Unfortunately, all of them were limited to single jets. It is of utter importance that the numerical studies are extended to multijet arrays to provide further insight into the local heat transfer effects of jet array boiling.

2.5 Numerical Framework

In the current study, subcooled nucleate boiling was modelled with the commercial CFD software suite, ANSYS Fluent 2021R1. The Eulerian multiphase model was used as the simulation framework with liquid as the primary phase and vapour as the dispersed phase. The Rensselaer Polytechnic Institute (RPI) wall-boiling model was implemented with the Eulerian multiphase model to predict the heat transfer of subcooled boiling. The mathematical descriptions of the numerical models used in ANSYS Fluent are presented in this section, as adapted from [44].

2.5.1 Eulerian Multiphase Framework

The Eulerian multiphase model treats the phases in a multiphase mixture as interpenetrating continua, where the volume of one phase cannot be occupied by another phase. The volume of the multiphase mixture thus consists of a portion of each phase of which the volumetric contribution is denoted by a volume fraction, α . The sum of the volume fractions of all phases must be one in each

control volume. The conservation of mass, momentum and energy equations are solved for each phase separately. The conservation equations are coupled with pressure and interphase exchange coefficients, which are dependent on the mixture type.

2.5.2 Governing Equations

The conservation of mass for phase q is:

$$\frac{\partial}{\partial t}(\alpha_q \rho_q) + \nabla \cdot (\alpha_q \rho_q \vec{u}_q) = \sum_{p=1}^n (\dot{m}_{pq} - \dot{m}_{qp}) \quad (17)$$

with α_q the volume fraction of phase q , ρ_q the density of phase q , \vec{u}_q the velocity of phase q , \dot{m}_{pq} the interphase mass transfer rate between phases p and q , and n the number of phases.

The momentum conservation equation for phase q is:

$$\begin{aligned} & \frac{\partial}{\partial t}(\alpha_q \rho_q \vec{u}_q) + \nabla \cdot (\alpha_q \rho_q \vec{u}_q \vec{u}_q) \\ &= -\alpha_q \nabla p + \nabla \cdot \bar{\tau}_q + \alpha_q \rho_q \vec{g} + \sum_{p=1}^n (\vec{R}_{pq} + \dot{m}_{pq} \vec{u}_{pq} - \dot{m}_{qp} \vec{u}_{qp}) \\ & \quad + (\vec{F}_q + \vec{F}_{lift,q} + \vec{F}_{wl,q} + \vec{F}_{vm,q} + \vec{F}_{td,q}) \end{aligned} \quad (18)$$

where $\bar{\tau}_q$ is the stress tensor, \vec{R}_{pq} the interfacial drag force between phases p and q , \vec{u}_{pq} the interphase velocity, \vec{g} the gravitational acceleration vector, p the pressure, \vec{F}_q an external body force, $\vec{F}_{lift,q}$ the lift force, $\vec{F}_{wl,q}$ the wall lubrication force, $\vec{F}_{vm,q}$ the virtual mass force, and $\vec{F}_{td,q}$ the turbulent dispersion force.

The energy conservation equation for phase q is:

$$\begin{aligned} & \frac{\partial}{\partial t} \left(\alpha_q \rho_q \left(e_q + \frac{\vec{u}_q^2}{2} \right) \right) + \nabla \cdot \left(\alpha_q \rho_q \vec{u}_q \left(h_q + \frac{\vec{u}_q^2}{2} \right) \right) \\ &= \nabla \cdot (\alpha_q k_q \nabla T_q + \bar{\tau}_q \cdot \vec{u}_q) + p \frac{\partial \alpha_q}{\partial t} + S_q \\ & \quad + \sum_{p=1}^n (Q_{pq} + \dot{m}_{pq} h_{pq} - \dot{m}_{qp} h_{qp}) \end{aligned} \quad (19)$$

where, h_q is the specific enthalpy of phase q , k_q the conductivity of phase q , T_q the temperature of phase q , Q_{pq} the energy exchange term between phases p and q , S_q the source term, and h_{pq} the difference in the specific enthalpies of phases p and q .

2.5.3 Turbulence Modelling

The mixture RNG k - ε model was used in the current work to model the turbulence of the multiphase mixture. It accounts for dispersed phase-induced turbulence by adding additional source terms in the turbulent kinetic energy and dissipation equations. The turbulent kinetic energy equation for the mixture is as follows:

$$\frac{\partial}{\partial t}(\rho_m k) + \nabla \cdot (\rho_m \vec{u}_m k) = -\nabla \cdot (\alpha_{k,m} \mu_{t,m} \nabla k) + G_{k,m} - \rho_m \varepsilon + S_{k,m} \quad (20)$$

where ρ_m is the mixture density, k the turbulent kinetic energy, \vec{u}_m the mixture velocity, ε the dissipation rate, $\alpha_{k,m}$ the inverse effective Prandtl number for k , $\mu_{t,m}$ the mixture dynamic viscosity,

$G_{k,m}$ the turbulence production rate, and $S_{k,m}$ the dispersed phase-induced turbulence production source term.

The dissipation rate equation for the mixture is as follows:

$$\frac{\partial}{\partial t}(\rho_m \varepsilon) + \nabla \cdot (\rho_m \vec{u}_m \varepsilon) = -\nabla \cdot (\alpha_{\varepsilon,m} \mu_{t,m} \nabla \varepsilon) + \frac{\varepsilon}{k} (C_1 G_{k,m} - C_2 \rho_m \varepsilon) - R_\varepsilon + S_{\varepsilon,m} \quad (21)$$

where $\alpha_{\varepsilon,m}$ is the inverse effective Prandtl number for ε , C_1 and C_2 are model constants, R_ε the RNG additional term, and $S_{\varepsilon,m}$ the dispersed phase-induced dissipation rate source term.

2.5.4 Interphase Transfer Models

The interfacial area concentration between phases is an important parameter for determining heat, mass and momentum transfer through the interface between phases. The interfacial area concentration is modelled with the Ishii interfacial area model [44] and is given by the following correlation:

$$A_i = \frac{6(1 - \alpha_p) \min(\alpha_p, \alpha_{p,crit})}{d_p (1 - \min(\alpha_p, \alpha_{p,crit}))} \quad (22)$$

with $\alpha_{p,crit} = 0.25$. The liquid-vapour mass transfer rate in equation (17) is determined based on the evaporation and condensation model, and is formulated as follows [44]:

$$\sum_{p=1}^n (\dot{m}_{pq}) = \dot{m}_{lv} = \frac{[h_{ls}(T_l - T_{sat}) + h_{vs}(T_v - T_{sat})]A_i}{h_{fg}} + \frac{\dot{q}_E A_w}{h_{fg} + C_{pl}(T_{sat} - T_l)} \quad (23)$$

where h_{fg} is the latent heat of vaporisation, C_{pl} is the specific heat capacity of the liquid phase, T the temperature with subscripts l , sat and v referring to the liquid phase, saturation state, and vapour phase respectively; A_w is the interfacial area density of the wall, and \dot{q}_E is the evaporative heat flux component of the RPI boiling model; h_{ls} and h_{vs} are the liquid- and vapour-side heat transfer coefficients respectively, which are calculated according to the Ranz-Marshall correlation [45]:

$$Nu_p = 2.0 + 0.6\sqrt{Re_p}Pr^{\frac{1}{3}} \quad (24)$$

or the Tomiyama correlation [46]:

$$Nu_p = 2.0 + 0.15Re_p^{0.8}Pr^{0.5} \quad (25)$$

The Tomiyama correlation is applicable to turbulent bubbly flows with lower Reynolds numbers than for the Ranz-Marshall correlation. The correlation used for each case is indicated in later chapters. The interfacial drag force is determined from the Ishii drag model [47], with the drag coefficient determined as follows:

$$C_D = \min(C_{D,vis}, C_{D,dis}) \quad (26)$$

where $C_{D,vis}$ and $C_{D,dis}$ are the drag coefficients in the viscous and distorted regimes respectively. They are derived from the following correlations [44]:

$$C_{D,vis} = \frac{24}{Re} (1 + 0.15Re^{0.75}) \quad (27)$$

$$C_{D,dis} = \frac{2}{3} \left(\frac{d_p}{\sqrt{\frac{\sigma}{g|\rho_q - \rho_p|}}} \right) \quad (28)$$

where σ is the surface tension, and Re the relative Reynolds number. The lift force is derived from the following relation [44]:

$$\vec{F}_{lift,q} = -C_l \rho_q \alpha_p (\vec{u}_q - \vec{u}_p) \times (\nabla \times \vec{u}_q) \quad (29)$$

where C_l is the lift coefficient derived from the modified Tomiyama model by Frank *et al.* [48]:

$$C_l = \begin{cases} \min[0.288 \tanh(0.121 Re_p), f(Eo')], & Eo' \leq 4 \\ f(Eo'), & 4 < Eo' \leq 10 \\ -0.27, & 10 < Eo' \end{cases} \quad (30)$$

where

$$f(Eo') = 0.00105 Eo'^3 - 0.0159 Eo'^2 - 0.0204 Eo' + 0.474 \quad (31)$$

and Eo' is a modified Eotvos number

$$Eo' = \frac{g(\rho_q - \rho_p) d_h^2}{\sigma} \quad (32)$$

with

$$d_h = d_p (1 + 0.163 Eo^{0.757})^{\frac{1}{3}} \quad (33)$$

$$Eo = \frac{g(\rho_q - \rho_p) d_p^2}{\sigma} \quad (34)$$

The wall lubrication force is determined by the following correlation [44]:

$$\vec{F}_{wl} = C_{wl} \rho_q \alpha_p |\vec{u}_q - \vec{u}_p|^2 \vec{n}_w \quad (35)$$

where \vec{n}_w is the unit normal pointing away from the wall, and C_{wl} the wall lubrication coefficient derived from the Antal *et al.* model [49]:

$$C_{wl} = \max\left(0, \frac{C_{w1}}{d_p} + \frac{C_{w2}}{y_w}\right) \quad (36)$$

with $C_{w1} = -0.01$, $C_{w2} = 0.05$, and y_w the distance to the nearest wall.

The turbulent dispersion force is derived from the Lopez de Bertodano model [50]:

$$\vec{F}_{td,q} = -\vec{F}_{td,p} = C_{TD} \rho_q k_q \nabla \alpha_p \quad (37)$$

where k_q is the turbulent kinetic energy of the primary phase.

In boiling flows, the density of the vapour (secondary phase) is much lower than the liquid (primary phase). As a result, the vapour accelerates relative to the liquid. The inertia of the liquid phase exerts a force on the accelerating vapour particles known as the virtual mass force. The inclusion of the virtual mass force can improve numerical stability as well as the accuracy of the results. The virtual mass force is determined by the following correlation [44]:

$$\vec{F}_{vm} = C_{vm} \alpha_p \rho_q \left(\frac{d_q \vec{u}_q}{dt} - \frac{d_p \vec{u}_p}{dt} \right) \quad (38)$$

with C_{vm} the virtual mass coefficient. For a spherical bubble in an infinite medium, the theoretical value for $C_{vm} = 0.5$. However, experimental and theoretical studies found that the interaction effects between vapour and liquid became important at higher vapour fractions ($\alpha_p > 0.15$), increasing the liquid mass transported by the bubbles. Various models have been proposed for C_{vm} as a function of vapour fraction. Ishii and Mishima [51] proposed:

$$C_{vm} = \frac{\alpha_p}{2} \frac{1 + 2\alpha_p}{1 - \alpha_p} \quad (39)$$

Van Wijngaarden and Jeffrey [52] proposed:

$$C_{vm} = 0.5 + \frac{3}{2} \alpha_p \quad (40)$$

Paladino and Maliska [53] proposed:

$$C_{vm} = 0.5 + \alpha_p \quad (41)$$

which all showed excellent correlation with the experimental data. The effects of the virtual mass coefficient are studied in Appendix A; however, all other results presented in the study are conducted with $C_{vm} = 0.5$.

The turbulence production and dissipation rate source terms in equations (20) and (21) respectively are derived from the Troshko-Hassan turbulence interaction model [54]. The turbulence production source term becomes

$$S_{k,m} = C_{ke} K_{pq} |\vec{u}_p - \vec{u}_q|^2 \quad (42)$$

where $C_{ke} = 0.75$ and K_{pq} is the fluid-fluid interphase exchange coefficient given as follows:

$$K_{pq} = \frac{\rho_p f}{6\tau_p} d_p A_i \quad (43)$$

with f the drag function and τ_p the particulate relaxation time. The dissipation rate source term becomes

$$S_{\varepsilon,m} = C_{td} \frac{1}{\tau_p} S_{k,m} \quad (44)$$

with $C_{td} = 0.45$ and τ_p the characteristic time of the induced turbulence:

$$\tau_p = \frac{2C_{VM}d_p}{3C_D|\vec{u}_p - \vec{u}_q|} \quad (45)$$

2.5.5 RPI Wall-Boiling Model

The RPI wall-boiling model of Kurul and Podowski [55] was developed to predict the boiling heat transfer in the subcooled nucleate-boiling regime. It partitions the total wall heat flux going into the liquid into three components, namely the liquid convective heat flux, quenching heat flux, and evaporative heat flux. The total wall heat flux can thus be written as

$$\ddot{q}_W = \ddot{q}_C + \ddot{q}_Q + \ddot{q}_E \quad (46)$$

where \ddot{q}_C represents the convective heat flux, \ddot{q}_Q the quenching heat flux, and \ddot{q}_E the evaporative heat flux. The heat flux components are illustrated in Figure 15 [43], which indicates that the convective heat flux approximates the heat transfer due to the single-phase forced convection, the evaporative heat flux models the evaporation of the microlayer, and the quenching heat flux the heat transfer due to the rewetting of the surface after bubble departure. The mechanism of the heat flux components depicted in Figure 15 is analogous to the boiling heat transfer mechanism during the bubble growth and departure process illustrated in Figure 9 and Figure 10.

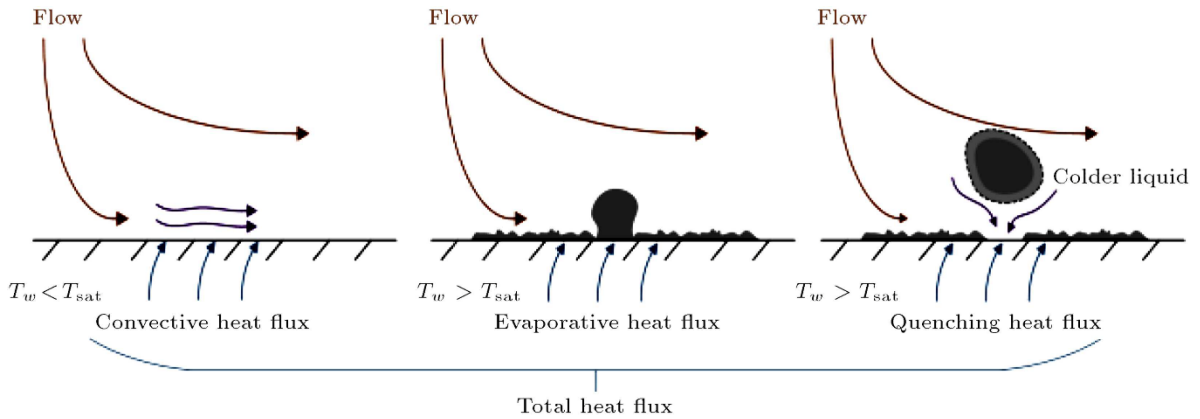


Figure 15: Schematic of the RPI boiling model, illustrating the heat flux components of the RPI wall-boiling model [43]

In the subcooled boiling regime, the liquid convective heat flux is determined by the following correlation:

$$\ddot{q}_C = h_c(T_w - T_l)(1 - A_b) \quad (47)$$

where h_c is the convective heat transfer coefficient derived from the log law used by the standard wall functions. T_w is the wall temperature, T_l is the liquid temperature and is determined with a wall function to adhere to the log-law. A_b is the area of influence and represents the portion of the wall that is covered by nucleating bubbles. The portion of the wall covered by liquid is thus represented by $(1 - A_b)$.

The quenching heat flux models the cyclic averaged transient heat transfer caused by liquid filling the void after a bubble departs from the wall. The quenching heat flux is determined by the following correlation [44]:

$$\ddot{q}_Q = C_{wt} \frac{2k_l}{\sqrt{\pi\lambda_l t}} (T_w - T_l) A_b \quad (48)$$

where C_{wt} is the bubble waiting time coefficient with a default value of 1, k_l is the liquid phase thermal conductivity, λ_l the liquid phase diffusivity, and t is the periodic time. The quenching heat flux is highly dependent on T_l , resulting in high mesh sensitivity in the near-wall region. Since the standard wall function approach is used, it is desired that the cells adjacent to the wall adhere to $30 < y^+ < 300$, limiting the minimum cell size in mesh refinement. In order to alleviate mesh dependence, T_l is evaluated at a fixed y^+ of 250, as proposed by Egorov and Menter [56].

The evaporative heat flux models the heat transfer causing vapour bubble formation at the wall. The evaporative heat flux is determined as follows [44]:

$$\ddot{q}_E = \frac{\pi}{6} D_w^3 N_w \rho_v h_{fg} f \quad (49)$$

where D_w is the vapour bubble departure diameter, N_w is the nucleation site density, ρ_v is the vapour density, and f is the bubble departure frequency. The area of influence is determined with the following correlation [44]:

$$A_b = \min \left(1, K \frac{N_w \pi D_w^2}{4} \right) \quad (50)$$

The upper bound of 1 is imposed on the area of influence to avoid numerical instabilities caused by unbound empirical approximations. Here, K is an empirical constant given by Del Valle and Kenning [57]:

$$K = 4.8e^{\left(-\frac{Ja_{sub}}{80}\right)} \quad (51)$$

where Ja_{sub} is the subcooled Jacob number:

$$Ja_{sub} = \frac{\rho_l C_{pl} \Delta T_{sub}}{\rho_v h_{fg}} \quad (52)$$

with $\Delta T_{sub} = T_{sat} - T_l$. The frequency of bubble departure is determined by the Cole [58] correlation for saturated pool boiling:

$$f = \frac{1}{t} = \sqrt{\frac{4g(\rho_l - \rho_v)}{3\rho_l D_w}} \quad (53)$$

It should be noted that the Cole correlation is based on the inertial growth of the vapour bubble, which does not occur in subcooled boiling. However, studies [40, 42] have shown that using it for low degrees of subcooling can still produce acceptable results. The nucleation site density is modelled with the following semi-empirical correlation, which depends on the wall superheat [44]:

$$N_w = C^n (T_w - T_{sat})^n \quad (54)$$

where $C = 210$ and $n = 1.805$ are empirical constants, as reported by Lemmert and Chawla [59].

The accurate prediction of the bubble departure diameter is very important in boiling simulations because the evaporation heat flux is highly dependent on the bubble departure diameter. The Unal relation [60] is used in the present study as it is not only based on empirical coefficients but considers

wall superheat, amount of subcooling, as well as the local pressure. The bubble departure diameter is determined as follows:

$$D_w = 2.4210^{-5} p^{0.709} \left(\frac{a}{b\sqrt{\varphi}} \right) \quad (55)$$

with

$$a = \frac{T_w - T_{sat}}{2\rho_v h_{fg}} \sqrt{\frac{\rho_s C_{ps} k_s}{\pi}} \quad (56)$$

$$b = \begin{cases} \frac{\Delta T_{sub}}{2 \left(1 - \frac{\rho_v}{\rho_l}\right)} e^{\left(\frac{\Delta T_{sub}}{3} - 1\right)} & \text{for } \Delta T_{sub} \leq 3 \\ \frac{\Delta T_{sub}}{2 \left(1 - \frac{\rho_v}{\rho_l}\right)} & \text{for } \Delta T_{sub} \geq 3 \end{cases} \quad (57)$$

$$\varphi = \max \left(\left(\frac{U_b}{0.61} \right)^{0.47}, 1.0 \right) \quad (58)$$

where U_b is the near-wall bulk velocity, h_{fg} is the latent heat of vaporisation and subscripts s , l and v denote the solid, liquid and vapour phases respectively.

2.5.6 Solution Method

The phase-coupled SIMPLE algorithm was implemented in the present study to achieve pressure-velocity coupling. Spatial discretisation was achieved with the first-order UPWIND method. The pressure was determined with the PRESTO! (PREssure STaggered Option) scheme. Time discretisation was achieved with the first-order implicit method, which was unconditionally stable; however, the single-phase Courant number was kept below one to ensure optimal convergence and solution accuracy. Body forces, as well as volume fractions, were solved implicitly. To further enhance convergence, truncated forms of the virtual mass force were used in cells where convergence issues were present. To limit heat transfer fluctuations caused by the drastic variation in the thermal properties and density of the fluid close to the heated surface due to phase change, a numerical noise filter was applied to the energy equation. The Fluent text commands used to enable the above settings as well as the suggested solver settings are included in the numerical procedure in Appendix C. All results presented in later chapters are time-averaged results, determined after the surface temperatures had levelled off and a steady state was reached. In the cases where boiling curves were presented, the heat flux was increased to the next point on the boiling curve after steady state has been reached for the current point on the boiling curve, and the simulation was run long enough to average the data for the current point over time. That is, the heat flux increased after a fixed time period for every point on the boiling curve. The processing code used for the time averaging and processing of the results, and the plotting thereof are included in Appendix D.

3 Computational Fluid Dynamics Model and Validation

In this Chapter, the numerical model is validated against the published results of two experimental studies of submerged and confined jets in the subcooled nucleate-boiling regime. The first validation case considers a single submerged jet, while the second validation case considers a confined jet array.

3.1 2D Axisymmetric Single Jet

3.1.1 Problem Description

Katto and Kunihiro [28] conducted an experimental study of the mechanism of burnout for saturated nucleate boiling of a single water jet at atmospheric pressure on a cylindrical heated copper block. The experimental set-up is illustrated in Figure 16 [28]. The experiment considered a single round water jet in the submerged configuration impinging on a conical heated copper block (2) with an upper surface diameter of 10 mm. The jet had a nozzle exit velocity of 2 m/s with 3 °C inlet subcooling at atmospheric pressure, translating to an inlet temperature of 97 °C. The nozzle (7) had an exit diameter of 1.6 mm with a jet-to-surface spacing of 3 mm, submerged 2 mm below the free surface. The water was heated by an electric heater (14) in the boiling water tank (10) upstream of the nozzle (7), ensuring a constant nozzle exit temperature. The flow rate of the jet was maintained by the water level in the boiling water tank (10) due to the difference in gravitational water head at the water-free surface and the nozzle exit. The water level in the boiler (1) was maintained by an overflow device (11) and the water temperature by an auxiliary heater (5). The temperature of the heated copper block was measured by four thermocouples (4) distributed along the centre line of the block. The temperature distribution of the thermocouples (4) was used in conjunction with the one-dimensional heat conduction equation to determine the applied heat flux and top surface temperature.

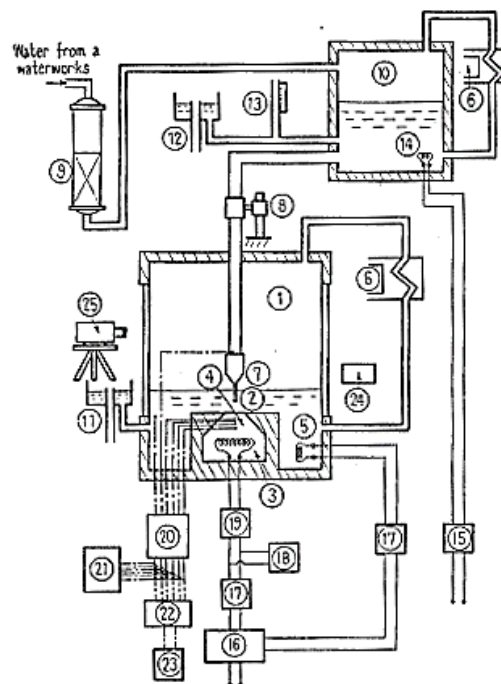


Figure 16: Experimental set-up used in the Katto and Kunihiro experimental study to investigate the burnout characteristics of jet impingement boiling [28]

The heated copper block consisted of two parts, the lower part was cylindrical with 11 heating elements embedded inside it, while the upper part had a conical shape facing upwards. The sides of the copper block were well insulated resulting in an estimated heat loss of less than 5% of the input heat [28].

Two numerical investigations were conducted into this experimental set-up: Narumanchi *et al.* [40] and Qiu *et al.* [42]. The latter considered the effects of conjugation heat transfer, while the former did not consider it. Both studies showed a good correlation with the experimental results, with the latter showing superior results due to the consideration of conjugate heat transfer in the solid copper block.

3.1.2 Numerical Modelling

As the objective of this study was to replicate the boiling curve of the experiment conducted by Katto and Kunihiro [28], the focus of the numerical model was the heat transfer from the heated copper block to the fluid directly in contact with the block and the top surface temperature. During the experiment, the conditions of the surrounding fluid and jet conditions were closely monitored and kept constant. As a result, the boundary conditions of the numerical model could be derived mostly from the experimental parameters with little uncertainty. Accurate boundary conditions can greatly reduce the required flow domain size without sacrificing accuracy resulting in reduced computational time.

3.1.2.1 Computational domain and boundary conditions

In the present study, the experiment was approximated by a 2D axisymmetric domain. Both the case considering conjugate heat transfer in the solid block and the case not considering it were investigated. The 2D axisymmetric computational domains of the case not considering conjugation and the case considering it are illustrated in Figure 17 and Figure 18 respectively. It is important to note the hydrostatic pressure gradient at the radial outlet pressure boundary; failure to add the hydrostatic pressure gradient at the radial outlet results in convergence issues for the continuity equation, especially at higher heat fluxes and finer meshes. The experimental set-up suggested that the results provided by Ref. [28] were for the stagnation point temperature; however, the results at the stagnation point were highly dependent on the mesh. To alleviate the mesh dependence, the area-weighted average temperature of the stagnation region was used rather than the stagnation point temperature. In both cases, the stagnation region was defined as the area directly below the jet with the same area as the nozzle exit. It should be noted that the liquid-side heat transfer coefficient was determined by the Ranz-Marshall correlation, given its superior performance to the Tomiyama correlation at higher bubble Reynolds numbers. The vapour bubbles were expected to have high Reynolds numbers due to the large density difference between the liquid and vapour phases in addition to the turbulent jet impinging on the heated surface.

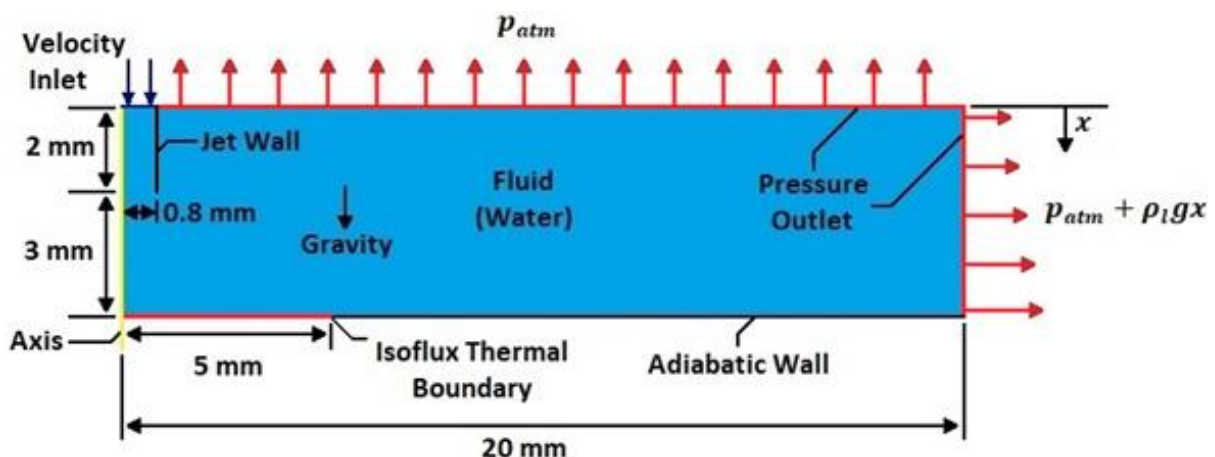


Figure 17: 2D Axisymmetric domain based on the Katto and Kunihiro experiment [28] without considering conjugation heat transfer effects [42]. Hydrostatic pressure gradient included at the radial outlet

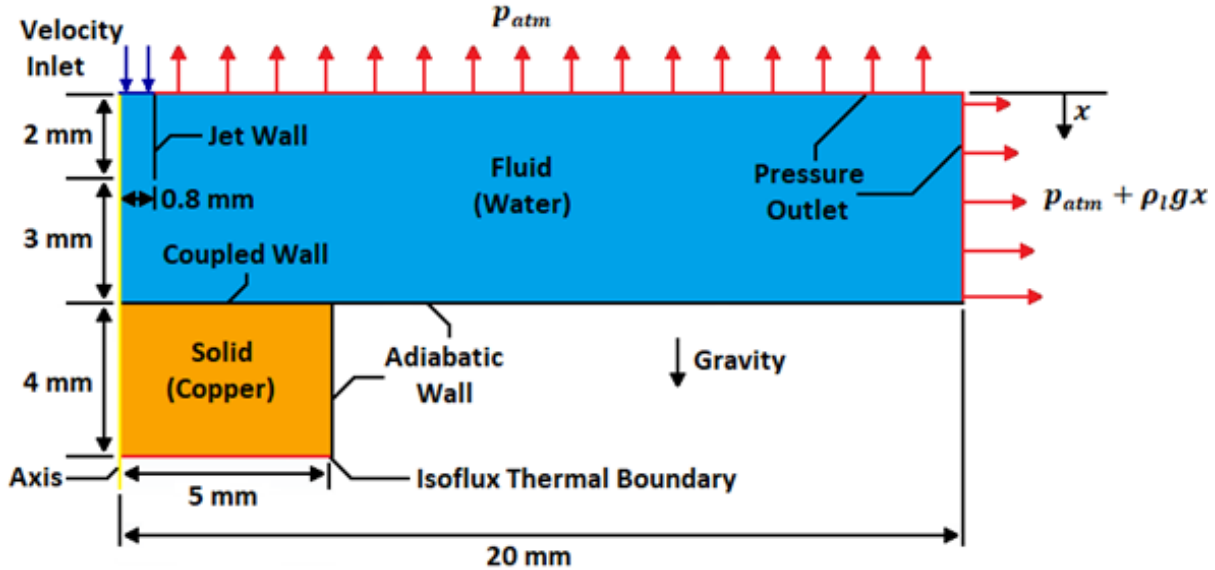


Figure 18: 2D Axisymmetric domain based on the Katto and Kunihiro experiment [28] considering conjugation heat transfer effects [42]. Hydrostatic pressure gradient included at the radial outlet

The inlet and outlet conditions for both cases are summarised in Table 2. The pipe length and diameter upstream of the nozzle exit were unknown and no information was available on the contraction of the nozzle. It was assumed that due to the section of pipe flow and the contraction upstream of the nozzle, some turbulence was present at the nozzle exit, which was why an inlet turbulence intensity of 5% was used as recommended by Ref. [61] for internal flow. As the flow rapidly contracted just upstream of the nozzle, it was highly unlikely to have a fully developed velocity profile, resulting in the choice of a uniform velocity profile at the inlet. Given that the top of the domain was open to atmospheric pressure, it was assumed that no vapour returned from the pressure outlet, resulting in the backflow vapour fraction of 0. The properties of water at atmospheric pressure are summarised in Table 3. The properties of copper are listed in Table 4.

Table 2: Inlet and outlet conditions of the 2D axisymmetric domain based on the Katto and Kunihiro experiment [28] for both the case with conjugation and the one without it

Inlet Boundary Condition	Value
Velocity [m/s]	2
Temperature [°C]	97
Turbulence intensity [%]	5
Outlet Boundary Condition	Value
Gauge pressure [Pa]	$\rho_l g x$
Backflow turbulence intensity [%]	5
Backflow turbulence viscosity ratio	10
Backflow vapour volume fraction	0

Table 3: Properties of water at 1 atm pressure [42]

	Water	
	Liquid	Vapour
Saturation temperature (°C)	100	
Surface tension (N/m)	0.059	
Latent heat (J/kg)	2.257E6	
Density (kg/m ³)	958	0.6
Specific heat (J/kg·K)	4219	2010
Dynamic viscosity (kg/m·s)	2.83E-4	1.23E-5
Thermal conductivity (W/m·K)	0.68	0.025

Table 4: Properties of copper [61]

Solid	Copper
Density (kg/m ³)	8978
Specific heat (J/kg·K)	381
Thermal conductivity (W/m·K)	387.6

3.1.2.2 Meshing and mesh independence

Since wall functions were used for near-wall treatment, the mesh had to satisfy the $y^+ \geq 30$ condition at the walls required by the RPI model [55]. As the flow had no velocity magnitude at the stagnation point and very low velocities in the stagnation region, meshing the stagnation region with $y^+ < 30$ could not be avoided. Five consecutively refined meshes with quadrilateral cells, with mesh densities ranging from 19.5 cells/mm² to 533 cells/mm² (cell counts ranging from 1 950 to 53 336), were tested for the case without conjugation at a heat flux of 50 W/cm² to evaluate mesh dependency. The boundary layer cell thickness was kept constant in all meshes to keep $y^+ \approx 30$ outside the stagnation region. The aspect ratio of all five meshes were kept below 10. A mapped uniform mesh with a cell size that satisfied the y^+ requirement for the wall-jet region outside the stagnation region, with a cell count of only 1 950 was used as the starting point and is illustrated in Figure 19.

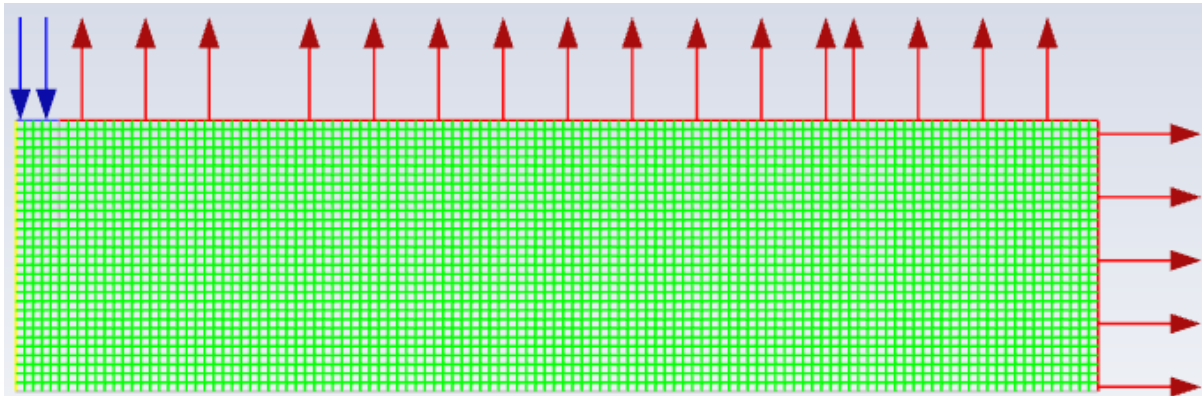


Figure 19: Coarse mesh for 2D axisymmetric domain used for the approximation of the Katto and Kunihiro experiment [28] without considering conjugation heat transfer effects [42]

The stagnation region and average wall superheats are the parameters of interest for the mesh independence study. The results of the study are summarised in Table 5. The average wall superheat varied around 0.05% and the stagnation region wall superheat varied around 0.1% when going from mesh density of 121 cells/mm² to 533 cells/mm². Therefore, mesh density of 121 cells/mm² (12 101 cells) was deemed sufficient to predict the boiling curve. The case with conjugation used the same mesh density for the fluid and solid regions.

Table 5: 2D Axisymmetric single-jet mesh refinement study results at 50 W/cm² applied heat flux.

Cell Count	Average Wall Superheat (°C)	Stagnation Region Wall Superheat (°C)	Maximum Change Relative to Previous Mesh (%)
1950	13.8813	11.7188	
4860	13.8128	11.7423	0.49
12101	13.8931	11.7357	0.056
30132	13.8991	11.7638	-0.043
53336	13.8882	11.7558	0.078

3.1.3 Results and Discussion

3.1.3.1 Boiling curve

The boiling curve predictions of both cases in the present study were plotted along with the boiling curves of the previous numerical studies and experimental data in Figure 20. The boiling curves of the current study illustrated in Figure 20 were based on the area-weighted average temperature of the stagnation region. The results with conjugation corresponded well with the experimental data, while a clear shift in the boiling curve occurred to the left when conjugation was not considered. In addition, the presence of the solid copper led to less variation in the temperature profile of the heated surface (not shown), discussed in detail in Section 3.1.3.5.

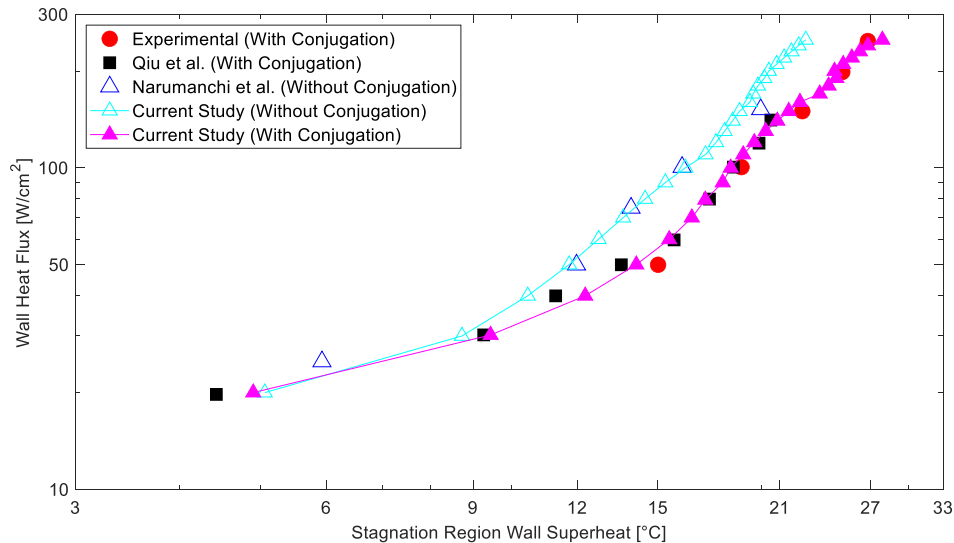


Figure 20: Boiling curve validation for the Katto and Kunihiro experiment [28] using the stagnation region wall temperature

The respective deviation from the results of the previous numerical investigations is accredited to the differences in the numerical model selection and set-up. The present study used the Tomiyama lift force model, applicable to deformable bubbles, whereas Narumanchi *et al.* used the Moraga *et al.* [62] lift force model, which is mainly applicable to solid spherical particles. Unlike the current study, Narumanchi *et al.* [40] did not evaluate the liquid temperature, used to determine the quenching heat flux, at a fixed y^+ of 250 as proposed by Egorov and Mentor, which could have a significant influence on the results. Qiu *et al.* [42] used modifications to the standard $k-\epsilon$ model in their study as opposed to the RNG $k-\epsilon$ model used in the current study, which could have a significant influence on the predicted heat transfer. Additionally, the interphase transfer models used in the Qiu *et al.* study were not disclosed, causing some uncertainty in the comparison. The present study is the only one that managed to capture the full boiling curve. It is accredited to the addition of the hydrostatic pressure gradient at the pressure outlet, which resulted in improved convergence and stability and which allowed for convergence at much higher heat fluxes towards the CHF point. The model in the present study diverged at a heat flux of 270 W/cm^2 , opposed to the ONBD of 250 W/cm^2 seen in the experiment.

3.1.3.2 Variation with flow time

Figure 21 shows the heated surface area-weighted average wall superheat, stagnation region area-weighted average wall superheat, and wall heat flux against flow time for the case without conjugation. The simulation mimicked an experimental set-up where the heat flux applied was ramped up each three seconds, as shown by the blue curve in the figure. Both the average wall superheat and stagnation region wall superheat increased drastically when the heat flux was increased before reducing to reach a steady state within the three-second time window. The average wall superheat fluctuated in the wall heat flux range of 50 to 100 W/cm^2 . The fluctuation was due to the exchange

between quenching and evaporative heat transfer as the dominant heat transfer mechanism over certain parts of the heated surface. For heat fluxes beyond 100 W/cm^2 , evaporative heat transfer was the dominant heat transfer mechanism over the entire heated surface resulting in less variation of the wall superheat. Although a numerical noise filter was used for the energy equation to alleviate the rapid fluctuations of the liquid properties in the vicinity of the heated surface, there was still some numerical noise present, such as the peaks at roughly 50 and 60 seconds of flow time. Figure 21 indicates that the wall superheats reached steady state for all heat fluxes in the first half of the flow time at each heat flux, which suggested that using only the second half of the flow time for each heat flux to obtain the boiling curve was a good assumption.

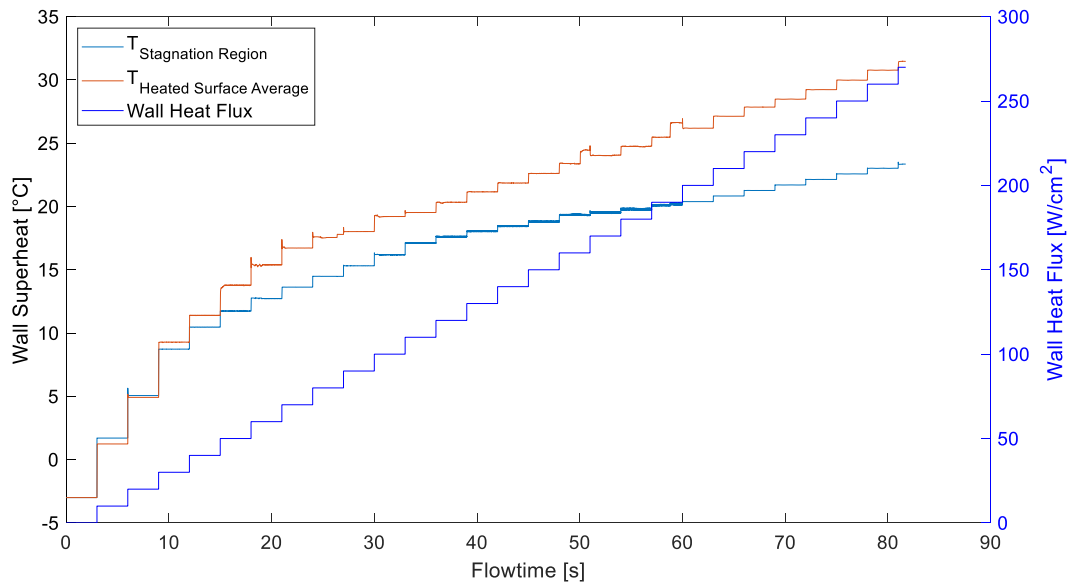


Figure 21: Stagnation region wall superheat, heated surface average wall superheat and wall heat flux vs flow time for 2D single-jet case without conjugation heat transfer effects

Figure 22 shows the heated surface area-weighted average wall superheat, stagnation region area-weighted average wall superheat, and wall heat flux against flow time for the case with conjugation. Here the ramping time window was increased to six seconds to allow the copper block's temperature to stabilise given its considerable thermal mass. The stagnation region and surface average temperatures as well as the wall heat flux are seen to fluctuate drastically in the 50 to 100 W/cm^2 heat flux range. These fluctuations were once again due to the exchange between quenching and evaporative heat transfer as the dominant heat transfer mechanism over certain parts of the heated surface. Again, for heat fluxes beyond 100 W/cm^2 , evaporative heat transfer was the dominant heat transfer mechanism over the entire heated surface resulting in less variation of the wall superheat and wall heat flux. Some fluctuations were present in the wall temperature and wall heat flux at higher heat fluxes and could be due to numerical noise.

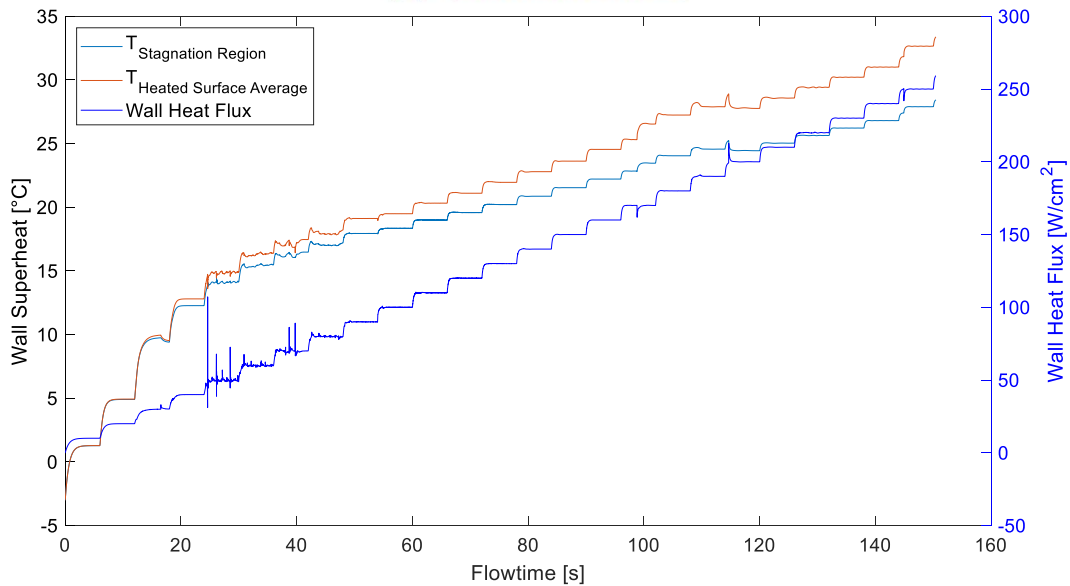


Figure 22: Stagnation region wall superheat, heated surface average wall superheat and wall heat flux vs flow time for 2D single-jet case with conjugation heat transfer effects

3.1.3.3 Contour plots

CFD allows for the extraction of additional information from simulations which is not typically available in experimental studies. It also makes it possible to illustrate complex flow physics such as the velocity and temperature fields of complex flow geometries and the boiling phenomenon. The velocity contours of the single water jet case with conjugation are illustrated for increasing applied heat fluxes in the fully developed nucleate-boiling regime in Figures 23 (a) to (e). The typical flow regions of jet impingement are visible, i.e. the free-jet region, stagnation region and the wall-jet region. The wall jet expanded as it moved radially along the heated surface, due to the vapour formation at the outer edges of the heated surface for lower heat fluxes, shown in Figure 23(a). At higher heat fluxes, shown in Figures 23 (b) to (e), the wall jet expanded closer to the stagnation region as well. The wall jet expanded with increasing heat flux, shown in Figures 23 (a) to (e), due to the increased rate of vapour formation pushing the wall jet away from the heated surface. The wall-jet velocity sped up as the heat flux increased, due to the high body forces caused by the vapour bubbles moving upwards, towards the top outlet. The jet in the free-jet region entrained the surrounding liquid, as can be seen by the widening of the jet in Figure 23(a). The jet in the free-jet region widened significantly with increasing heat flux, due to vapour formation in the stagnation region, causing vapour bubbles to move up into the jet blocking the flow to some extent, as illustrated in Figures 23 (c) to (e).

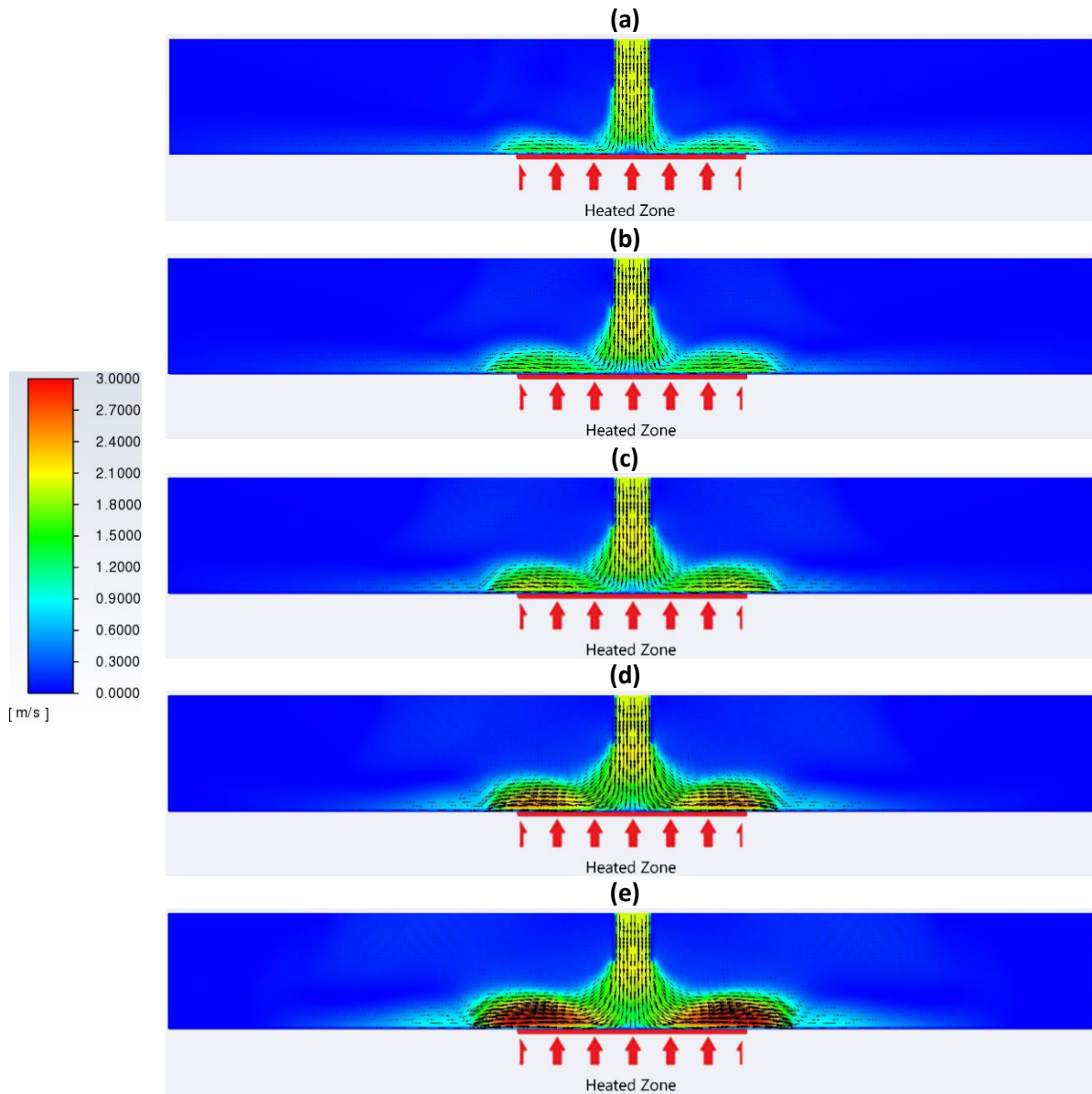


Figure 23: Single-jet velocity contours [m/s] with overlaid vectors, at various wall heat fluxes: (a) 50 W/cm², (b) 100 W/cm², (c) 150 W/cm², (d) 200 W/cm², and (e) 250 W/cm²

The liquid temperature contours of the single water jet case with conjugation are illustrated in Figures 24 (a) to (e), for increasing applied heat fluxes in the fully developed nucleate-boiling regime portion of the boiling curve. The jet broke through the layer of warm liquid above the heated surface to rewet the surface. The jet then pushed the warm liquid above the surface radially outwards, which caused the fluid at the outer edges of the heated surface to heat up, allowing for more vapour formation. Further out, the warmer liquid rose from the heated surface and moved back towards the jet centre line due to the jet entrainment causing recirculating flow. The bulk liquid temperature increased with the applied heat flux, shown in Figures 24 (a) to (e), due to the increased amount of vapour condensing in the subcooled fluid causing the fluid temperature to increase. The region of cold liquid above the heated surface also increased with increasing heat flux. This was somewhat surprising but was expected due to the reduced amount of liquid in the domain because of increased vapour formation. At higher heat fluxes, the rate of vapour formation was so high that the vapour did not condense above the heated surface, but escaped from the top of the domain, and only the vapour that was pushed out radially condensed closer to the radial outlet, resulting in the increased liquid temperature outside the heated region, as illustrated in Figure 24(e). The liquid temperature in the top portion of the domain next to the jet was much lower than for the rest of the domain for some of

the applied heat fluxes due to the pressure outlet boundary condition, which resulted in reversed flow at the top boundary causing subcooled fluid to enter the top outlet. This process was an unphysical phenomenon that did not accurately represent the experiment. The reversed flow was limited by reducing the pressure equation under relaxation factor; however, the reversed flow could not be prevented entirely.

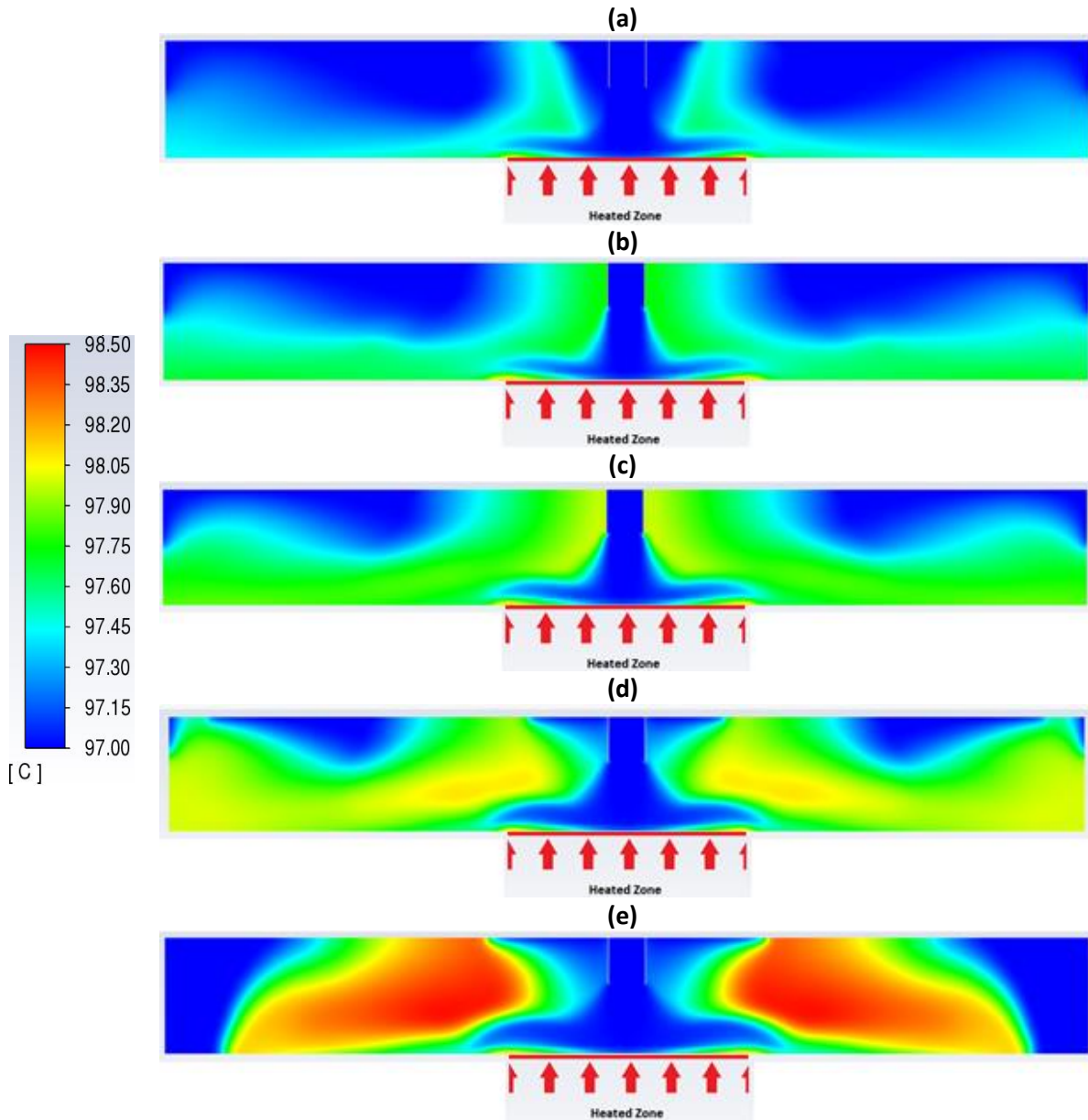


Figure 24: Single-jet liquid temperature contours [°C] at various wall heat fluxes: (a) 50 W/cm², (b) 100 W/cm², (c) 150 W/cm², (d) 200 W/cm², and (e) 250 W/cm²

Figures 25 (a) to (e) show the vapour volume fraction contours for the same applied heat fluxes. Most of the vapour was formed towards the outer edges of the heated surface due to the lower local convective heat transfer, resulting in more intense boiling. The vapour was pushed radially outwards by the jet; however, some of the vapour managed to depart up away from the surface before condensing in the subcooled liquid, especially at higher heat fluxes. Almost no vapour was present in and above the stagnation region at low heat fluxes, shown in Figures 25 (a) to (c), indicating that the jet was effective at breaking through the vapour layer above the surface. At higher heat fluxes, shown in Figures 25 (c) to (e), vapour formation occurred in the stagnation region, preventing the jet from rewetting the surface. The amount of vapour present in the region directly above the heated surface

increased with increasing heat flux, supporting the statement that the vapour did not condense as quickly above the heated surface for high heat fluxes, resulting in a lower liquid temperature in the region directly above the heated surface.

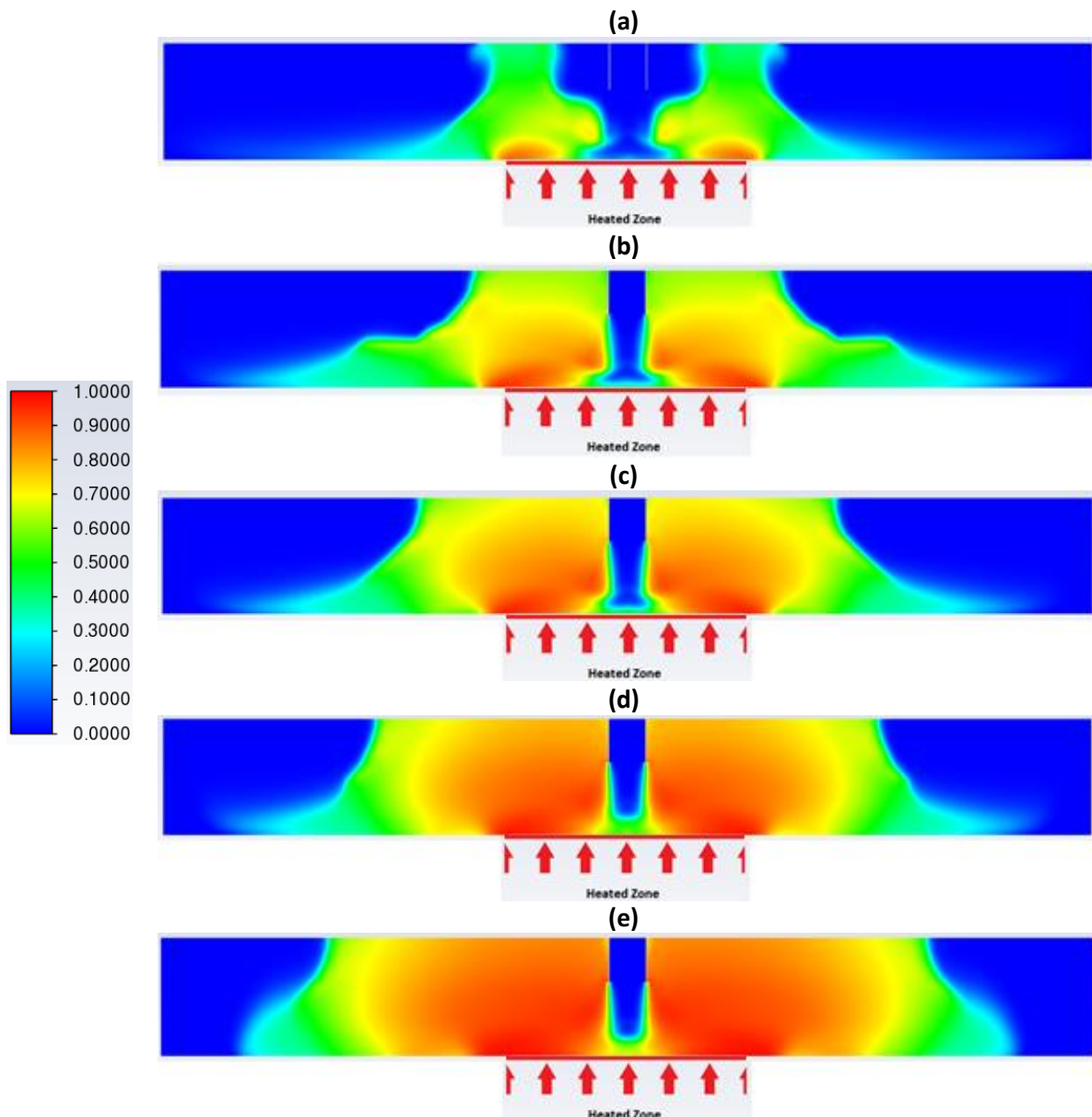


Figure 25: Single-jet vapour volume fraction contours at various wall heat fluxes: (a) 50 W/cm², (b) 100 W/cm², (c) 150 W/cm², (d) 200 W/cm², and (e) 250 W/cm²

3.1.3.4 Distributions of vapour

The vapour distribution plots are shown in Figure 26 for the single water jet at various heat fluxes in the fully developed nucleate-boiling regime. The vapour fraction in the stagnation region increased with increasing heat flux. The vapour outside the stagnation region also increased with increasing heat flux; however, the vapour was not pushed out radially as far as for the lower heat fluxes, indicating that the influence of the jet on the vapour was less significant at higher heat fluxes.

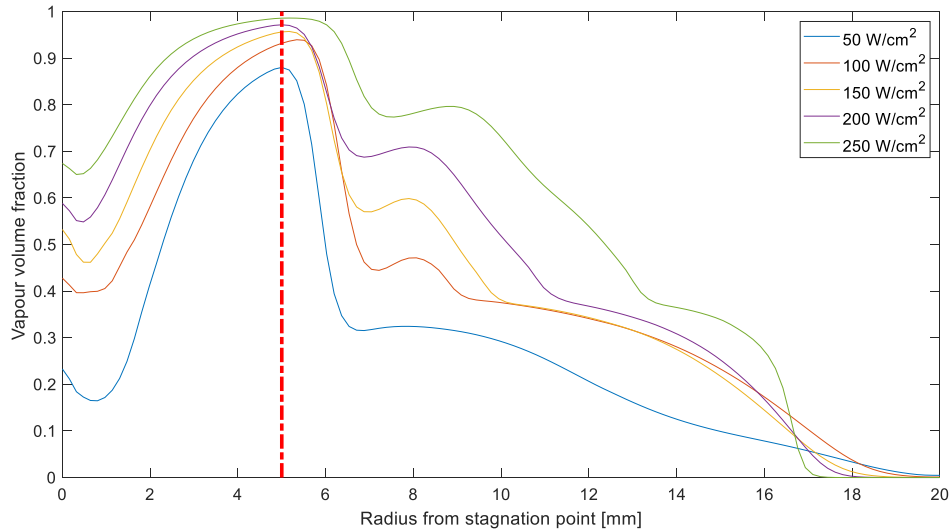


Figure 26: Vapour distribution plots for 2D axisymmetric case with conjugation at various heat fluxes

3.1.3.5 Effect of conjugation

As mentioned in Section 3.1.3.1, including the effects of conjugation heat transfer in the heated copper block resulted in less variation in the heated surface temperature due to the thermal mass of the copper. Figure 27 shows the minimum, average and maximum surface temperatures for the full boiling curve of the single-water jet for both the case with and without conjugation. The difference between the three curves was much less for the case with conjugation than for the case without due to the increased heat transfer into the stagnation region resulting in a lower temperature for the case not considering conjugation. Further, the average surface temperatures for the case with and without conjugation were similar. Therefore, if the average heat transfer performance of jet impingement boiling was of interest, the effects of conjugate heat transfer could be neglected without sacrificing too much accuracy.

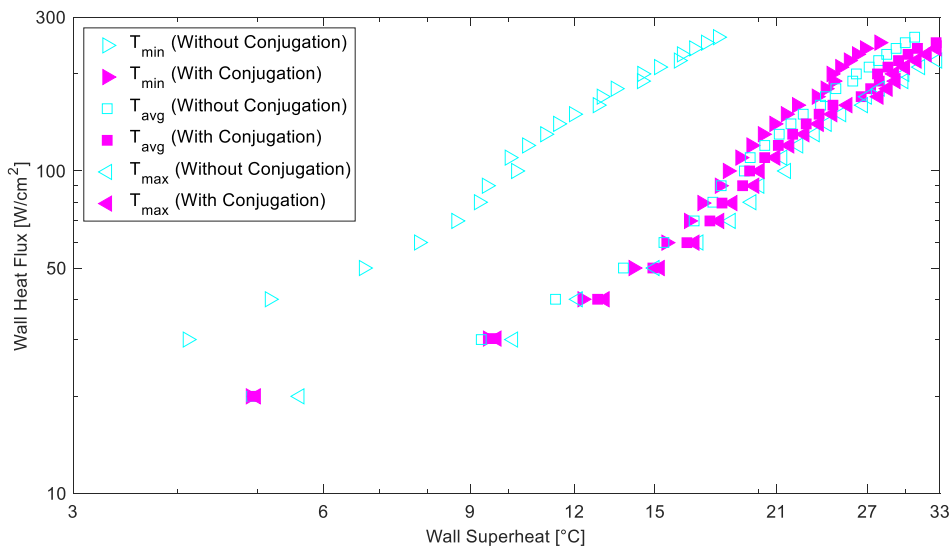


Figure 27: Single-jet boiling curve based on minimum, average and maximum surface temperatures for both the case without conjugation heat transfer as well as the case with conjugation heat transfer

Figure 28 shows the contributions of the three heat flux components of the RPI boiling model to the total heat flux for the full boiling curve for the single-water jet for both the case with and without conjugation. The evaporative heat flux contribution was higher for the case with conjugation, while the quenching heat flux contribution was lower. Compared with the results of Qiu *et al.* [42], also shown in the figure, the convective and quenching heat flux contributions of the present study with

conjugation were lower, while the evaporative heat flux contribution was higher. It is important to note that for the current study, the evaporative heat flux contribution approached one, while the quenching heat flux approached zero. Therefore, the evaporative heat flux contribution of the RPI boiling model would reach one at the ONBD, which marked the end of the fully developed nucleate-boiling regime where the standard RPI boiling model applied. This is an important observation for design purposes where the ONBD or CHF is not known beforehand.

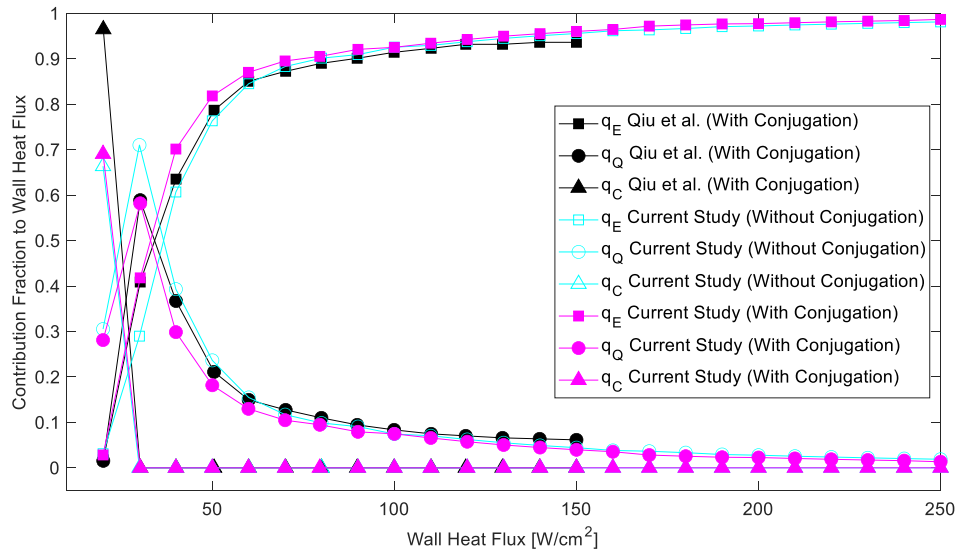


Figure 28: Contribution of the RPI boiling model heat flux components to the wall heat flux for the single jet without and with conjugation heat transfer, as well as the results of the study by Ref. [42]

3.2 3D Multijet Array with Cross-flow

3.2.1 Problem Description

Most jet impingement boiling CHF correlations available in the literature are based on experiments done with water, resulting in large errors in predicting the CHF for refrigerants and fluorochemicals. Devahdhanush and Mudawar [63] conducted an experimental study of the cooling performance of both single round jets and confined jet arrays. The focus of the study was the dependence of critical heat flux on key geometrical parameters and operating conditions. The heated surfaces were examined after the CHF tests to investigate flow characteristics and surface temperature due to jet-to-jet interactions. For all experiments, R-134a refrigerant was used as the heat transfer fluid. The results of the study were combined with FC-72 experimental data to formulate a CHF correlation for these two commonly used fluids in cooling applications. The study considered round jets with boiling, configured in confined jet arrays impinging on square surfaces.

3.2.1.1 Experimental loop

Figure 29 [63] provides a schematic of the flow loop. The refrigerant was pumped through the loop by one of the two gear pump assemblies. The gear pumps were coupled magnetically to fan-cooled motors. The motors were driven by variable frequency drives for precise flow rate control. The refrigerant then flowed through one of the two turbine flow meters to ensure that the desired flow rate was achieved. The refrigerant flowed through a control valve just upstream of the jet impingement module. The control valve was used to regulate the flow resistance, and thus pressure and flow rate. The control valve also helped to alleviate pressure oscillations in the jet impingement module. Downstream of the jet impingement module, the refrigerant (single-phase or two-phase) flowed through an air-cooled fin-and-tube condenser to return to the single-phase state. To ensure that the required degree of subcooling was achieved, the refrigerant then passed through a SWEP plate heat exchanger, cooled by distilled water. The flow then returned to the gear pump, completing

the flow loop. Most of the refrigerant in the loop was stored in the liquid reservoir; the fluid temperature and pressure were regulated by an assembly of heaters and a modular cooling system controlled by a PID controller.

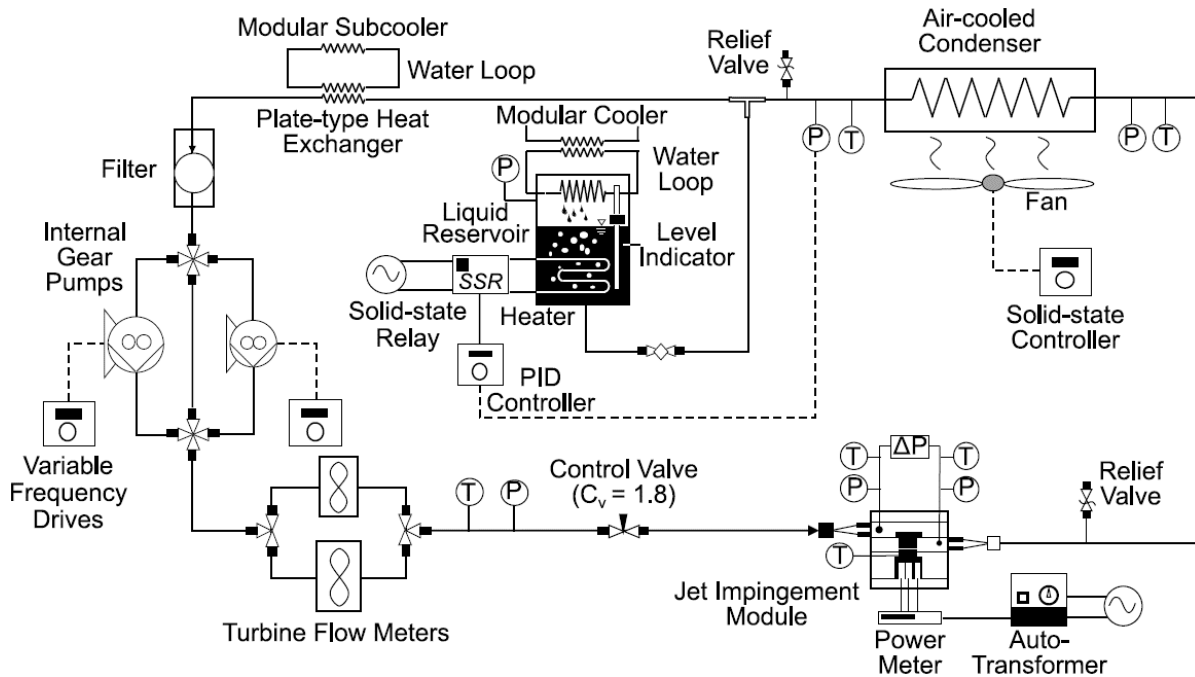


Figure 29: Devahdhanush and Mudawar experimental loop schematic [63]

3.2.1.2 Test module

An exploded view of the test module is given in Figure 30. The test module consisted of a heated block, jet plate, and inlet-and-outlet plenum housings. The jet plate and heated block were the main components that changed between test set-ups. Different housings were made for every test set-up to ensure that the heated block and jet plate were flush with the housings. All housings had the same outer dimensions to simplify the process of changing the experimental set-up between experiments. It should be noted that the outlet plenum housings had a thickness of 4.724 mm in all experiments, which resulted in a jet-to-surface spacing of 4.724 mm for all cases. The heated blocks were machined out of C10100 copper, the housings and cover plates were made of G-7 and G-10 epoxy-fibreglass composites and the jet plates (orifices) were machined out of 6061 aluminium alloy [63].

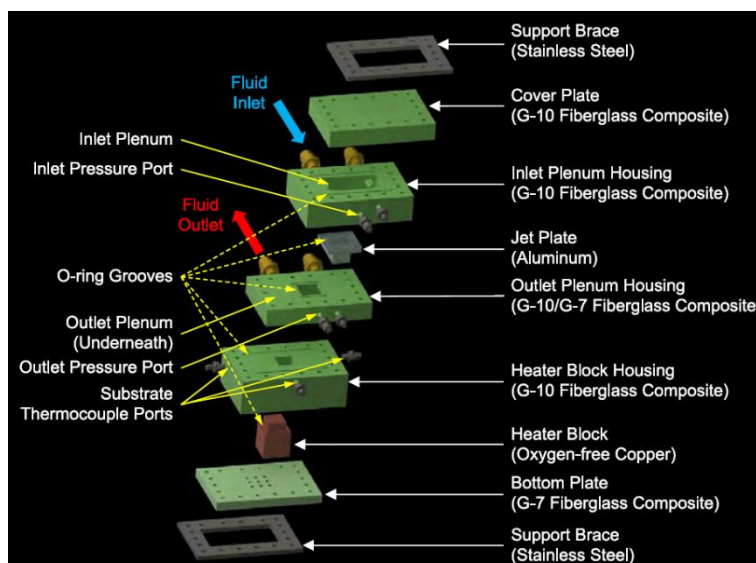


Figure 30: Exploded view of jet impingement test module [63]

Figure 31 shows the modelled geometry as well as the dimensions of the jet plates (left) and heated surfaces (right). Refrigerant entered the jet plate from the top, indicated by the blue arrows, and entered the jet chamber from the nozzle outlets, indicated in blue on the right figure. Refrigerant left the jet chamber from the sides, indicated by the red arrows. The heated surface is represented by the mustard yellow portion and the insulation housing by the green portion.

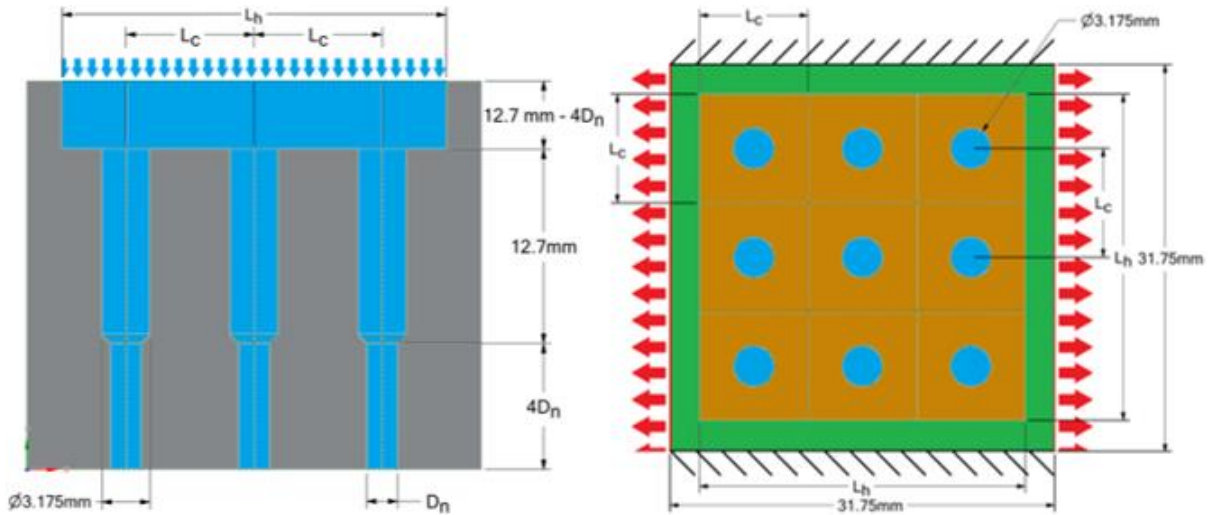


Figure 31: Sectional view of jet plate (left) and top view of jet plate and heated block (right)

To ensure uniform flow across the jets, the nozzles consisted of two portions, namely a 3.175 mm diameter upper tube with a length of 12.7 mm and a lower tube with the actual nozzle diameter, D_n , and four nozzle diameters in length. The angle of the V-contraction was the same as that of the drill bit used to drill the upper tube. The contractions in the nozzles also minimised the pressure drop in the jet impingement module. The jet-to-jet spacing is given by the characteristic length:

$$L_c = \frac{L_h}{\sqrt{N}} \quad (59)$$

with L_h the heated surface side length and N the number of evenly distributed jets in a cross-section. The uniformly distributed jets subdivided the heated surface area into unit jet cells with side lengths of L_c . Each unit jet cell had a jet impinging on its centre [63].

Figure 32 shows the thermocouple locations inside the heated blocks. The number of thermocouples in the block depended on the block size. For the small block, only thermocouple $T_{tc,1}$ was present, for the medium block, thermocouples $T_{tc,1}$ and $T_{tc,2}$ was present. For the large block, all three thermocouples were present. For all cases, the thermocouples were situated 6.35 mm below the heated surface. The total thickness of the heated blocks was not specified; however, the thickness was much more than the distance between the thermocouple plane and the top of the heated block. Cartridge heaters were embedded in the heated blocks. The number of heaters increased with the heated surface size, the small block had one heater, the medium block four and the large block nine. The heater block was insulated from the fibreglass insulation layer by a glass wool-filled gap, resulting in negligible heat loss from the sides of the heated block [63].

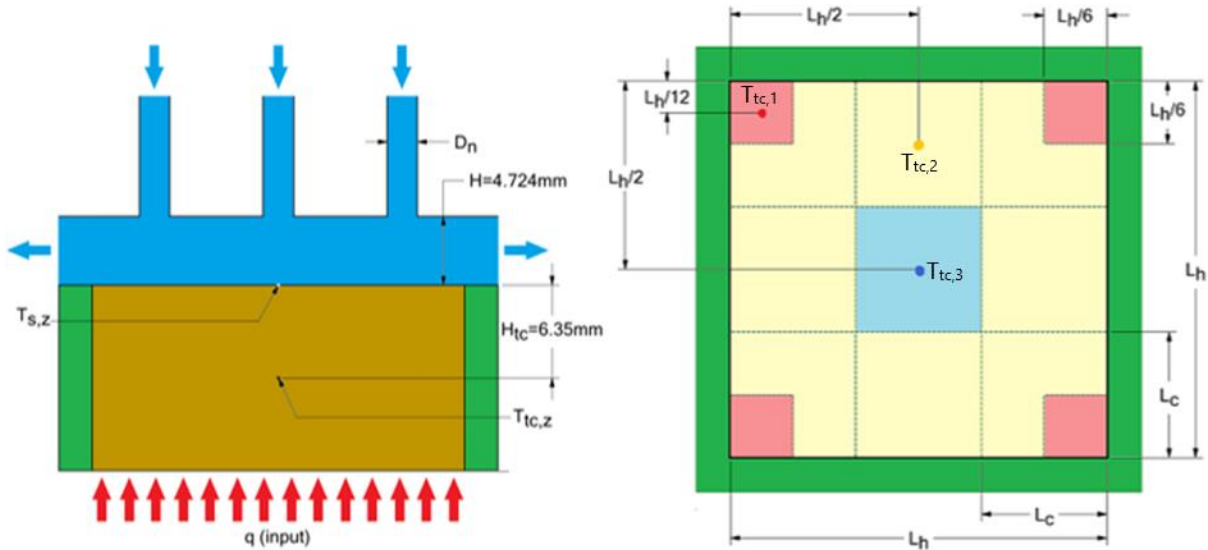


Figure 32: Heated block thermocouple locations

The experimental study considered various combinations of design parameters and operating conditions. Since the focus of the experimental study was on CHF, all cases were tested up to the CHF. Unfortunately, the results of the fully developed nucleate-boiling regime were only reported for a single case. Given that the focus of the current study was on fully developed nucleate boiling, the fully documented case was of particular interest and served as a validation case for the present study. The experimental set-up and operating conditions of the fully documented case are listed in Table 6 [63].

Table 6: 3D Jet array in nucleate-boiling regime parameters, adapted from Ref. [63]

Parameter	Value/Configuration
Number of jets, N	9 (3x3 Array)
Nozzle outlet diameter, D_n (mm)	2.06
Heated surface side length L_h (mm)	25.4
Average jet nozzle velocity, U_n (m/s)	4
Inlet temperature, T_{in} ($^{\circ}C$)	20.14
Flow loop pressure (Pa)	771278

3.2.1.3 Data reduction and processing

Under the assumption of one-dimensional heat conduction in the solid, the temperature measurements of the thermocouples in the solid block were used to determine the heated surface temperature. Since one-dimensional heat conduction was assumed, heat loss from the sides of the block was neglected. With a constant heat flux applied to the bottom of the block, the heated surface temperature was then approximated by the one-dimensional Fourier conduction equation:

$$T_{s,z} = T_{tc,z} - \frac{\dot{q}H_{tc}}{k_s} \quad (60)$$

where k_s is the thermal conductivity of the copper block, \dot{q} is the input heat flux (electrical heat divided by surface area), and subscript z denoting the thermocouple number, i.e. 1, 2 or 3. Each thermocouple produced an approximation of the local surface temperature of the unit cell situation directly above it. The unit cells approximated by each of the thermocouples for the large surface are illustrated by the coloured shaded regions in Figure 32. Thermocouple 1 approximated the surface temperature of the unit cell shaded in blue ($T_{s,1}$), Thermocouple 2 the surface temperature of the seven-unit cells shaded in yellow ($T_{s,2}$) and Thermocouple 3 the surface temperature of the unit cell shaded in red ($T_{s,3}$).

Therefore, it was necessary to use area-weighted averaging of the local surface temperatures to approximate the average surface temperature:

$$T_s = \frac{\sum A_z T_{s,z}}{A_s} \quad (61)$$

In the cases where the small block was used, only Thermocouple 1 was used and was taken as the average surface temperature. In the cases where the medium block was used, both Thermocouples 1 and 2 were used. The average surface temperature is given by:

$$T_s = \frac{T_{s,1} + 8T_{s,2}}{9} \quad (62)$$

In the cases where the large block, thus all three thermocouples, was used, the average surface temperature is given by:

$$T_s = \frac{T_{s,1} + 7T_{s,2} + T_{s,3}}{9} \quad (63)$$

The thermodynamic equilibrium qualities were determined at the inlet and outlet of the test module for each case, with the following expression as example of the outlet:

$$x_e = \frac{h - h_f}{h_{fg}} \quad (64)$$

where h is the inlet or outlet enthalpy. The thermodynamic equilibrium quality x_e at the test module outlet gives insight into the state of the fluid over the heated surface as well as the CHF mechanism. A negative quality indicates a subcooled CHF mechanism. A quality between zero and one indicates a saturated CHF mechanism. A higher outlet quality indicates higher vapour content over the heated surface and in the jet chamber. The enthalpy at the outlet is given by:

$$h_{out} = h_{in} + \frac{\dot{q}A_s}{\dot{m}} \quad (65)$$

with h_{in} the inlet enthalpy, \dot{q} the applied heat flux, A_s the heated surface area and \dot{m} the total R-134a inlet mass flow rate. To ensure accurate results, the data were averaged over a period of at least 150 seconds for each applied heat flux for every case after reaching a steady state [63].

3.2.1.4 Uncertainties

Maximum uncertainties in the measurements of temperature, absolute pressure, differential pressure, volume flow rate, and heat input were reported to be ± 0.1 °C, $\pm 0.1\%$, $\pm 0.1\%$, $\pm 0.15\%$, and $\pm 1.49\%$ respectively. By considering a conservative $\pm 1\%$ uncertainty in length measurements, the maximum uncertainty in heat flux was determined to be $\pm 2.05\%$. The maximum uncertainty in \dot{q} at CHF was determined to be $\pm 4.35\%$, comprising of both heat flux measurement uncertainty and CHF isolation error (capturing the absolute maximum heat flux before the drastic drop in heat flux). [63]

3.2.2 Numerical Modelling

3.2.2.1 Computational domain and boundary conditions

Once again, the experiment was approximated by two cases, by neglecting and considering the effects of conjugation heat transfer in the solid. Since the jet array consisted of multiple round jets impinging on a square target, the domain was not axisymmetric and required a 3D mesh. The

computational requirements could be reduced significantly by only modelling a quarter of the domain with symmetry planes. The computational domains are illustrated in Figure 33 and Figure 34, for the two cases respectively. Again, note the hydrostatic pressure gradient distribution at the side outlet, shown in the right-side figures. The quarter of the domain that was modelled is shown by the two burgundy lines (symmetry planes) in the left-side figures.

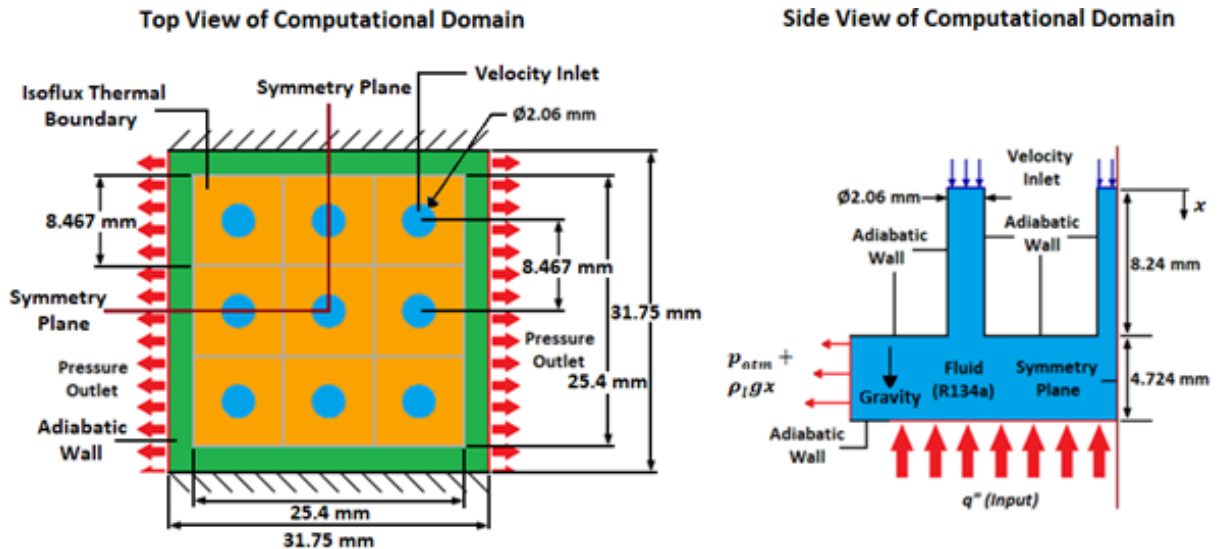


Figure 33: 3D Quarter symmetry multijet array domain, adapted from the experiments of Devahdhanush and Mudawar [63] without considering conjugation heat transfer effects (no solid modelled)

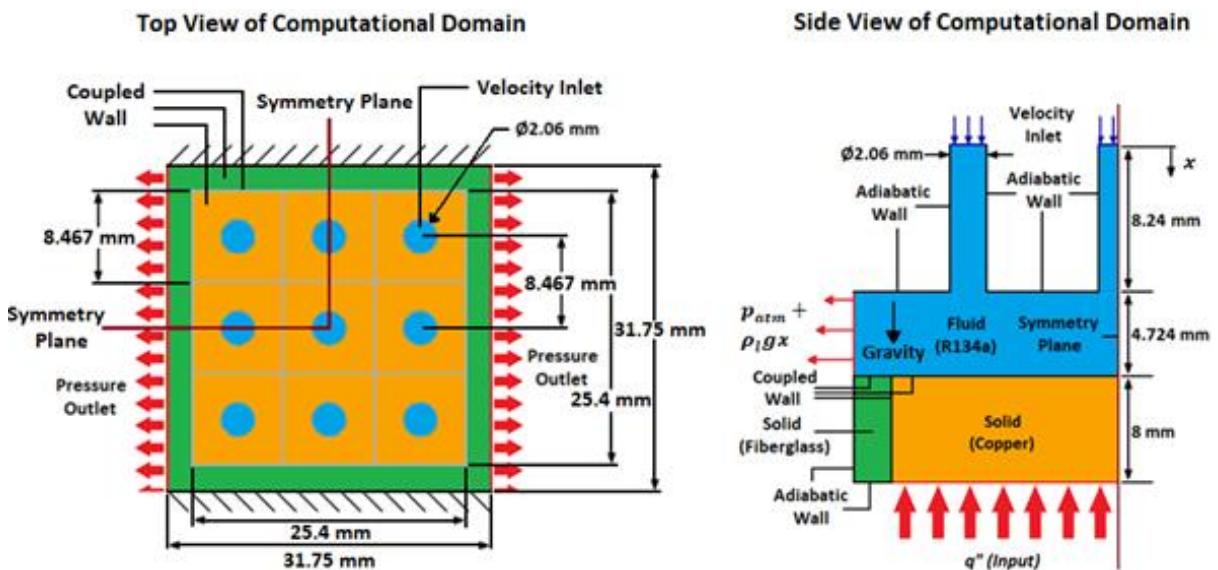


Figure 34: 3D Quarter symmetry multijet array domain, adapted from the experiments of Devahdhanush and Mudawar [63] considering conjugation heat transfer effects (with solid copper and fibreglass insulation)

In the experiment, R134a exited the jet nozzles at a velocity of 4 m/s with 9 °C of subcooling at a pressure of 771 278 Pa, translating to an inlet temperature of 20.14 °C. Given the high degree of subcooling, changes in the properties of the liquid, especially density and viscosity, was expected to be significant which could result in large deviations in the numerical results from the experimental data if not accounted for. Therefore, the properties of R134a at the saturation pressure are listed in Table 7 as a function of temperature. Note that the saturation pressure differed from the one reported for the experiment [63], since the pressure corresponding to a saturation temperature of 29.14 °C in Coolprop [64] was slightly different from the one listed in the experiment [63]. The properties of the fibreglass insulation used in the experiment were not reported. The fibreglass properties used for the

insulation in the present study are listed in Table 8 [61] at a reference temperature of 25 °C. Given the good heat insulative properties of the fibreglass, heat transfer through the insulation section was expected to be minimal and thus not to have a significant influence on the results obtained, and therefore the use of constant properties was deemed sufficient. The inlet and outlet conditions used for both cases in the present study are summarised in Table 9. Note that like for the single jet cases in section 3.1, an inlet turbulence of 5% were used for the multijet array cases.

Table 7: Properties of R134a at saturation pressure [35]

Fluid	R134a			
Saturation pressure (Pa)	751340			
Saturation temperature (°C)	29.14			
Surface tension (N/m)	0.0075			
	Liquid			Vapour
Temperature (°C)	20.14	25	29.14	29.14
Density (kg/m ³)	1224	1206	1190	36.60
Specific heat (J/kg·K)	1405	1423	1446	1059
Dynamic viscosity (N·s/m ²)	2.070E-04	1.949E-04	1.851E-04	1.187E-05
Thermal conductivity (W/m·K)	0.0832	0.0811	0.0794	0.0142
Specific enthalpy (J/kg)	227700	234500	240500	414400

Table 8: Properties of fibreglass [61]

Solid	Fiberglass
Density (kg/m ³)	1749
Specific heat (J/kg·K)	1115
Thermal conductivity (W/m·K)	0.7208

Table 9: Inlet and outlet conditions of the 3D quarter symmetry multijet domain based on the experiments of Devahdhanush and Mudawar [63] for both the case with conjugation and the one without it

Inlet Boundary Condition	Value
Velocity [m/s]	4
Temperature [°C]	20.14
Turbulence intensity [%]	5
Outlet Boundary Condition	Value
Gauge pressure [Pa]	$\rho_l g x$
Backflow turbulence intensity [%]	5
Backflow turbulence viscosity ratio	10
Backflow vapour volume fraction	0

3.2.2.2 Meshing and mesh independence

As in the previous case, the mesh had to satisfy the $y^+ \geq 30$ condition at the walls since standard wall functions were used for the RPI model. To investigate mesh independence, four consecutively refined meshes with polyhedral cells with mesh densities ranging from 25.32 cells/mm³ to 130.8 cells/mm³, with cell counts ranging from 126 858 to 655 370, were tested for the case without conjugation at a wall heat flux of 80 W/cm². Prism boundary layer mesh refinement was used for all meshes to keep the boundary layer cell thickness constant and $y^+ \approx 30$ for the heated surface outside the stagnation regions. The maximum aspect ratio of the mesh cells was again kept below 10. A polyhedral mesh with a prism boundary layer that satisfied the y^+ requirement for the wall-jet region outside the stagnation regions, with a cell count of only 126 858, was used as the starting point and is illustrated in Figure 35.

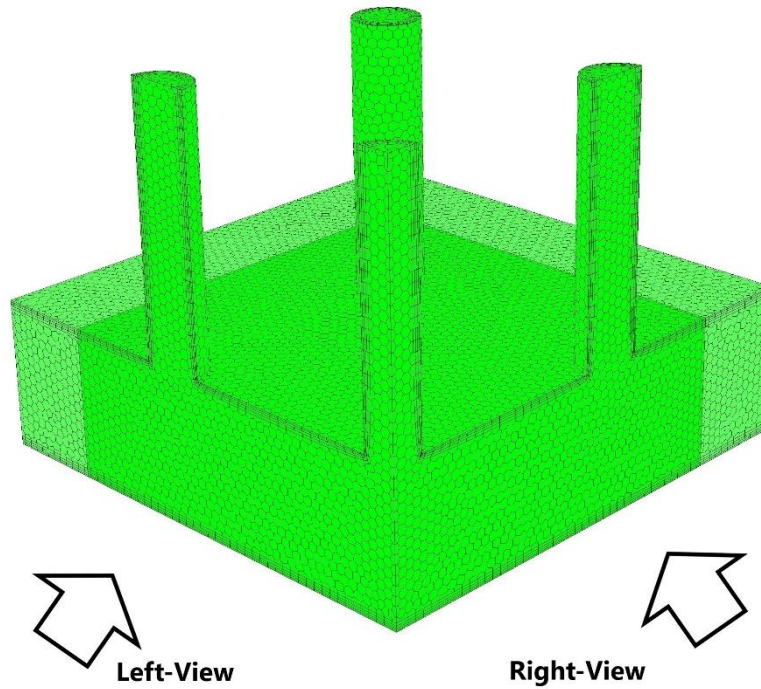


Figure 35: Coarse mesh for the 3D multijet array quarter symmetry domain without considering conjugation heat transfer effects (no solid modelled). The left and right views are referred to in figures presented in later chapters.

The average wall superheat was the parameter of interest for the mesh independence study. The results of the study are summarised in Table 5. The average wall superheat varied by less than 0.3% from mesh density of 65 cells/mm³ to 130.83 cells/mm³. Therefore, a mesh density of 65 cells/mm³ with 325 840 cells was used for the prediction of the boiling curve in the nucleate-boiling regime. The case with conjugation used the same mesh parameters for the fluid region and the solid region. It should be noted that mesh independence could be reached by using the default standard wall functions; therefore, not requiring the evaluation of T_l at a fixed y^+ of 250, as proposed by Egorov and Menter [56].

Table 10: 3D multijet array mesh refinement study results at a wall heat flux of 80 W/cm²

Cell Count	Average Wall Superheat (°C)	Change Relative to Previous Mesh (%)
126858	20.06	-
194131	20.24	0.92
325840	20.40	0.77
655370	20.46	0.29

3.2.3 Results and Discussion

3.2.3.1 Boiling curve

Figure 36 shows the boiling curve predictions of both cases in the present study with the boiling curve results of the experimental study [63]. The effect of conjugation in the numerical model was much less than in the single-jet case presented above. However, the agreement with the experiment was not as good as for the single-jet case, with a maximum error of 21%, a slight overprediction of the nucleate-boiling regime slope of the boiling curve, and an overprediction of the onset of the nucleate boiling departure point. Narumanchi *et al.* [40] state that errors of up to 30% are acceptable for numerical predictions of jet impingement boiling. The case considering conjugation heat transfer in the solid yielded slightly better results and less variation in the temperature profile of the heated surface. The same thermocouple locations, area-weighted averaging and one-dimensional heat conduction equation used in the experimental study by Devahdhanush and Mudawar [63] yielded

results nearly identical to the actual average surface temperature, as illustrated in Figure 36, by T_{calc} . Another possible cause for the overprediction of wall superheat is the fact that the Cole bubble departure frequency is not suitable for high degrees of subcooled boiling (9 °C in this case). When considering conjugation, the heating period to reach a steady state was much longer than that of the 2D axisymmetric case (which had only 3 °C of subcooling). The deviation from the experimental data could also be due to the limitations of the RNG k- ϵ model based on the mixture of the two phases and its ability to capture the turbulence due to jet-to-jet interactions. There was also some uncertainty in the properties of R134a and the actual saturation temperature corresponding to the outlet pressure used in the experiment. The fact that the numerical model failed to predict the onset of nucleate boiling departure could be attributed to the standard RPI boiling model only being applicable to the fully developed nucleate-boiling regime and the Cole bubble departure frequency model was not applicable to significantly subcooled boiling.

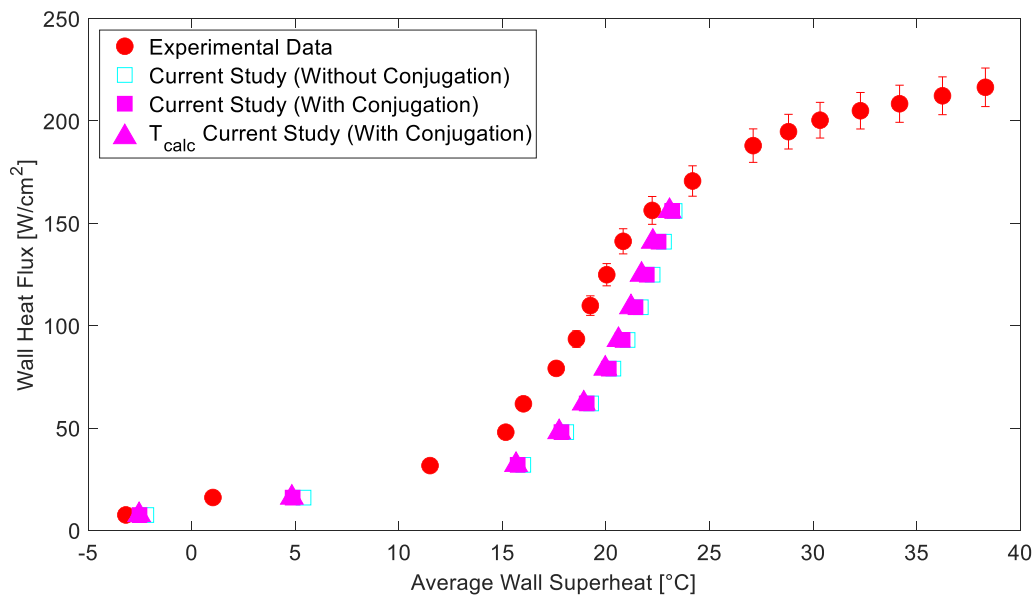


Figure 36: Boiling curve validation of the multijet array numerical model against the experiment of the Devahdhanush and Mudawar [63] study using the average heated wall temperature

3.2.3.2 Variation with flow time

Figure 37 shows the heated surface area-weighted average wall superheat and wall heat flux against flow time for the case without conjugation. Ten-second time windows were used for each ramped applied heat flux to allow steady state to be reached in each window. The average wall superheat increased drastically when the heat flux was increased before reducing to reach a steady state. Unlike the 2D single-jet case, the average wall heat superheat did not have severe fluctuations in any wall heat flux range. Figure 37 indicates that the wall superheats reached steady state for all heat fluxes in the first half of the flow time at that heat flux, suggesting that using only the second half of the flow time for each heat flux to obtain the boiling curve was as good an assumption as before.

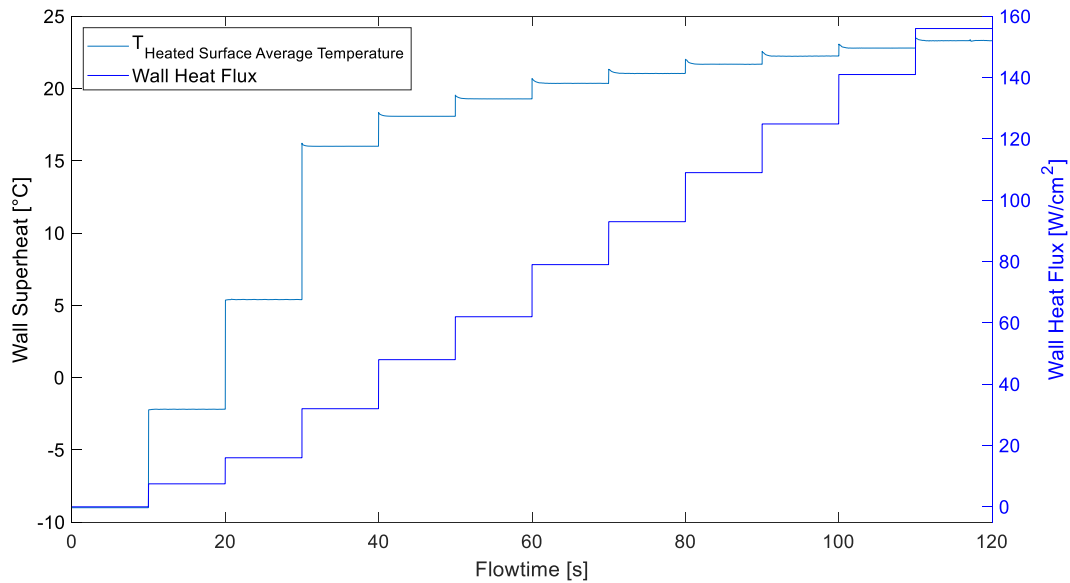


Figure 37: Heated surface average wall superheat and wall heat flux vs flow time for 3D multijet array case without conjugation heat transfer effects.

Figure 38 shows the heated surface area-weighted average wall superheat and wall heat flux against flow time for the case with conjugation. Unlike for the 2D case, the temperature of the solid block was ramped up with the heat flux by means of a patch function using the one-dimensional heat conduction equation and the results of the case without conjugation for the top surface temperature to determine the corresponding initial temperature field in the solid block for each heat flux. Use of patch functions reduced the required flow time and thus computational time to reach steady state significantly. The time window at each ramp of the applied heat flux had to be increased significantly from before to allow for convergence within that window. A value of 60 seconds was used. Again, the average wall temperature had almost no fluctuations, indicating that the numerical noise filter worked well. The heat flux fluctuated somewhat at the higher heat fluxes, which was due to convergence difficulties at those high heat fluxes, and especially the highest one. The wall superheat overshoot for each heat flux before reducing to a steady temperature, due to the results without conjugation used for the patch being slightly higher than the conjugation results. Figure 38 shows that the wall superheat temperatures reached steady state for all heat fluxes in the first half of the flow time at that heat flux, suggesting that using only the second half of the flow time for each heat flux to obtain the boiling curve was as good an assumption as before.

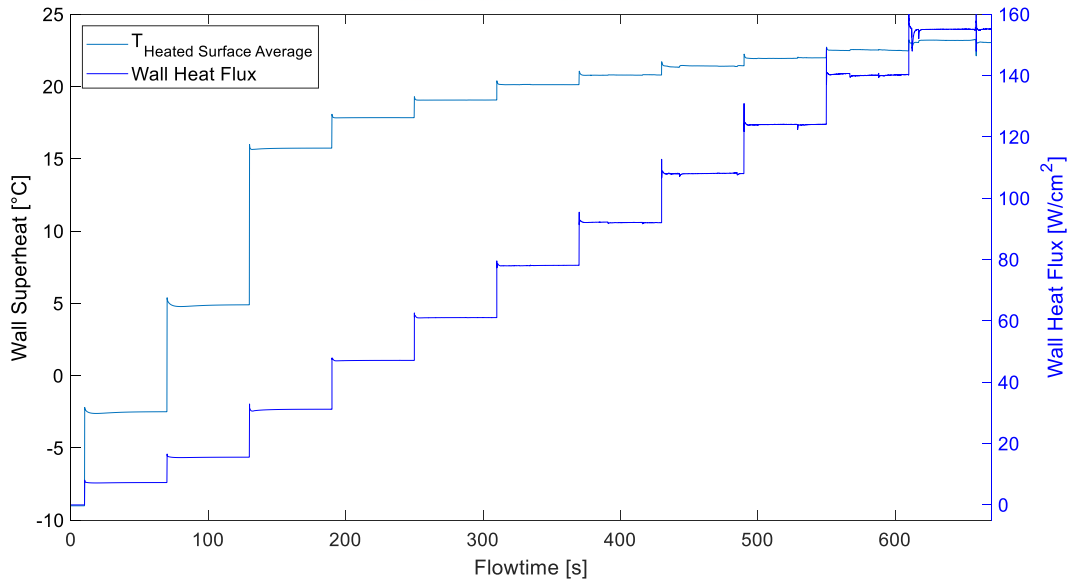


Figure 38: Heated surface average wall superheat and wall heat flux vs flow time for 3D multijet array case with conjugation heat transfer effects

3.2.3.3 Sensitivity Analysis

There is some uncertainty about the pressure and saturation temperature of the experimental setup, which could result in large errors in the numerical results. Therefore, a sensitivity analysis was conducted on the 3D multijet array case without conjugation, to investigate the effect of the pressure and liquid subcooling on the numerical results. Although it is known that the degree of subcooling is a function of the saturation temperature which in turn is a function of pressure, the numerical model's dependency on only the pressure and subcooling were investigated, by varying the system pressure and inlet temperature, respectively. The errors disclosed in section 3.2.1.4 were used to determine the upper and lower bounds on the pressure and subcooling used in the sensitivity study. Since the present study used the saturation pressure corresponding to a saturation temperature of 29.14 °C in Coolprop [64] instead of the pressure reported for the experiment [63], the experimental pressure was also considered in the sensitivity analysis. The results of the sensitivity analysis are summarised in Table 11. The average wall temperature and superheat decreases for increasing pressure, while the average wall temperature and superheat increases with subcooling. Thus, the error relative to the experimental results decreases for increasing pressure and decreasing subcooling. Thus, the experimental uncertainties regarding saturation pressure and temperature could have a significant influence on the accuracy of the numerical results.

Table 11: Sensitivity analysis of numerical model for the 3D multijet array case without conjugation at 109 W/cm²

Pressure Sensitivity		
Pressure (Pa)	Average Wall Temperature (°C)	Average Wall Superheat (°C)
743827	50.872	21.732
751340	50.823	21.683
758854	50.716	21.576
771278	50.571	21.431
Experimental Result	48.386	19.246
Subcooling Sensitivity		
Subcooling (°C)	Average Wall Temperature (°C)	Average Wall Superheat (°C)
8.8	50.581	21.441
9	50.823	21.683
9.2	51.080	21.940
Experimental Result	48.386	19.246

3.2.3.4 *Contour plots*

The jet velocity contours of the multijet array with conjugation are illustrated in Figures 39 (a) to (c) for three selected wall heat fluxes. Again, the typical flow regions of jet impingement are visible, i.e. the free-jet region, stagnation region and the wall-jet region. In addition to the typical flow regions of jet impingement, the wall jets formed a fountain effect where they met, resulting in additional stagnation regions between the jets. The fountain effect can also be observed where the wall jets collided with the side walls of the domain, forming additional stagnation regions against the wall. The presence of cross-flow is clearly visible in the fountains formed closer to the outlet of the domain, where they were forced towards the outlet. There are also signs of washback from the side wall at the jets closest to the wall, showing a narrower free-jet region on the side closest to the wall. The effects of the upper confinement wall can be seen in the jet fountains washing back down from the top wall into the domain. The effects of the confinement wall are clearer for the higher heat fluxes, as can be observed in the wider fountains in Figures 39 (b) and (c). The effects of confinement were expected to be more severe at higher mass flow rates and lower jet-to-surface spacings (to be explored in the next chapter) than those shown here for a low flow rate. Again, the wall jets expanded with increasing heat flux, Figures 39 (a) to (c), due to the higher formation rate of vapour pushing the wall jets away from the wall. Unlike the single-jet case, the velocity magnitude of the wall jets did not apparently increase with increasing heat flux, due to the lower density ratio between the liquid and vapour phases of R134a than for water, resulting in lower vapour velocities in the bubbles departing from the wall. The width of the jets in the free-jet region increased with increasing heat flux, again due to the formation of vapour closer to the stagnation point, causing some blockage and causing the jet to expand.

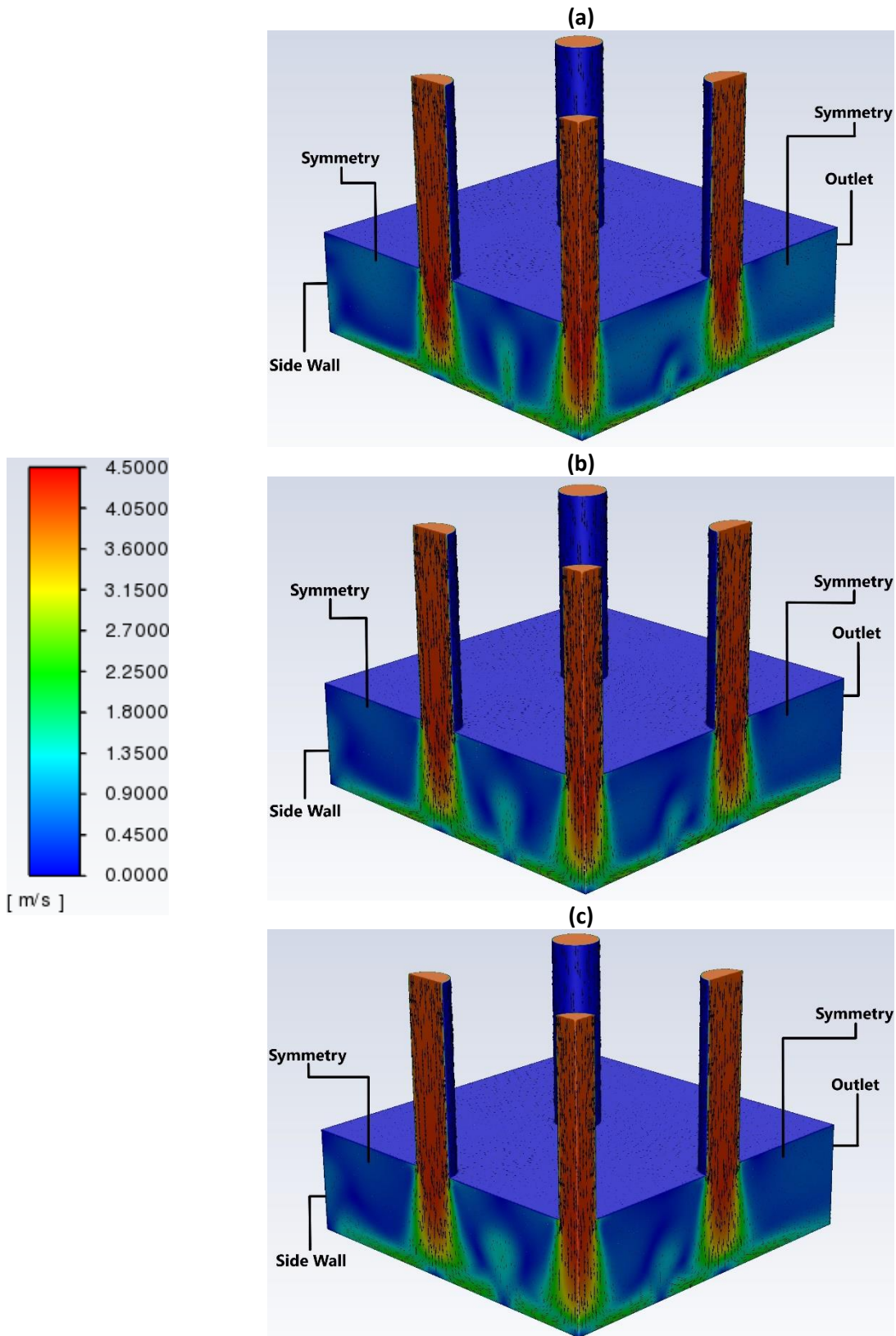


Figure 39: Liquid velocity contours [m/s] of the multijet array considering conjugation, using R134a as heat transfer fluid, at various wall heat fluxes: (a) 62 W/cm², (b) 109 W/cm², and (c) 156 W/cm²

The liquid temperature contours of the multijet array with conjugation are illustrated in Figure 40(a, b) and Figure 41 for increasing wall heat fluxes. The fountain effects between the wall jets are clearly visible for the lowest heat flux, illustrated in Figure 40(a), with the cooler fountains forming at the

secondary stagnation regions between the jets. The cool fountains are not that clearly visible for the higher heat fluxes, shown in Figure 40(b) and Figure 41; however, are still present, indicating that the jet-to-jet interactions had an influence on the average heat transfer, given that regions with lower subcooling were formed at the secondary stagnation regions, which in turn caused quicker vapour bubble collapse. A warmer region was formed between the side jets and the side wall and became more prominent with increasing heat fluxes, shown in Figures 40 (a) to 41. It was expected that vapour bubbles would be more likely to get stuck in this region. Removing the side wall could help reduce cross-flow currents and alleviate the region of warm liquid. The presence of cross-flow is clearly visible at the lowest heat flux, shown in Figure 40(a), with the side jet closest to the outlet causing a wider low-temperature region than for the other jets. The cool wall jets clearly visible for the lowest heat flux diminished with increasing heat flux.

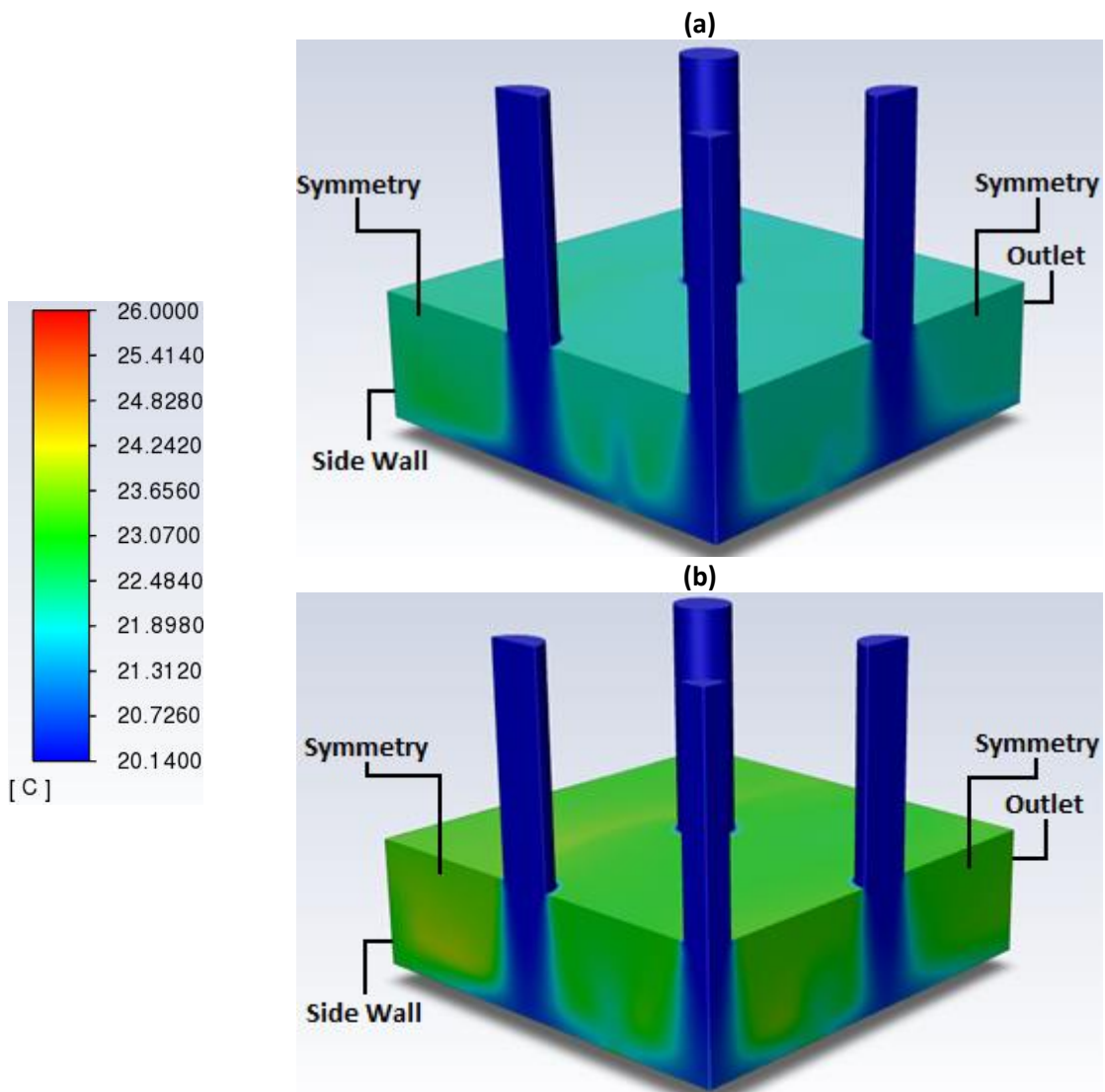


Figure 40: Liquid temperature contours [$^{\circ}\text{C}$] of the multijet array considering conjugation, using R134a as heat transfer fluid, at various wall heat fluxes: (a) 62 W/cm^2 and (b) 109 W/cm^2

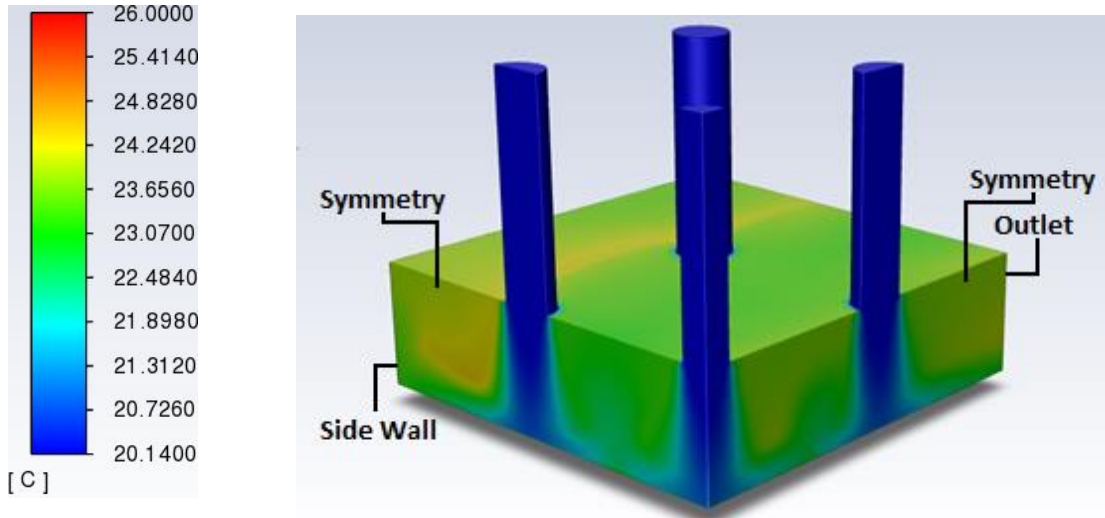


Figure 41: Liquid temperature contours [°C] of the multijet array considering conjugation, using R134a as heat transfer fluid, at 156 W/cm²

Figure 42 and Figure 43(a, b) show the vapour volume fraction contours of the multijet array with conjugation for increasing wall heat fluxes. The vapour bubbles formed at the secondary stagnation regions between the jets. This was expected, given that fountain formation between the colliding wall jets reduced the convective heat transfer and corresponded with the literature for single-phase liquid jet arrays. Vapour bubbles were trapped against the upper confinement wall close to the jet nozzle outlet. Since there were no outlets in the confinement wall and due to the interaction between the confinement wall and fountains, the vapour was pushed towards the jets and got trapped due to the high pressure at the nozzle outlet. Some of the vapour getting trapped at the nozzle outlet could also be due to numerical issues with a few high-aspect ratio cells around the nozzle exit, as can be seen for the low heat fluxes in Figure 42 and Figure 43(a). The jets were effective at breaking through the vapour and rewetting the heated surface for all heat fluxes, with the jets rewetting the heated surface in the primary stagnation regions as well as the wall-jet regions. Vapour trails towards the outlet are clearly visible at the confinement wall for the higher heat fluxes, indicating the presence of cross-flow. Another indication of cross-flow is the presence of vapour bubbles being pushed into the jet closest to the outlet for the highest heat flux, shown in Figure 43(b).

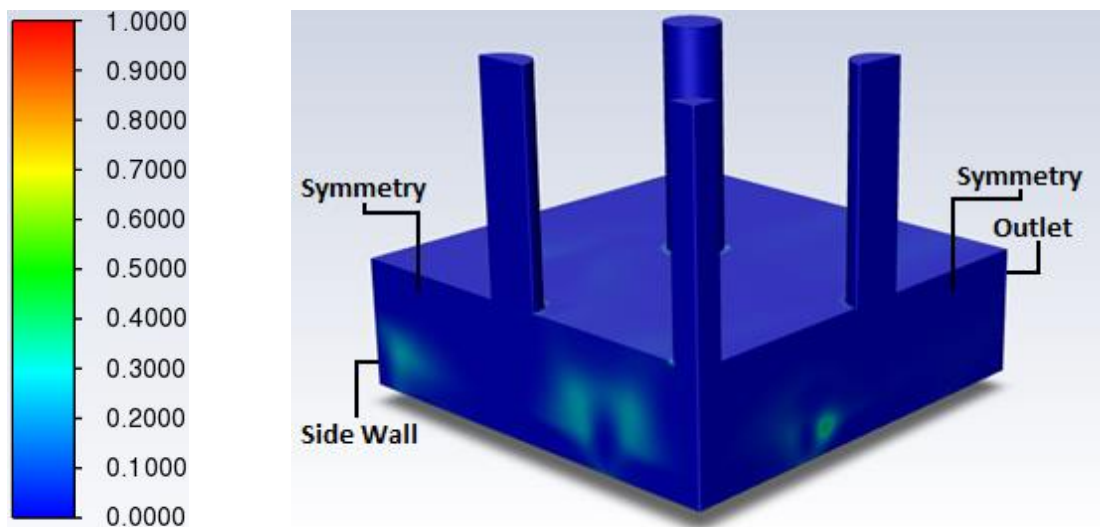


Figure 42: Vapour volume fraction contours of the multijet array considering conjugation, using R134a as heat transfer fluid, at 62 W/cm²

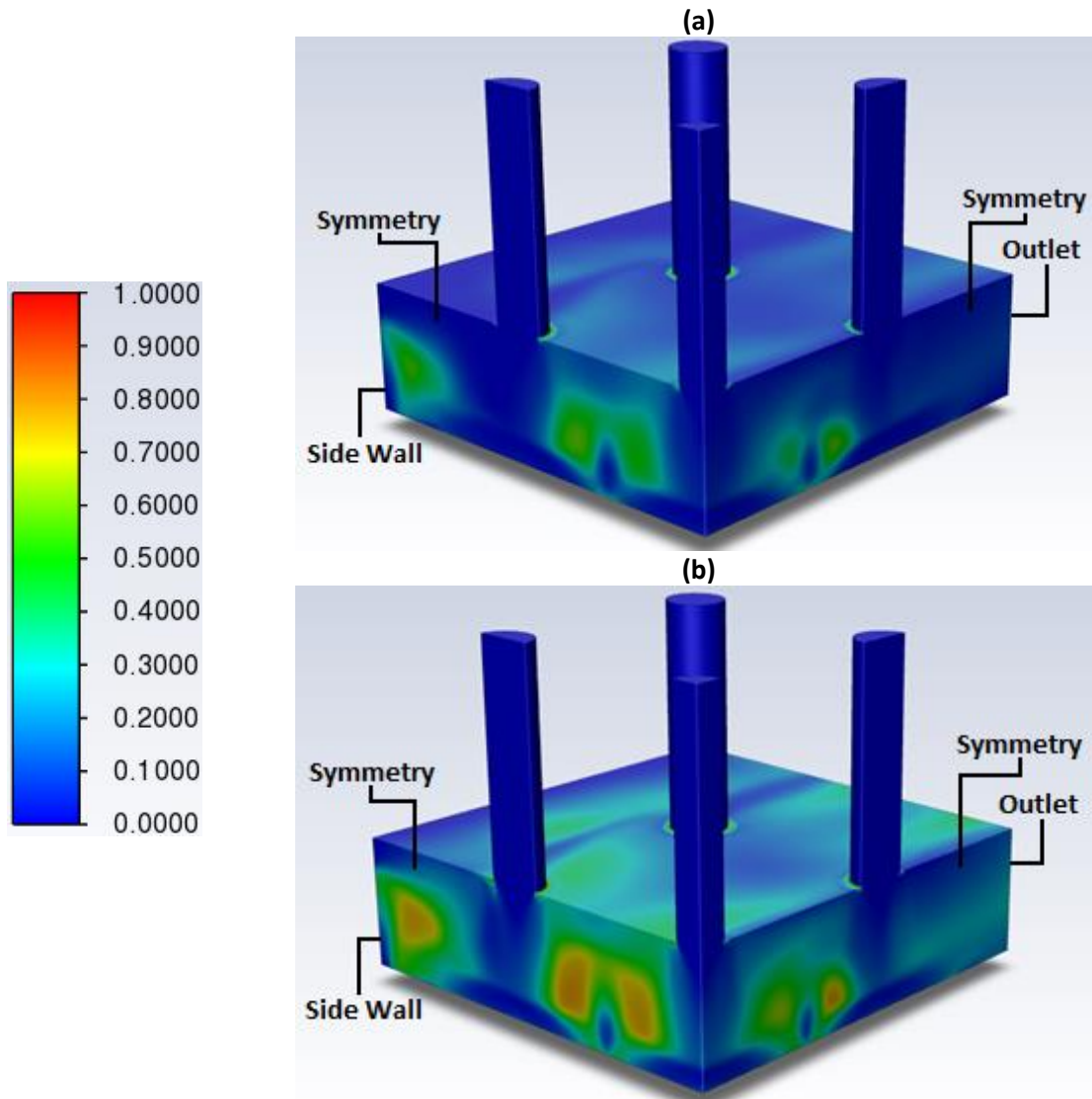


Figure 43: Vapour volume fraction contours of the multijet array considering conjugation, using R134a as heat transfer fluid, at various wall heat fluxes: (a) 109 W/cm² and (b) 156 W/cm²

Figure 44(a) to (c) shows the temperature contours of the copper block and insulation for increasing heat fluxes. A visible increase in the temperature gradients of the copper block can be observed for increasing heat flux going from Figures 44 (a) to (c). Heat spread from the copper block to the insulation and a clear temperature gradient is visible in the insulation. The temperature of the top wall of the insulation, in contact with the liquid, was well below the fluid saturation temperature (29.14 °C) for all heat fluxes, indicating that heat transfer between the insulation and the liquid was limited to convective heat transfer, and therefore, was minimal. The temperature of the top wall of the insulation remained nearly constant for increasing heat flux, shown in Figures 44 (a) to (c), indicating that heat spreading through the insulation was minimal and that most of the heat going into the fluid went through the top surface of the copper block.

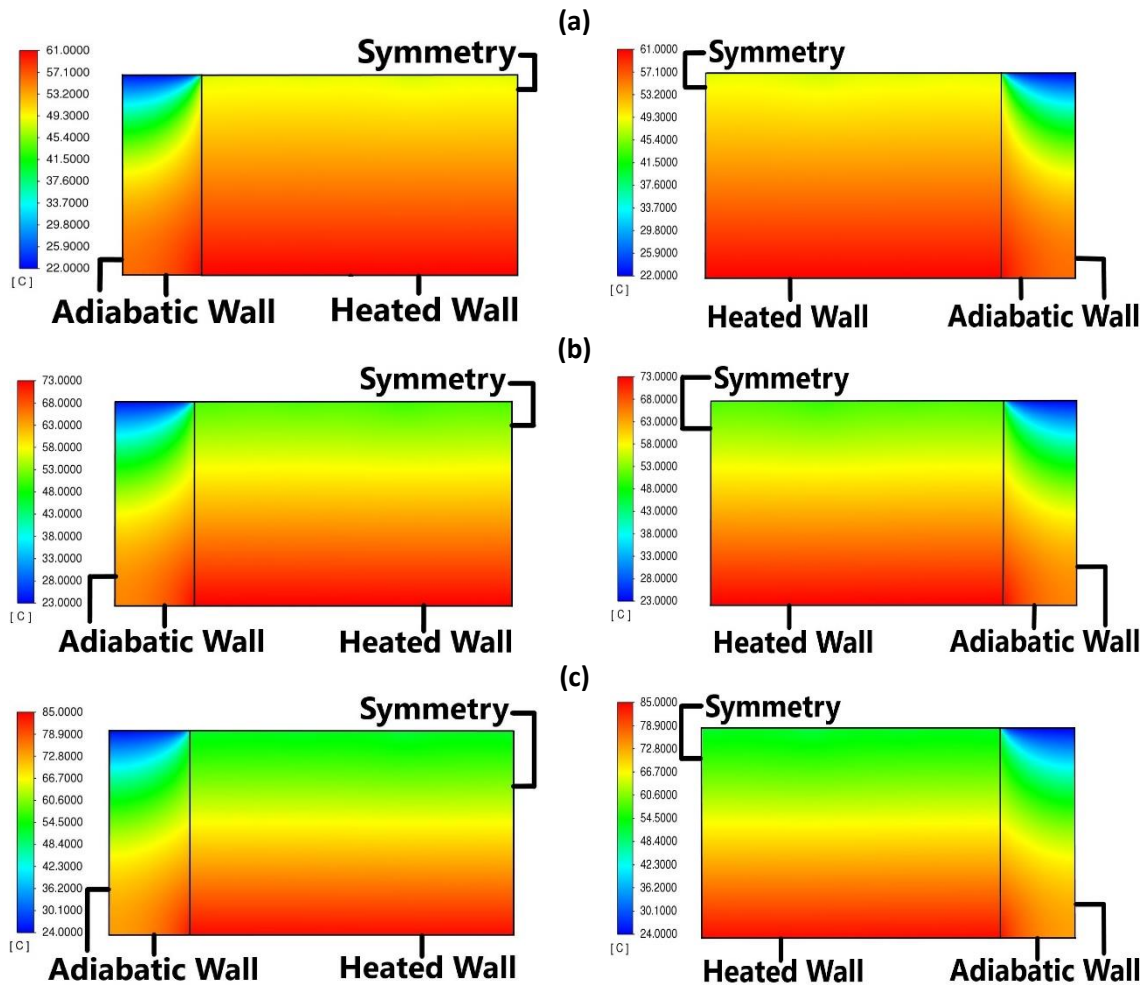


Figure 44: Solid temperature contours [°C] for the multijet array considering conjugation, using R134a as heat transfer fluid, at various wall heat fluxes: (a) 62 W/cm², (b) 109 W/cm², and (c) 156 W/cm². Figures on the left are the left-side view, figures on the right are the right-side view.

Figures 45 (a) to (c) show the heated surface wall temperature contours of the multijet array alongside the surface heat flux contours, for increasing wall heat fluxes. For all heat fluxes, the surface temperature was a minimum in the stagnation regions between the jets and the stagnation regions in the jet centres. The local minimum surface temperature is due to the reduced convective heat transfer rates in the stagnation regions between the jets, resulting in vapour bubble formation in these regions and thus the lower wall temperature due to evaporative heat transfer. The surface heat flux was also a maximum in the secondary stagnation regions between the jets, roughly twice the total wall heat flux for all cases, indicating evaporative heat transfer. For the highest heat flux, shown in Figure 45 (c), the surface heat flux in this region was higher than the CHF of the experiment, shown in Figure 36, confirming that evaporative heat transfer dominated in this region. The size of the secondary stagnation regions increased with increasing heat flux, shown in Figures 45 (a) to (c), causing larger low-temperature zones. The increased vapour formation at higher heat fluxes caused the wall jets to expand, increasing the interaction between colliding wall jets and thus the size of the secondary stagnation regions (low-temperature zones). The low-surface temperatures in the jet stagnation regions occurred because of the high quenching heat flux in the jet centres where the jet was highly efficient at breaking through the vapour to rewet the surface and where vapour formation was at a minimum. The surface heat flux was also higher in the jet centres. For all heat fluxes, the maximum surface temperature occurred in the wall jet regions, because the quenching heat transfer dominated in these regions, resulting in low evaporative heat transfer. The reduced heat transfer in the wall jet region was also visible in the surface heat flux contours with the minimum heated surface heat flux occurring in the wall jet region. The heat flux on the insulation wall was two orders of magnitude lower

than the lowest heat flux on the heated surface. The heat flux on the insulation wall remained almost constant for all heat fluxes, indicating that essentially all the heat going into the fluid went through the heated surface. The corresponding contour for the case not considering conjugation is illustrated in Figure A - 2, in Appendix A. The surface temperature variations were substantially higher for the case not considering conjugation, with much lower surface temperatures in the secondary stagnation regions between the jets and much higher surface temperatures in the wall-jet regions.

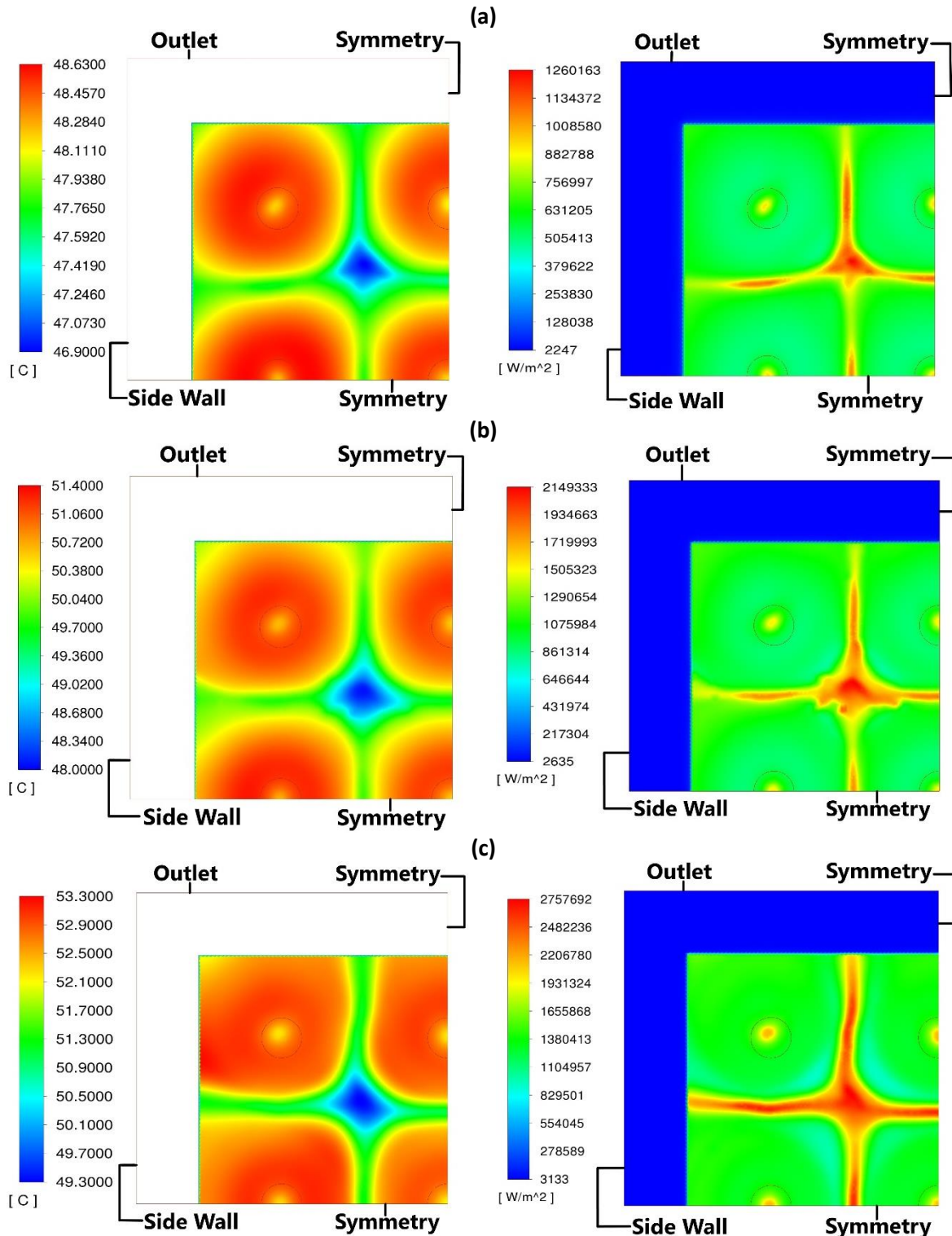


Figure 45: Heated surface temperature contours [°C] (left) and surface heat flux contours [W/m²] (right) of the multijet array considering conjugation, using R134a as heat transfer fluid, at various wall heat fluxes: (a) 62 W/cm², (b) 109 W/cm², and (c) 156 W/cm²

Figure 46(a) to (c) show the wall heat transfer coefficient contours as calculated from the jet inlet temperature using equation (2) and the heated surface temperature for the multijet array considering the effects of conjugation. The heat transfer coefficient was the highest in the stagnation regions in the jet centres and between the jets. This was expected due to the high quenching heat transfer experienced by the jets in the jet stagnation regions and high evaporative heat transfer in the stagnation regions between the jets where the convective heat transfer was at a minimum. The heat transfer coefficient was the lowest in the wall-jet regions where phase change and thus evaporative heat transfer was the lowest and quenching heat transfer dominated. The heat transfer coefficients increased with increasing heat flux, as illustrated in Figures 46 (a) to (c). Again, the size of the secondary stagnation regions between jets increased, as indicated by the larger areas with high heat transfer coefficients.

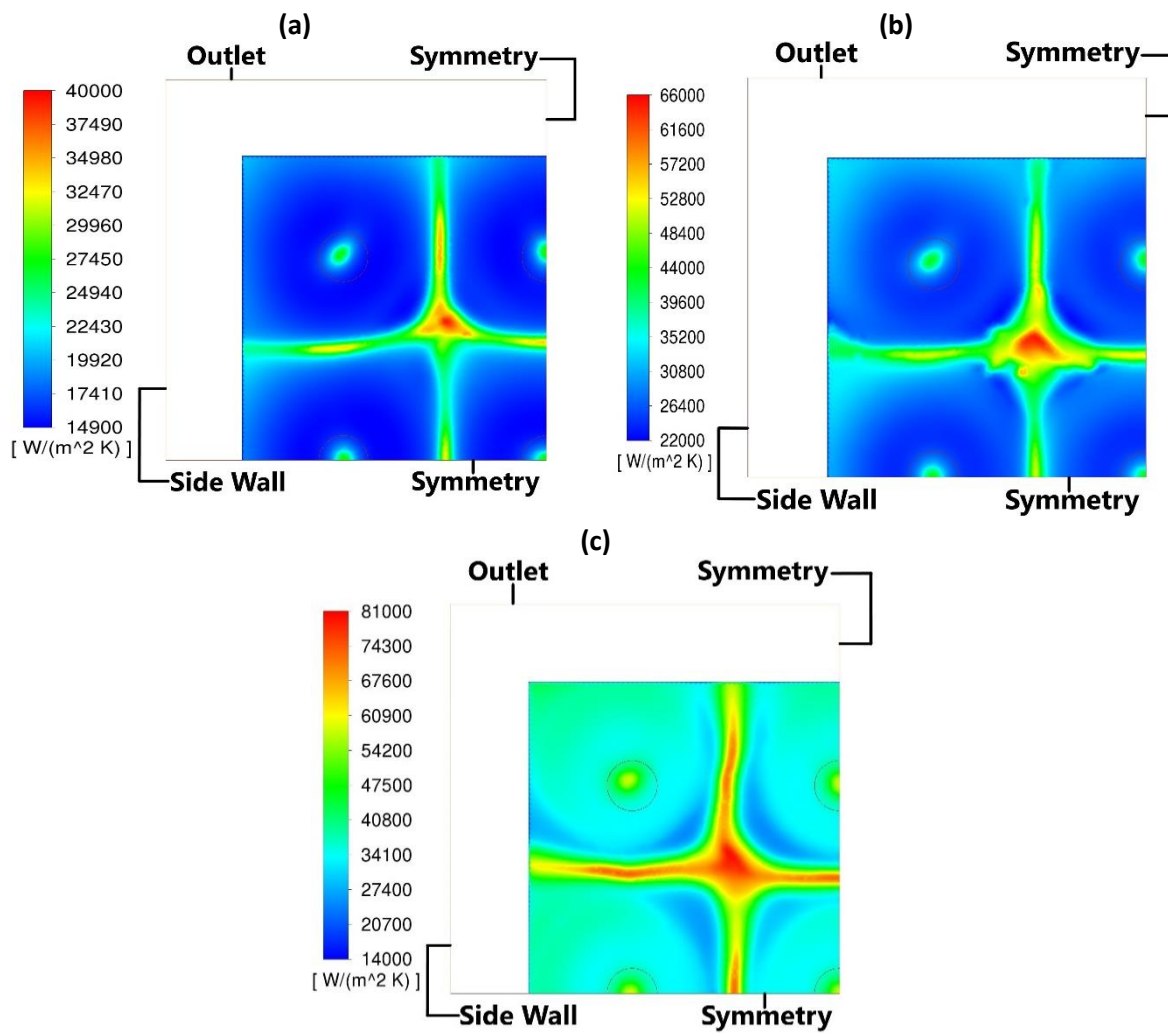


Figure 46: Wall heat transfer coefficient contours [$W/m^2 \cdot K$] of the multijet array considering conjugation, using R134a as heat transfer fluid, at various wall heat fluxes: (a) 62 W/cm^2 , (b) 109 W/cm^2 , and (c) 156 W/cm^2

Iso-surfaces of 0.5 vapour volume fraction, coloured by velocity magnitude, are illustrated in Figure 47(a) to (b) for the multijet array case considering conjugation. These iso-surfaces indicate the vapour bubble formation. For the lowest heat flux, no vapour bubbles were visible because the maximum vapour fraction was below 0.5 in the entire domain. For the middle heat flux, shown in Figure 47(a), vapour bubbles started to appear above the secondary stagnation regions. Appearance of vapour bubbles above the secondary stagnation regions was expected given that the vapour started to form in the secondary stagnation regions first and got trapped between the jets and the confinement wall,

causing the vapour volume fraction to exceed 0.5 here first. The velocity magnitude on the bubble surface was close to zero for the middle heat flux, shown in Figure 47(a). Large vapour bubbles were present for the highest heat flux, shown in Figure 47(b). Here the vapour bubble surface velocity magnitude was the highest close to the heated surface in the secondary stagnation regions between the jets, confirming the influence of the fountain effect on the vapour bubbles. There also was minimal vapour in the jet regions, indicating that the jets were effective at breaking through the vapour layer above the wall to rewet the surface. The vapour moved downstream towards the exit of the domain, indicating the presence of cross-flow. The presence of cross-flow was also confirmed by the elongation of the vapour bubbles towards the exit of the flow domain, illustrated in Figure 47(b).

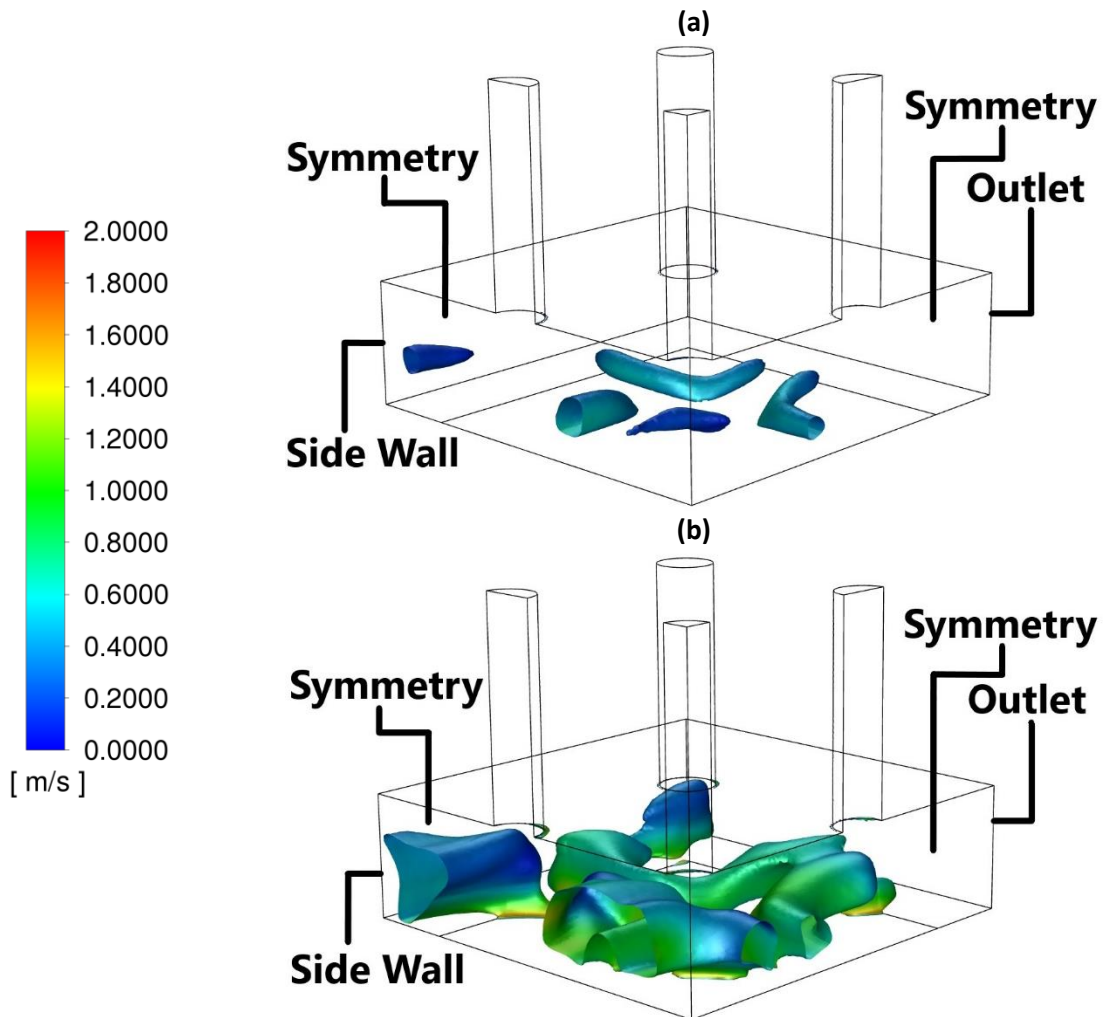


Figure 47: Iso-surfaces of vapour volume fraction of 0.5 coloured by velocity magnitude for the multijet array considering conjugation, using R134a as heat transfer fluid, at various wall heat fluxes: (a) 109 W/cm² and (b) 156 W/cm²

3.2.3.5 Effect of conjugation

Figure 48 shows the boiling curves based on the minimum, average and maximum surface temperatures for the multijet array for the case considering conjugate heat transfer as well as for the case not considering it. Similar trends to the single-jet case were observed. The variation in the surface temperature was drastically lower for the case considering conjugation than for the case not considering it due to the thermal mass of the copper block and spanwise conduction within the block, alleviating local hotspots by conducting the heat to the colder surrounding areas. As stated for the single-jet case, when the average surface temperature was of interest, not considering conjugation could provide excellent results, even more so for the multijet array where the average surface temperature of the case considering conjugation and the case not considering it was nearly identical.

The fibreglass insulation did an excellent job in preventing heat spreading from the heated copper block and as a result, the heat flux on the heated wall differed by less than 1 W/cm^2 from the input heat flux at the bottom of the copper block.

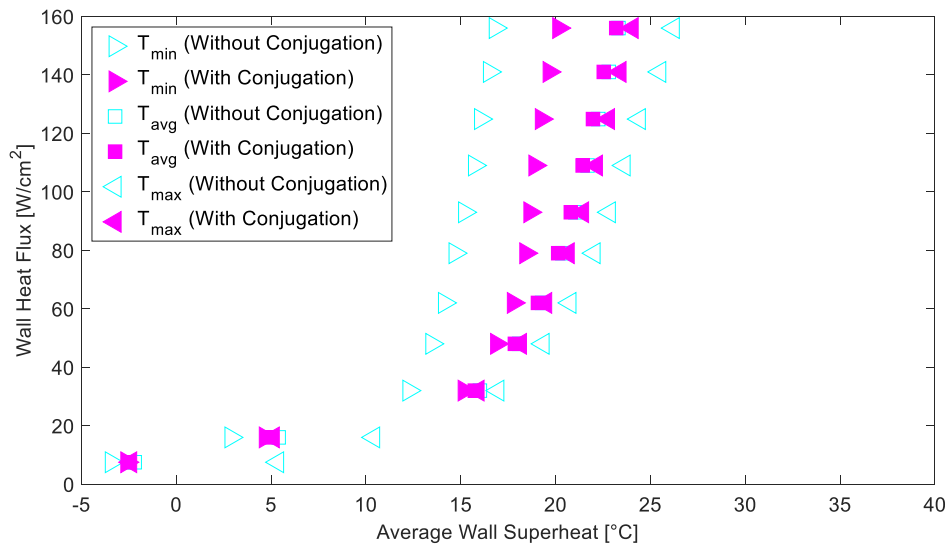


Figure 48: R134a multijet array boiling curve based on minimum, average and maximum surface temperatures for both the case without conjugation heat transfer as well as the case with conjugation heat transfer

Figure 49 shows the contributions of the three heat flux components of the RPI boiling model to the wall heat flux for the boiling curve, for the multijet array case for both the case considering conjugation heat transfer as well as the case not considering it. Compared with the results of the single-jet case, shown in Figure 28, the evaporative heat flux contribution was lower. The reduced evaporative heat flux contribution made sense given that the Cole bubble departure frequency model [58] was not applicable to subcooled boiling, resulting in lower evaporative heat transfer. The contribution of the evaporative heat flux to the total heat flux only reached one at a much higher heat flux than the ONBD of the experiment. The delayed unity contribution of the evaporative heat flux to the total heat flux suggests that the Cole bubble departure frequency model [58] should not be used for high degrees of subcooling because it will not correctly predict the ONBD and will therefore also lead to inaccuracy in predicting the fully developed nucleate-boiling regime.

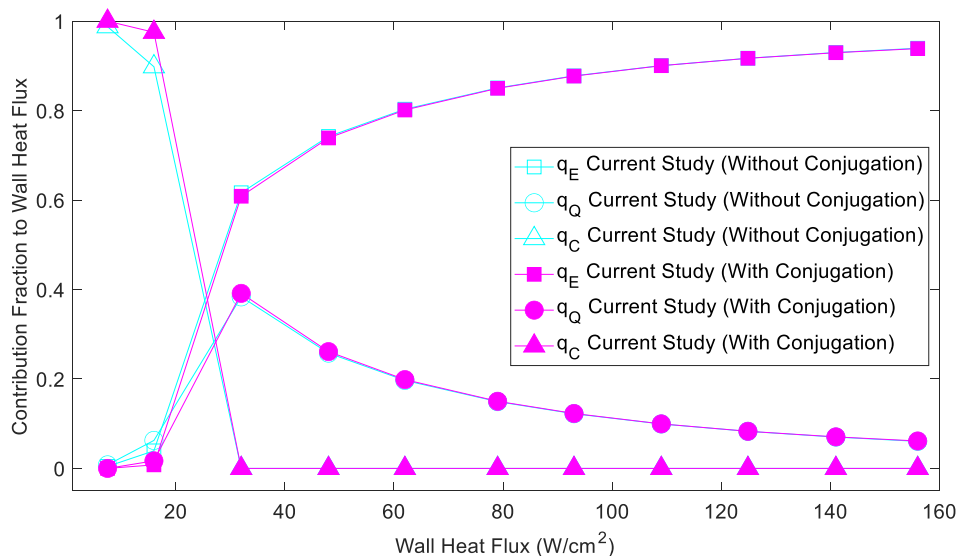


Figure 49: Contribution of the RPI boiling model heat flux components to the wall heat flux for the R134a jet array without and with conjugation heat transfer

4 Parametric Analyses

To investigate the influence of certain design parameters on heat transfer, the total heat transfer coefficient (HTC) is defined as follows:

$$HTC_{Total} = \frac{\dot{q}_W}{T_W - T_{in}} \quad (66)$$

where \dot{q}_W is the total wall heat flux, T_W the average wall temperature, and T_{in} the temperature at the jet inlet. Given that the RPI boiling model approximated the total heat flux with three heat flux components, separate heat transfer coefficients for each of the components can be defined as follows:

$$\begin{aligned} HTC_{Total} &= HTC_{Convection} + HTC_{Quenching} + HTC_{Evaporative} \\ &= \frac{\dot{q}_C}{T_W - T_{in}} + \frac{\dot{q}_Q}{T_W - T_{in}} + \frac{\dot{q}_E}{T_W - T_{in}} = \frac{\dot{q}_W}{T_W - T_{in}} \end{aligned} \quad (67)$$

where subscripts *C*, *Q* and *E* denote the convective, quenching, and evaporative heat flux components respectively. Given that the focus of the present study was on jets in the fully developed nucleate-boiling regime, the convective heat flux was zero for all cases in this section and is not illustrated. All results in this Chapter represent the time-averaged results obtained over at least 20 convective time scales based on the jet velocity and jet-to-surface spacing, i.e. after a quasi-steady state has been reached. The parametric studies conducted in this Chapter are based on the conjugate models of the single round water jet and multijet array.

4.1 2D Axisymmetric Single Jet

To investigate the influence of jet-to-surface spacing and jet Reynolds number on the average heat transfer of a single round water jet, the domain, shown in Figure 18, used for the validation of the Katto and Kunihiro experiment, was modified by moving the top (free-surface) outlet to ten jet diameters above the heated surface and varying the jet nozzle exit height to change H/D . The length of the jet pipe upstream of the nozzle exit was kept constant for all H/D cases to ensure that the nozzle outlet velocity profile and turbulence quantities were consistent for all cases. The jet Reynolds number was varied by changing the jet velocity, while keeping the diameter constant. Reynolds numbers of 10 000, 15 000, 20 000 were tested, corresponding to jet velocities of 1.85 m/s, 2.77 m/s and 3.69 m/s, for jet-to-surface spacings of $H/D = 1, 2, 4, \text{ and } 8$, while keeping the wall heat flux at the value of 50 W/cm^2 for all cases. H/D was varied by changing the jet height, since changing the jet diameter changes the jet area to heated surface area ratio, mass flowrate (for constant velocity), and jet Reynolds number. The jet Reynolds numbers for the study were selected to ensure that the jets are fully turbulent for each case (since the RPI boiling model is only applicable to turbulent flow) and that boiling occurs over the entire surface for each case at the selected heat flux, that is compare fully developed boiling to fully developed boiling. The H/D values were selected since the optimal heat transfer usually lies within $2 \leq H/D \leq 8$ [16].

The velocity contour plots for the 20 000 Reynolds number case are shown in Figure 50 for jet-to-surface spacings of $H/D = 1, 2, 4, \text{ and } 8$ at a wall heat flux of 50 W/cm^2 . Note that the part of the upstream pipe extending above the top outlet was omitted in Figures 50 (b) to (d). It was evident that jet spreading increased with increasing jet-to-surface spacing, shown in Figures 50 (a) to (d). For the lower jet-to-surface spacing, shown in Figures 50 (a) to (c), the potential core struck the surface. The potential core did not strike the surface for $H/D = 8$, shown in Figure 50 (d), because the jet-to-surface spacing was high enough for the jet decay region to be present, where the jet-shearing layers extended all the way to the jet centre causing the velocity profile to become flatter and wider. The decay of the jet velocity profile occurred at slightly lower jet-to-surface spacing for lower jet Reynolds numbers (not shown here). The wall-jet velocity decreased for increasing jet-to-surface

spacing, shown in Figures 50 (a) to (d), due to the shear stresses in the jet-shearing layers, resulting in reduced jet kinetic energy. The wall-jet thickness reduced for increasing jet-to-surface spacing, due to the reduced kinetic energy, resulting in less liquid entrainment in the wall-jet region. It was somewhat surprising that the distance that the wall-jet region spread out from the stagnation region was not apparently influenced by the jet-to-surface spacing.

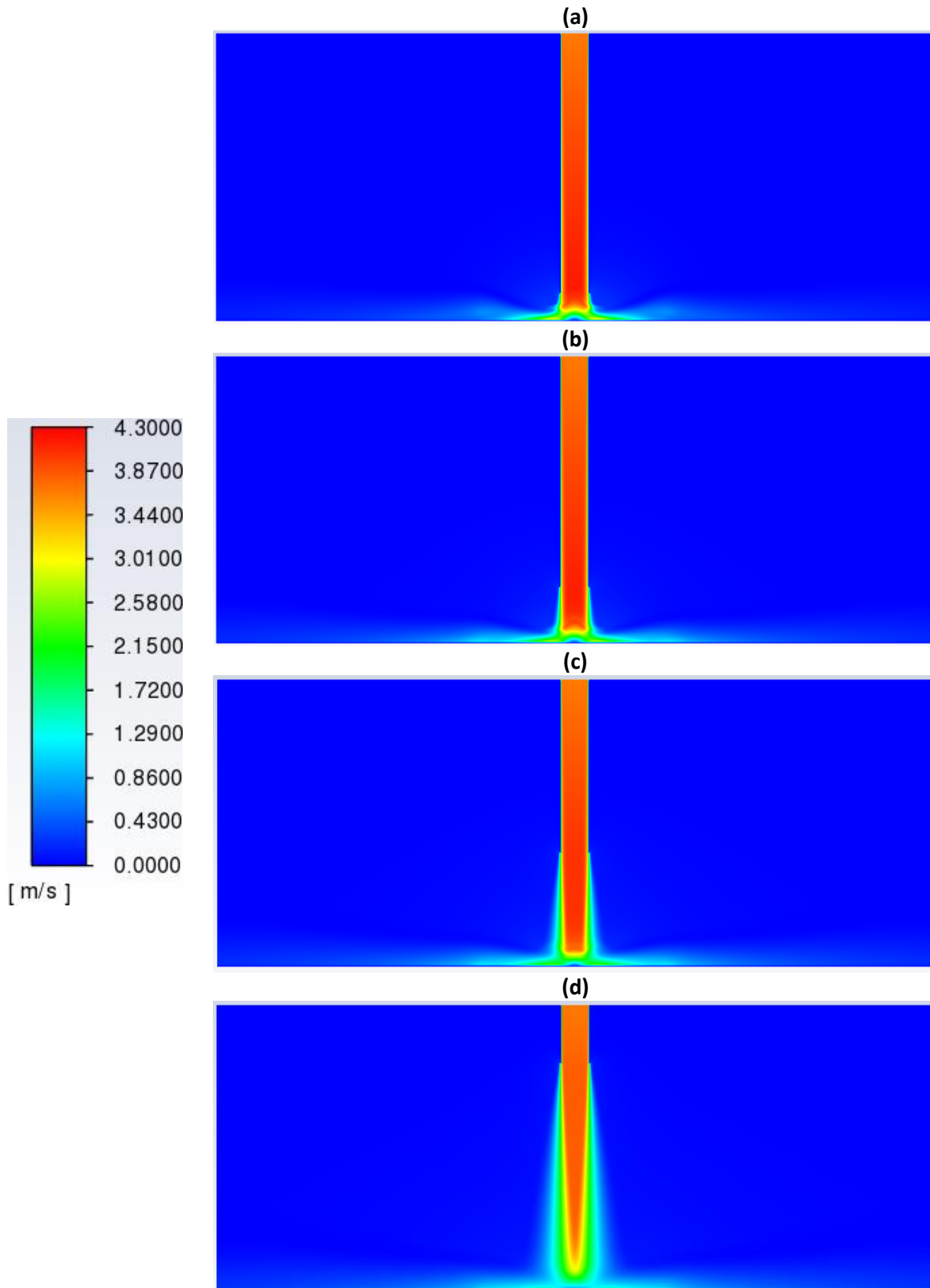


Figure 50: Velocity contours [m/s] for the single-jet case with $Re = 20000$ for various jet-to-surface spacings, at 50 W/cm^2 with conjugation: (a) $H/D = 1$, (b) $H/D = 2$, (c) $H/D = 4$, and (d) $H/D = 8$

Figure 51 shows the liquid velocity contours for the single-jet case at $H/D = 8$, for various jet Reynolds numbers at a wall heat flux of 50 W/cm^2 . The potential core extended further from the nozzle outlet for increasing jet Reynolds numbers (jet velocity in this case), shown in Figures 51 (a) to (c), while jet spreading decreased for increasing jet Reynolds numbers, as expected.

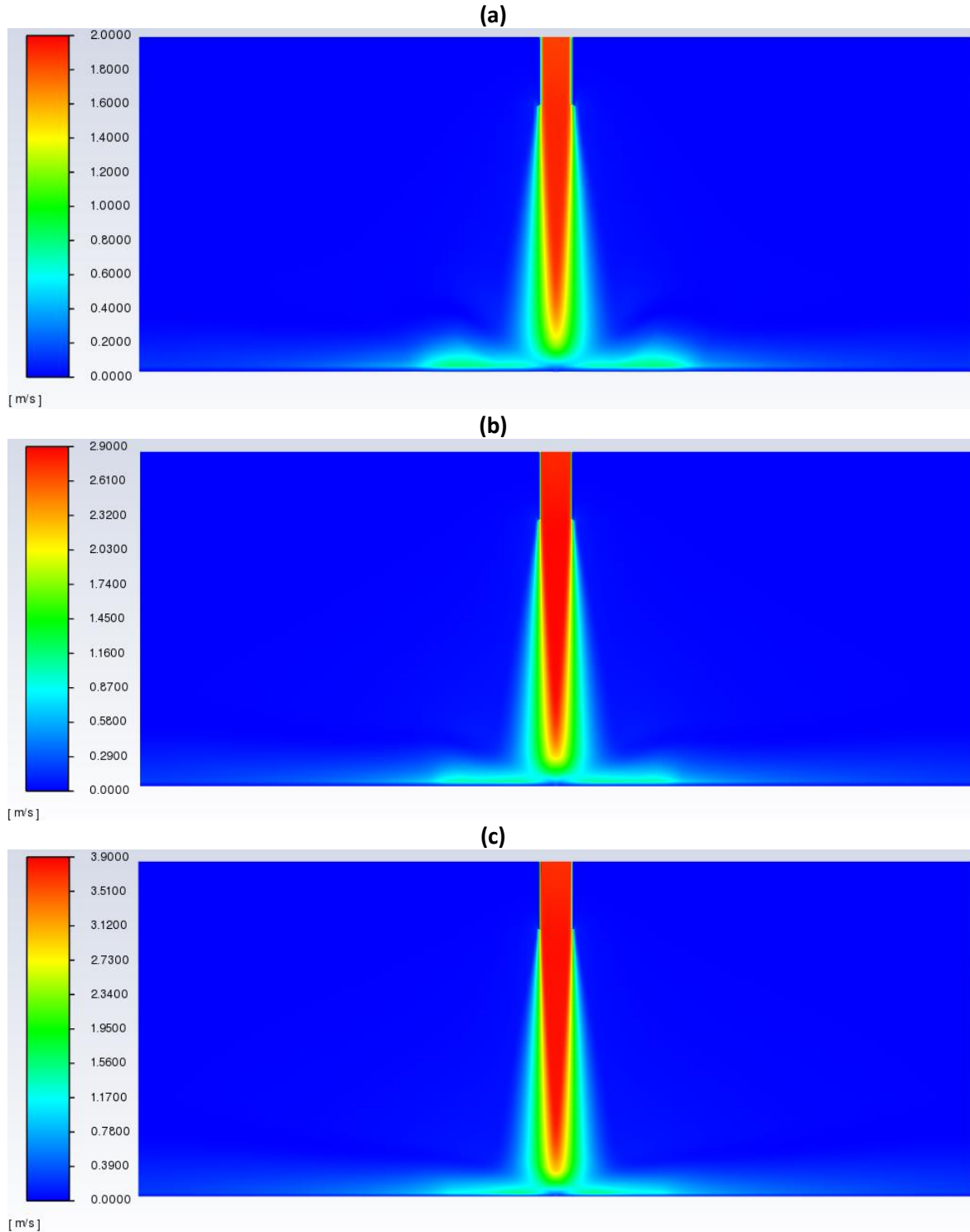


Figure 51: Velocity contours [m/s] for the single-jet case with $H/D = 8$ for various jet Reynolds numbers, at 50 W/cm^2 with conjugation: (a) $Re = 10\,000$, (b) $Re = 15\,000$, (c) $Re = 20\,000$

Figure 52 shows the vapour volume fraction distributions for the single-jet case with $Re = 20\,000$ for various jet-to-surface spacings at a wall heat flux of 50 W/cm^2 . The jet was highly efficient at rewetting the surface by pushing the vapour out radially for the $H/D = 1$ case, the vapour volume fraction dipped right outside the end of the heated section, due to vapour departure from the wall. The jet became less effective at rewetting the surface as H/D increased, resulting in more vapour in the heated section. It is not clear what the reason was for the maximum vapour volume fraction being the highest for the $H/D = 2$ case. This could be because the jet was the most efficient at pushing the vapour radially outwards at this spacing, but not as efficient at rewetting the surface, causing lower quenching heat transfer than for the $H/D = 1$ case. It could also be due to some numerical error or inconsistency. The vapour volume fraction in the stagnation region increased for jet-to-surface spacing higher than for $H/D = 4$, because the potential core no longer reached the surface, resulting in a more uniform jet velocity profile.

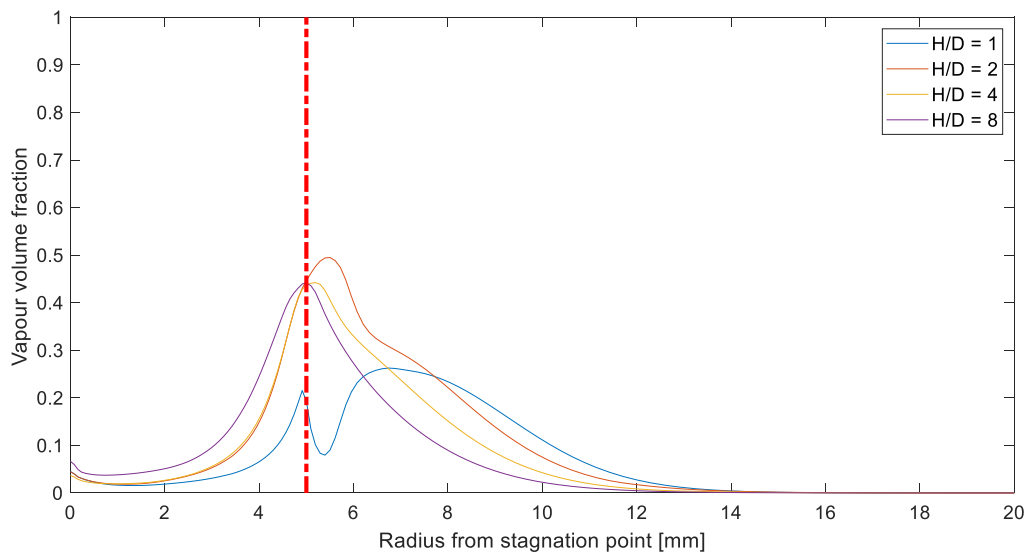


Figure 52: Vapour volume fraction distribution plots for the single-jet case with $Re = 20\,000$ for various jet-to-surface spacings, at 50 W/cm^2 with conjugation

Figure 53 shows the vapour volume fraction distributions for the single-jet case with $H/D = 8$ for various jet Reynolds numbers at a wall heat flux of 50 W/cm^2 . The vapour volume fraction increased for decreasing jet Reynolds number over the entire domain, indicating that the jet was more efficient at rewetting the surface for higher jet Reynolds numbers (and jet velocity in this case), resulting in higher quenching and reduced evaporation. There was a significant increase in the amount of vapour in the stagnation region going from $Re = 15\,000$ to $Re = 10\,000$, because the potential core no longer struck the heated surface, due to increased jet spreading at lower jet velocities.

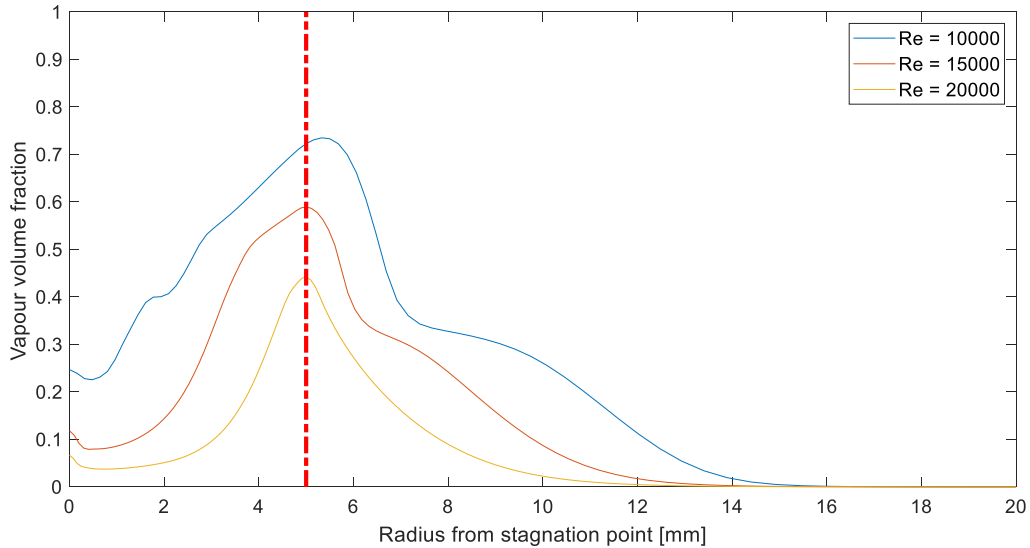


Figure 53: Vapour volume fraction distribution plots for the single-jet case with $H/D = 8$ for various jet Reynolds numbers, at 50 W/cm^2 with conjugation

Figure 54 shows the wall temperature profiles of the heated surface for the single-jet case with conjugation and $Re = 20\,000$ for various jet-to-surface spacings at a heat flux of 50 W/cm^2 . The temperature profiles did not drastically change shape for different H/D ratios; however, there was a shift upwards for increasing H/D , indicating a decrease in heat transfer for increasing H/D . There was quite a large jump in the surface temperature going from $H/D = 1$ to $H/D = 2$, indicating a significant decrease in heat transfer. It would thus be expected that the optimal heat transfer occurred at a H/D close to one.

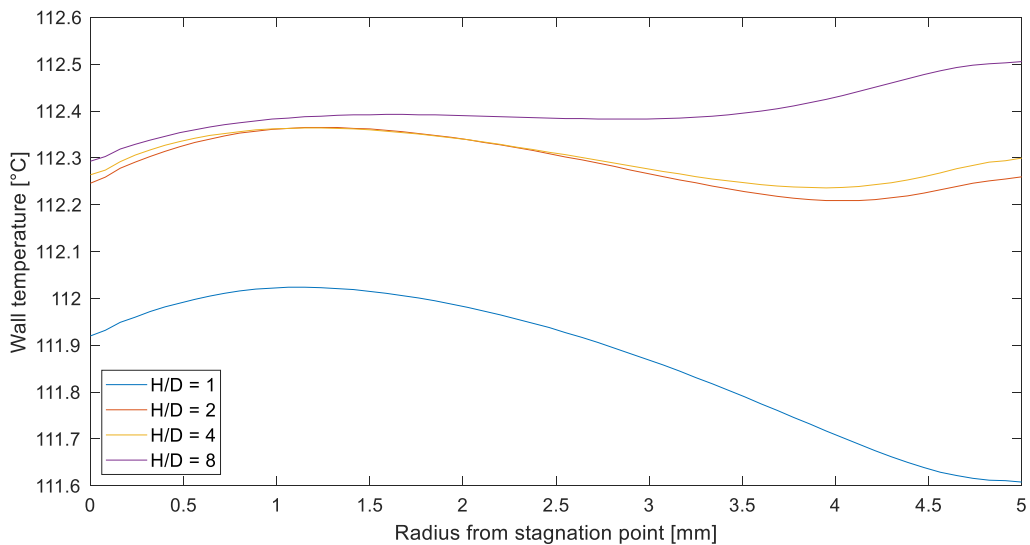


Figure 54: Heated wall temperature plots $[\text{°C}]$ for the single-jet case with $Re = 20\,000$ for various jet-to-surface spacings, at 50 W/cm^2 with conjugation

Figure 55 shows the wall temperature profiles for the single-jet case with $H/D = 8$ at 50 W/cm^2 for various jet Reynolds numbers. The trend was clear that the wall temperature increased for decreasing jet Reynolds numbers. Again, the temperature profiles were not significantly influenced by the jet Reynolds number.

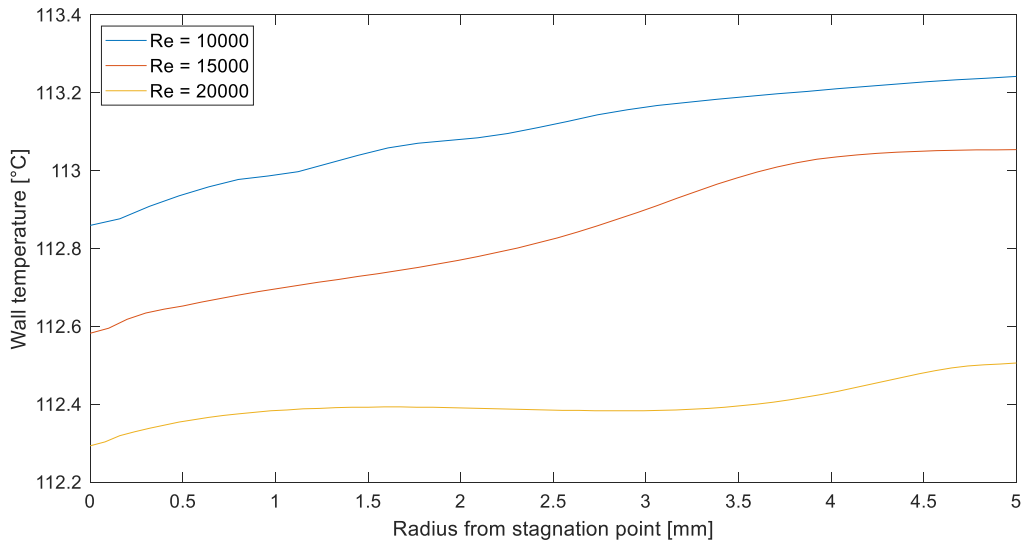


Figure 55: Heated wall temperature plots [°C] for the single-jet case with $H/D = 8$ for various jet Reynolds numbers, at 50 W/cm^2 with conjugation

The resulting heat transfer coefficients and pressure drop over the impinging device are provided in Figure 56 as a function of both parameters varied. Figure 56(a) shows that the total heat transfer coefficient increased for increasing H/D for low jet Reynolds numbers, while the coefficient decreased for increasing H/D for high jet Reynolds numbers. The influence of jet-to-surface spacing on the total heat transfer coefficient was less apparent at higher Reynolds numbers. This was expected given that there was less jet spreading in the free-jet region and thus less jet decay at higher Reynolds numbers. As a result, at low jet Reynolds numbers and small jet-to-surface spacing, the jet covered only a small portion of the heated surface, while at large jet-to-surface spacing, the jet covered a much larger portion of the heated surface due to jet spreading. At high jet Reynolds numbers and small jet-to-surface spacing, the jet had enough kinetic energy to spread out rapidly over the entire heated surface, while the kinetic energy reduced with an increase in the jet-to-surface spacing, resulting in less spreading over the heated surface due to the minimal jet spreading in the free-jet region. The quenching heat transfer coefficient, illustrated in Figure 56(b), followed the same trend as for the total heat transfer coefficient. The same arguments made for the total heat transfer coefficient held for the quenching heat transfer coefficient. As illustrated in Figure 56(c), the evaporative heat transfer coefficient increased with H/D for all jet Reynolds numbers. This relationship suggests that the jet became less efficient at wetting the surface with increasing jet-to-surface spacing, resulting in higher heat transfer due to phase change. Figure 56(d) shows that the pressure drop over the impinging device increased almost linearly with jet Reynolds number, thus with flowrate and jet velocity, and decreased almost linearly for increasing H/D .

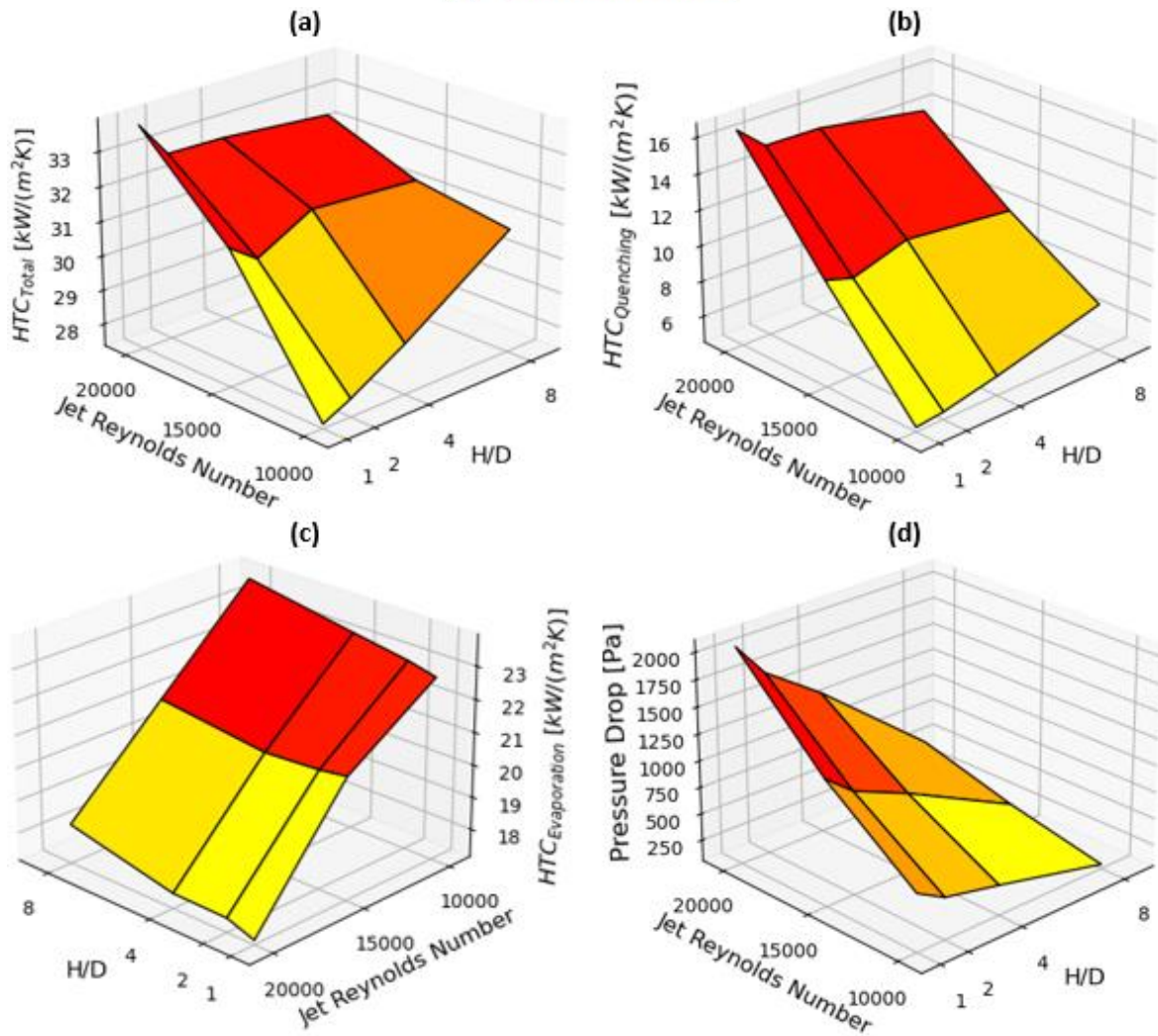


Figure 56: Heat transfer coefficient (HTC) as calculated for a single water jet as a function of jet Reynolds number (Re) and jet-to-surface spacing (H/D), at 50 W/cm^2 with conjugation: (a) based on the total heat flux, (b) based on the quenching heat flux component, and (c) based on the evaporative heat flux component. (d) is the pressure drop over the impinging device

4.2 3D Jet Array

4.2.1 Jet-to-Surface Spacing and Reynolds Number

To investigate the influence of jet Reynolds number and jet-to-surface spacing on the average heat transfer of a multijet array using R134a as heat transfer fluid, a parametric study was conducted on the geometry illustrated in Figure 34. Reynolds numbers of 30 000, 40 000 and 50 000 were tested for jet-to-surface spacings of $H/D = 1, 2, 4$ and 8 at a wall heat flux of 100 W/cm^2 . The Reynolds number was varied by varying the jet velocity, while keeping the jet diameter constant. Again, the Reynolds numbers were selected to ensure that the jets were fully turbulent and that boiling occurred over the entire surface for each case, while the H/D values were selected since the optimal heat transfer usually lies within $2 \leq H/D \leq 8$ [16].

Figure 57 and Figure 58 show the velocity contours and vectors for the multijet array with $Re = 50\,000$ and a wall heat flux of 100 W/cm^2 at various jet-to-surface spacings. The effects of confinement were clearly visible for low jet-to-surface spacings, shown in Figure 57 (a), with a significant amount of backwash from the confinement wall. Figure 57 (a, b) and Figure 58 (a) indicate strong cross-flow currents for the low jet-to-surface spacings in the jet fountain formed between the jets in the right-side view. The cross-flow appeared to be the most significant for $H/D = 4$, with the jet closest to the outlet in the right-side view of Figure 58 (a), being pushed away from the jet centre line. The jet fountains which formed between the jets and at the side wall seemed to diminish for the $H/D = 8$ case, shown in Figure 58 (b), due to the significant loss of the jet kinetic energy, resulting in less severe wall-jet interactions. As for the single-jet case, the potential core struck the surface for $H/D = 1, 2,$ and 4 but not for $H/D = 8$. Again, the wall-jet velocity decreased for increasing jet-to-surface spacing, shown in Figure 57(a) to Figure 58(b), due to the shear stresses in the jet-shearing layers, resulting in reduced jet kinetic energy. It was also evident that the wall-jet thickness reduced for increasing jet-to-surface spacing, due to the reduced kinetic energy, resulting in less liquid entrainment in the wall-jet region.

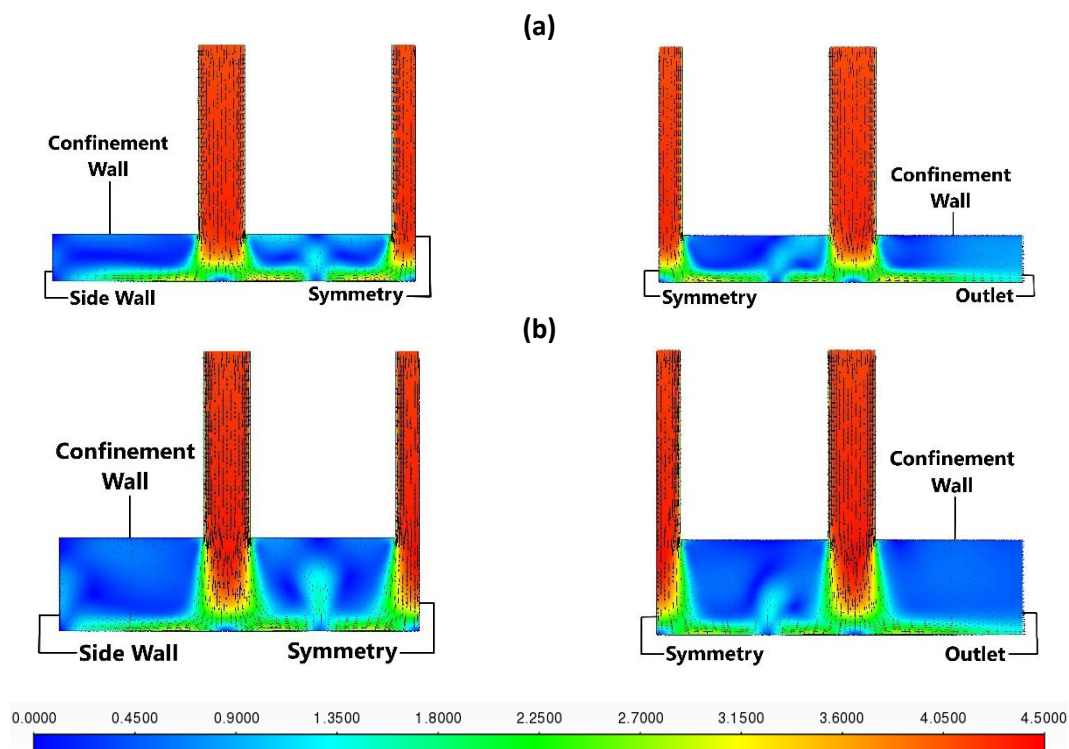


Figure 57: Liquid velocity contours [m/s] for the multijet array case with $Re = 50\,000$ for various jet-to-surface spacings, at 100 W/cm^2 with conjugation: (a) $H/D = 1$ and (b) $H/D = 2$. Figures on the left are the left-side view, figures on the right are the right-side view. The views are shown in Fig. 35.

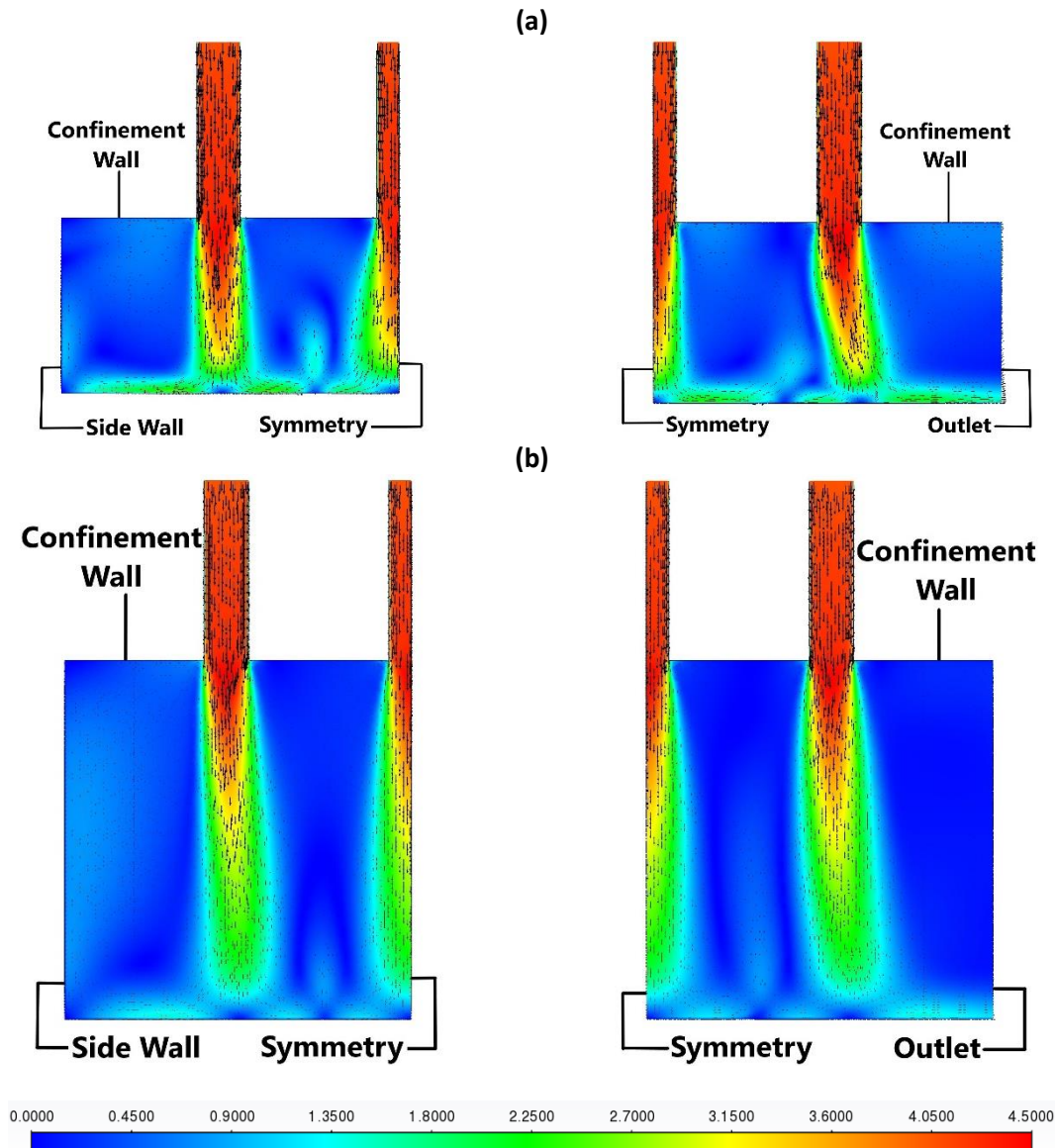


Figure 58: Liquid velocity contours [m/s] for the multijet array case with $Re = 50\,000$ for various jet-to-surface spacings, at 100 W/cm^2 with conjugation: (a) $H/D = 4$ and (b) $H/D = 8$. Figures on the left are the left-side view, figures on the right are the right-side view. The views are shown in Fig. 35.

Figure 59(a) to (c) shows the liquid velocity contours with overlaid velocity vectors for the multijet array with $H/D = 8$ and 100 W/cm^2 for various jet Reynolds numbers. There was hardly any difference between the liquid velocity contours of the three different Reynolds numbers. There was a slight reduction in the jet spreading for increasing Reynolds numbers, which was expected due to the lower velocity. There was no notable change in the potential core length for the different Reynolds numbers. However, the intensity of the fountain effect did increase slightly for increasing Reynolds numbers, which was expected given the higher wall-jet velocities. The influence of cross-flow on the jets decreased for increasing jet Reynolds numbers, indicating that the faster jets were likely to be more effective at rewetting the heated surface due to their increased kinetic energy. Therefore, it was expected that the jets with higher Reynolds numbers would achieve higher quenching heat transfer coefficients than for the jets with low Reynolds numbers.

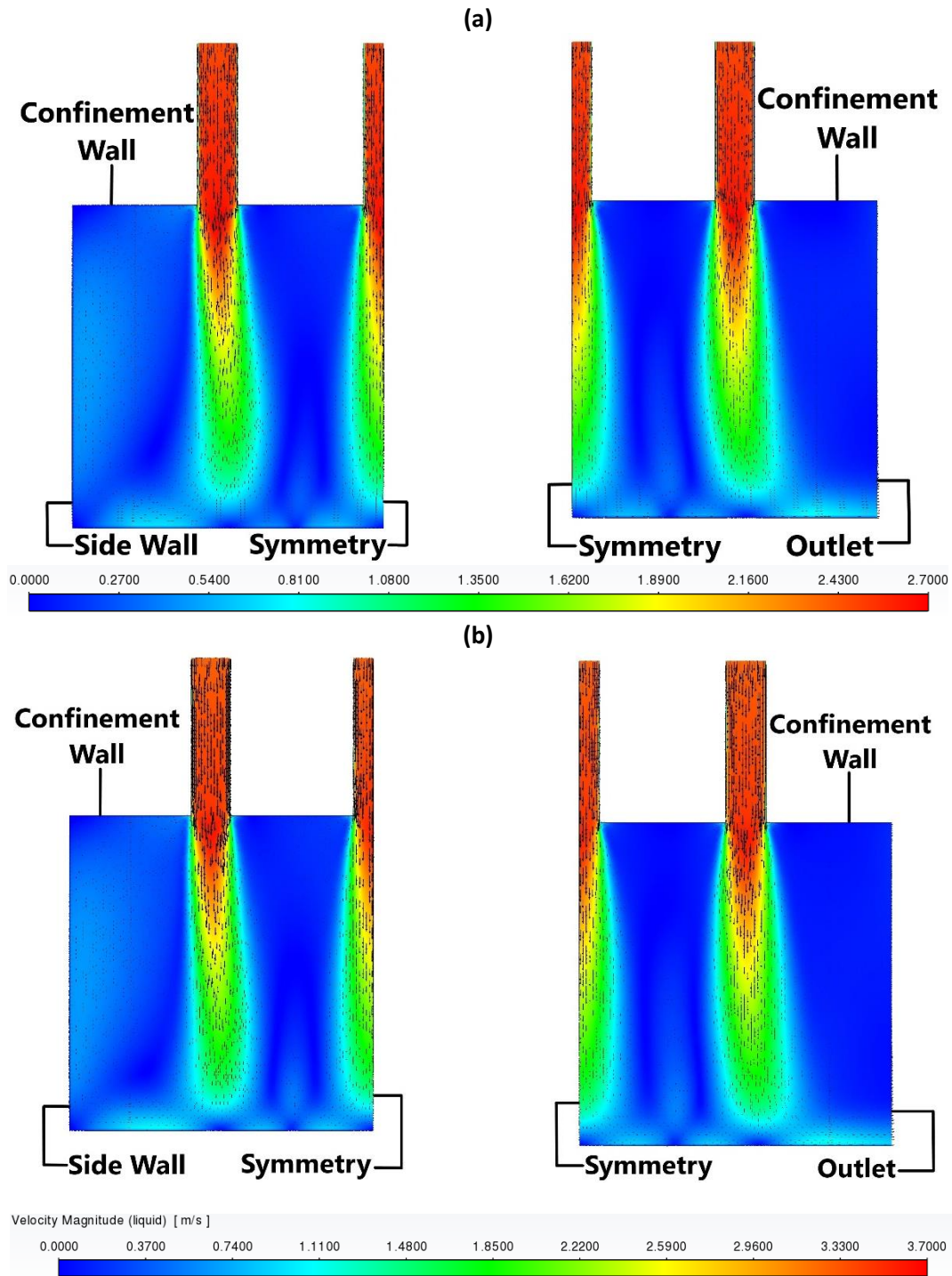


Figure 59: Liquid velocity contours [m/s] for the multijet array case with $H/D = 8$ for various jet Reynolds numbers, at 100 W/cm^2 with conjugation: (a) $Re = 30\,000$, (b) $Re = 40\,000$ and (c) $Re = 50\,000$. Figures on the left are the left-side view, figures on the right are the right-side view. The views are shown in Fig. 35.

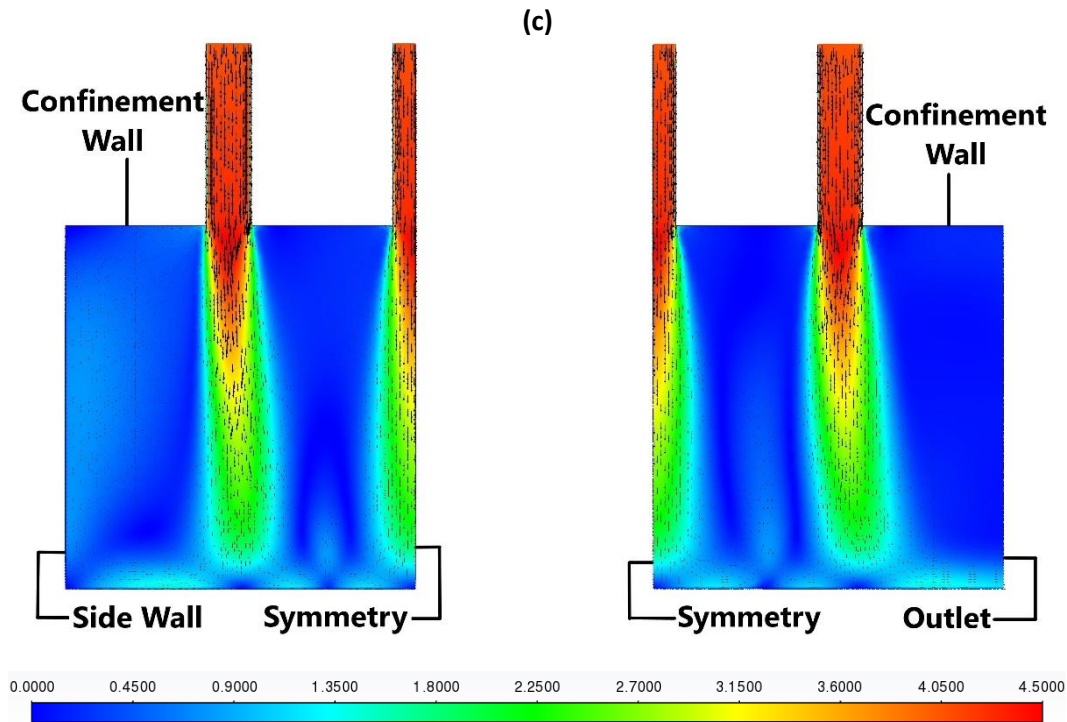


Figure 59 (continued): Liquid velocity contours [m/s] for the multijet array case with $H/D = 8$ for various jet Reynolds numbers, at 100 W/cm^2 with conjugation: (a) $Re = 30\,000$, (b) $Re = 40\,000$ and (c) $Re = 50\,000$. Figures on the left are the left-side view, figures on the right are the right-side view. The views are shown in Fig. 35.

Figure 60(a) to (d) shows the vapour volume fraction contours alongside the surface heat flux contours for the multijet array with $Re = 50\,000$ and 100 W/cm^2 , for various jet-to-surface spacings. Severe cross-flow was present for the $H/D = 1$ case, shown in Figure 60(a), and the presence of cross-flow could be observed in the vapour trails that are pushed out of the heated section. The intensity of the cross-flow reduced as the jet-to-surface spacing increased, Figure 60(a) to (d), which agreed well with the literature for single-phase jets, provided in Table 1. The area occupied by the wall jets increased with jet-to-surface spacing for $H/D = 1$ to shown in Figure 60(a) to (c) Figure 60(d). The increase in the area occupied by the wall jets for larger jet-to-surface spacings was due to the increased jet spreading in the free-jet region, resulting in larger wall jet areas where quenching heat transfer dominated. The increase in the wall-jet area was also observed in the surface heat flux contours where the heat flux in the wall-jet regions was lower than for the rest of the surface, indicating that evaporative heat transfer was limited. The jet stagnation regions had a higher heat flux than for the wall-jet regions. The jet stagnation region areas increased with jet-to-surface spacing for $H/D = 1$ to $H/D = 8$, shown in Figures 60(a) to (d), while the heat flux in the jet stagnation regions decreased. The increase in the jet stagnation region area and decrease in jet stagnation region heat flux was also due to the increased jet spreading in the free-jet region, resulting in lower kinetic energy in the jet stagnation regions and thus a decrease in quenching heat transfer.

For all jet-to-surface spacings, the maximum surface heat flux occurred in the secondary stagnation regions between the jets. This was expected because the wall jets collided in this region, resulting in a significant decrease in the convective and quenching heat transfer and as a result, evaporative heat transfer dominated in this region. As expected, most of the vapour occupied the secondary stagnation regions between the jets, given the increased evaporative heat flux and thus vapour formation. The high vapour occupation in the secondary stagnation regions was also due to the vapour which formed in the wall-jet regions being pushed away by the jets into the secondary stagnation regions between the jets. The vapour in the secondary stagnation regions occupied the largest area for the $H/D = 1$ case, shown in Figure 60(a), due to the high jet kinetic energy, resulting in larger secondary stagnation regions. The secondary stagnation region areas decreased for increasing jet-to-surface spacing for

$H/D = 1$ to 4, shown in Figure 60(a) to (c) which could be due to the drastic variation between the dominating heat transfer method over the surface, with quenching heat transfer dominating in the jet stagnation regions and wall-jet region, and evaporative heat transfer dominating in the secondary stagnation regions. For the larger jet-to-surface spacings, except for $H/D = 4$, the variation in the heat flux contours reduced and became much more uniform for the $H/D = 8$ case, shown in Figure 60(d), which was almost uniform except for the secondary stagnation regions between the jets. The two low heat flux regions (spots), shown in Figure 60(c), were due to bubbles departing from the surface. From the surface heat flux contours, shown in Figure 60, it seemed that $H/D = 2$ had the highest quenching heat flux contribution due to the large wall-jet areas and high heat fluxes in these regions. Therefore, it was expected that this jet-to-surface spacing ($H/D = 2$) would yield the highest critical heat flux of the jet-to-surface spacings tested.

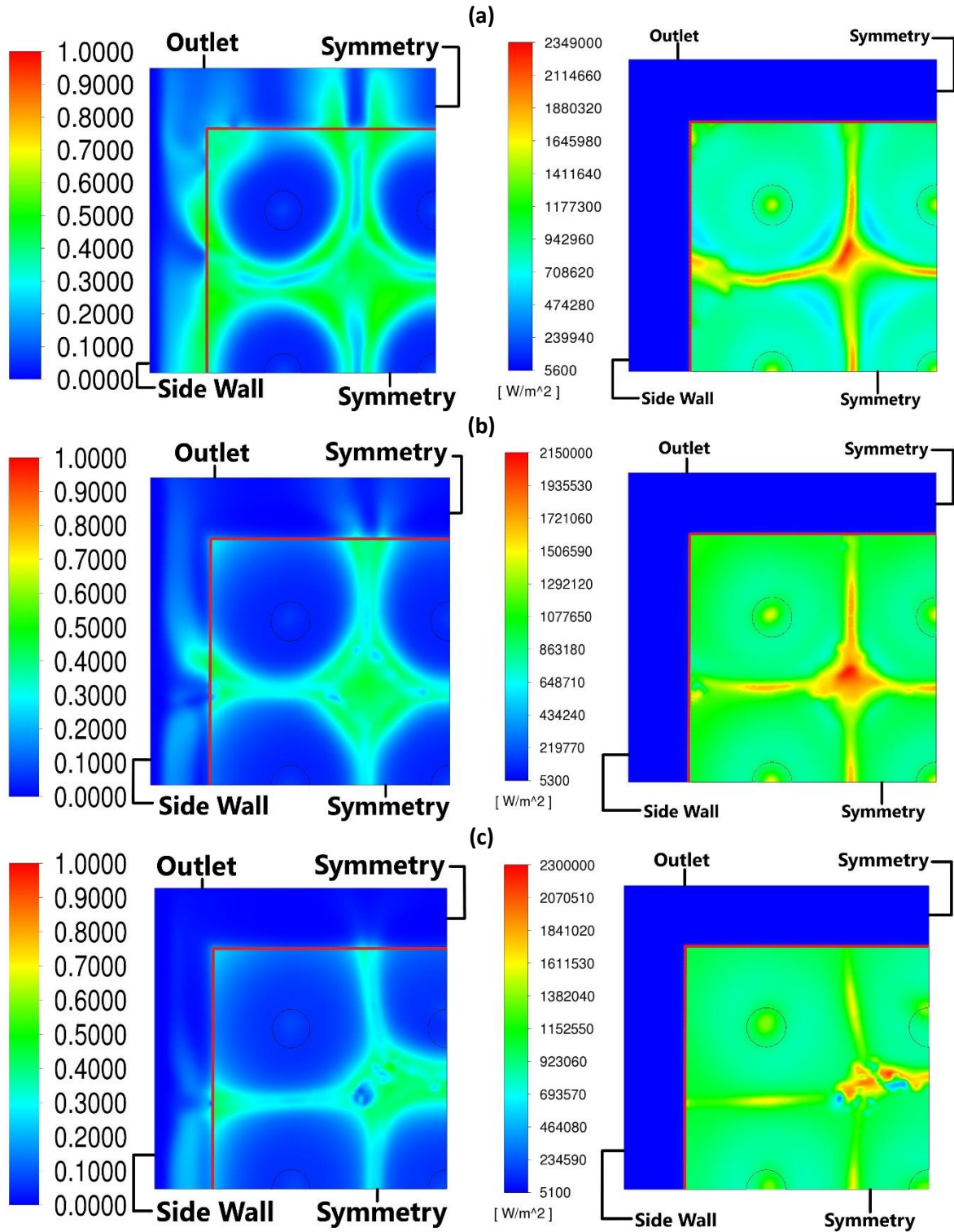


Figure 60: Vapour volume fraction contours (left) and surface heat flux contours $[W/m^2]$ (right) for the multijet array case with $Re = 50\ 000$ for various jet-to-surface spacings, at $100\ W/cm^2$ with conjugation: (a) $H/D = 1$, (b) $H/D = 2$, (c) $H/D = 4$, and (d) $H/D = 8$. The red line in the figures encloses the heated region.

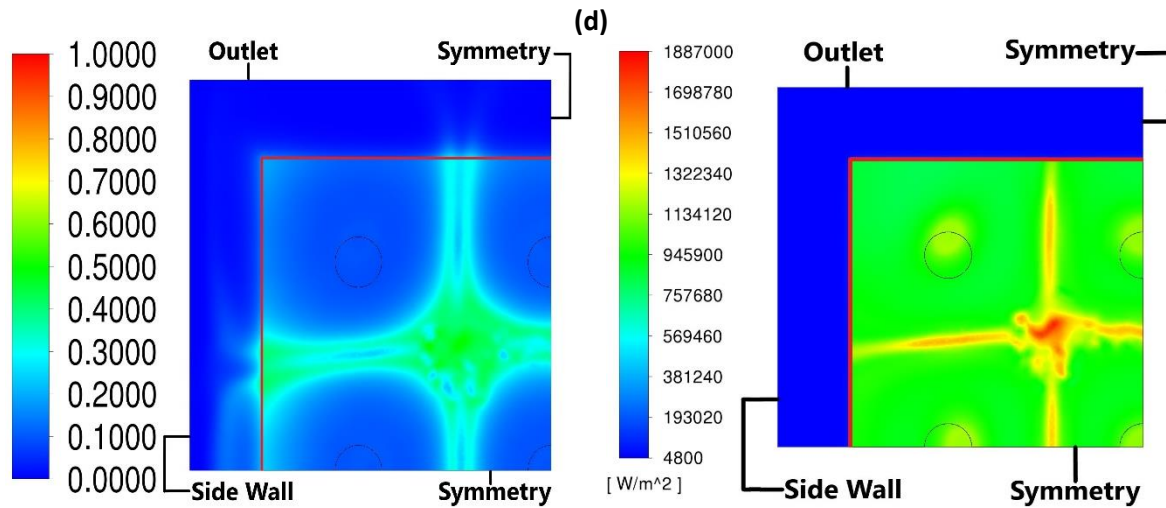


Figure 60 (continued): Vapour volume fraction contours (left) and surface heat flux contours $[W/m^2]$ (right) for the multijet array case with $Re = 50\,000$ for various jet-to-surface spacings, at $100\,W/cm^2$ with conjugation: (a) $H/D = 1$, (b) $H/D = 2$, (c) $H/D = 4$, and (d) $H/D = 8$. The red line in the figures encloses the heated region.

Figure 61(a) to (c) shows the vapour volume fraction contours alongside the surface heat flux contours for the multijet array with $H/D = 8$ and $100\,W/cm^2$, for various jet Reynolds numbers. The vapour contours indicate that the area of the wall-jet regions was the smallest for $Re = 30\,000$, shown in Figure 61(b), and increased for increasing jet Reynolds numbers, shown in Figures 61(a) to (c). The maximum surface heat flux also occurred for $Re = 30\,000$ and decreased for increasing jet Reynolds numbers due to the lower jet kinetic energy for low jet Reynolds numbers, resulting in lower quenching heat transfer and thus higher evaporative heat transfer for lower jet Reynolds numbers. Therefore, the critical heat flux increased for increasing jet Reynolds numbers.

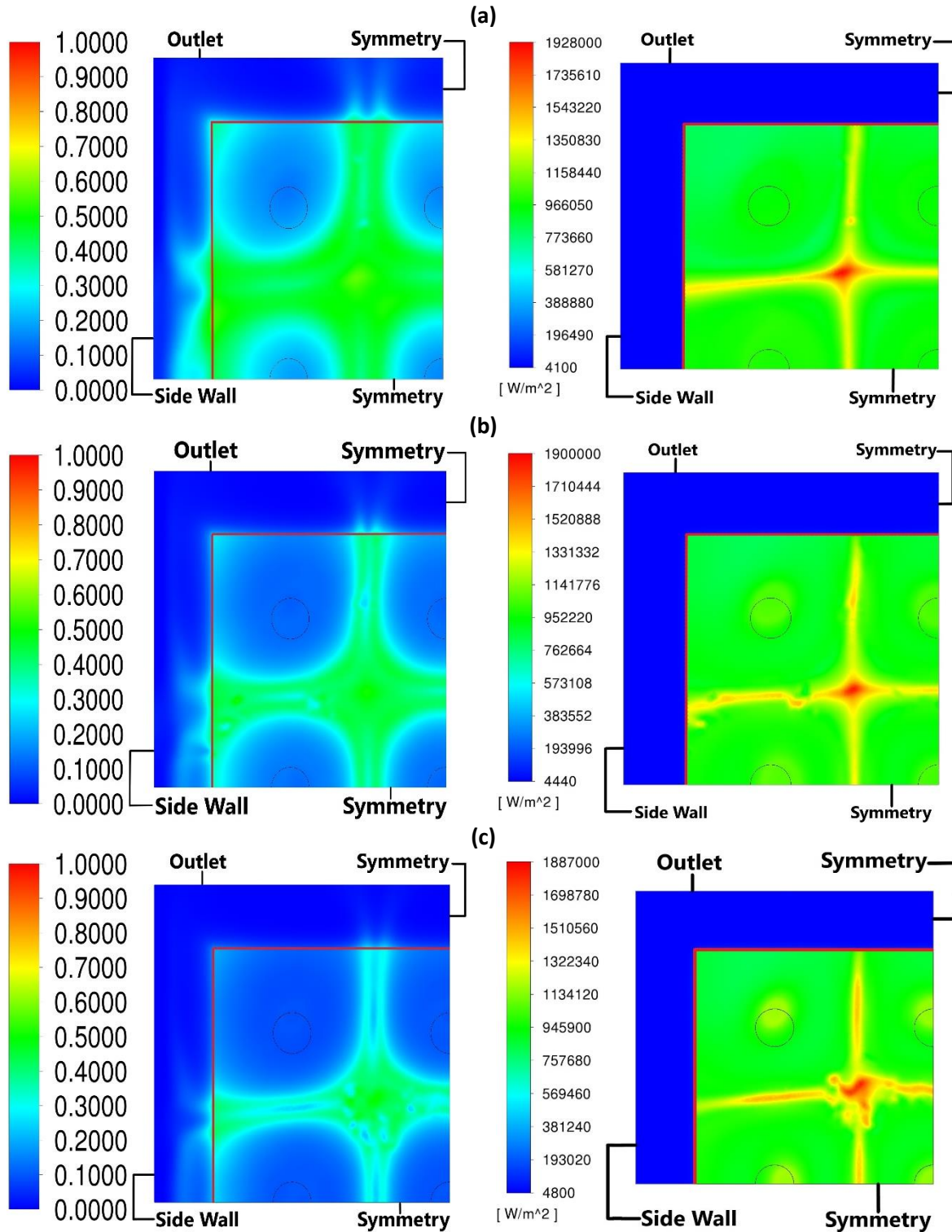


Figure 61: Vapour volume fraction contours (left) and surface heat flux contours $[W/m^2]$ (right) for the multijet array case with $H/D = 8$ for various jet Reynolds numbers, at $100 W/cm^2$ with conjugation: (a) $Re = 30\ 000$, (b) $Re = 40\ 000$, and (c) $Re = 50\ 000$. The red line in the figures encloses the heated region.

The heated surface temperature contours are shown alongside the surface heat flux contours in Figure 62(a) to (d) for the multijet array case with $Re = 50\ 000$ and $100 W/cm^2$ for various jet-to-surface spacings. Here the wall jet and stagnation regions are clearly visible on the surface temperature contours, with the maximum temperatures occurring in the wall-jet regions where quenching heat transfer dominated and the minimum wall temperatures in the secondary stagnation regions where evaporative heat transfer dominated. As expected, an inverse relationship existed

between the surface temperature and surface heat flux, with the lowest surface temperature corresponding to the highest surface heat flux. The area of the high temperature wall-jet region increased from $H/D = 1$ to $H/D = 2$; however, the maximum surface temperature in this region decreased, suggesting that the jets spread out more in the free-jet region but did not lose as much kinetic energy, resulting in improved quenching heat transfer. Increasing the jet-to-surface spacing beyond $H/D = 2$ resulted in disrupted wall jets, with the wall-jet region almost disappearing for $H/D = 8$. The disruption of the wall jets at higher jet-to-surface spacings was due to the high jet spreading resulting in reduced jet kinetic energy and quenching heat transfer, and as a result, evaporative heat transfer dominated and increased vapour formation interfered with the wall jets, reducing the quenching heat transfer even further. The maximum as well as minimum wall temperature reduced for increasing jet-to-surface spacing, indicating higher evaporative heat transfer. The surface temperature contours indicated that for jet-to-surface spacings beyond $H/D = 2$, the jets became less effective at rewetting the surface, and as a result, produced lower quenching heat transfer. The influence of the jets on the wall temperature became less apparent for large jet-to-surface spacings and seemed to approach pool boiling for $H/D = 8$. Again, $H/D = 2$ seemingly yielded the highest quenching heat transfer and was expected to yield the highest critical heat flux.

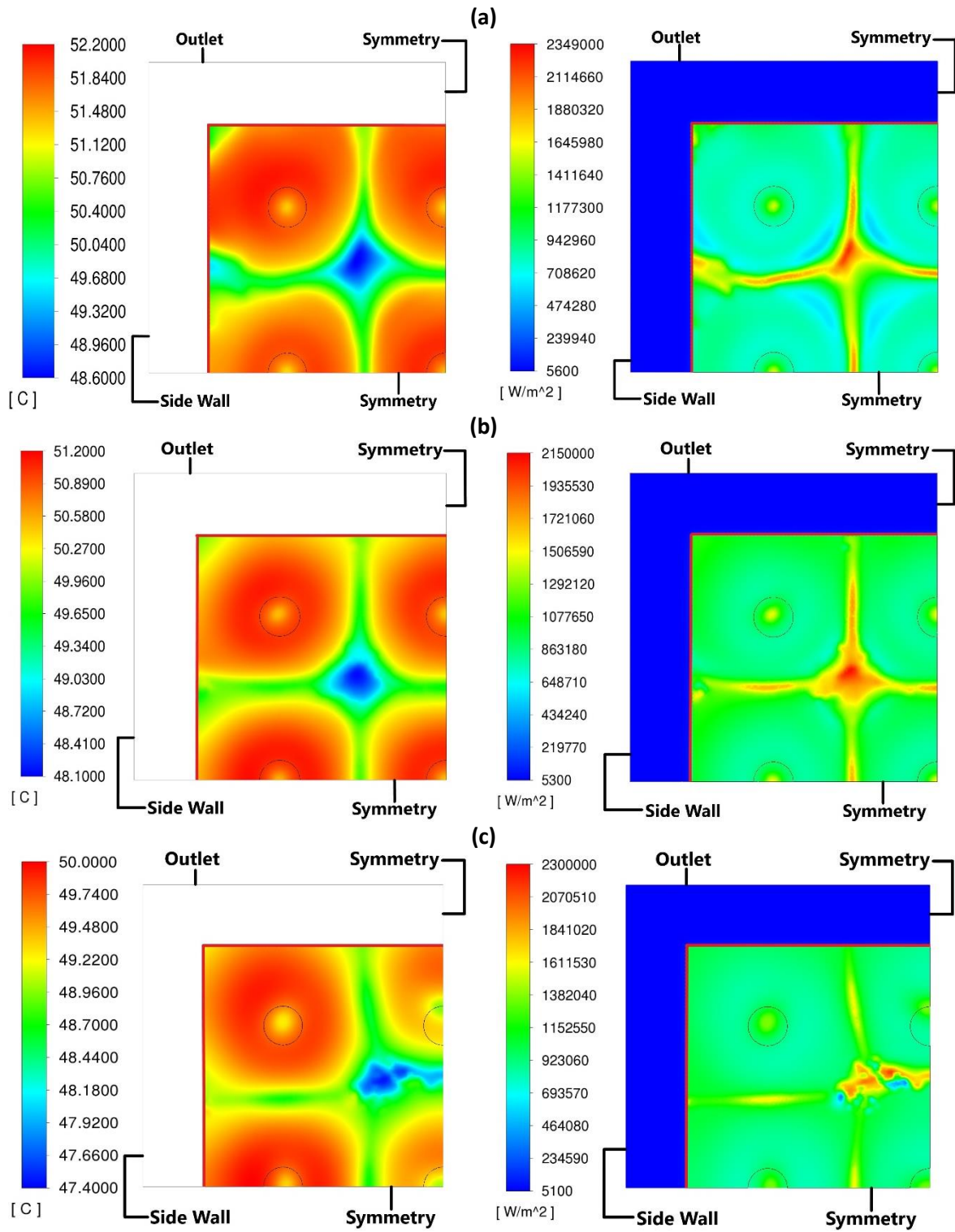


Figure 62: Heated surface temperature contours [°C] (left) and surface heat flux contours [W/m²] (right) for the multijet array case with $Re = 50\,000$ for various jet-to-surface spacings, at 100 W/cm^2 with conjugation: (a) $H/D = 1$, (b) $H/D = 2$, (c) $H/D = 4$, and (d) $H/D = 8$. The red line in the figures encloses the heated region.

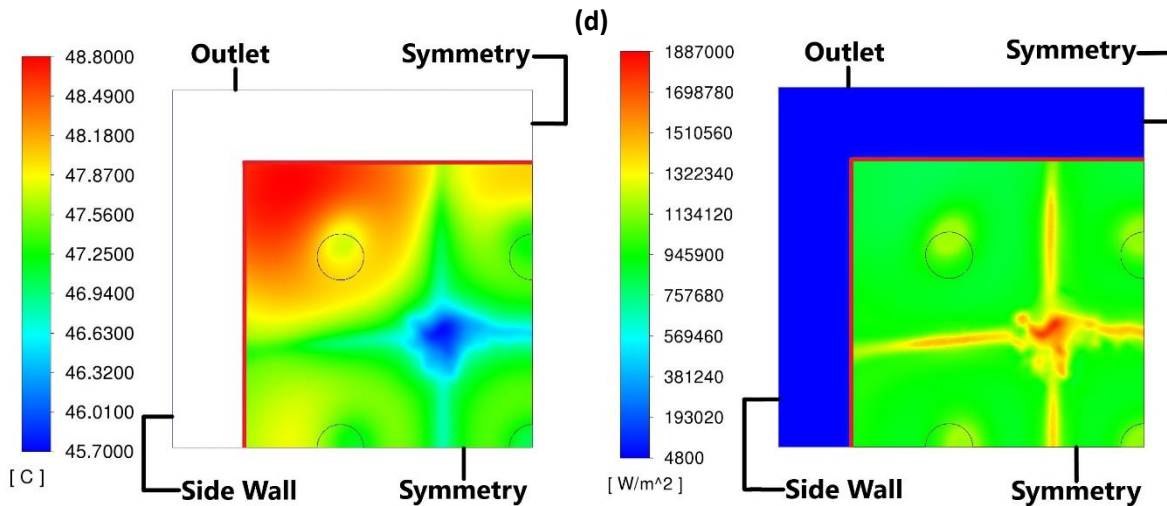


Figure 62 (continued): Heated surface temperature contours [$^{\circ}\text{C}$] (left) and surface heat flux contours [W/m^2] (right) for the multijet array case with $Re = 50\,000$ for various jet-to-surface spacings, at $100\text{ W}/\text{cm}^2$ with conjugation: (a) $H/D = 1$, (b) $H/D = 2$, (c) $H/D = 4$, and (d) $H/D = 8$. The red line in the figures encloses the heated region.

Figure 63(a) to (c) shows the heated surface temperature contours alongside the surface heat flux contours for the multijet array case with $H/D = 8$ and $100\text{ W}/\text{cm}^2$ for various jet Reynolds numbers. The minimum as well as maximum surface temperatures increased for increasing Reynolds numbers, shown in Figure 63(a) to (c). This increase was somewhat unexpected but could be attributed to the increased intensity of the wall-jet interactions at higher Reynolds numbers along with increased cross-flow intensity, hindering the heat transfer. The quenching heat transfer still increased with the jet Reynolds number, resulting in reduced evaporative heat transfer and thus increased surface temperature. The critical heat flux was expected to increase with the jet Reynolds number due to the improved quenching heat transfer, resulting in a lower contribution of the evaporative heat transfer to the total heat transfer, and thus a delay in dry-out. The reduced contribution of the evaporative heat transfer was visible in the surface heat flux contours where the maximum surface heat flux reduced for increasing jet Reynolds numbers, indicating reduced evaporative heat transfer and thus delayed critical heat flux.

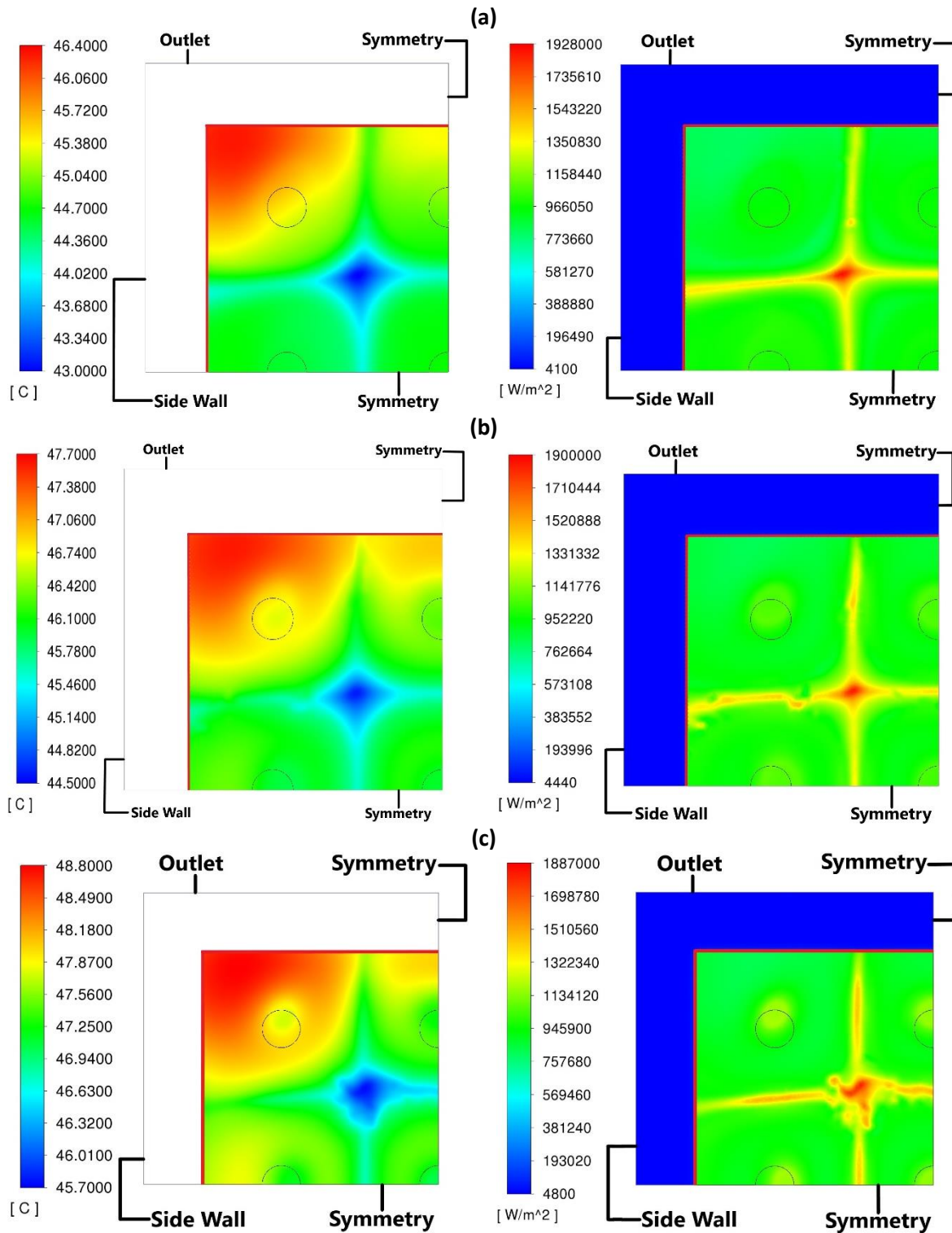


Figure 63: Heated surface temperature contours [°C] (left) and surface heat flux contours [W/m²] (right) for the multijet array case with $H/D = 8$ for various jet Reynolds numbers, at 100 W/cm² with conjugation: (a) $Re = 30\,000$, (b) $Re = 40\,000$, and (c) $Re = 50\,000$. The red line in the figures encloses the heated region.

Figure 64 gives the resulting heat transfer coefficients and pressure drop over the jet array as a function of both parameters varied. Figure 64(a) indicates that the total heat transfer coefficient decreased for increasing jet Reynolds numbers at all H/D values. The decrease in the total heat transfer coefficient became more apparent at high H/D values, which was somewhat unexpected; however, it could be due to jet-to-jet interactions reducing the effectiveness of the jets, as mentioned earlier. The total heat transfer coefficient was nearly unaffected by the jet Reynolds number for low

H/D ratios, which aligned with the observations of experimental studies. The quenching heat transfer coefficients are illustrated in Figure 64(b). The quenching heat transfer coefficient achieved a maximum at $H/D = 2$ and a minimum at $H/D = 8$, confirming earlier observations, indicating that jet-to-jet interactions were present, which could explain why the total heat transfer coefficient reduced for increasing jet Reynolds number. Figure 64(c) shows the evaporative heat transfer coefficients. The evaporative heat transfer coefficient increased with H/D and decreased with jet Reynolds number, indicating that the fluid boiled more vigorously due to lower quenching heat transfer. Therefore, it was expected that the critical heat flux would increase with jet Reynolds number and decrease with H/D . It was also expected that the optimal CHF would be in the region of $1 < H/D < 2$. The pressure drop over the jet array is illustrated in Figure 64(d). The pressure drop increases with jet Reynolds number, that is with both flowrate and jet velocity, while the pressure drop did not follow such clear trend for H/D . For a jet Reynolds number of 30 000, the pressure drop decreased for increasing H/D , however, for jet Reynolds numbers of 40 000 and 50 000 the pressure drop was the highest for $H/D = 1$, a minimum for $H/D = 2$, and increased when increasing H/D beyond $H/D = 2$. The pressure drop over the jet array was somewhat surprising and is inversely proportional to the quenching heat transfer coefficient in Figure 64(b). The pressure drop results suggest that jet-to-jet interaction plays a significant role on the pressure drop over the jet array, which is why the pressure drop increased when H/D was increased beyond 2.

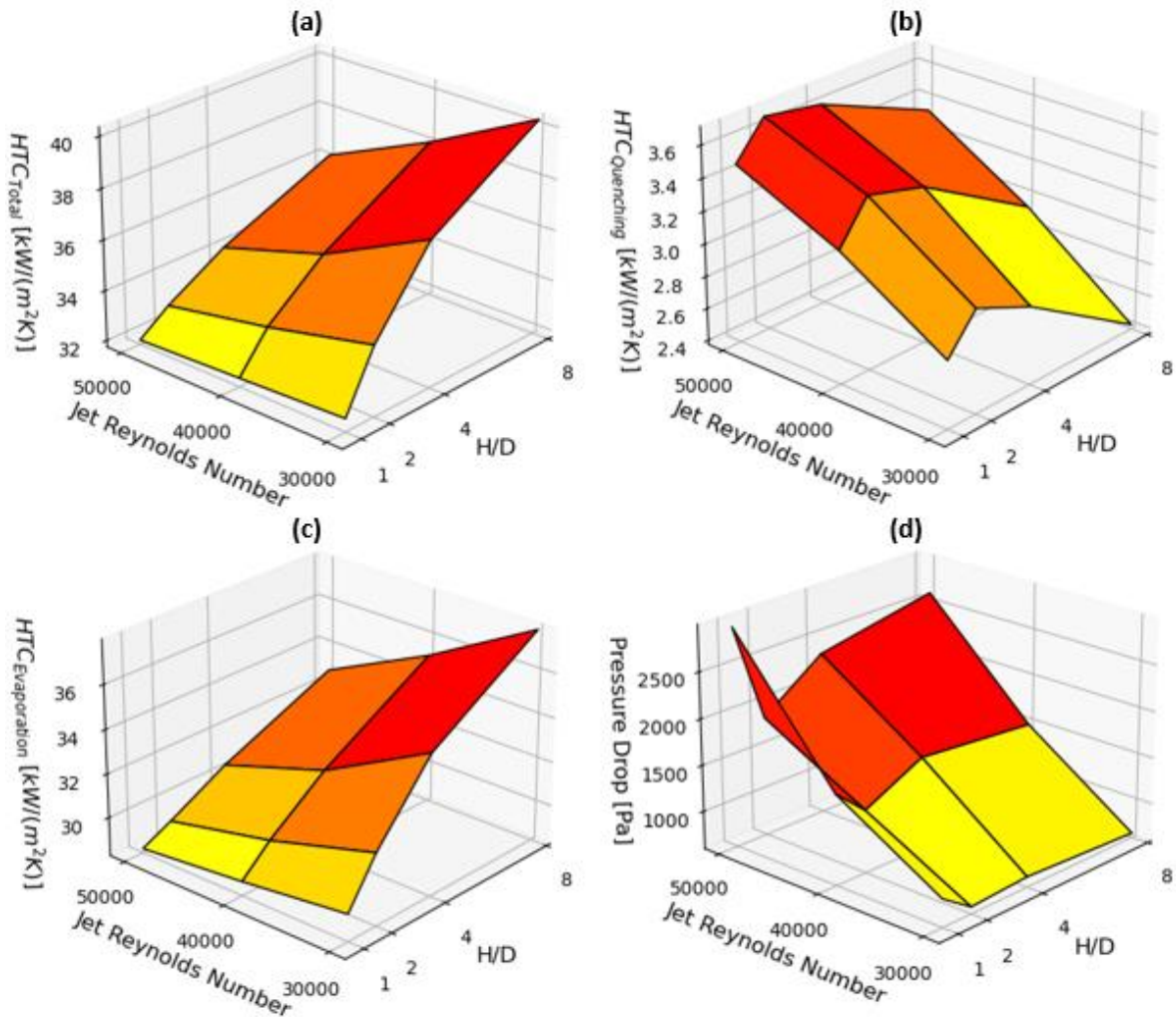


Figure 64: Heat transfer coefficient (HTC) as calculated for a multijet array as a function of jet Reynolds number (Re) and jet-to-surface spacing (H/D), at 100 W/cm^2 with conjugation: (a) based on the total heat flux, (b) based on the quenching heat flux component, and (c) based on the evaporative heat flux component. (d) is the pressure drop over the jet array.

4.2.2 Jet-to-Jet Spacing

Investigating the effects of jet-to-jet spacing is a more complex task than investigating the effects of jet-to-surface spacing or jet Reynolds number, since it is impossible to vary the jet-to-jet spacing without changing other jet parameters as well, particularly the jet area to heated surface area ratio. To isolate the effects of jet-to-jet spacing, two approaches were used to vary the jet-to-jet spacing. The first was to use the domain, shown in Figure 34, and vary the jet-to-jet spacing by varying the jet nozzle diameter, while keeping $H/D = 2$. As a result, the other jet parameters such as the mass flow rate, jet velocity and jet Reynolds number could not all stay the same. Therefore, three separate cases were tested for this approach: constant mass flow rate, constant jet Reynolds number, and constant jet velocity. The second approach was to keep all other jet parameters (mass flow rate, jet diameter, jet velocity, H/D , and jet Reynolds number) constant and increase the size of the domain, shown in Figure 34, to vary the jet-to-jet spacing. The domain modifications for the second approach are illustrated in Figure 65, where $L_C = 2.06 \times (p_{jet}/D)$, $L_h = 3L_C$, and $L_T = L_h + L_C$, with p_{jet}/D the driving parameter. The only parameter that changes for this approach is the jet area to heated surface area ratio. For both approaches, jet-to-jet spacings of $p_{jet}/D = 2, 4, 6, \text{ and } 8$ were tested at a wall heat flux of 50 W/cm^2 .

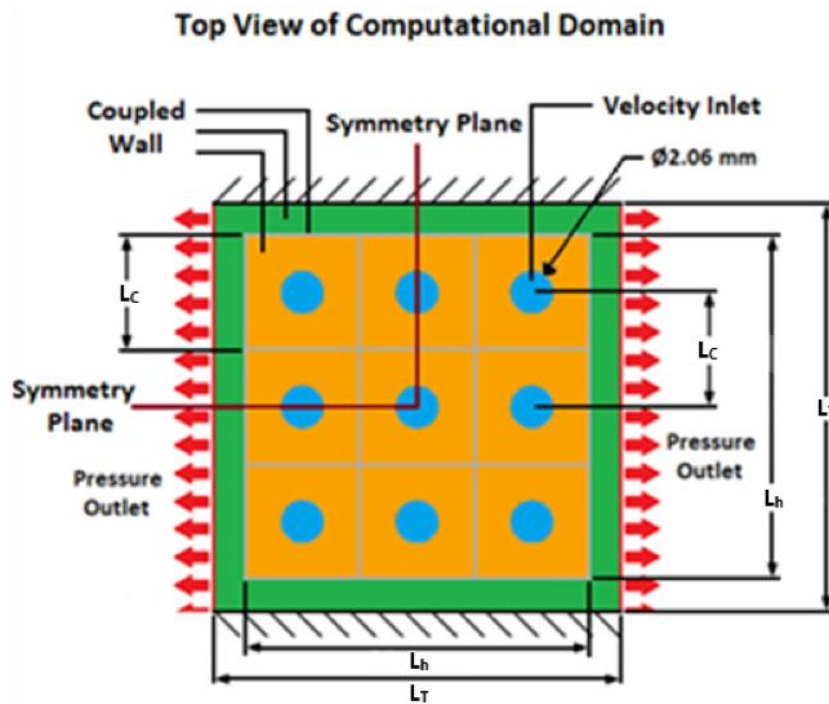


Figure 65: Domain modifications for the jet-to-jet spacing parametric study keeping all other jet parameters constant

Figure 66(a) to (d) shows the liquid velocity contours with overlaid velocity vectors for the 3D multijet array with $H/D = 2$ and $V_{jet} = 4.01 \text{ m/s}$, at 50 W/cm^2 for various jet-to-jet spacings. For $p_{jet}/D = 2$, shown in Figure 66(a), the interaction between the wall jets was intense with large fountains forming between the colliding wall jets and against the side wall. Washback from the confinement wall was also severe causing additional entrainment into the jets. Intense cross-flow was visible in the jets closest to the outlet, with the jet being pushed away from its centre line. High velocities were also visible at the outlet of the domain, indicating intense cross-flow. Interaction between the jets became less intense for increasing jet-to-jet spacing, shown in Figures 66(a) to (d), with the fountain effect diminishing rapidly when increasing p_{jet}/D beyond 4. Cross-flow also diminished for increasing jet-to-jet spacing, with the jets behaving like single jets for $p_{jet}/D = 8$, shown in Figure 66 (d).

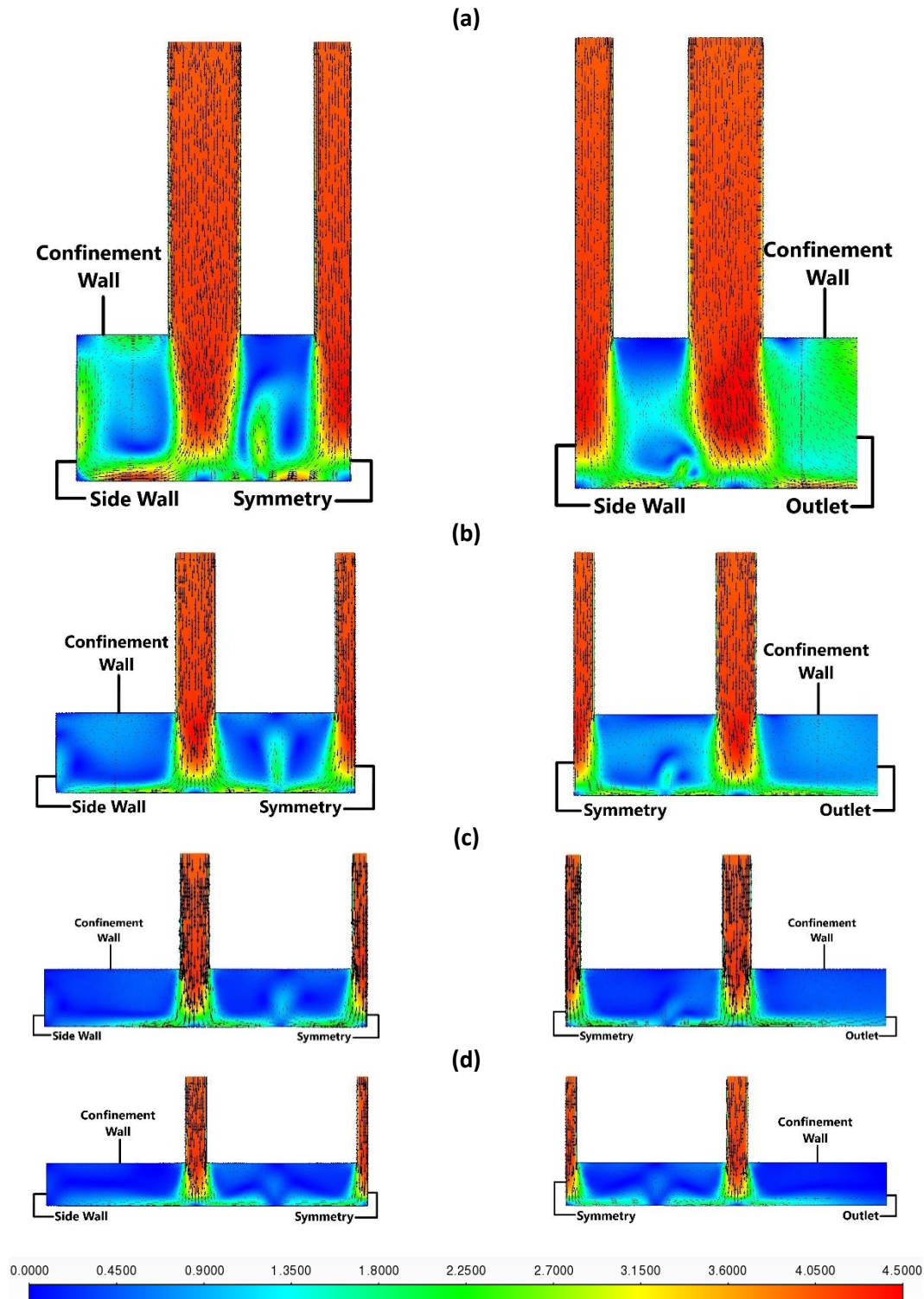


Figure 66: Liquid velocity contours [m/s] for the multijet array case with $V_{jet} = 4.01$ m/s and $H/D = 2$ for various jet-to-jet spacings, at 50 W/cm² with conjugation: (a) $p_{jet}/D = 2$, (b) $p_{jet}/D = 4$, (c) $p_{jet}/D = 6$, and (d) $p_{jet}/D = 8$. Figures on the left are the left-side view. The views are shown in Fig. 35.

Figure 67(a) to (d) shows the vapour volume fraction contours alongside the surface heat flux contours for the 3D multijet array case with $H/D = 2$ and $V_{jet} = 4.01$ m/s, at 50 W/cm², for various jet-to-jet spacings. For low jet-to-jet spacings, shown in Figure 67 (a) and (b), vapour formation only occurred in the secondary stagnation regions between the jets at low rates. The occurrence of vapour formation only in the secondary stagnation regions suggested that jet-to-jet interaction was high for low jet-to-jet spacings, resulting in quenching heat transfer over the entire surface, which prevented

boiling from occurring. The heat flux in the jet stagnation regions was a maximum for $p_{jet}/D = 2$, shown in Figure 67 (a), and decreased for increasing jet-to-jet spacing. The surface heat flux contours, shown in Figure 67 (a) and (b), indicated that the surface heat flux had a maximum in the secondary stagnation region where boiling occurred, and a rather uniform heat flux in the wall-jet regions, supporting the previous statement that quenching heat transfer was the dominant heat transfer mechanism. For larger jet-to-jet spacings, shown in Figure 67 (c) and (d), vapour formation (the boiling front) occurred closer to the stagnation region. The increased secondary stagnation regions were accompanied by higher heat fluxes in these regions, indicating that evaporative heat transfer was the dominant heat transfer mechanism in these regions. The increase was due to sufficient space between the jets, causing the wall jets to heat up moving outwards and to start boiling. The maximum surface heat flux value reached a minimum for $p_{jet}/D = 4$, shown in Figure 67 (b), while the minimum surface heat flux reached a maximum for $p_{jet}/D = 6$, shown in Figure 67 (b), with a maximum surface heat flux close to that of $p_{jet}/D = 4$. The minimum surface heat flux started to decrease again, increasing the jet-to-jet spacing beyond $p_{jet}/D = 6$ (Figure 67(d)), while the maximum surface heat flux increased drastically, indicating evaporative heat transfer. This decrease suggested that the optimal heat transfer as well as highest critical heat flux should occur in the range of $4 \leq p_{jet}/D \leq 6$ for a constant jet velocity of 4 m/s. Figure 67(d) shows that cross-flow and jet-to-jet interaction did not have a significant influence on the jets, since the jet nozzles were almost in the centre of the vapourless regions and the jet stagnation regions in the surface heat flux plots were located close to the jet centre, indicating that the jets behaved as single jets.

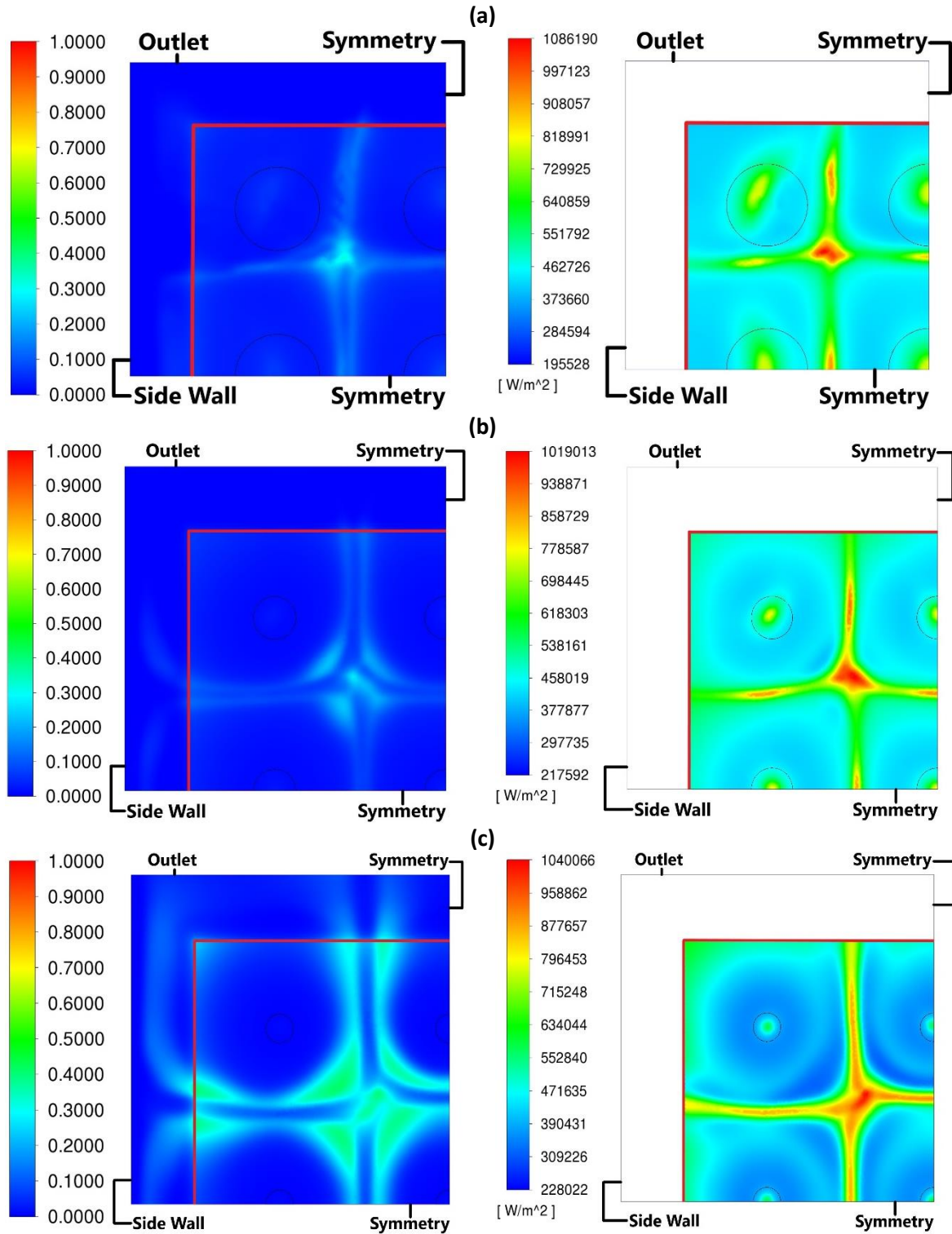


Figure 67: Vapour volume fraction contours (left) and surface heat flux contours $[W/m^2]$ (right) for the multijet array case with $V_{jet} = 4.01$ m/s and $H/D = 2$ for various jet-to-jet spacings, at 50 W/cm^2 with conjugation: (a) $p_{jet}/D = 2$, (b) $p_{jet}/D = 4$, (c) $p_{jet}/D = 6$, and (d) $p_{jet}/D = 8$. The red line in the figures encloses the heated region.

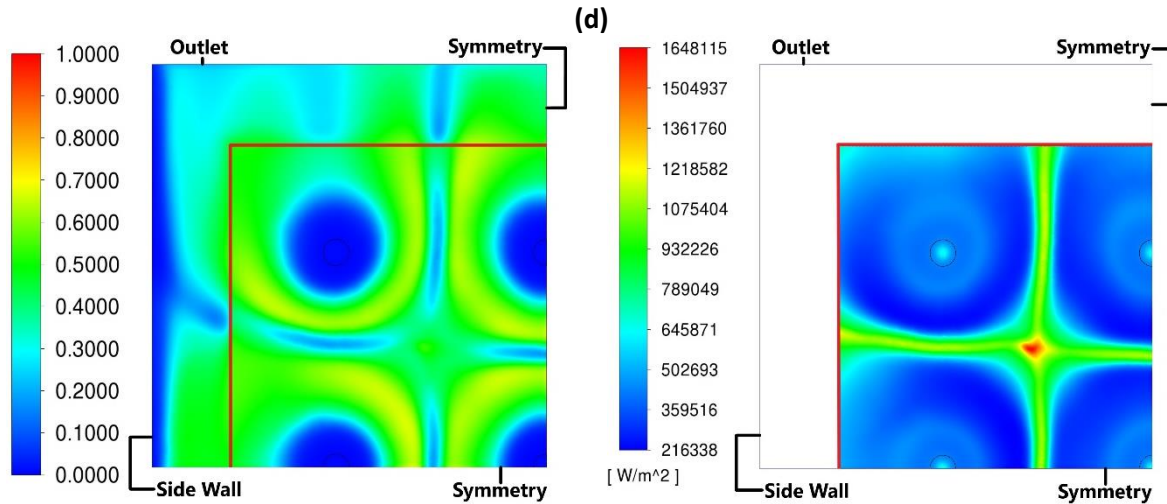


Figure 67 (continued): Vapour volume fraction contours (left) and surface heat flux contours $[W/m^2]$ (right) for the multijet array case with $V_{jet} = 4.01$ m/s and $H/D = 2$ for various jet-to-jet spacings, at 50 W/cm² with conjugation: (a) $p_{jet}/D = 2$, (b) $p_{jet}/D = 4$, (c) $p_{jet}/D = 6$, and (d) $p_{jet}/D = 8$. The red line in the figures encloses the heated region.

Figure 68(a) to (d) shows the heated surface temperature contours alongside the surface heat flux contours for the 3D multijet array case with $H/D = 2$ and $V_{jet} = 4.01$ m/s, at 50 W/cm² for various jet-to-jet spacings. As expected, the surface temperature was the lowest in the secondary stagnation regions between the jets, where the evaporative heat transfer was the dominant mechanism of heat transfer, as indicated by the vapour contour plots, shown in Figure 67. The low temperature region (the secondary stagnation region) grew for increasing jet-to-jet spacing, shown in Figures 68(a) to (d), reaching what appeared to be a maximum for $p_{jet}/D = 6$, shown in Figure 68(c). The temperature of the secondary stagnation region decreased for increasing jet-to-jet spacing and reached a minimum for $p_{jet}/D = 8$, shown in Figure 68(d), indicating that the area where evaporation occurred grew with jet-to-jet spacing. Surprisingly, the surface temperature in the wall-jet regions decreased for increasing jet-to-jet spacing, indicating that the wall jets could also start to boil to some extent for large enough p_{jet}/D . The surface heat flux contours indicated that the heat flux in the wall jets also decreased for increasing jet-to-jet spacing and that they experienced a drastic drop increasing the jet-to-jet spacing beyond $p_{jet}/D = 4$, shown in Figure 68(b). The drop in the local surface heat flux suggested that the quenching heat flux reduced in the wall-jet region. The surface heat flux in the jet stagnation regions decreased for increasing jet-to-jet spacing. This was a surprising observation and could be due to the reduced jet diameter rather than the increased jet-to-jet spacing, given that the CHF scales according to $(V_{jet}/D)^{1/3}$ [33], as discussed in Section 2.4.3.1, and the jet velocity were kept constant for the cases shown in Figure 68(a) to (d). It could be observed from the surface temperature contours as well as the surface heat flux contours that the jet stagnation regions moved closer to the jets' centre lines, indicating that cross-flow reduced for increasing jet-to-jet spacing due to better exit pathways for the spent flow.

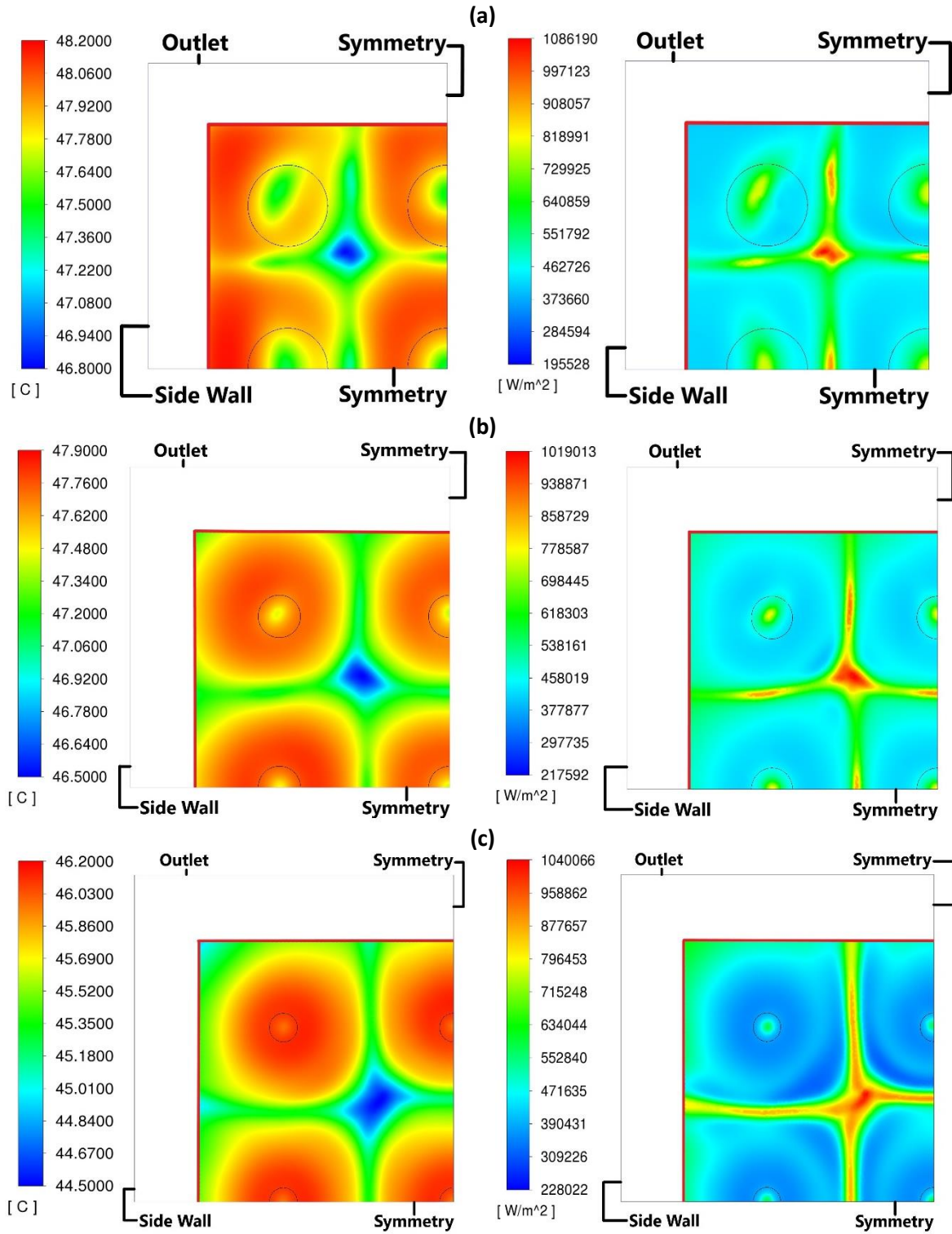


Figure 68: Heated surface temperature contours [°C] (left) and surface heat flux contours [W/m²] (right) for the multijet array case with $V_{jet} = 4.01$ m/s and $H/D = 2$ for various jet-to-jet spacings, at 50 W/cm² with conjugation: (a) $p_{jet}/D = 2$, (b) $p_{jet}/D = 4$, (c) $p_{jet}/D = 6$, and (d) $p_{jet}/D = 8$. The red line in the figures encloses the heated region.

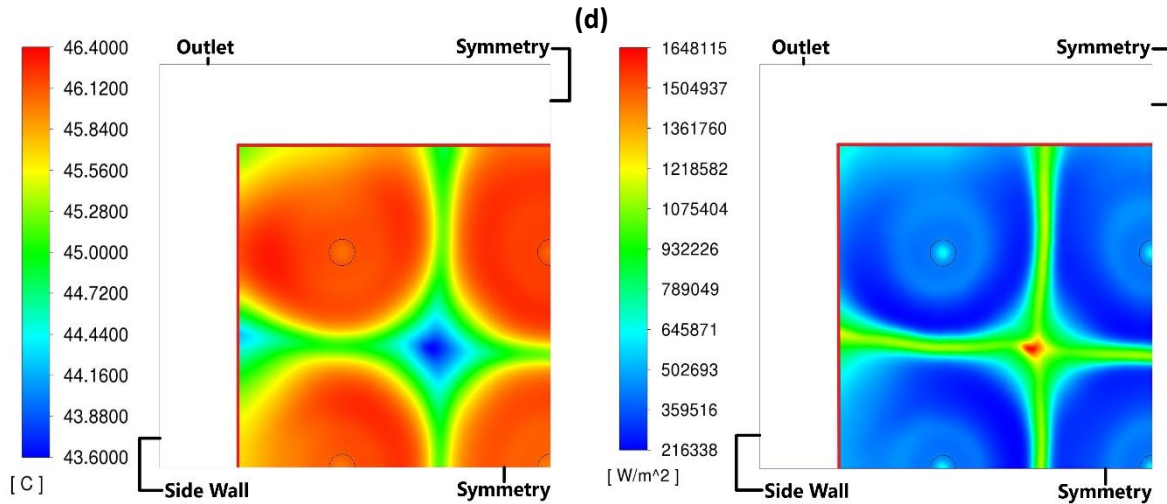


Figure 68 (continued): Heated surface temperature contours [$^{\circ}\text{C}$] (left) and surface heat flux contours [W/m^2] (right) for the multijet array case with $V_{\text{jet}} = 4.01 \text{ m/s}$ and $H/D = 2$ for various jet-to-jet spacings, at $50 \text{ W}/\text{cm}^2$ with conjugation: (a) $p_{\text{jet}}/D = 2$, (b) $p_{\text{jet}}/D = 4$, (c) $p_{\text{jet}}/D = 6$, and (d) $p_{\text{jet}}/D = 8$. The red line in the figures encloses the heated region.

The resulting heat transfer coefficients for the jet-to-jet spacing investigation are given in Figure 69(a) to (c) as a function of p_{jet}/D for both approaches followed. Figure 69(a) shows that the total heat transfer coefficient increased with p_{jet}/D for the first approach with constant jet velocity; however, the coefficient stayed close to constant moving from $p_{\text{jet}}/D = 6$ to $p_{\text{jet}}/D = 8$. Figure 69(b) shows the quenching heat transfer coefficients, indicating that for the first approach with constant jet velocity, the quenching heat transfer coefficient was at a maximum for $p_{\text{jet}}/D = 2$ and decreased for increasing jet-to-jet spacing, reducing rapidly for $p_{\text{jet}}/D > 4$. The decrease in the quenching heat transfer coefficient suggested that the highest CHF would be achieved for $p_{\text{jet}}/D = 2$; however, $p_{\text{jet}}/D = 2$ would not produce the best heat transfer in the fully developed nucleate-boiling regime as was seen in the total heat transfer coefficient, which suggested that the optimal heat transfer coefficient in the nucleate-boiling regime would be achieved for $6 \leq p_{\text{jet}}/D \leq 8$. Figure 69(c) shows that the evaporative heat transfer coefficient increased for increasing jet-to-jet spacing for the first approach with constant velocity. Therefore, evaporation heat transfer became the dominant heat transfer mechanism for an increasing portion of the surface and should reach CHF sooner for increasing jet-to-jet spacing.

For the first approach with constant Reynolds numbers, the total heat transfer coefficient (Figure 69(a)) reduced when increasing from $p_{\text{jet}}/D = 2$ to $p_{\text{jet}}/D = 4$. Increasing the jet-to-jet spacing beyond $p_{\text{jet}}/D = 4$ resulted in an increase in the total heat transfer coefficient, indicating that an optimal total heat transfer coefficient, for a given Reynolds number, in the fully developed nucleate-boiling regime may be achieved for a p_{jet}/D outside the tested range. The increase in the total heat transfer coefficient for $p_{\text{jet}}/D > 4$ could also be caused by the increase in the jet velocity, due to the decrease in jet nozzle diameter. The quenching heat transfer coefficient (Figure 69(b)) reached a maximum at $p_{\text{jet}}/D = 4$, indicating that the highest CHF should be achieved for $p_{\text{jet}}/D = 4$. For $p_{\text{jet}}/D > 4$, the quenching heat transfer coefficient decreased. The evaporative heat transfer coefficient, Figure 69(c), reached a minimum for $p_{\text{jet}}/D = 4$, also indicating that the optimal CHF should be achieved for $p_{\text{jet}}/D = 4$.

The total heat transfer coefficient for the first approach with constant mass flow rate also decreased initially for increasing jet-to-jet spacing and started to increase again for $p_{\text{jet}}/D > 6$. Therefore, for a constant mass flow rate, decreasing the diameter of the jets could result in optimal heat transfer for $p_{\text{jet}}/D > 8$. The quenching heat transfer coefficient, shown in Figure 69(b), reached a maximum for $p_{\text{jet}}/D = 6$, indicating that for a given mass flow rate, the highest CHF should be achieved

for $p_{jet}/D = 6$. The evaporative heat transfer coefficient, shown in Figure 69(c), followed the same trend as for the case with constant Reynolds number, and the coefficient reached a minimum at $p_{jet}/D = 6$, supporting the statement that the highest CHF should be achieved for $p_{jet}/D = 6$.

The total heat transfer coefficient, shown in Figure 69 (a), for the second approach indicated a similar increase to that of the first approach with constant jet velocity; however, the heat transfer coefficient did not start to level off at high jet-to-jet spacing, indicating that the optimal heat transfer coefficient in the fully developed nucleate-boiling regime may be achieved for $p_{jet}/D > 8$. The quenching heat transfer coefficient, shown in Figure 69 (b), followed the same trend as in the first approach with constant jet velocity, indicating that the maximum CHF should be achieved for $p_{jet}/D = 2$. The evaporative heat transfer coefficient, shown in Figure 69(c), followed the same trend as in the first approach with constant jet velocity, supporting the statement that the maximum CHF should be achieved for $p_{jet}/D = 2$. The only variable other than p_{jet}/D which did not stay constant in the second approach was the area ratio of the total jet area to the heated surface area; however, the area ratio was not expected to have a significant impact on the trends observed in Figure 69(a) to (c).

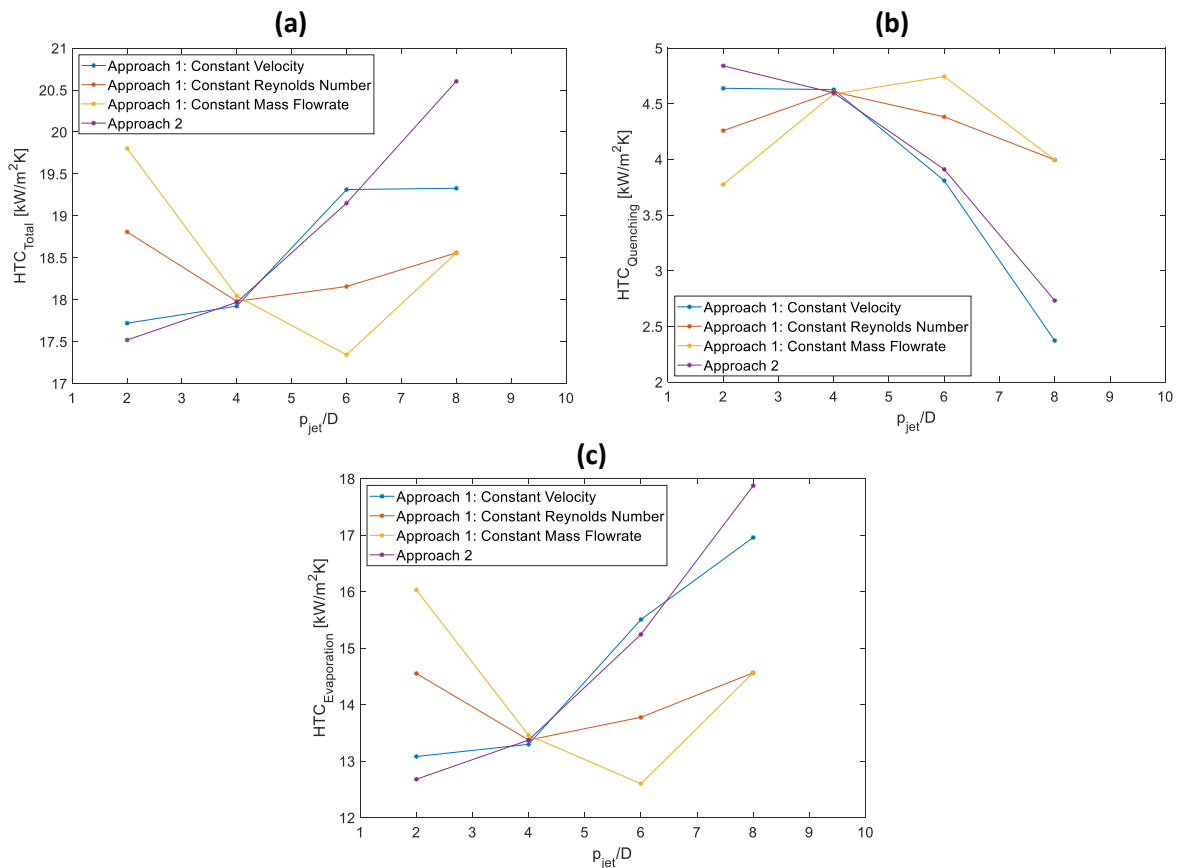


Figure 69: Heat transfer coefficient (HTC) as calculated for a multijet array as a function of jet-to-jet spacing (p_{jet}/D), at 50 W/cm^2 with conjugation: (a) based on the total heat flux, (b) based on the quenching heat flux component, and (c) based on the evaporative heat flux component.

5 Conclusions and Future Work

5.1 Conclusions

The dissertation presented an investigation into the simulation of jet impingement in the fully developed nucleate-boiling regime for electronics cooling applications. Various modelling approaches were investigated to determine the best practice for modelling jet impingement boiling heat transfer from heated surfaces. Various jet parameters were investigated to determine their influence on heat transfer. The main conclusions of the study follow in the next sections.

Chapter 3 validated the numerical models against experiments, which gave confidence in the modelling approach used in this research, ensuring that heat transfer could be successfully predicted. The study focused on round jets impinging on heated surfaces in the nucleate-boiling regime. Both single- and multijet arrays were considered. The working fluids were water and R134a, corresponding to the experiments. Key findings from this chapter are:

- (1) Conjugate heat transfer in the solid heating block is an important factor to be considered should the heating scheme in the experimental set-up have significant thickness and mass, confirming the findings in the literature. Ignoring the effects of conjugation could result in inaccurate predictions of surface temperature profile and thus heat transfer coefficient.
- (2) The RPI boiling model could, at most times, successfully predict the ONBD. However, special care should be taken in cases where the ONBD or CHF is not known in advance as the model could fail to predict it, which may be detrimental to design purposes.
- (3) Including the hydrostatic pressure gradient at the side outlets of jet impingement devices is essential to simulate the heat transfer higher up the boiling curve. Failing to add it results in numerical instability at higher heat fluxes.

Chapter 4 consisted of a parametric study presenting the influence of jet Reynolds number and jet-to-surface spacing on the average heat transfer of single- and multijet arrays. For the multijet arrays, the influence of jet-to-jet spacing on the average heat transfer was also investigated. Key findings from this chapter are:

- (1) For single submerged jets, the total heat transfer coefficient increased with velocity, while the evaporative heat transfer coefficient decreased. As a result, the CHF also increased with velocity in agreement with experimental investigations in the literature.
- (2) For single submerged jets, the total heat transfer coefficient increased with jet-to-surface spacing at jet Reynolds number of $Re = 10\,000$, but decreased at $Re > 10\,000$. Therefore, an optimal jet-to-surface spacing existed, which aligned with the literature.
- (3) For single submerged jets, the pressure drop and thus the required pumping power increased with jet velocity for a constant jet diameter, but decreased for increasing jet-to-surface spacing. As a result, the increase in heat transfer coefficient with higher jet velocities comes at the expense of higher pumping power. While the increase in heat transfer coefficient with increasing jet-to-surface spacing at lower jet Reynolds numbers is accompanied by a reduced pressure drop and thus require a lower pumping power. Therefore, an optimal point between heat transfer performance and pumping power requirements exists.
- (4) For confined multijet arrays, the total heat transfer coefficient decreased for increasing jet-to-surface spacing for all tested jet Reynolds numbers. However, the total heat transfer coefficient was not a function of jet-to-surface spacing at jet $Re = 50\,000$. The reason was that jet-to-jet interactions at increased jet-to-surface spacings were not as strong at these flow rates due to reduced jet spreading. The evaporative heat transfer coefficient increased with jet-to-target spacing at $30\,000 \leq Re \leq 50\,000$. The quenching heat flux peaked at $H/D = 2$, which showed that there existed an optimal jet-to-surface spacing, resulting in optimal CHF.

- (5) For confined multijet arrays, when the total heat transfer coefficient decreased with increasing jet Reynolds number, the evaporative heat flux also reduced. As a result, the CHF increased with the jet Reynolds number.
- (6) For confined multijet arrays, the pressure drop of the array increased with jet velocity for constant jet diameter. The pressure drop was a maximum for $H/D=1$, a minimum for $H/D=2$, and increased with H/D for $2 \leq H/D \leq 8$. Since, jet-to-jet interaction increases with jet-to-surface spacing, the results suggest that the jet-to-jet interaction plays a dominant role in the pressure drop over the jet array.
- (7) For a constant jet velocity in confined multijet arrays, the total heat transfer coefficient increased with jet-to-jet spacing up to $p_{jet}/D = 6$, where it stayed constant up to $p_{jet}/D = 8$. The increase in the total heat transfer coefficient was caused by the increase in the evaporative heat transfer coefficient. The quenching heat transfer coefficient decreased for increasing jet-to-jet spacing, resulting in a lower CHF.
- (8) For a constant total mass flow rate, the total heat transfer coefficient decreased for increasing jet-to-jet spacing up to $p_{jet}/D = 6$, where it started to increase again. An optimal total heat transfer coefficient could be reached at a jet-to-jet spacing outside the tested range of $2 \leq p_{jet}/D \leq 8$. The evaporative heat transfer coefficient followed the same trend as for the total heat transfer coefficient. The quenching heat transfer coefficient reached a maximum at $p_{jet}/D = 6$, indicating that the optimal CHF existed.

5.2 Future work

This research study proved that the RPI boiling model could successfully predict the heat transfer of jet impingement boiling, which was essential for design purposes. It proved that parametric investigations could be conducted using CFD, aligning well with the experimental findings. It was shown that jet impingement boiling could meet the heat extraction requirements of modern-day electronic components and devices.

However, more attention must be paid to the following unexplained facets regarding jet impingement boiling and the numerical modelling thereof:

- The influence of jet-to-jet spacing on heat transfer needs to be considered over a wider range of jet-to-surface spacing and jet Reynolds numbers/velocities to find the optimal jet-to-jet spacing for various configurations.
- The present research highlighted the importance of the management of spent flow and the influence of cross-flow on the heat transfer. It is thus of great importance to investigate different methods of spent flow management and their influence on heat transfer.
- Since most experimental studies on jet impingement boiling have considered highly subcooled boiling, where the Cole bubble departure frequency model is not applicable, experimental studies considering lower degrees of subcooling to saturated boiling are of interest to validate the numerical models. There is also a need for a bubble departure frequency model, which can be applied to high degrees of subcooled flow boiling.

Before jet impingement boiling can be widely implemented in electronics cooling, the following challenges must be met:

- The influence of the jet parameters on pressure drop has not been studied extensively. However, this influence is an important design consideration since it is essential for determining the pumping power requirements.
- The influence of the heat transfer fluids on heat transfer as well as the operating pressure is important for design purposes, given that many applications, such as embedded electronic cooling methods, require dielectric heat transfer fluids and low operating pressures. Heat transfer fluids is also important consideration as the saturation temperature as well as the available latent heat is highly dependent on it.

- The influence of the heated surface condition on heat transfer is also an important consideration, as the CHF is highly dependent on the surface condition, such as porous surfaces. Surface augmentation is another important consideration that needs to be investigated, such as grooves or pin-fins.

References

- [1] C. de Brún, R. Jenkins, T. Lupton, R. Lupoi, R. Kempers and A. Robinson, "Confined jet array impingement boiling," *Experimental Thermal and Fluid Science*, vol. 86, pp. 224-234, 2017.
- [2] F. Zhou, S. N. Joshi, Y. Liu and E. M. Dede, "Near-junction cooling for next-generation power electronics," *International Communications in Heat and Mass Transfer*, vol. 108, 2019.
- [3] A. C. Kheirabadi and D. Groulx, "Cooling of server electronics: A design review of existing technology," *Applied Thermal Engineering*, vol. 105, pp. 622-638, 2016.
- [4] S. S. Murshed and C. N. d. Castro, "A critical review of traditional and emerging techniques and fluids for electronics cooling," *Renewable and Sustainable Energy Reviews*, vol. 78, pp. 821-833, 2017.
- [5] D. B. Tuckerman and R. F. W. Pease, "High-performance heat sinking for VLSI," *IEEE Electron Device Letters*, vol. 2, no. 5, 1981.
- [6] S. G. Kandlikar and W. J. Grande, "Evolution of microchannel flow passages-thermohydraulic performance and fabrication technology," *Heat Transfer Engineering*, vol. 24, no. 1, pp. 3-17, 2003.
- [7] M. S. El-Genk and A. F. Ali, "Saturation boiling critical heat flux of PF-5060 dielectric liquid on microporous copper surfaces," *ASME Journal of Heat Transfer*, vol. 137, no. 4, 2015.
- [8] S. Fan and F. Duan, "A review of two-phase submerged boiling in thermal management of electronic cooling," *International Journal of Heat and Mass Transfer*, vol. 150, 2020.
- [9] S. Lee, V. S. Devahdhanush and I. Mudawar, "Frequency analysis of pressure oscillations in large length-to-diameter two-phase micro-channel heat sinks," *International Journal of Heat and Mass Transfer*, vol. 116, pp. 273-291, 2018.
- [10] I. Mudawar, "Recent advances in high-flux, two-phase thermal management," *Journal of Thermal Science and Engineering Applications*, vol. 5 (2), 2013.
- [11] M. J. Rau and S. V. Garimella, "Two-phase jet impingement: Liquid-vapor interactions and heat transfer mapping for multiscale surface enhancement design," *Encyclopedia of Two-Phase Heat Transfer and Flow*, vol. 2, 2018.
- [12] L. Qiu, S. Dubey, F. Choo and F. Duan, "Recent developments of jet impingement nucleate boiling," *International Journal of Heat and Mass Transfer*, vol. 89, pp. 42-58, 2015.
- [13] R. Wu, Y. Fan, T. Hong, H. Zou, R. Hu and X. Luo, "An immersed jet array impingement cooling device with distributed returns for direct body liquid cooling of high power electronics," *Applied Thermal Engineering*, vol. 162, 2019.
- [14] M. Banooni and S. Molana, "Investigation of heat transfer processes involved liquid impingement jets: A review," *Brazilian Journal of Chemical Engineering*, vol. 30, no. 3, pp. 413-435, 2013.

- [15] R. Farrelly, A. McGuinn, T. Persoons and D. B. Murray, "Fluctuating and time averaged heat transfer," Trinity College Dublin, Dublin, 2009.
- [16] N. Zuckerman and N. Lior, "Jet impingement heat transfer: Physics, correlations, and numerical modeling," *Advances in Heat Transfer*, vol. 39, pp. 565-631, 2006.
- [17] Y. Koizumi, M. Shoji, M. Monde, Y. Takata and N. Nagai, "Pool Boiling," in *Boiling Research and Advances*, Saga, Elsevier, 2017, pp. 2-3.
- [18] S. Nukiyama, "The maximum and minimum values of the heat Q transmitted from metal to boiling water under atmospheric pressure," *Japan Society of Mechanical Engineers*, vol. 37, pp. 367-374, 1934.
- [19] Y. A. Cengel and A. J. Ghajar, "Pool Boiling," in *Heat and Mass Transfer Fundamentals and Applications*, New York, McGraw Hill Education, 2015, pp. 601-612.
- [20] Y. Koizumi, M. Shoji, M. Monde, Y. Takata and N. Nagai, "Flow Boiling," in *Boiling Research and Advances*, Saga, Elsevier, 2017, pp. 4-8.
- [21] M. G. Cooper and A. J. P. Lloyd, "The Microlayer in Nucleate Pool Boiling," *International Journal of Heat and Mass Transfer*, vol. 12, pp. 895-913, 1969.
- [22] Y. Koizumi, M. Shoji, M. Monde, Y. Takata and N. Nagai, "Heat Transfer Mechanisms Revealed by MEMS Thermal Measurement," in *Boiling Research and Advances*, Saga, Elsevier, 2017, pp. 22-35.
- [23] M. Gradeck, A. Kouachi, M. Lebouché, F. Volle, D. Maillet and J. Boreau, "Boiling curves in relation to quenching of a high temperature moving surface with liquid jet impingement," *International Journal of Heat and Mass Transfer*, vol. 52, no. 5-6, pp. 1094-1104, 2009.
- [24] L. Qiu, S. Dubey, F. Choo and F. Duan, "Recent developments of jet impingement nucleate boiling," *International Journal of Heat and Mass Transfer*, vol. 89, no. 0017-9310, pp. 42-58, 2015.
- [25] M. J. Rau and S. V. Garimella, "Local two-phase heat transfer from arrays of confined and submerged impinging jets," *International Journal of Heat and Mass Transfer*, vol. 67, no. 0017-9310, pp. 487-498, 2013.
- [26] N. M. Dukle and D. K. Hollingsworth, "Liquid crystal images of the transition from jet impingement convection to nucleate boiling Part II: Nonmonotonic distribution of the convection coefficient," *Experimental Thermal and Fluid Science*, vol. 12, no. 3, pp. 288-297, 1996.
- [27] R. J. Copeland, "Boiling heat transfer to a water jet impinging on a flat surface (Ph.D. thesis)," Southern Methodist University, Dallas, TX, 1970.
- [28] Y. Katto and M. Kunihiro, "Study of the mechanism of burn-out in boiling system of high burn-out heat flux," *JSME International Journal*, vol. 16, no. 99, pp. 1357-1366, 1973.

- [29] C. Struble and L. Witte, "An in situ technique for measuring heat transfer from a power transistor to a boiling liquid," *Journal of Heat Transfer*, vol. 116, no. 2, pp. 495-498, 1994.
- [30] D. Zhou and C. Ma, "Local jet impingement boiling heat transfer with R113," *Heat Mass Transfer*, vol. 40, no. 6-7, pp. 539-549, 2004.
- [31] R. Cardenas and V. Narayanan, "Heat transfer characteristics of submerged jet impingement boiling of saturated FC-72," *International Journal of Heat and Mass Transfer*, vol. 55, pp. 4217-4231, 2012.
- [32] Z. Zhao, Y. Peles and M. Jensen, "Water jet impingement boiling from structured-porous surfaces," *International Journal of Heat and Mass Transfer*, vol. 63, pp. 445-453, 2013.
- [33] M. D. Clark, J. A. Weibel and S. V. Garimella, "Identification of nucleate boiling as the dominant heat transfer mechanism during confined two-phase jet impingement," *International Journal of Heat and Mass Transfer*, vol. 128, no. 0017-9310, pp. 1095-1101, 2019.
- [34] Y. Li, Y. Chen and Z. Liu, "Correlations for boiling heat transfer characteristics of high-velocity circular jet impingement on the nano-characteristic stagnation zone.," *International Journal of Heat and Mass Transfer*, vol. 72, pp. 177-185, 2014.
- [35] M. Monde, K. Kitaguchi, T. Inoue and Y. Mitsutake, "Critical heat flux in a forced convective subcooled boiling with an impinging jet," *Journal of Heat Transfer*, vol. 118, no. 1, pp. 241-243, 1996.
- [36] Y.-h. Qiu and Z.-h. Liu, "Nucleate boiling on the superhydrophilic surface with a small water impingement jet," *International Journal of Heat and Mass Transfer*, vol. 51, no. 7-8, pp. 1683-1690, 2008.
- [37] Z.-H. Liu, T.-F. Tong and Y.-H. Qiu, "Critical heat flux of steady boiling for subcooled water jet impingement on the flat stagnation zone," *Journal of Heat Transfer*, vol. 126, no. 2, pp. 179-183, 2004.
- [38] F. Hong, C. Zhang, W. He, P. Cheng and G. Chen, "Confined jet array impingement boiling of subcooled aqueous ethylene glycol solution," *International Communications in Heat and Mass Transfer*, vol. 56, pp. 165-173, 2014.
- [39] F. Cui, F. Hong and P. Cheng, "Comparison of normal and distributed jet array impingement boiling of HFE-7000 on smooth and pin-fin surfaces," *International Journal of Heat and Mass Transfer*, vol. 126, pp. 1287-1298, 2018.
- [40] S. Narumanchi, A. Troshko, D. Bharathan and V. Hassani, "Numerical simulations of nucleate boiling in impinging jets: Applications in power electronics cooling," *International Journal of Heat and Mass Transfer*, vol. 51, no. 1-2, pp. 1-12, January 2008.
- [41] S. Abishek, R. Narayanaswamy and V. Narayanan, "Effect of heater size and Reynolds number on the partitioning of surface heat flux in subcooled jet impingement boiling," *International Journal of Heat and Mass Transfer*, vol. 59, pp. 247-261, 2013.

- [42] L. Qiu, S. Dubey, F. H. Choo and F. Duan, "Effect of conjugation on jet impingement boiling heat transfer," *International Journal of Heat and Mass Transfer*, vol. 91, no. 0017-9310, pp. 584-593, 2015.
- [43] K. Esmailpour, A. Azizi and S. Hosseinalipour, "Numerical study of jet impingement subcooled boiling on superheated surfaces," *Scientia Iranica*, vol. 26, no. 4, pp. 2369-2381, 2019.
- [44] ANSYS Inc., "ANSYS Fluent Theory Guide," *Release 21.1*, January 2021.
- [45] W. E. Ranz and W. R. Marshall, "Evaporation from drops, Part 1," *Chemical Engineering Progress*, vol. 48, no. 3, pp. 141-146, 1952.
- [46] A. Tomiyama, "Struggle with computational bubble dynamics," in *Third International Conference on Multiphase Flow*, Lyon, France, June 8-12, 1998.
- [47] M. Ishii, "Two-fluid model for two-phase flow," in *Second International Workshop on Two-phase Flow Fundamentals*, RPI, Troy, NY., 1979.
- [48] T. Frank, J. Shi and A. D. Burns, "Validation of Eulerian multiphase flow models for nuclear safety applications," in *Third International Symposium on Two-Phase Flow Modeling and Experimentation*, Pisa, Italy, 2004.
- [49] S. P. Antal, R. T. Lahey and J. E. Flaherty, "Analysis of phase distribution in fully developed laminar bubbly two-phase flow," *International Journal of Multiphase Flow*, vol. 17, no. 5, pp. 635-652, 1991.
- [50] M. Lopez de Bertodano, "Turbulent bubbly flow in a triangular duct," Rensselaer Polytechnic Institute, New York, 1991.
- [51] M. Ishii and K. Mishima, "Two-fluid model and hydrodynamic constitutive relations," *Nuclear Engineering and Design*, vol. 82, no. 2-3, pp. 107-126, 1984.
- [52] L. van Wijngaarden and D. J. Jeffrey, "Hydrodynamic interaction between gas bubbles in liquid," *Journal of Fluid Mechanics*, vol. 77, no. 1, pp. 27-44, 1976.
- [53] E. E. Paladino and C. R. Maliska, "Virtual mass in accelerated bubbly flows," Computational Fluid Dynamics Laboratory, Federal University of Santa Catarina, Florianopolis, 2003.
- [54] A. A. Troshko and Y. A. Hassan, "A two-equation turbulence model of turbulent bubbly flow," *International Journal of Multiphase Flow*, vol. 22, no. 11, pp. 1965-2000, 2001.
- [55] N. Kurul and M. Z. Podowski, "On the modeling of multidimensional effects in boiling channels," in *Proceedings of the 27th National Heat Transfer Conference*, Minneapolis, Minnesota, USA, 1991.
- [56] Y. Egorov and F. Menter, "Experimental implementation of the RPI wall boiling model in CFX-5.6," Technical Report ANSYS/TR-04-10, ANSYS GmbH, 2004.
- [57] V. H. Del Valle and D. Kenning, "Subcooled flow boiling at high heat flux," *International Journal of Heat and Mass Transfer*, vol. 28, no. 10, pp. 1907-1920, 1985.

- [58] R. Cole, "A photographic study of pool boiling in the region of the critical heat flux," *AIChE Journal*, vol. 6, pp. 533-542, 1960.
- [59] M. Lemmert and L. M. Chawla, Influence of flow velocity on surface boiling heat transfer coefficient in Heat Transfer in Boiling. E. Hahne and U. Grigull, Eds., Academic Press and Hemisphere, New York, NY, 1977.
- [60] H. C. Unal, "Maximum bubble diameter, maximum bubble growth time and bubble growth rate during subcooled nucleate flow boiling of water up to 17.7MN/m^2 ," *International Journal of Heat and Mass Transfer*, vol. 19, pp. 643-649, 1976.
- [61] ANSYS Inc., "ANSYS Fluent User's Guide," *Release 21.1*, January 2021.
- [62] F. J. Moraga, R. T. Bonetto and R. T. Lahey, "Lateral forces on spheres in turbulent uniform shear," *International Journal of Multiphase Flow*, vol. 25, pp. 1321-1372, 1999.
- [63] V. Devahdhanush and I. Mudawar, "Critical heat flux of confined round single jet and jet array impingement boiling," *International Journal of Heat and Mass Transfer*, vol. 169, no. 0017-9310, 2021.
- [64] I. H. Bell, J. Wronski, S. Quoilin and V. Lemort, "Pure and pseudo-pure fluid thermophysical property evaluation and the Open-Source Thermophysical Property Library CoolProp," *Industrial & Engineering Chemistry Research*, vol. 53, no. 6, pp. 2498-2508, 2014.

Appendix A: Influence of Virtual Mass Coefficient

The influence of the virtual mass coefficient used in equation (38) on the average surface temperature and the stagnation region surface temperature for the single axisymmetric jet not considering conjugation are summarised in Table A - 1. Both the stagnation region surface temperature and the average surface temperature increase with increasing virtual mass coefficient. For the current case, the numerical results approach the experimental results for increasing virtual mass coefficient. However, the smaller error should not be considered to be an improvement, since the case considering conjugation may move further away from the experimental results for increasing virtual mass coefficient, due to the higher surface temperature predicted compared to the case without conjugation for $C_{VM} = 0.5$.

Table A - 1: Influence of virtual mass coefficient on wall temperature for the single axisymmetric jet without conjugation, at 50 W/cm².

Virtual Mass Coefficient	Stagnation Region Surface Temperature [°C]	Average Surface Temperature [°C]
0	111.67	113.67
0.25	111.70	113.77
0.5	111.74	113.87
0.75	111.79	114.08
1	111.86	114.19
1.25	111.95	114.43
1.5	112.06	114.55
Experimental	115.01	-

The influence of the virtual mass coefficient used in equation (38) on the vapour bubbles is illustrated in Figure A - 1 for the single axisymmetric jet not considering conjugation. The virtual mass coefficient has a significant influence on the vapour bubble shape and size as well as the maximum vapour volume fraction. The maximum vapour volume fraction is the lowest for the case neglecting the virtual mass force, that is $C_{VM} = 0$, and remains close to constant for $C_{VM} \geq 0.5$. The influence of the liquid jet on the vapour clouds is seen to be highly dependent on the virtual mass coefficient, which could have a significant influence on the rewetting of the surface. It is therefore expected that the choice of the virtual mass coefficient could have a significant influence in the prediction of the CHF. Since no information regarding the vapour bubbles is available from the experiment of Katto and Kunihiro [28], the bubble shapes in Figure A - 1 provide little information about the correct virtual mass coefficient. Therefore, all other results in this dissertation used a virtual mass coefficient of 0.5, corresponding to spherical bubbles according to the literature.

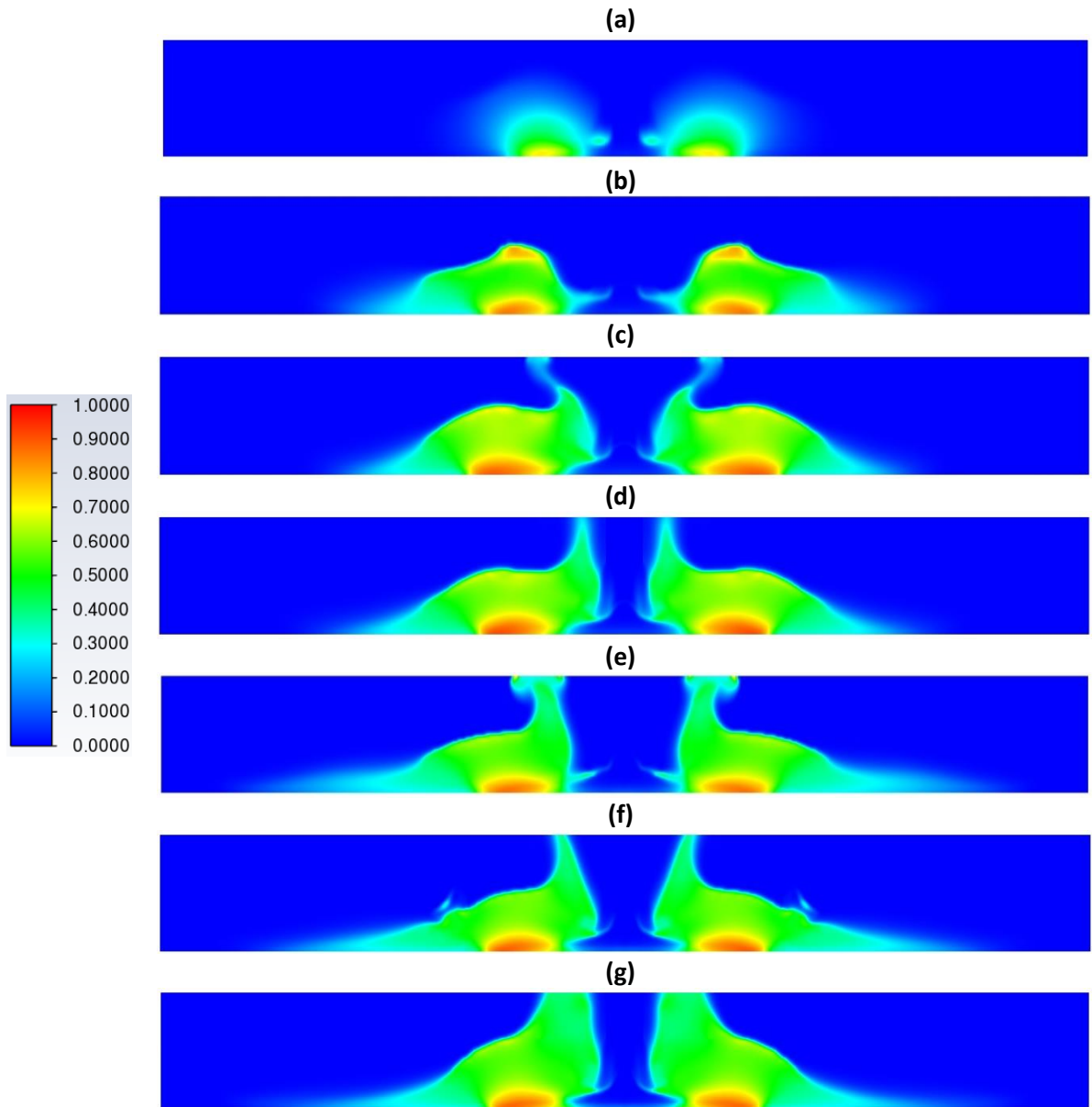


Figure A - 1: Vapour volume fraction contours for the single axisymmetric jet not considering conjugation for various virtual mass coefficients: (a) $C_{VM} = 0$, (b) $C_{VM} = 0.25$, (c) $C_{VM} = 0.5$, (d) $C_{VM} = 0.75$, (e) $C_{VM} = 1$, (f) $C_{VM} = 1.25$, and (g) $C_{VM} = 1.5$.

Appendix B: Surface Temperature and Heat Flux Contours for 3D Multijet Array Without Considering Conjugation

Figures A - 2 (a) to (c) show the heated surface wall temperature contours of the multijet array case not considering conjugation alongside the surface heat flux contours, for increasing wall heat fluxes. For ease of comparison to the case considering conjugation, the same contours for the case considering conjugation are shown again in Figures A - 3 (a) to (c), for increasing wall heat fluxes. Like the case considering conjugation, the surface temperature for the case not considering conjugation was a minimum in the stagnation regions between the jets and in the jet centres. The minimum surface temperatures were significantly lower for the case not considering conjugation, shown in Figures A - 2 (a) to (c), than the case considering it, shown in Figures A - 3 (a) to (c), at all heat fluxes. The lower minimum surface temperatures were due to the uniform heat flux for the case not considering conjugation, resulting in a lower local heat flux than the case considering conjugation. As for the case considering conjugation, the maximum surface temperature for the case not considering conjugation occurred in the wall jet regions. The maximum surface temperatures were significantly higher for the case not considering conjugation, shown in Figures A - 2 (a) to (c), than the case considering it, shown in Figures A - 3 (a) to (c), at all heat fluxes. The higher maximum surface temperatures were due to the uniform heat flux for the case not considering conjugation, resulting in a higher local heat flux in the wall jet regions than the case considering conjugation.

The surface heat flux for the insulation was zero for the case not considering conjugation as shown in Figures A - 2 (a) to (c), whereas the surface heat flux for the insulation was nonzero for the case considering conjugation, shown in Figures A - 3 (a) to (c). The difference between the local surface heat flux of the insulation for the two cases was due to the heat spreading from the copper block to the surrounding insulation in the case considering conjugation. The lower surface temperature variation and heat spreading for the case considering conjugation, highlighted the importance of considering the effects of conjugate heat transfer when the heating block used in the experiment had significant thermal mass.

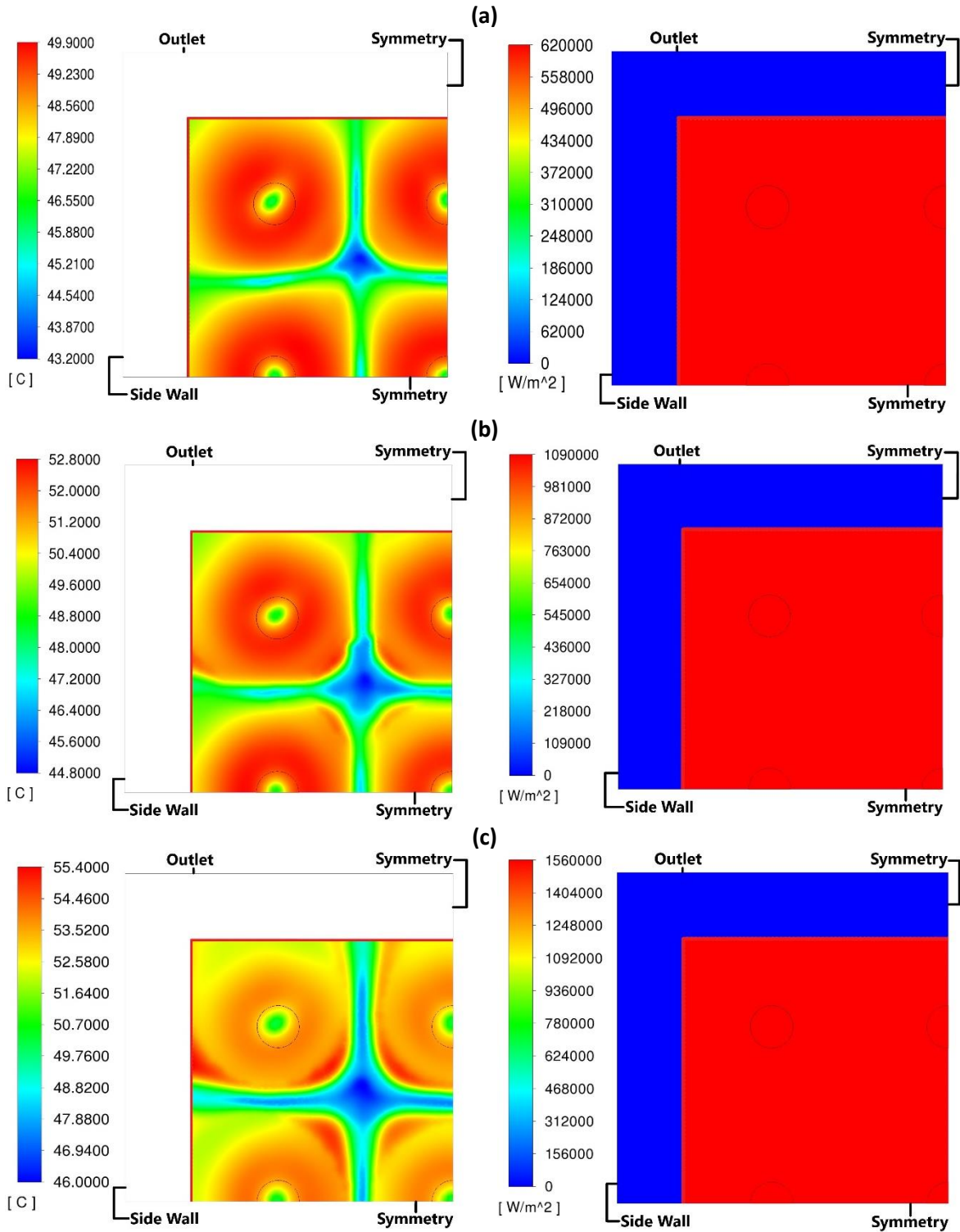


Figure A - 2: Heated surface temperature contours [°C] (Left) and surface heat flux contours [W/m²] (Right) of the multi-jet array without considering conjugation, using R134a as heat transfer fluid, at various wall heat fluxes: (a) 62 W/cm², (b) 109 W/cm², and (c) 156 W/cm².

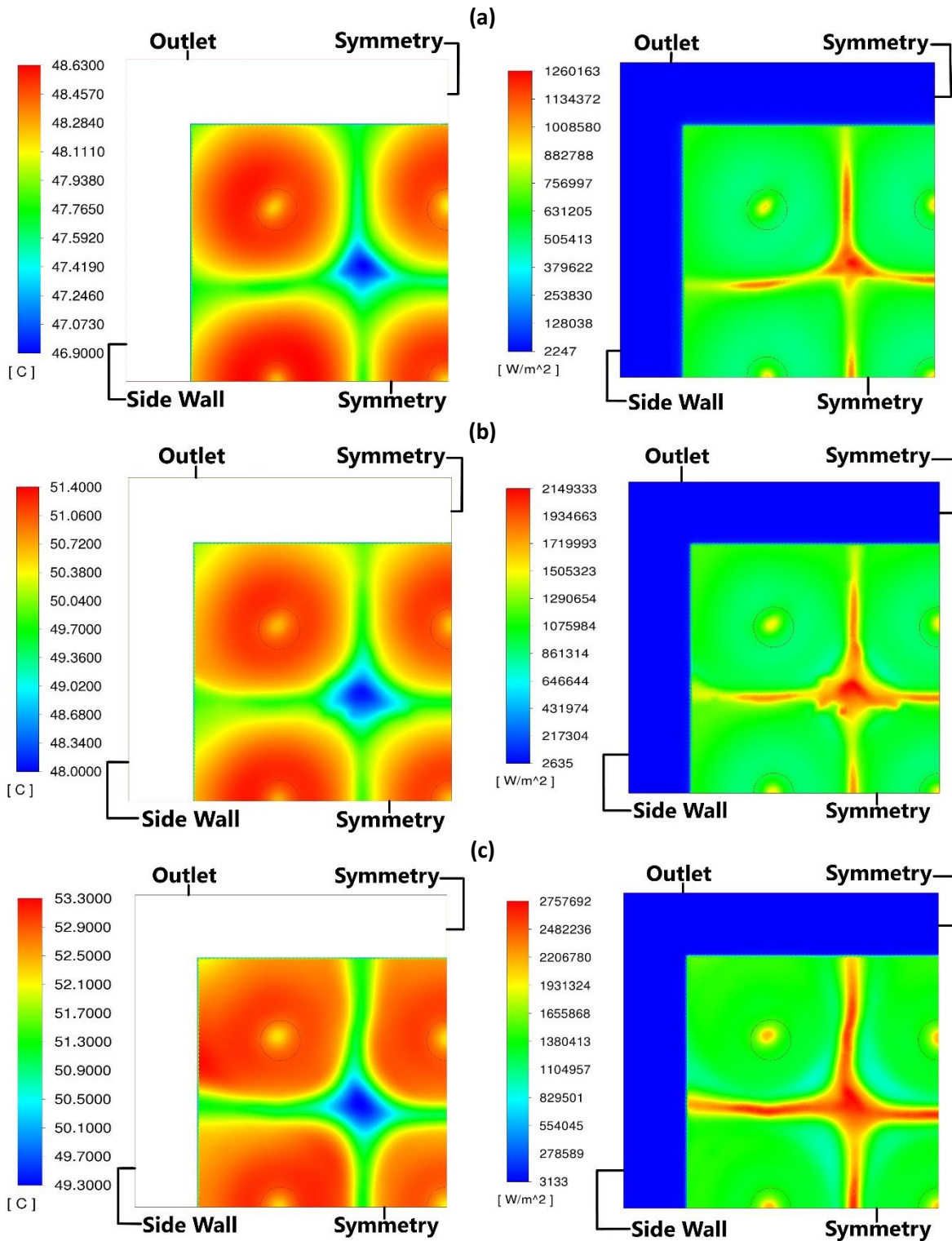


Figure A - 3: Heated surface temperature contours [°C] (Left) and surface heat flux contours [W/m²] (Right) of the multi-jet array considering conjugation, using R134a as heat transfer fluid, at various wall heat fluxes: (a) 62 W/cm², (b) 109 W/cm², and (c) 156 W/cm².

Appendix C: Numerical Procedure

Body forces play a dominant role in the governing equations in multi-phase flow, so to ensure optimal solution stability, the body forces must be solved implicitly. This is achieved by using the following Text User Interface (TUI) command:

```
solve/set/numerics yes yes yes 1
```

where, the first “yes” is to solve the body forces implicitly, the second to solve rotating frame problems using absolute velocities (Fluent default), and the third to limit the PRESTO! scheme to first-order terms. The last input (1 in this case) is the 1st-order to higher-order blending factor and can range from 0 to 1. It is important to note that to solve the virtual mass force implicitly, the Virtual Mass Implicit tick box (not ticked by default) must be selected in the Phase Interaction tab of the Eulerian Multiphase model.

Even though the body forces and the virtual mass force are solved implicitly, numerical stability issues may still exist. To alleviate the numerical stability issues, truncated forms of the virtual mass force must be used in cells where convergence issues are present. This is achieved by selecting the Virtual Mass Implicit Option 2, in the Phase Interaction tab of the Eulerian Multiphase model.

Since the thermal properties and density of the multiphase mixture are highly dependent on the fluid temperature and phase compositions (liquid and vapour volume fractions), drastic variations in the mixture properties occur during phase change, which can result in drastic fluctuations in the heat transfer. To limit these fluctuations, a numerical noise filter is applied to the energy equation using the following TUI command:

```
solve/set/advanced/energy – numerical – noise – filter yes
```

Unfortunately, no information regarding how the numerical noise filter is applied in Fluent is available, however, significant improvement in the results as well as numerical stability were observed when the filter was applied.

For cases where the volume fraction equation and vapour momentum equations struggle to converge, increasing the number of smoothing sweeps for the vapour node-based smoothing and reducing the smoothing relaxation factor can help alleviate convergence issues. This is achieved with the following TUI command,

```
solve/set/surface – tension yes 4 1 yes
```

where, the first “yes” enables node-based smoothing (essential for tetrahedral and polyhedral meshes), 4 represents the number of smoothing sweeps (ranging between 1 and 5), 1 represents the smoothing relaxation factor (ranging between 0 and 1), and the last “yes” enables the use of VOF gradients at the nodes for curvature calculation (essential for tetrahedral and polyhedral meshes).

Although enabled by default in ANSYS Fluent 2021 R1, it is important to take into account the local liquid volume fraction in the RPI boiling model convective and quenching heat flux equations. This is achieved by using the following TUI command:

```
solve/set/multiphase – numeric/boiling – parameters/liquid – vof – factor yes
```


For cases where the bad quality cells are present in the domain, convergence difficulties may be experienced, especially in the turbulence equations. In such cases it is important to enable the poor mesh numerics option in ANSYS Fluent by using the following TUI commands:

solve/set/poor – mesh – numerics/solution – and – quality – based? yes 0.2 5

solve/set/poor – mesh – numerics/enable? yes 1

solve/set/poor – mesh – numerics/cell – quality – based? yes

solve/set/poor – mesh – numerics/gradient – quality – based? yes 0.2

By enabling these options, Fluent solves alternative forms of the governing equations to improve convergence and stability in the bad cells. It should be noted that should the computational grid contain many bad cells, remeshing may be the best decision for optimal results. It should be noted that in cases where tetrahedral or polyhedral cells are used, or in cases where the cells have aspect ratios larger than 10, the Warped-Face Gradient Correction option must be enabled in the methods tab of Fluent.

For Eulerian multiphase simulations, it is suggested that the multigrid solver settings are adjusted as follows. The pressure multigrid cycle should be set to F-Cycle and the termination criteria should be dropped two orders of magnitude to 0.001, the number of post-sweeps for the scalar parameters should be increased to 2 sweeps, while the number of post-sweeps for the coupled parameters should be increased to 3 sweeps. When the coarsen by factor is increased beyond 2, it is suggested that the aggressive coarsening model should be used. These settings are changed in the Advanced options under the Controls tab in Fluent. The optimal under-relaxation factors found for the present study are summarised in Table A - 2.

Table A - 2: Under-relaxation factors used in the present study.

Parameter	Suggested Under-Relaxation Factor
Pressure	0.6
Density	0.6
Body Forces	1
Momentum	0.2
Vaporization Mass	1
Volume Fraction	0.3
Turbulent Kinetic Energy	0.3
Turbulent Dissipation Rate	0.3
Turbulent Viscosity	0.6
Energy	0.95

Appendix D: Data Processing

The numerical results in this study were processed using the code presented in this section. The data from Fluent were written to a Fluent report file. The Fluent report files were then imported to Matlab and saved as matrices for easier processing.

Data Processing Code for 2D Axisymmetric Jet

The raw simulation data for the 2D axisymmetric jets were then time-averaged and processed to obtain the required results using the Matlab code in Figure A - 4 for the case not considering conjugation and the Matlab code in Figure A - 5 for the case considering conjugation. After the results were time-averaged and processed, the results were plotted with the Matlab code in Figure A - 6. The results of the single jet parametric study were also analysed using the Matlab code in Figure A - 5, however the 3D contours presented in Figure 56 were created using the Python code shown in Figure A - 7. The 3D contours were created in Python rather than Matlab Due to the superior quality 3D contours of matplotlib in Python, compared to matplotlib in Matlab.

```
function
[flowtime,T_stag_data,T_avg_data,T_max_data,T_min_data,q_conv_data,q_quen
ch_data,q_evap_data,q_tot_data...
,T_stag,T_avg,T_max,T_min,q_conv,q_quench,q_evap,q_tot,q_conv_cont,q_que
nch_cont,q_evap_cont,q_tot_cont] =
Results_Processing_Without_Conjugation(FILENAME,N)

Loading Fluent report output file

load(FILENAME);
time_step = SimulationResults(:,1);
flowtime = SimulationResults(:,2);
T_stag_data = SimulationResults(:,3) - 273.15;
T_avg_data = SimulationResults(:,4) - 273.15;
T_max_data = SimulationResults(:,5) - 273.15;
T_min_data = SimulationResults(:,6) - 273.15;
q_conv_data = SimulationResults(:,7)/10000;
q_quench_data = SimulationResults(:,8)/10000;
q_evap_data = SimulationResults(:,9)/10000;
q_tot_data = SimulationResults(:,10)/10000;
clear SimulationResults
n = floor(length(time_step)/N);

Creating output matrices

T_stag = zeros(n,1); T_avg = zeros(n,1); T_max = zeros(n,1); T_min =
zeros(n,1);
q_conv = zeros(n,1); q_quench = zeros(n,1); q_evap = zeros(n,1);
q_tot = zeros(n,1);

Filling output matrices with time-averaged results (unvectorized code)
for i=1:n
T_stag(i,1) = mean(T_stag_data(((i-1)*N + 1):(i*N)));
T_avg(i,1) = mean(T_avg_data(((i-1)*N + 1):(i*N)));
T_max(i,1) = mean(T_max_data(((i-1)*N + 1):(i*N)));
T_min(i,1) = mean(T_min_data(((i-1)*N + 1):(i*N)));
q_conv(i,1) = mean(q_conv_data(((i-1)*N + 1):(i*N)));
q_quench(i,1) = mean(q_quench_data(((i-1)*N + 1):(i*N)));
q_evap(i,1) = mean(q_evap_data(((i-1)*N + 1):(i*N)));
q_tot(i,1) = mean(q_tot_data(((i-1)*N + 1):(i*N)));
end
```

Determining average HTC and contributions of heat flux components

```

j = 3:n;
q_conv_cont = q_conv(j) ./max(q_tot(j),q_conv(j));
q_quench_cont = q_quench(j) ./max(q_tot(j),q_conv(j));
q_evap_cont = q_evap(j) ./max(q_tot(j),q_conv(j));
q_tot_cont = q_tot(j);
end

```

Figure A - 4: Data processing Matlab code for single axisymmetric jet without conjugation.

```

function
[q_tot,q_quench,q_conv,q_evap,T_avg,T_max,T_min,T_stag,h_avg,Flow_Time,q
_q_cont,q_e_cont,q_c_cont,q_t,Tavg,Tmax,Tstag] =
Results_Processing(FILENAME,T_in,N_heat,N_avg)

```

Loading Fluent report output file

```

load(FILENAME)
W_m2_to_W_cm2 = 1/10000;
Kelvin_to_Celcius = -273.15;
Time_Step = SimulationResults(:,1);
Flow_Time = SimulationResults(:,2);
q_q = SimulationResults(:,8)*W_m2_to_W_cm2;
Tmax = SimulationResults(:,5) + Kelvin_to_Celcius;
Tmin = SimulationResults(:,6) + Kelvin_to_Celcius;
Tavg = SimulationResults(:,4) + Kelvin_to_Celcius;
q_e = SimulationResults(:,9)*W_m2_to_W_cm2;
q_t = SimulationResults(:,10)*W_m2_to_W_cm2;
Tstag = SimulationResults(:,3) + Kelvin_to_Celcius;
q_c = q_t - q_e - q_q;
q_q_c = q_q./q_t; q_e_c = q_e./q_t; q_c_c = q_c./q_t;
clear simulationresults
n = floor(length(Time_Step)/(N_heat + N_avg));

```

Creating output matrices

```

q_quench = zeros(n,1); q_tot = zeros(n,1); q_evap = zeros(n,1);
q_conv = zeros(n,1);
q_q_cont = zeros(n,1); q_c_cont = zeros(n,1); q_e_cont = zeros(n,1);
T_max = zeros(n,1); T_avg = zeros(n,1); T_stag = zeros(n,1); T_min =
zeros(n,1);

```

Filling output matrices with time-averaged results (unvectorized code)

```

for i=1:n
q_tot(i) = mean(q_t(((i-1)*(N_heat + N_avg) + N_heat +
1):((i)*(N_heat + N_avg))));
q_quench(i) = mean(q_q(((i-1)*(N_heat + N_avg) + N_heat +
1):((i)*(N_heat + N_avg))));
q_evap(i) = mean(q_e(((i-1)*(N_heat + N_avg) + N_heat +
1):((i)*(N_heat + N_avg))));
T_avg(i) = mean(Tavg(((i-1)*(N_heat + N_avg) + N_heat +
1):((i)*(N_heat + N_avg))));
T_max(i) = mean(Tmax(((i-1)*(N_heat + N_avg) + N_heat +
1):((i)*(N_heat + N_avg))));
T_min(i) = mean(Tmin(((i-1)*(N_heat + N_avg) + N_heat +
1):((i)*(N_heat + N_avg))));
T_stag(i) = mean(Tstag(((i-1)*(N_heat + N_avg) + N_heat +
1):((i)*(N_heat + N_avg))));
q_conv(i) = mean(q_c(((i-1)*(N_heat + N_avg) + N_heat +
1):((i)*(N_heat + N_avg))));
q_q_cont(i) = mean(q_q_c(((i-1)*(N_heat + N_avg) + N_heat +
1):((i)*(N_heat + N_avg))));
q_c_cont(i) = mean(q_c_c(((i-1)*(N_heat + N_avg) + N_heat +
1):((i)*(N_heat + N_avg))));

```

```

q_e_cont(i) = mean(q_e_c(((i-1)*(N_heat + N_avg) + N_heat +
1):(i)*(N_heat + N_avg))));
end

```

Determining average HTC

```

h_avg = q_tot./(T_avg - T_in);
end

```

Figure A - 5: Data processing Matlab code for single axisymmetric jet with conjugation.

```

clear all
clc

```

Without Conjugation

```

[flowtime,T_stag_data,T_avg_data,T_max_data,T_min_data,q_conv_data,q_que
nch_data,q_evap_data,q_tot_data...,T_stag,T_avg,T_max,T_min,q_conv,q_que
nch,q_evap,q_tot,q_conv_cont,q_quench_cont,q_evap_cont,q_tot_cont]...
=Results_Processing_Without_Conjugation("Full_boiling_curve_NC",30000);

```

With Conjugation

```

[q_tot_c,q_quench_c,q_conv_c,q_evap_c,T_avg_c,T_max_c,T_min_c,T_stag_c,h
_avg_c,Flow_Time_c,q_q_cont_c,q_e_cont_c,q_c_cont_c,q_t_data,Tavg_data,T
max_data,Tstag_data]
=Results_Processing("Full_boiling_curve",97,50000,10000);

```

Experimental Results

```

load Validation_data

```

Plots

Boiling Curve

```

figure(1)
clf
loglog(T_exp,q_exp,"o",'MarkerEdgeColor','r','MarkerFaceColor','r',"Mark
erSize",12)
hold on
plot(T_Qiu,q_Qiu,"s",'MarkerEdgeColor','k','MarkerFaceColor','k',"Marker
Size",12)
plot(T_nar,q_nar,"^",'MarkerEdgeColor','b',"MarkerSize",12)
plot((T_stag(3:end)-100),q_tot(3:end),"-c^","MarkerSize",10)
plot((T_stag_c(2:end)-100),q_tot_c(2:end),"-
m^",'MarkerEdgeColor','m','MarkerFaceColor','m',"MarkerSize",10)
hold off
xticks([3,6,9,12,15,21,27,33])
xticklabels([3,6,9,12,15,21,27,33])
yticks([10,50,100,300])
yticklabels([10,50,100,300])
axis([3,33,10,300])
a = get(gca,'XTickLabel');
set(gca,'XTickLabel',a,'fontsize',14)
xlabel("Stagnation Region Wall Superheat [" + string(char(176)) +
"C]", "fontsize",14)
ylabel("Wall Heat Flux [W/cm^2]", "fontsize",14)
legend("Experimental (With Conjugation)","Qiu et al. (With
Conjugation)","Narumanchi et al. (Without Conjugation)"...
,"Current Study (Without Conjugation)","Current Study (With
Conjugation)","location","northwest","fontsize",14)

```

Boiling Curve Illustrating the Effects of Conjugation

```

figure(2)
clf
loglog((T_min(3:end)-
100),q_tot(3:end),">",'MarkerEdgeColor','c',"MarkerSize",10)
hold on

```



```
plot((T_stag_c(2:end)-  
100),q_tot_c(2:end),">","MarkerEdgeColor","m","MarkerFaceColor","m","Mar  
kerSize",10)  
plot((T_avg(3:end)-  
100),q_tot(3:end),"s","MarkerEdgeColor","c","MarkerSize",10)  
plot((T_avg_c(2:end)-  
100),q_tot_c(2:end),"s","MarkerEdgeColor","m","MarkerFaceColor","m","Mar  
kerSize",10)  
plot((T_max(3:end)-  
100),q_tot(3:end),"<","MarkerEdgeColor","c","MarkerSize",10)  
plot((T_max_c(2:end)-  
100),q_tot_c(2:end),"<","MarkerEdgeColor","m","MarkerFaceColor","m","Mar  
kerSize",10)  
hold off  
xticks([3,6,9,12,15,21,27,33])  
xticklabels([3,6,9,12,15,21,27,33])  
yticks([10,50,100,300])  
yticklabels([10,50,100,300])  
axis([3,33,10,300])  
a = get(gca,'XTickLabel');  
set(gca,'XTickLabel',a,'fontsize',14)  
xlabel("Wall Superheat [" + string(char(176)) + "C]","fontsize",14)  
ylabel("Wall Heat Flux [W/cm^2]","fontsize",14)  
legend("T_{min} (Without Conjugation)", "T_{min} (With  
Conjugation)", "T_{avg} (Without Conjugation)"...  
,"T_{avg} (With Conjugation)", "T_{max} (Without  
Conjugation)", "T_{max} (With  
Conjugation)","location","northwest","fontsize",14)
```

Contributions of RPI Wall Boiling Model Heat Flux Components

```
figure(3)  
clf  
plot(q_nom_Qiu,q_evap_Qiu,"ks-  
","MarkerEdgeColor","k","MarkerFaceColor","k","MarkerSize",10)  
hold on  
plot(q_nom_Qiu,q_quench_Qiu,"ko-  
","MarkerEdgeColor","k","MarkerFaceColor","k","MarkerSize",10)  
plot(q_nom_Qiu,q_conv_Qiu,"k^-  
","MarkerEdgeColor","k","MarkerFaceColor","k","MarkerSize",10)  
plot(q_tot_cont,q_evap_cont,"cs-",q_tot_cont,q_quench_cont,"co-  
",q_tot_cont,q_conv_cont,"c^-","MarkerSize",10)  
plot(q_tot_c(2:end),q_e_cont_c(2:end),"ms-  
",q_tot_c(2:end),q_q_cont_c(2:end),"mo-  
",q_tot_c(2:end),q_c_cont_c(2:end),"m^-  
","MarkerFaceColor","m","MarkerSize",10)  
hold off  
axis([10,250,-0.05,1])  
set(gca,'XTickLabel',a,'fontsize',14)  
xlabel("Wall Heat Flux [W/cm^2]","fontsize",14)  
ylabel("Contribution Fraction to Wall Heat Flux","fontsize",14)  
legend("q_E Qiu et al. (With Conjugation)","q_Q Qiu et al. (With  
Conjugation)","q_C Qiu et al. (With Conjugation)","q_E Current Study  
(Without Conjugation)"...  
,"q_Q Current Study (Without Conjugation)","q_C Current Study  
(Without Conjugation)","q_E Current Study (With Conjugation)"...  
,"q_Q Current Study (With Conjugation)","q_C Current Study (With  
Conjugation)","location","east","fontsize",14)
```

Wall Heat Flux and Wall Temperature vs Flowtime (Without Conjugation)

```
figure(4)
clf
plot(flowtime,T_stag_data - 100)
hold on
plot(flowtime,T_avg_data - 100)
yyaxis right
plot(flowtime,max(q_tot_data,q_conv_data),"b-")
hold off
xlabel("Flowtime [s]","fontsize",14)
yyaxis left
ylabel("Wall Superheat [" + string(char(176)) + "C]","fontsize",14)
yyaxis right
ylabel("Wall Heat Flux [W/cm^2]","fontsize",14)
legend("T_{Stagnation Region}","T_{Heated Surface Average}","Wall Heat Flux","location","northwest","fontsize",14)
ax = gca;
ax.YColor = 'k'; %Red
ax.YColor = 'b'; %Blue
a = get(gca,'XTickLabel');
set(gca,'XTickLabel',a,'fontsize',14)
```

Wall Heat Flux and Wall Temperature vs Flowtime (With Conjugation)

```
figure(5)
clf
plot(Flow_Time_c,Tstag_data - 100)
hold on
plot(Flow_Time_c,Tavg_data - 100)
yyaxis right
plot(Flow_Time_c,q_t_data,"b-")
hold off
xlabel("Flowtime [s]","fontsize",14)
yyaxis left
ylabel("Wall Superheat [" + string(char(176)) + "C]","fontsize",14)
yyaxis right
ylabel("Wall Heat Flux [W/cm^2]","fontsize",14)
legend("T_{Stagnation Region}","T_{Heated Surface Average}","Wall Heat Flux","location","northwest","fontsize",14)
ax = gca;
ax.YColor = 'k'; %Red
ax.YColor = 'b'; %Blue
a = get(gca,'XTickLabel');
set(gca,'XTickLabel',a,'fontsize',14)
```

Figure A - 6: Matlab code for plots of the single axisymmetric jet.

```
import numpy as np
```

Meshgrid of H/D

```
H_D = np.array([[1,2,4,8],
                [1,2,4,8],
                [1,2,4,8]])
```

Meshgrid of Reynolds Numbers

```
Re = np.array([[30000,30000,30000,30000],
               [40000,40000,40000,40000],
               [50000,50000,50000,50000]])
```

Meshgrid of Total HTC (Extracted From Processing Code)

```
HTC_Tot = np.array([[32.2537,34.5091,37.4803,40.1903],
                   [32.0740,33.5383,35.3797,37.9457],
                   [31.9043,32.7666,34.1155,36.0293]])
```

Meshgrid of Quenching HTC (Extracted From Processing Code)

```
HTC_Quench = np.array([[2.7879,3.0085,2.8511,2.3991],
                       [3.1852,3.4355,3.3355,2.9076],
                       [3.4697,3.6855,3.6202,3.3071]])
```

Meshgrid of Evaporative HTC (Extracted From Processing Code)

```
HTC_Evap = np.array([[29.4658,31.5006,34.6292,37.7911],
                     [28.8888,30.1028,32.0442,35.0381],
                     [28.4346,29.0810,30.4953,32.7222]])
```

Contour Plots

```
%matplotlib qt5
from matplotlib import pyplot as plt
from matplotlib import cm
```

Total HTC

```
fig1, ax1 = plt.subplots(subplot_kw={"projection": "3d"})
surf1 = ax1.plot_surface(H_D[0:4,0:4], Re[0:4,0:4], HTC_Tot[0:4,0:4], cmap = 'autumn_r',
edgecolor="black")
ax1.set_xlabel("H/D",fontsize=12)
ax1.set_ylabel("Jet Reynolds Number",fontsize=12)
ax1.set_zlabel("$HTC_{Total}$" + " " + "$[kW/(m^2K)]$",fontsize=12)
ax1.set_xlim(0.5,4)
ax1.set_ylim(29000,51000)
ax1.set_xticks([1,2,4,8])
ax1.set_yticks([30000,40000,50000])
plt.show()
```

Quenching HTC

```
fig2, ax2 = plt.subplots(subplot_kw={"projection": "3d"})
surf2 = ax2.plot_surface(H_D[0:4,0:4], Re[0:4,0:4], HTC_Quench[0:4,0:4], cmap = 'autumn_r',
edgecolor="black")
ax2.set_xlabel("H/D",fontsize=12)
ax2.set_ylabel("Jet Reynolds Number",fontsize=12)
ax2.set_zlabel("$HTC_{Quenching}$" + " " + "$[kW/(m^2K)]$",fontsize=12)
ax2.set_xlim(0.5,4)
ax2.set_ylim(29000,51000)
ax2.set_xticks([1,2,4,8])
ax2.set_yticks([30000,40000,50000])
plt.show()
```

Evaporative HTC

```
fig3, ax3 = plt.subplots(subplot_kw={"projection": "3d"})
surf3 = ax3.plot_surface(H_D[0:4,0:4], Re[0:4,0:4], HTC_Evap[0:4,0:4], cmap = 'autumn_r',
edgecolor="black")
ax3.set_xlabel("H/D",fontsize=12)
ax3.set_ylabel("Jet Reynolds Number",fontsize=12)
ax3.set_zlabel("$HTC_{Evaporation}$" + " " + "$[kW/(m^2K)]$",fontsize=12)
ax3.set_xlim(0.5,4)
ax3.set_ylim(29000,51000)
ax3.set_xticks([1,2,4,8])
ax3.set_yticks([30000,40000,50000])
plt.show()
```

Figure A - 7: Python code for contours of the single axisymmetric jet parametric study.

Matlab Data Processing Code for 3D Jet Array

The raw simulation data for the 3D multijet arrays were then time-averaged and processed to obtain the required results using the Matlab code in Figure A - 8 for the case not considering conjugation and the Matlab code in Figure A - 9 for the case considering conjugation. After the results were time-averaged and processed, the results were plotted with the Matlab code in Figure A - 10. The results of the multijet array parametric study were also analysed using the Matlab code in Figure A - 9, however the 3D contours presented in Figure 64 were created using the Python code shown in Figure A - 11. Again, the 3D contours were created in Python rather than Matlab Due to the superior quality 3D contours of matplotlib in Python, compared to matplotlib in Matlab.

```
function
[q_tot,q_quench,q_conv,q_evap,T_avg,T_calc,q_liquid,q_vapour,h_avg,h_avg
_calc,q_conv_cont,...
q_quench_cont,q_evap_cont,q_tot_cont,Flow_Time,T_min,T_max,q_t,Tavg,q_li
q] = Results_Processing_no_conjugation(FILENAME,T_in,N_heat,N_avg)

Loading Fluent Report Output File

load(FILENAME)
W_m2_to_W_cm2 = 1/10000;
Kelvin_to_Celcius = -273.15;
Time_Step = SimulationResults(:,1);
Flow_Time = SimulationResults(:,13);
Tavg = SimulationResults(:,8) + Kelvin_to_Celcius;
Tcalc = SimulationResults(:,9);
q_t = SimulationResults(:,2).*W_m2_to_W_cm2;
q_e = SimulationResults(:,3).*W_m2_to_W_cm2;
q_q = SimulationResults(:,4).*W_m2_to_W_cm2;
q_liq = SimulationResults(:,5).*W_m2_to_W_cm2;
q_vap = SimulationResults(:,6).*W_m2_to_W_cm2;
max_vap_vof = SimulationResults(:,7);
Tmin = SimulationResults(:,15) + Kelvin_to_Celcius;
Tmax = SimulationResults(:,14) + Kelvin_to_Celcius;
clear simulationresults
n = floor(length(Time_Step)/(N_heat + N_avg));
```


Creating output matrices

```
q_quench = zeros(n,1); q_tot = zeros(n,1); q_evap = zeros(n,1);
q_liquid = zeros(n,1); T_calc = zeros(n,1);
T_avg = zeros(n,1); max_vapour_vof = zeros(n,1); q_vapour =
zeros(n,1); T_max = zeros(n,1);
T_min = zeros(n,1);
```

Filling output matrices with time-averaged results (unvectorized code)

```
for i=1:n
    q_tot(i) = mean(q_t(((i-1)*(N_heat + N_avg) + N_heat +
1):((i)*(N_heat + N_avg))));
    q_quench(i) = mean(q_q(((i-1)*(N_heat + N_avg) + N_heat +
1):((i)*(N_heat + N_avg))));
    q_evap(i) = mean(q_e(((i-1)*(N_heat + N_avg) + N_heat +
1):((i)*(N_heat + N_avg))));
    q_liquid(i) = mean(q_liq(((i-1)*(N_heat + N_avg) + N_heat +
1):((i)*(N_heat + N_avg))));
    q_vapour(i) = mean(q_vap(((i-1)*(N_heat + N_avg) + N_heat +
1):((i)*(N_heat + N_avg))));
    T_avg(i) = mean(Tavg(((i-1)*(N_heat + N_avg) + N_heat +
1):((i)*(N_heat + N_avg))));
    T_calc(i) = mean(Tcalc(((i-1)*(N_heat + N_avg) + N_heat +
1):((i)*(N_heat + N_avg))));
    T_min(i) = mean(Tmin(((i-1)*(N_heat + N_avg) + N_heat +
1):((i)*(N_heat + N_avg))));
    T_max(i) = mean(Tmax(((i-1)*(N_heat + N_avg) + N_heat +
1):((i)*(N_heat + N_avg))));
    max_vapour_vof(i) = mean(max_vap_vof(((i-1)*(N_heat + N_avg) +
N_heat + 1):((i)*(N_heat + N_avg))));
end
```

Determining average HTC and contributions of heat flux components

```
q_conv = q_tot - q_evap - q_quench;
h_avg = (q_tot./W_m2_to_W_cm2)./(T_avg - T_in);
h_avg_calc = (q_tot./W_m2_to_W_cm2)./(T_calc - T_in);
j = 1:n;
q_conv_cont = q_conv(j)./max(q_tot(j),q_conv(j));
q_quench_cont = q_quench(j)./max(q_tot(j),q_conv(j));
q_evap_cont = q_evap(j)./max(q_tot(j),q_conv(j));
q_tot_cont = max(q_tot(j),q_conv(j));
end
```

Figure A - 8: Data processing Matlab code for multi-jet array without conjugation.

```
function
[q_tot,q_quench,q_conv,q_evap,T_avg,q_input,h_avg,Flow_Time,T_min,T_max,
T_calc,max_vapour_vof,q_conv_c ...
,q_quench_c,q_evap_c,q_tot_c,q_t,Tavg,q_liq] =
Results_Processing(FILENAME,T_in,N_heat,N_avg)
```

Loading Fluent report output file

```
load(FILENAME)
W_m2_to_W_cm2 = 1/10000;
Kelvin_to_Celcius = -273.15;
Time_Step = SimulationResults(:,1);
Flow_Time = SimulationResults(:,13);
Tavg = SimulationResults(:,8) + Kelvin_to_Celcius;
Tcalc = SimulationResults(:,9);
q_in = SimulationResults(:,14).*W_m2_to_W_cm2;
q_t = SimulationResults(:,2).*W_m2_to_W_cm2;
```

```

q_e = SimulationResults(:,3).*W_m2_to_W_cm2;
q_q = SimulationResults(:,4).*W_m2_to_W_cm2;
q_liq = SimulationResults(:,5).*W_m2_to_W_cm2;
q_vap = SimulationResults(:,6).*W_m2_to_W_cm2;
max_vap_vof = SimulationResults(:,7);
Tmax = SimulationResults(:,15) + Kelvin_to_Celcius;
Tmin = SimulationResults(:,16) + Kelvin_to_Celcius;
clear simulationresults
n = floor(length(Time_Step)/(N_heat + N_avg));

Creating output matrices
q_quench = zeros(n,1); q_tot = zeros(n,1); q_evap = zeros(n,1);
q_liquid = zeros(n,1); T_calc = zeros(n,1);
q_input = zeros(n,1); T_avg = zeros(n,1); max_vapour_vof =
zeros(n,1); q_vapour = zeros(n,1); T_max = zeros(n,1);
T_min = zeros(n,1);

Filling output matrices with time-averaged results (unvectorized code)
for i=1:n
    q_input(i) = mean(q_in(((i-1)*(N_heat + N_avg) + N_heat +
1):((i)*(N_heat + N_avg))));
    q_tot(i) = mean(q_t(((i-1)*(N_heat + N_avg) + N_heat +
1):((i)*(N_heat + N_avg))));
    q_quench(i) = mean(q_q(((i-1)*(N_heat + N_avg) + N_heat +
1):((i)*(N_heat + N_avg))));
    q_evap(i) = mean(q_e(((i-1)*(N_heat + N_avg) + N_heat +
1):((i)*(N_heat + N_avg))));
    q_liquid(i) = mean(q_liq(((i-1)*(N_heat + N_avg) + N_heat +
1):((i)*(N_heat + N_avg))));
    q_vapour(i) = mean(q_vap(((i-1)*(N_heat + N_avg) + N_heat +
1):((i)*(N_heat + N_avg))));
    T_avg(i) = mean(Tavg(((i-1)*(N_heat + N_avg) + N_heat +
1):((i)*(N_heat + N_avg))));
    T_max(i) = mean(Tmax(((i-1)*(N_heat + N_avg) + N_heat +
1):((i)*(N_heat + N_avg))));
    T_min(i) = mean(Tmin(((i-1)*(N_heat + N_avg) + N_heat +
1):((i)*(N_heat + N_avg))));
    T_calc(i) = mean(Tcalc(((i-1)*(N_heat + N_avg) + N_heat +
1):((i)*(N_heat + N_avg))));
    max_vapour_vof(i) = mean(max_vap_vof(((i-1)*(N_heat + N_avg) +
N_heat + 1):((i)*(N_heat + N_avg))));
end

Determining average HTC and contributions of heat flux components
q_conv = q_tot - q_evap - q_quench;
h_avg = (q_tot./W_m2_to_W_cm2)./(T_avg - T_in);
j = 1:n;
q_conv_c = q_conv(j)./max(q_tot(j),q_conv(j));
q_quench_c = q_quench(j)./max(q_tot(j),q_conv(j));
q_evap_c = q_evap(j)./max(q_tot(j),q_conv(j));
q_tot_c = max(q_input(j),q_conv(j));
end

```

Figure A - 9: Data processing Matlab code for multi-jet array with conjugation.

```

clear all
T_in = 20.14;
load("Experimental")
T_super_heat_exp = Experimental(:,1);
q_tot_exp = Experimental(:,2);
T_avg_exp = T_super_heat_exp + 29.14;

```



```
h_avg_exp = (q_tot_exp.*10000)./(T_avg_exp - T_in);  
err_q = 0.3*q_tot_exp;  
err_T = 0.3*T_super_heat_exp;  
clear Experimental
```

Without Conjugation

```
[q_tot_liq_new,q_quench_liq_new,q_conv_liq_new,q_evap_liq_new,T_avg_liq_new,T_avg_calc_new...  
,q_liquid_liq_new,q_vapour_liq_new,h_avg_liq_new,h_avg_calc_new,q_conv_c  
,q_quench_c,q_evap_c,q_tot_c,Flow_Time_liq_new,T_min_NC,T_max_NC,q_tot_data_liq_new,T_avg_data_liq_new,q_conv_data_liq_new] =  
Results_Processing_no_conjugation("Full_Boiling_Curve_Without_Conjugation",T_in,9000,1000);
```

With Conjugation

```
[q_tot,q_quench,q_conv,q_evap,T_avg,q_input,h_avg,Flow_Time,T_min,T_max,T_calc,max_vapour_vof,q_conv_cont ...  
,q_quench_cont,q_evap_cont,q_tot_cont,q_tot_data,T_avg_data,q_conv_data] =  
Results_Processing("Full_Boiling_Curve_With_Conjugation",T_in,30000,30000);
```

Plots Boiling Curve

```
figure(1)  
clf  
plot(T_super_heat_exp,q_tot_exp,"o","MarkerFaceColor","r","Color","r","MarkerSize",12)  
hold on  
plot(T_avg_liq_new(1:end) - 29.14,q_tot_liq_new(1:end),"s","Color","c","MarkerSize",14)  
plot(T_avg(1:end) - 29.14,q_input(1:end),"s","MarkerFaceColor","m","Color","m","MarkerSize",14)  
plot(T_calc(1:end) - 29.14,q_input(1:end),"^","MarkerFaceColor","m","Color","m","MarkerSize",14)  
errorbar(T_super_heat_exp,q_tot_exp,0.0435*q_tot_exp,"ro")  
hold off  
axis([-5,40,0,250])  
set(gca,'fontsize',16)  
xlabel("Average Wall Superheat [°C]","FontSize",16)  
ylabel("Wall Heat Flux [W/cm2"],"FontSize",16)  
legend("Experimental Data","Current Study (Without Conjugation)"...  
, "Current Study (With Conjugation)","T_{calc} Current Study (With Conjugation)", "location", "northwest", "FontSize",16)
```

Contributions of RPI Wall Boiling Model Heat Flux Components

```
figure(2)  
clf  
plot(q_tot_c,q_evap_c,"cs-",q_tot_c,q_quench_c,"co-",q_tot_c,q_conv_c,"c^-","MarkerSize",14)  
hold on  
plot(q_tot_cont,q_evap_cont,"ms-",q_tot_cont,q_quench_cont,"mo-",q_tot_cont,q_conv_cont,"m^-","MarkerSize",14,"MarkerFaceColor","m")  
hold off  
axis([1,160,-0.05,1])  
set(gca,'fontsize',16)  
xlabel("Wall Heat Flux (W/cm2)","fontsize",16)  
ylabel("Contribution Fraction to Wall Heat Flux","fontsize",16)
```

```

legend("q_E Current Study (Without Conjugation)", "q_Q Current Study (Without Conjugation)", ...
      "q_C Current Study (Without Conjugation)", "q_E Current Study (With Conjugation)", ...
      "q_Q Current Study (With Conjugation)", "q_C Current Study (With Conjugation)", "location", "east", "fontSize", 16)

```

Boiling Curve Illustrating the Effects of Conjugation

```

figure(3)
clf
plot(T_min_NC(1:end) - 29.14, q_tot_liq_new(1:end), ">", "Color", "c", "MarkerSize", 14)
hold on
plot(T_min(1:end) - 29.14, q_input(1:end), ">", "MarkerFaceColor", "m", "Color", "m", "MarkerSize", 14)
plot(T_avg_liq_new(1:end) - 29.14, q_tot_liq_new(1:end), "s", "Color", "c", "MarkerSize", 14)
plot(T_avg(1:end) - 29.14, q_input(1:end), "s", "MarkerFaceColor", "m", "Color", "m", "MarkerSize", 14)
plot(T_max_NC(1:end) - 29.14, q_tot_liq_new(1:end), "<", "Color", "c", "MarkerSize", 14)
plot(T_max(1:end) - 29.14, q_input(1:end), "<", "MarkerFaceColor", "m", "Color", "m", "MarkerSize", 14)
hold off
axis([-5, 40, 0, 160])
set(gca, "fontSize", 16)
xlabel("Average Wall Superheat [" + string(char(176)) + "C]", "FontSize", 16)
ylabel("Wall Heat Flux [W/cm^{2}]", "FontSize", 16)
legend("T_{min} (Without Conjugation)", "T_{min} (With Conjugation)", "T_{avg} (Without Conjugation)" ...
      , "T_{avg} (With Conjugation)", "T_{max} (Without Conjugation)", "T_{max} (With Conjugation)" ...
      , "location", "northwest", "FontSize", 16)

```

Wall Heat Flux and Wall Temperature vs Flowtime (Without Conjugation)

```

figure(4)
clf
plot(Flow_Time_liq_new, T_avg_data_liq_new - 29.14)
hold on
yyaxis right
plot(Flow_Time_liq_new, max(q_tot_data_liq_new, q_conv_data_liq_new), "b-")
hold off
xlabel("Flowtime [s]", "fontSize", 14)
yyaxis left
ylabel("Wall Superheat [" + string(char(176)) + "C]", "fontSize", 14)
yyaxis right
ylabel("Wall Heat Flux [W/cm^2]", "fontSize", 14)
legend("T_{Heated Surface Average Temperature}", "Wall Heat Flux", "location", "northwest", "fontSize", 14)
ax = gca;
a = get(gca, 'XTickLabel');
set(gca, 'XTickLabel', a, 'fontSize', 14)
ax.YColor = 'k'; %Red
ax.YColor = 'b'; %Blue
axis([0, 120, -5, 160])

```

Wall Heat Flux and Wall Temperature vs Flowtime (With Conjugation)

```
figure(5)
clf
plot(Flow_Time,T_avg_data - 29.14)
hold on
yyaxis right
plot(Flow_Time,max(q_tot_data,q_conv_data),"b-")
hold off
xlabel("Flowtime [s]","fontsize",14)
yyaxis left
ylabel("Wall Superheat [" + string(char(176)) + "C]","fontsize",14)
yyaxis right
ylabel("Wall Heat Flux [W/cm^2]","fontsize",14)
legend("T_{Heated Surface Average}","Wall Heat Flux","location","northwest","fontsize",14)
ax = gca;
a = get(gca,'XTickLabel');
set(gca,'XTickLabel',a,'fontsize',14)
ax.YColor = 'k'; %Red
ax.YColor = 'b'; %Blue
axis([0,670,-5,160])
```

Figure A - 10: Matlab code for plots of the multi-jet array.

```
import numpy as np
```

Meshgrid of H/D

```
H_D = np.array([[1,2,4,8],
               [1,2,4,8],
               [1,2,4,8]])
```

Meshgrid of Reynolds Numbers

```
Re = np.array([[30000,30000,30000,30000],
              [40000,40000,40000,40000],
              [50000,50000,50000,50000]])
```

Meshgrid of Total HTC (Extracted From Processing Code)

```
HTC_Tot = np.array([[32.2537,34.5091,37.4803,40.1903],
                   [32.0740,33.5383,35.3797,37.9457],
                   [31.9043,32.7666,34.1155,36.0293]])
```

Meshgrid of Quenching HTC (Extracted From Processing Code)

```
HTC_Quench = np.array([[2.7879,3.0085,2.8511,2.3991],
                       [3.1852,3.4355,3.3355,2.9076],
                       [3.4697,3.6855,3.6202,3.3071]])
```

Meshgrid of Evaporative HTC (Extracted From Processing Code)

```
HTC_Evap = np.array([[29.4658,31.5006,34.6292,37.7911],
                    [28.8888,30.1028,32.0442,35.0381],
                    [28.4346,29.0810,30.4953,32.7222]])
```

Contour Plots

```
%matplotlib qt5
from matplotlib import pyplot as plt
from matplotlib import cm
```

Total HTC

```
fig1, ax1 = plt.subplots(subplot_kw={"projection": "3d"})
surf1 = ax1.plot_surface(H_D[0:4,0:4], Re[0:4,0:4], HTC_Tot[0:4,0:4], cmap = 'autumn_r',
edgecolor="black")
ax1.set_xlabel("H/D",fontsize=12)
ax1.set_ylabel("Jet Reynolds Number",fontsize=12)
ax1.set_zlabel("$HTC_{Total}$" + " " + "$[kW/(m^{2}K)]$",fontsize=12)
ax1.set_xlim(0.5,4)
ax1.set_ylim(29000,51000)
ax1.set_xticks([1,2,4,8])
ax1.set_yticks([30000,40000,50000])
plt.show()
```

Quenching HTC

```
fig2, ax2 = plt.subplots(subplot_kw={"projection": "3d"})
surf2 = ax2.plot_surface(H_D[0:4,0:4], Re[0:4,0:4], HTC_Quench[0:4,0:4], cmap = 'autumn_r',
edgecolor="black")
ax2.set_xlabel("H/D",fontsize=12)
ax2.set_ylabel("Jet Reynolds Number",fontsize=12)
ax2.set_zlabel("$HTC_{Quenching}$" + " " + "$[kW/(m^{2}K)]$",fontsize=12)
ax2.set_xlim(0.5,4)
ax2.set_ylim(29000,51000)
ax2.set_xticks([1,2,4,8])
ax2.set_yticks([30000,40000,50000])
plt.show()
```

Evaporative HTC

```
fig3, ax3 = plt.subplots(subplot_kw={"projection": "3d"})
surf3 = ax3.plot_surface(H_D[0:4,0:4], Re[0:4,0:4], HTC_Evap[0:4,0:4], cmap = 'autumn_r',
edgecolor="black")
ax3.set_xlabel("H/D",fontsize=12)
ax3.set_ylabel("Jet Reynolds Number",fontsize=12)
ax3.set_zlabel("$HTC_{Evaporation}$" + " " + "$[kW/(m^{2}K)]$",fontsize=12)
ax3.set_xlim(0.5,4)
ax3.set_ylim(29000,51000)
ax3.set_xticks([1,2,4,8])
ax3.set_yticks([30000,40000,50000])
plt.show()
```

Figure A - 11: Python code for contours of the multi-jet array parametric study.